DISCLAIMER

INL/RPT-25-85834
ANL/NSE-25/29

Gas-Cooled High-Temperature Pebble-Bed Reactor Reference Plant Model Updates

JUNE 2025

Mustafa K. Jaradat,
David Reger,
Victor Coppo Leite, and
Javier Ortensi

Idaho National Laboratory

Zhiee Jhia Ooi,
Ling Zou, and
Rui Hu

Argonne National Laboratory

Cole Takasugi

U.S. Nuclear Regulatory Commission

Idaho National Laboratory

Argonne NATIONAL LABORATORY

Battelle Energy Alliance manages INL for the U.S. Department of Energy's Office of Nuclear Energy

INL/RPT-25-85834 ANL/NSE-25/29

Gas-Cooled High-Temperature Pebble-Bed Reactor Reference Plant Model Updates

Mustafa K. Jaradat,
David Reger,
Victor Coppo Leite, and
Javier Ortensi
Idaho National Laboratory
Zhiee Jhia Ooi,
Ling Zou, and
Rui Hu
Argonne National Laboratory
Cole Takasugi
U.S. Nuclear Regulatory Commission

June 2025

Idaho National Laboratory
Reactor System Design and Analysis
Idaho Falls, Idaho 83415

http://www.inl.gov

Prepared for the
Office of Nuclear Regulatory Research
U. S. Nuclear Regulatory Commission
Washington, D. C. 20555
Task Order No.:
31310019F0015 and 31310021F0005

ABSTRACT

This work presents the latest improvements to, and investigations performed with, the pebble-bed high-temperature gas-cooled reactor (PB-HTGR) reference plant models for the United States Nuclear Regulatory Commission. These models serve as the foundation for the future development of detailed design evaluation models based on license applications. The reference plant models have been developed with the Comprehensive Reactor Analysis Bundle, or BlueCRAB, which is the code suite proposed for non-light-water reactor systems safety analysis. It incorporates various simulation tools developed by the Nuclear Energy Advanced Modeling and Simulation program, including the Griffin code for reactor physics, the Pronghorn and SAM codes for core thermal fluids, the BISON code for solid conduction and fuel performance, and the SAM code for system analysis.

The primary objective of the work that was performed was to assess BlueCRAB's level of readiness for modeling a PB-HTGR. To do so, we first developed numerical models in BlueCRAB that include the key physics for this technology to ensure an adequate level of fidelity for modeling PB-HTGR core performance and for performing multiphysics simulations for equilibrium core conditions and different accident scenarios. Then we simulated transient scenarios, including depressurized and pressurized loss of forced cooling accidents, over-cooling, and control rod withdrawal events with delayed and prompt supercritical reactivity insertions. The analysis in this report includes comparisons of the 2D thermal fluid porous media models in Pronghorn and SAM, and comparisons of coupled SAM/Griffin/SAM and coupled Pronghorn/Griffin for depressurized and pressurized loss of forced cooling, over-cooling, and control rod withdrawal events. In addition, we compare 3D, 2D, and 0D/PKE neutronic models for the two control rod withdrawal scenarios with coupled Pronghorn/Griffin.

The comparisons show that the BlueCRAB models lead to physically intuitive solutions for the scenarios examined. The changes in the various scalar and vector fields, such as neutron flux, power, temperature, density, pressure, and velocity, are within the expected ranges, and their distributions can be explained by the system response of the transients and the geometric and material variations. Several comparisons suggest that the porous media models in Pronghorn and SAM can lead to similar solutions, even though they are based on different methodologies.

This work further highlights the need for flexible tools with various levels of fidelity to cover the breadth and depth of needs that may arise in future technical evaluations of the PB-HTGR. We believe that the BlueCRAB capabilities will be a significant asset for confirmatory analyses in order to resolve important safety questions.

Page intentionally left blank

CONTENTS

FIGURES

TABLES

ACRONYMS

DLOFC	depressurized loss of forced cooling
HTC	heat transfer coefficient
HTR-PM	High-Temperature Gas Cooled Reactor–Pebble-Bed Module
IQS	improved quasi-static
KLAK	Kleine Absorber Kugel Systeme
MOOSE	Multiphysics Object-Oriented Simulation Environment
NEAMS	Nuclear Energy Advanced Modeling and Simulation
NRC	Nuclear Regulatory Commission
PB-HTGR	pebble-bed high-temperature gas-cooled reactor
PBR	pebble-bed reactor
PIRT	Phenomena Identification and Ranking Table
PKE	point kinetics equation
PLOFC	pressurized loss of forced cooling
RCCS	reactor cavity cooling system
RIA	reactivity insertion accident
RPV	reactor pressure vessel
SAM	System Analysis Module
TRISO	tristructural isotropic
UOC	unprotected over-cooling
VSOP	Very Superior Old Programs

Page intentionally left blank

ACKNOWLEDGMENTS

The authors would like to acknowledge the support and assistance from Stephen Bajorek, Tarek Zaki, Andrew Bielen, Nazila Tehrani, and Jason Thompson of the United States Nuclear Regulatory Commission in the completion of this work. This work would not have been possible without the contributions from the Idaho National Laboratory Griffin development team: Yaqi Wang, Josh Hanophy, Olin Calvin, and Namjae Choi. This work would not have been possible without the contributions from members of the Idaho National Laboratory Pronghorn development team: Mauricio Tano. This work was performed in conjunction with Idaho National Laboratory, Argonne National Laboratory, and the U.S. Nuclear Regulatory Commission under Task Order Agreement No. 31310019F0015 and 31310021F0005. This research made use of the resources of the High Performance Computing Center at Idaho National Laboratory, which is supported by the Office of Nuclear Energy of the U.S. Department of Energy and the Nuclear Science User Facilities under Contract No. DE-AC07-05ID14517.

Page intentionally left blank

Gas-Cooled High-Temperature Pebble-Bed Reactor Reference Plant Model Updates

1. INTRODUCTION

This report presents the development of reference plant models of a pebble-bed high-temperature gas-cooled reactor (PB-HTGR) for the United States Nuclear Regulatory Commission (NRC) with the High-Temperature Gas Cooled Reactor–Pebble-Bed Module (HTR-PM) as the reference. The purpose of this work is to demonstrate the readiness of the Comprehensive Reactor Analysis Bundle, or BlueCRAB, tool suite to model a PB-HTGR. In the following sections, the system of the HTR-PM is described first, followed by a brief description of the transient scenarios that were simulated for this work. Next, the modeling methodology is discussed, including the meshing of the 2D and 3D geometries, the neutronics and thermal fluids modeling approaches, as well as the coupling strategies of the different models. Then the modeling results are discussed, starting with the steady-state equilibrium conditions followed by the results from the transient scenarios. Finally, the findings of the report are summarized and areas of future work are suggested.

1.1. System Description

The HTR-PM design is based on the combined experience of the German pebble-bed reactor program of the 1960s through the 1990s and the Chinese HTR-10 program [1] during the 2000s. Currently, two HTR-PM reactors are in operation at the Shidao Bay nuclear power plant in China. We selected the HTR-PM reactor for this study because of the availability of open literature data, the HTR-PM is the only pebble-bed reactor currently in operation, and its design is contemporaneous with past concepts.

The HTR-PM reactor layout can be found in Reference [2]. The full system layout is shown in Figure 1. The main characteristics include a cylindrical pebble-bed region surrounded by radial, top cavity, lower, and upper reflectors. The pebble bed has an average packing factor of 0.61 with roughly 420,000 pebbles. The outer diameter of the pebbles is 6 cm. The radial reflector includes various orifices for the control rod channels, Kleine Absorber Kugel Systeme (KLAK) channels (shutdown system), and fluid riser channels. The HTR-PM design specifications are listed in Table 1.

1	Reactor core
2	Side reflector & carbon thermal shield
3	Core barrel
4	Reactor pressure vessel (RPV)
5	Steam generator
6	Steam generator vessel
7	Coaxial hot-gas duct
8	Water cooling panel
9	Blower
10	Fuel discharging tube
11	Control rod driving system
12	Small absorber sphere unit
13	Fuel charging tube
14	Top cavity

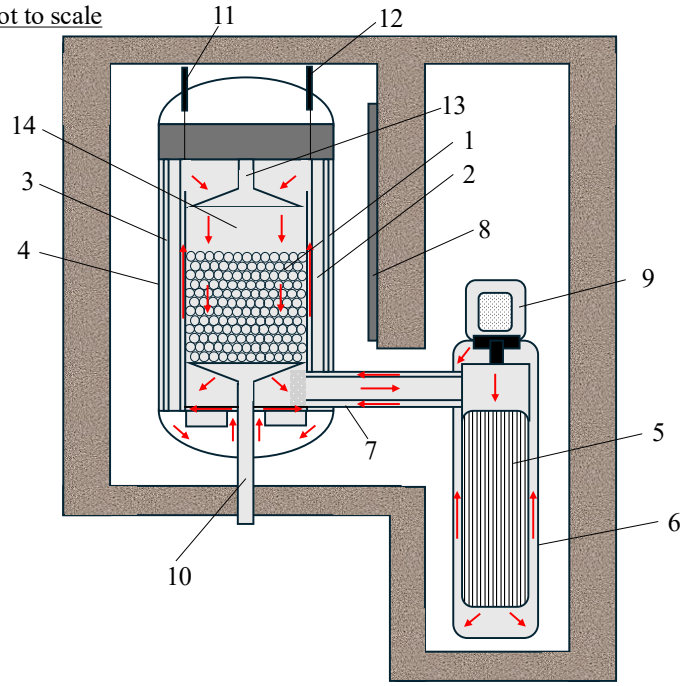

Figure 1. Full system layout of the HTR-PM, reproduced from Reference [3].

The HTR-PM has a core thermal power of 250 MW. It is helium-cooled and operates at 7 MPa during steady-state normal operating conditions. Helium enters the core at 523.15 K and exits at 1023.15 K at a mass flow rate of 96 kg/s. Helium flows into the core through the outer channel of the coaxial duct and upward through the riser channels into the top plenum. It then flows downward through the pebble bed where heat is removed by the helium flow. The hot helium then enters the bottom plenum located below the pebble bed before flowing out of the core through the inner channel of the coaxial duct to the steam generator, where it is cooled. After exiting the steam generator at the bottom, the cold helium then flows upward along the steam generator vessel back to the blower to complete the circuit.

In the HTR-PM, the reactor cavity cooling system (RCCS) is designed as a passive system to remove the heat from the reactor pressure vessel (RPV) and reactor cavity to the final heat sink (the atmosphere) under normal operating conditions and accident scenarios, ensuring the thermal integrity of the RPV and the cavity concrete [3]. Water cooling panels consisting of vertical cooling tubes and a cylindrical plate are placed on the surface of the reactor cavity concrete. The cooling tubes are welded uniformly on the plate. During accident scenarios, heat is transferred via thermal radiation and natural convection in the reactor cavity from the RPV surface to the water cooling panels. The heated water in the tubes flows upward to the air-water heat exchangers in the air-cooling tower where heat is finally transferred to the atmosphere.

Table 1. HTR-PM core specifications [2–4].

Parameter	Value
Core power (MWth)	250.00
Core inlet temperature (K)	523.15
Core outlet temperature (K)	1023.15
Core outlet pressure (MPa)	7.0
Primary helium flow rate (kg/s)	96.0
Pebble-bed radius (m)	1.50
Pebble-bed height (m)	11.00
Reflector outer radius (m)	2.50
Control rods channels	24
Reactivity shutdown channels	4
Barrel outer radius (m)	2.69
Bypass outer radius (m)	1.69
Vessel outer radius (m)	3.00
Number of pebbles	419,384 (420,000)
Pebble types	1 pebble type
Pebble packing fraction (average)	0.61
Average number of passes	15
Average pebble residence time (days)	70.5
Steam pressure (MPa)	13.9
Steam generator temperature (K)	844.15
Feedwater temperature (K)	478.15

The pebble and tristructural isotropic (TRISO) design specifications used in the equilibrium core are included in Tables 2 and 3, respectively. These specifications are based on the uranium oxide fuel tested in the HTR-10 prototype [5]. There are some discrepancies in the buffer layer thickness from the references, 90 μm in Reference [6] versus 95 μm in Reference [5]. We opted for the 90-μm design.

Table 2. HTR-PM pebble specifications [4, 7].

Parameter	Value
Fueled region radius (cm)	2.5
Shell layer thickness (cm)	0.5
Pebble diameter (cm)	6.0
Heavy metal loading per pebble (g)	6.95
Number of particles per pebble	11,668
Particle packing (%)	7.034
Discharge burnup (MWd/kg, J/m^3)	90, 4.82×10^{14}
Fuel layer matrix density (kg/m^3)	1,730
Shell layer graphite density (kg/m^3)	1,730

Table 3. HTR-PM TRISO particle specifications [5, 6].

Parameter	Value
Fuel kernel radius (cm)	0.025
Buffer outer radius (cm)	0.034
IPyC outer radius (cm)	0.038
SiC outer radius (cm)	0.0415
OPyC outer radius (cm)	0.0455
Particle diameter (cm)	0.091
Fuel type	UO_2
Fuel enrichment	8.6%
Fuel kernel density (kg/m^3)	10,400
Buffer graphite density (kg/m^3)	1,100
IPyC, OPyC graphite density (kg/m^3)	1,900
SiC density (kg/m^3)	3,180

1.2. Scenario Selection And Description

In addition to steady-state normal operating conditions, several transient scenarios were simulated in this work. These scenarios can largely be grouped into transients driven by thermal fluids or neutronics. The thermal-fluids-driven transients are protected depressurized loss of forced cooling (DLOFC), protected pressurized loss of forced cooling (PLOFC), and unprotected over-cooling (UOC), whereas the neutronics-driven transient selected for this work is reactivity insertion accident (RIA) via control rod withdrawal.

1.2.1. Loss of Forced Cooling

The protected DLOFC and PLOFC transients were selected because they are among the scenarios for which safety-related phenomena are identified through the Phenomena Identification and Ranking Table (PIRT) process for the HTR-PM [8]. The DLOFC scenario assumes that a rapid depressurization occurs in the core and causes the reactor to undergo an emergency shutdown. In this work, the rupture was assumed to occur at the coaxial duct, which isolates the core from the remainder of the primary circuit. Possible scenarios following depressurization such as air ingress were not modeled in the current work and will be addressed in future work. DLOFC is considered the bounding condition for determining the peak value

of the maximum fuel temperature under design basis accidents [8]. Given that the core is depressurized, the buoyancy force cannot establish significant natural circulation in the core because there is very little convection effect for helium under atmospheric pressure. As a result, conduction and thermal radiation are the dominant mechanisms for decay heat to transfer from the fuel to the RPV.

On the other hand, the PLOFC transient is characterized by the reactor SCRAM from normal operating conditions and the loss of forced cooling in the core. During PLOFC, the reactor remains pressurized and stays at full system pressure [8]. During PLOFC, natural circulation is established by the pressurized helium in the core due to the buoyancy effect. Consequently, it is expected that decay heat is distributed widely in the core. Due to the natural circulation in the core, the maximum fuel temperature is typically not a concern in the PLOFC scenario as it stays far below the safety limit.

1.2.2. Unprotected Over-Cooling Accident

The UOC transient is one of the exercises recommended by the OECD-NEA PBMR-400 transient benchmark report [9]. It intends to simulate the opening of a bypass valve where ”cold” helium is injected into the core inlet plenum while other system parameters, such as pressure and control rod positions, are kept unchanged. Given that no bypass valve is included in the current model, the change of helium temperature is achieved by changing the secondary coolant temperature of the heat exchanger. The transient is initiated by applying a temperature decrease of 50 K to the inlet helium temperature over 10 seconds, followed by no changes in the system parameters for 300 seconds. After that, the inlet temperature is raised back up by 50 K to the normal operation value over 10 seconds. As forced convection is present in the core, fuel temperature is expected to remain well below the safety limit. Additionally, given that the transient lasts for less than an hour, no significant temperature changes are expected in regions outside of the pebble bed, such as the side reflectors, core barrel, and RPV. The UOC transient is intended to investigate the system’s response and reactivity feedback mechanisms to sudden changes in core temperature.

1.2.3. Reactivity Insertion Accident

The standard assumption for the control rod withdrawal scenario in pebble-bed reactors is either a control system error or operator error that causes a continuous withdrawal of the highest-worth control rod at the maximum control rod drive speed. In this scenario, a rapid withdrawal of the control rod from its initial position until it is out of the active core region is assumed. When the reactor protection system detects the reactivity insertion, it initiates the insertion of all control and shutdown elements and thus fulfills the reactivity control function.

To test the physics included in the numerical models, we simulated two fictional control rod withdrawal events: delayed-supercritical and prompt-supercritical events. The two transients involve the inadvertent movement of one and two control rods, respectively. Also, it is assumed that the reactor protection system is not activated. Instead, the control rod is reinserted back to its initial position after a certain amount of time. These events test the physics for delayed- and prompt-supercritical reactivity insertion events and the corresponding feedback physics.

2. METHODOLOGY

Multiphysics coupled simulations were performed for the HTR-PM reactor using the Comprehensive Reactor Analysis Bundle (CRAB, or alternatively, BlueCRAB) code suite. Specifically, this work utilized the Griffin [10] code for reactor physics, the Pronghorn [11] and System Analysis Module (SAM) [12] codes for core thermal fluids, the BISON [13] code for solid conduction and fuel performance, and SAM for system-level analysis. Griffin is a time-dependent finite-element-based reactor physics code with weak form formulations for diffusion, spherical harmonics (PN), and discrete ordinates (SN) transport, and it has a variety of equivalence techniques. Pronghorn is a multidimensional thermal fluids code for advanced nuclear reactors that is capable of intermediate-fidelity, coarse-mesh computational fluid dynamics for advanced nuclear reactors. BISON is a nuclear fuel performance code that can model light-water reactor (LWR) fuel rods, TRISO particle fuel, metallic rod and plate fuel, and other fuel forms. SAM is a system analysis tool for advanced non-LWR safety analysis; it is capable of system-level modeling with built-in components as well as higher-fidelity flow modeling with its multi-D flow models.

In this work, Griffin was used for the neutronics calculations, while porous media models developed separately using Pronghorn and SAM were used for the thermal fluids calculations of the core. Outside of the core, the primary loop and RCCS were modeled using SAM's component system. As a result, two sets of coupled models were developed, namely the SAM/Griffin/SAM model and the Pronghorn/Griffin model. For the remainder of this report, the coupled models are named following this format: the first name is the code used for modeling the porous media core, the second name is the code for modeling the neutronics, and the third name is the code for modeling the primary loop and RCCS. For instance, with the Pronghorn/Griffin/SAM model, Pronghorn's porous media model was used for thermal fluids calculations in the core, Griffin for neutronics calculation, and SAM for thermal fluids calculations in the primary loop and RCCS.

The applicability of the point reactor approximation is always an important question in reactor physics due to the underlying assumption of the separability of the neutron population density from the flux shape. Some scenarios that involve large changes to the flux distribution—i.e., control rod movement—can invalidate this assumption, and it is common practice to apply penalties to the point kinetics equation (PKE) parameters (reactivity, mean generation time, or delayed neutron fraction). Another approach is to rely on a spatial dynamics solution to better understand the accuracy of the PKE solution in specific scenarios. Ideally, one would rely on a high-fidelity coupled transport calculation that can serve as a reference solution to provide confidence in the results. In this work, we deployed Griffin's multigroup diffusion solver in 3D to provide such a reference solution. In addition, we also developed a 2D model equivalent of this reference 3D model. In the future, Griffin's SN transport is recommended as a reference solution. The PKE theory and Griffin PKE model are discussed in Section 2.2.4.

The porous media approach was adopted for modeling the core. Two 2D R-Z axisymmetric models of the core were developed with Pronghorn and SAM. The primary difference between the two models is that SAM is a finite-element-based code while Pronghorn is a finite-volume-based code. The 2D models are necessary to capture the relatively complex fluid flow and heat transfer phenomena in the core, especially during certain transient scenarios. In the remainder of this section, details of the models, including the meshing, coupling, assumptions, and simplifications, are discussed.

2.1. Meshing

The geometric representation of the reactor structures and components is shown in Figure 2. The pebbles and helium coolant flow in the negative axial direction. The pebbles enter the core through the upper cavity (4), then flow to the pebble-bed region (1) and exit through the outlet cone (2) and the chute (3). The coolant enters the bottom of the riser channel (9), flows to the cold plenum (6), and continues to the pebble-bed region

(1) until it exits the core at the sides of the hot plenum (8).

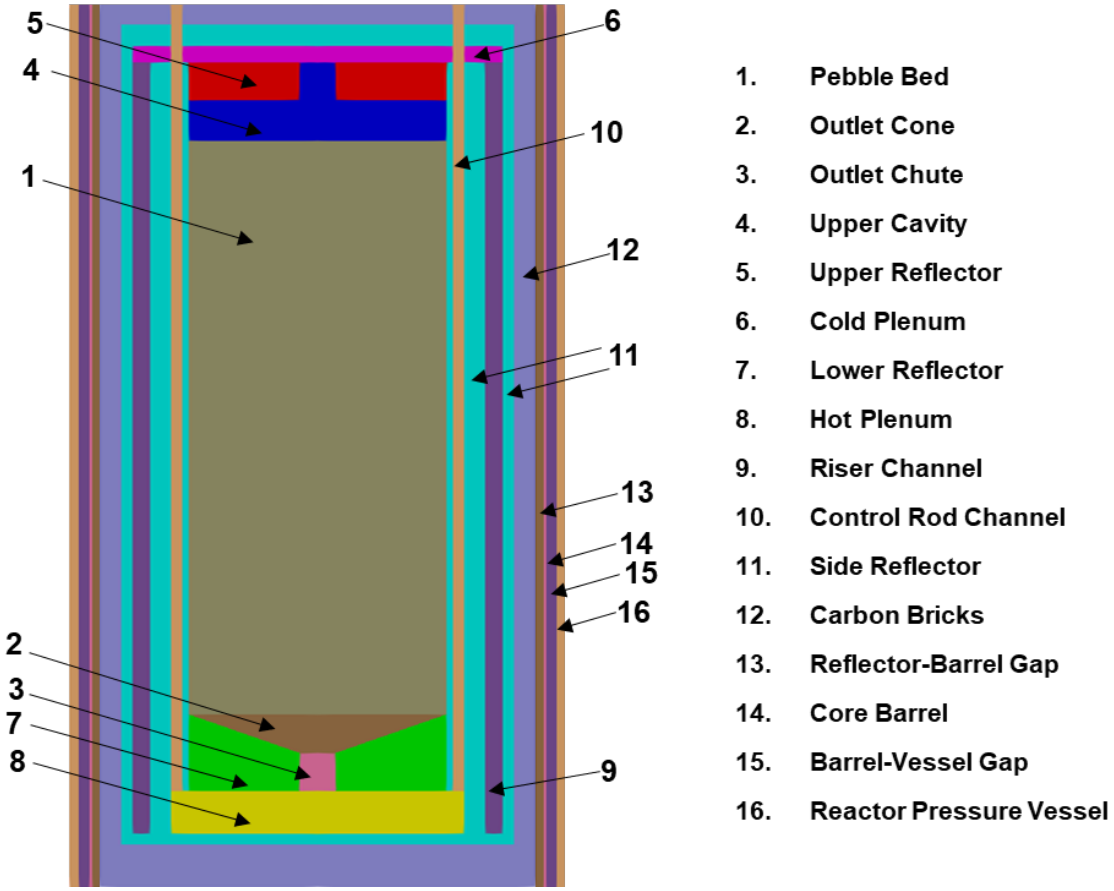

Figure 2. HTR-PM geometric regions.

The finite element mesh used in the 2D and 3D models was developed using CUBIT [14] via the Python application programming interface. Figure 3 shows the computational mesh of the 2D and 3D models. In order to minimize the number of elements and thus the computational cost, the mesh was generated with quadrilateral elements that can be easily extruded in 3D. For the 3D cylindrical geometry, there is always a compromise on how to mesh the center of the geometry, and we chose to keep quadrilateral elements to maintain the core regions in a single block ID region, with single geometry regions in the Exodus [15] format. It should be mentioned that the computational mesh presented in Figure 3 was used for thermal fluids calculations, while the neutronics computational mesh omits the region beyond the carbon bricks region, namely the core barrel (14), RPV (16), and the two gaps (13, 15). Figure 4 shows examples of the meshing used in the analysis of the 3D model.

2.2. Core Neutronics Modeling Approach And Assumptions

This section describes the developed neutronics model used in the analysis performed with Griffin. Section 2.2.1 discusses the cross-section generation procedure briefly. Section 2.2.2 describes the baseline model developed to compare the coupled Pronghorn/Griffin and SAM/Griffin models. Then, Section 2.2.3 presents the model developed to simulate the reactivity insertion accident using Griffin in 3D and 2D. Section 2.2.4 briefly describes the PKE developed model.

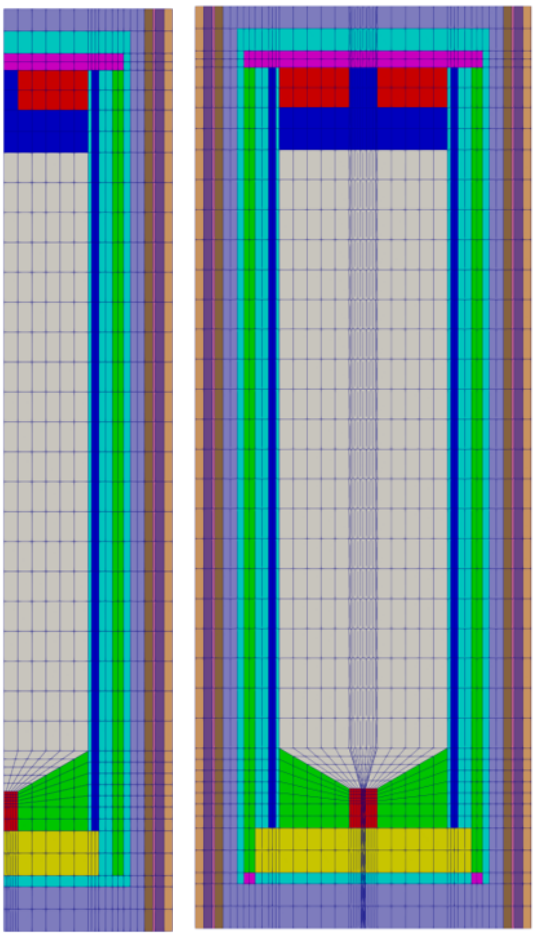

(a) 2D (b) 3D

Figure 3. HTR-PM computational mesh for 2D and 3D simulations of the Pronghorn/Griffin model.

2.2.1. Neutron Cross Sections

The lattice physics code DRAGON [16] was selected to prepare multigroup microscopic cross sections for this work. DRAGON includes a number of transport solvers and self-shielding models that have been in use at Idaho National Laboratory. The DRAGON data libraries used in this work are based on the ENDF/B-VIII.r0 evaluation [17]. The neutron leakage affects the local spectrum significantly, and it will have an impact on the cross-section homogenization. Nevertheless, the adopted approach satisfies the required cross-section tabulation needed to perform a preliminary analysis. The microscopic cross sections were condensed from 281 to nine energy groups and homogenized over the pebble. The nine-energy-group structure is provided in Table 4. This group structure will be optimized in future work during the deployment of the native Griffin cross-section methodologies [18].

The reactor feedback mechanism in the HTR-PM is attributed to changes in the temperature of the fuel (UO_2 kernel) and moderator for each pebble type and burnup group, and to changes in the temperature of the graphite reflector. The tabulation values for the cross sections generated for 294 isotopes are shown in Table 5 and are intended to support transient analyses. A detailed description of the cross-section generation procedure can be found in Reference [19].

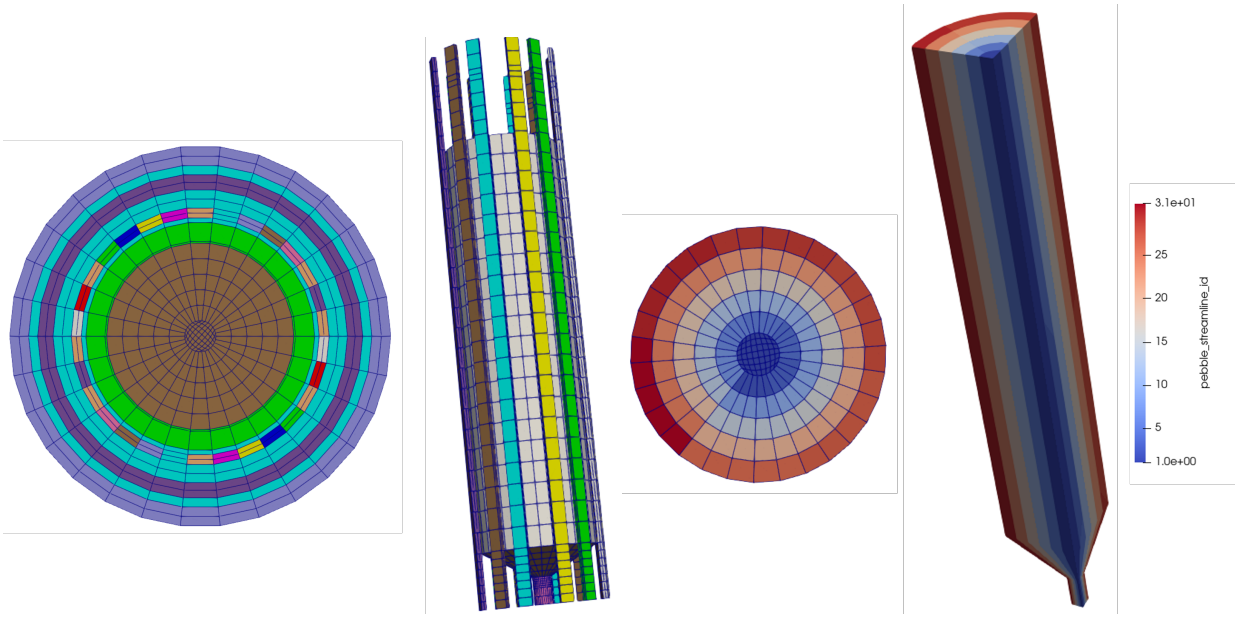

(a) Control Rod Mesh (b) Depletion Streamlines Mesh

Figure 4. HTR-PM computational mesh of the control rod region and pebble depletion streamlines used in 3D simulations of the Pronghorn/Griffin model.

Table 4. Cross-section energy group boundaries of the nine-group structure.

Group	Upper Energy (eV)	Lower Energy (eV)
1	1.96403000E+07	1.95007703E+05
2	1.95007703E+05	907.500671
3	907.500671	17.5647602
4	17.5647602	3.88216996
5	3.88216996	2.33006096
6	2.33006096	1.29303801
7	1.29303801	0.820037127
8	0.820037127	0.137999400
9	0.137999400	1.10002700E-04

Table 5. Microscopic cross-section tabulation parameters of the HTR-PM.

Parameter	Unit	Value
Burnup	J/cm^3	0.00, 2.78917×10^8, 5.38949×10^8
Fuel temperature	K	500, 700, 900, 1100, 1300, 1600, 2000
Moderator temperature	K	300, 500, 700, 900, 1100, 1300, 1600, 2000

2.2.2. Baseline Model

The HTR-PM baseline neutronics model was developed using Griffin, considering a 2D R-Z axisymmetric geometry with homogenized core regions. The main purpose of this simplified model is to provide a means to compare results from the coupled models of Pronghorn/Griffin and SAM/Griffin/SAM. The model consists

of 12 distinct regions, as shown in Figure 5. The descriptions of the various regions and their porosity are included in Table 6.

The pebble depletion calculation is performed using Griffin's streamline depletion capabilities in 1D, as discussed in Reference [20]. The Griffin baseline neutronics model uses six equally spaced streamlines centered within the active core elements (as shown on the *right* of Figure 5) to represent pebble depletion. The streamlines are located at radii of $r = 12.5, 37.5, 62.5, 87.5, 112.5, 137.5$ cm, representing channels whose right boundary is located at $r = 25, 50, 75, 100, 125, 150$ cm, respectively. The pebble velocity is assumed to be uniform so that the fraction of the volumetric flow rate of pebbles through each channel is proportional to the channel area. Axially, the six channels are straight in the cylindrical pebble-bed region and begin at the top of this region and end at the bottom of the outlet chute region.

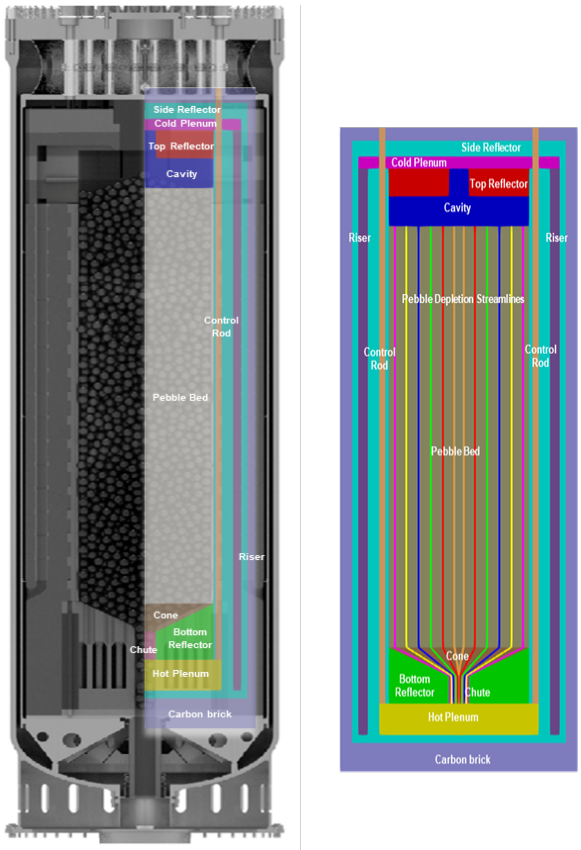

(a) 2D Equilibrium Core Model (b) 1D Streamline Model

Figure 5. Geometry of the HTR-PM baseline model used in neutronics calculations with Griffin.

With the exception of the detailed fuel composition, the neutronics characteristics of the fuel were adopted from Reference [7]. The fuel has a heavy metal loading of about 6.95 g per pebble, discharging at an average burnup of 90 MWd/kg and burning with an average power density of 3.215 MW/m^3 for a core with a power of 250 MW, a volume of 77.8 m^3, and a packing fraction of 0.61. The pebble speed is 15.6 cm/day, resulting in a pebble reloading rate of 5,949 pebbles per day. The discharge burnup of 90 MWd/kg is converted to 4.82×10^8 J/cm^3 using the heavy metal density per pebble volume of 61.9 kg/m^3. A total of 10 burnup groups were used to form the base discretization of the burnup variable. The first nine groups have a width of 5.35×10^7 J/cm^3 (10 MWd/kg), covering the burnup up to the average discharge limit of 4.82×10^7 J/cm^3; the last burnup group contains all discharge burnups. A summary of the streamline depletion specifications and the characteristics of the fuel are included in Table 7 and Table 8, respectively.

Table 6. Explanation of each region's solid fraction and material as depicted in Figure 5.

Region No.	Region name	Material	Porosity
1	Pebble bed	Pebbles/Helium	0.39
2	Cone	Pebbles/Helium	0.39
3	Chute	Pebbles/Helium	0.39
4	Upper reflector	Graphite/Helium	0.30
5	Lower reflector	Graphite/Helium	0.30
6	Cavity	Helium	1.00
7	Hot plenum	Graphite/Helium	0.20
8	Cold plenum	Graphite/Helium	0.20
9	Side reflector	Graphite	0.00
10	Carbon brick	Graphite	0.00
11	Homogenized riser / side reflector	Graphite/Helium	0.32
12	Empty control rod channel	Graphite/Helium	0.28

*Note that the values of the porosity for Regions 4, 5, 7, 8, 11, and 12 are due to the presence of structures and components.

Table 7. HTR-PM model streamline depletion specifications.

Parameter	Value
Number of streamlines	6 (equally spaced)
Number of pebble types	1
Number of burnup groups	10 (from 0–100 at 10 MWd/kgU intervals)
Discharge burnup (MWd/kgU, J/cm^3)	90, 4.82×10^8
Number of burnup groups (base)	10
Base discretization $\Delta\tau_b$ (J/cm^3)	5.35×10^7
Pebble speed (cm/day)	15.6
Pebble unloading rate (pebbles/day)	5,949

Table 8. HTR-PM fuel composition.

Isotope	Atom Density (1/b·cm)
U-234	1.09×10^{-7}
U-235	1.36×10^{-5}
U-238	1.42×10^{-4}
O-16	3.11×10^{-4}
O-17	1.18×10^{-7}
Graphite	8.54×10^{-2}
Si-28	3.14×10^{-4}
Si-29	1.59×10^{-5}
Si-30	1.05×10^{-5}
C-12	3.40×10^{-4}

2.2.3. Special Model for RIA

The main motivation for developing a 3D fully coupled model is to simulate an RIA due to a single rod movement or multiple rod movements. This results in a localized perturbation of the neutron flux and temperature distributions. To evaluate this impact on transient calculations, we compared the 3D model results to those of reduced-order models with 2D and a PKE. The HTR-PM design consists of 24 control rod channels and six secondary shutdown (KLAK) channels [21].

To mimic the effect of the control rod movement in the 3D model with that of the 2D model, an equivalent 2D model was developed by splitting the control rod region in the 2D model into two regions while preserving the volumes of each region. Figure 6 shows the neutronics 3D model with 24 control rod channels and 6 KLAK channels, where each control rod channel is homogenized with the surrounding graphite. Additionally, Figure 6 shows the equivalent 2D model that was developed. In the model the first region in the control rod channel represents a single control rod channel or two, and the second region the remaining control rods and KLAK channels. The B-10 concentration in the 2D equivalent control rod model was adjusted to match the worth of a single control rod or two control rods of the 3D model. Section 3.1 provides more details of the 3D and 2D equilibrium core results and the worth of a single control rod and two control rods.

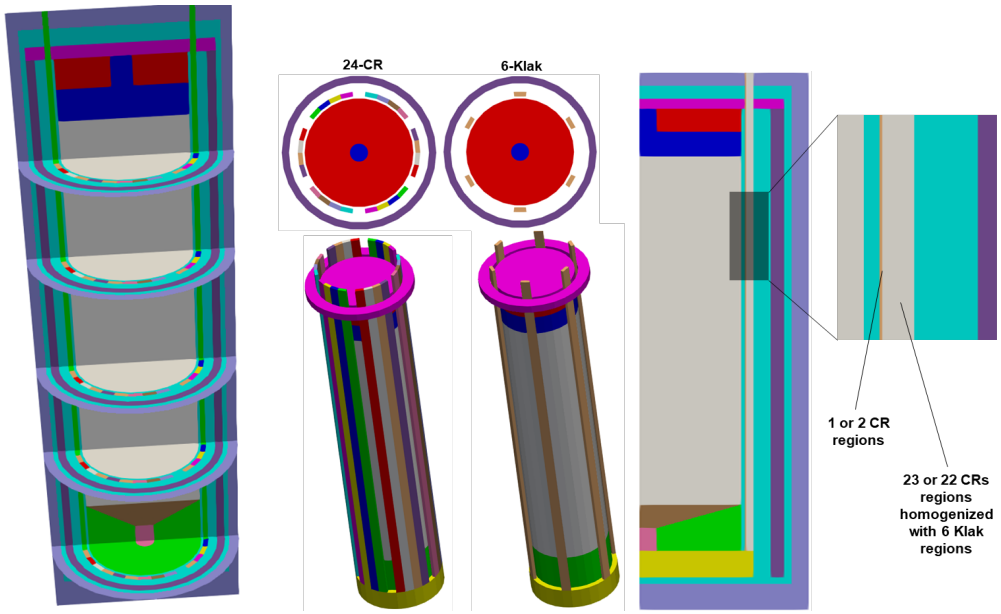

(a) 3D Model (b) 3D Control Rods (c) 2D Equivalent Model

Figure 6. 3D core model with control rod region and the equivalent 2D core model.

2.2.4. Griffin Point Kinetics

The point kinetics equation (PKE) can be derived from the multigroup transport equation and the delayed neutron precursor balance equation. The first assumption is to make the point reactor approximation via separation of variables (flux factorization). In essence, we assume that only the neutron density is time-dependent and that the neutron angular flux distribution (fundamental mode eigenfunction) is time-independent:

$$\phi_g(\vec{x}, \vec{\Omega}, t) = p(t)\Psi_{g,0}(\vec{x}, \vec{\Omega}) \tag{1}$$

After introducing the point reactor approximation, we integrate over angle and space, sum over the energy groups, and introduce a weighting function, typically the neutron importance or adjoint flux distribution, to arrive at:

$$\frac{dp(t)}{dt} = \frac{\rho(t) - \beta_{eff}}{\Lambda} p(t) + \sum_{i=1}^{I} \lambda_i C_i(t) \tag{2}$$

$$\frac{dC_i(t)}{dt} = \frac{\beta_i}{\Lambda} p(t) + \lambda_i C_i(t), \quad i = 1..I, \tag{3}$$

where t is time, p is the reactor power or neutron population, ρ is the reactivity introduced in the system, β_{eff} is the effective delayed neutron fraction, Λ is the neutron mean generation time, C_i is the concentration of the i-th neutron precursor group, and λ_i is the decay constant of the i-th neutron precursor group.

The Griffin PKE solver can be deployed in a 0D context to provide an approximation to the neutron transport equation. The PKE parameters Λ, β_{eff}, and λ_i can be calculated with Monte Carlo methods or from deterministic methods, such as Griffin. We assume that the neutron flux shape (forward and adjoint) does not change with time, which can be a significant approximation in some cases, such as for control rod movement. One of the most challenging components of the PKE model is the reactivity (ρ) model. Reactors that exhibit strong local feedback effects (strong thermalization) can be problematic, as opposed to reactors that exhibit global feedback effects (fast reactors). Traditionally, we couple a PKE model to a thermal fluids or system model to compute the global parameters for feedback, assuming that the power distribution in the core does not change significantly during the transient .

Reactivity models can vary significantly in complexity and the amount of effort required by the analyst. The Griffin PKE action system enables the user to couple the various components of the feedback mechanism separately. Griffin supports several reactivity modeling capabilities:

- Separable (linear combination) model: Relies on linear interpolation methods in the Multiphysics Object-Oriented Simulation Environment (MOOSE) framework with a parametrization of purely independent variables that leads to an incomplete physics model since it removes correlated physics that are potentially "weakly" dependent. This removal does not imply that the various feedback mechanisms are treated as linear functions.
- Partially correlated models: Use multivariate interpolation methods in MOOSE (n-linear, n-cubic, splines, etc.). This leads to an improved physics model since these methods include some correlated physics and off-diagonal dependencies in a dependency matrix (state point matrix)—e.g., moderator temperature effects on fuel temperature feedback due to spectrum hardening.
- Fully correlated models: Use the stochastic tools module in MOOSE [22] and the PyTorch MOOSE interface to generate and use surrogate models that can be directly employed in Griffin [23, 24].

The separable, or linear combination, model is used to represent the reactivity in the PKE model developed for the HTR-PM as

$$\rho(t) = \rho_{cr}(cr_{pos}(t)) + \rho_{fuel}(T_{fuel}(t)) + \rho_{mod}(T_{mod}(t)) + \rho_{ref}(T_{ref}(t)), \tag{4}$$

where ρ_{cr} is the inserted reactivity due to control rod movement, and ρ_{fuel}, ρ_{mod}, and ρ_{ref} are the feedback reactivities of the fuel, moderator, and reflector, respectively.

2.2.5. Reactor Physics Assumptions and Limitations

The following assumptions are made:

1. A 2D R-Z representation of the reactor core is used in some analyses, and it constitutes an adequate representation of the reactor geometry.

2. The multigroup neutron diffusion equation provides an accurate enough flux solution for the core and reflector regions for equilibrium core and time-dependent calculations.

3. The homogenized control rods in 3D and the control gray curtain in 2D are used to model the control rods and are not corrected using equivalence methods.

4. The multigroup cross sections are prepared using an infinite, reflected domain in the lattice physics calculation. The intracore neutron leakage significantly affects the local spectrum and will have an impact on the cross-section homogenization [25]. Nevertheless, cross sections serve as an initial set to perform preliminary calculations until more sophisticated methods are available in Griffin.

5. No streaming correction is applied to the pebble region. Although we could apply a Lieberoth [26] type streaming correction, the Griffin online cross-sections method includes an accurate streaming correction based on the Benoist method [27] and will be deployed in the future.

6. A flux-limited approximation of the isotope transport cross sections is sufficient to build acceptable diffusion coefficients for this reactor.

7. A 1D streamline depletion is sufficient to capture the pebble flow since experiments show that the flow is axially dominated [28].

2.3. Core Thermal Fluids Modeling Approach And Assumptions

2.3.1. SAM 2D Core Model

This section discusses the SAM 2D core model. The layout of the SAM 2D core model is shown in Figure 7. The 2D core is an axisymmetric domain in the R-Z coordinates. The pebble bed, chute, cone, top cavity, hot plenum, and upper and lower reflectors are modeled as porous regions that contain a mixture of coolant and solid, while the remaining components of the core are modeled as pure solid. The porosities of the porous regions are tabulated in Table 6.

The core is modeled primarily with SAM's multi-D capability. Several components, such as the riser, control rod channel (bypass), and cold (inlet) plenum, are modeled separately with SAM's 0D/1D component system. The coupling between the 2D core model and these 0D/1D components is achieved through the MOOSE $MultiApp$ capability [29]. More details on the coupling approach are provided in Section 2.5.2.

Figure 8(a) shows the mesh of the SAM 2D core, while Figure 8(b) shows the 2D core model without the regions modeled with 0D/1D components. As shown in Figure 8(a), the riser, control rod channel, and cold plenum are meshed to capture the heat conduction across these porous regions. Additionally, the outlet of the core is moved from the outer surface of the hot plenum to the bottom surface to improve the convergence of the model. The modification results in a more evenly distributed flow pattern in the hot plenum, as helium now flows straight down from the pebble-bed region to the outlet. Outside of the pebble bed, the helium gaps between the graphite block and core barrel, and between the core barrel and the RPV, are modeled as solid structures where the thermal conductivity and heat capacity of the gaps are adjusted to replicate the thermal radiation across the gaps. Constant material properties are used in the SAM 2D model, as tabulated in Table 10. Temperature-dependent helium properties from the National Institute of Standards and Technology (NIST) Chemistry WebBook are used for modeling the coolant [30].

The correlations used in the 2D SAM model are summarized in Table 9. In the pebble bed, chute, and cone, the KTA correlations are used for calculating the heat transfer coefficient (HTC) in the pebble region, the HTC between the fluid and the wall, and the frictional pressure drop, while the ZBS correlation is used for calculating the effective thermal conductivity of the pebble-bed region [31, 32]. The ZBS correlation calculates the effective thermal conductivity with consideration of solid-to-solid conduction, solid-to-fluid

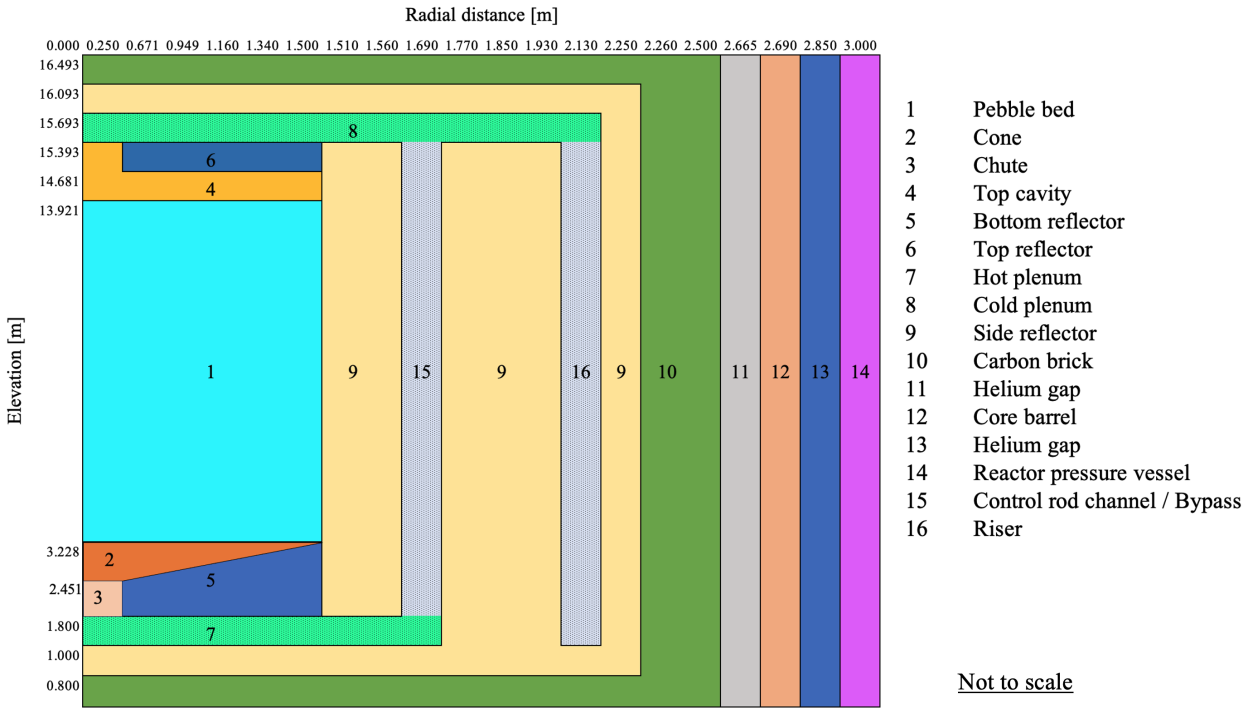

Figure 7. Layout of the HTR-PM core. Fluid flows in Regions 8, 15, and 16 are modeled using 0D/1D SAM components.

Table 9. Correlations used in the SAM 2D model.

Regions	HTC	Wall HTC	Friction	Effective thermal conductivity
Pebble bed, chute, cone	KTA	KTA	KTA	ZBS
Upper, lower reflector, hot plenum, top cavity	Dittus–Boelter	Dittus–Boelter	Churchill	ZBS

conduction/convection, and solid-to-solid radiation. Note that in SAM, no distinction is made between the frictional pressure drop in the bulk of the pebble bed and wall drag. Meanwhile, in the top cavity, hot plenum, and upper and lower reflectors, the Dittus–Boelter correlation is used for calculating both the HTC and the wall HTC, the Churchill correlation for frictional pressure drop, and the ZBS correlation for effective thermal conductivity.

2.3.2. Pronghorn 2D Core Model

A detailed depiction of the geometry and materials in the Pronghorn thermal-hydraulics model is shown in Figure 2. In this model, the cold fluid from the circulators enters the core via the vertical risers in the reflector region. The flow then enters the cold plenum, where it is diverted into the cavity, upper reflector, and control and shutdown system bypass channels. From the upper cavity, the fluid enters the active core region, then the lower reflector, and finally the outlet or hot plenum. Detailed explanations of the parameters and correlations used in each region are compiled in Table 11.

The Pronghorn model uses a weakly compressible formulation for solving momentum and continuity in a porous medium. Heat transfer between the fluid and solid phases is considered through a volumetric heat

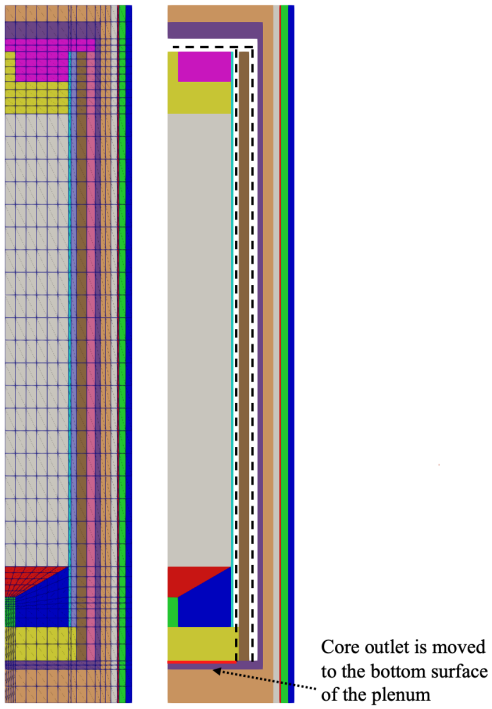

Figure 8. Developed mesh of the (a) SAM 2D model, and (b) 2D core model without the regions modeled with 0D/1D components.

Table 10. Material properties of different regions used in the 2D SAM model.

Regions	Thermal Conductivity (W/m·K)	Specific Heat Capacity (J/kg·K)	Density (kg/m^3)
RPV	38.0	525.0	7,800.0
Core barrel	17.0	540.0	7,800.0
Helium gaps	4.0	6.0	5,000.0
Pebble bed, upper and lower reflectors	26.0	1780.0	1,697.0
Side reflectors, carbon bricks	26.0	1780.0	1,697.0
Riser, control rod channel	17.7	1780.0	1,697.0
Hot plenum	20.8	1780.0	1,697.0

source (or sink) term. An effective thermal conductivity is employed, which can account for heat conduction, radiation, and some convective effects (e.g., recirculation zones). Reference [33] details these formulations. The helium properties are modeled through MOOSE's fluid properties module [34].

The boundary conditions for the Pronghorn thermal-hydraulics model of the HTR-PM include:

- The inlet helium flow rate is set to 96.0 kg/s.
- The inlet fluid temperature is set to 523.15 K.
- The outlet fluid pressure is set to 7.0×10^6 Pa.
- The velocity inlet, pressure outlet, slip-wall, and symmetry boundary conditions are used for the fluid mass, momentum, and energy equations.
- The solid energy equations have adiabatic boundary conditions except for the outside of the pressure vessel.

- Radiative and convective boundary conditions are applied between the RPV and RCCS panel with an inner diameter of 4 m, a constant temperature set to 70 °C, and surface emissivities assumed to be 0.8.

The following assumptions are applicable to the developed Pronghorn thermal fluids model:

- Porous medium equations capture most of the important effects in the core.
- The flow in the plena is approximated for the lack of detailed information about the geometry and will require either empirical or computational-fluid-dynamics-computed closure models to be improved, but it is not expected to change the core temperature results significantly.
- Wall effects for convection, radiation, and conduction heat transfer are approximated and not explicitly treated.
- The weakly compressible flow governing equations neglect acoustic effects.
- There is no convective heat transfer between the fluid and reflector regions, so only conduction is considered.
- Slip-wall and symmetry boundary conditions are used for the fluid mass, momentum, and energy equations.
- The conjugate heat transfer between helium and pebbles is treated as a volumetric phenomenon.
- The solid energy equation boundaries are all adiabatic except for the outside of the pressure vessel.

ID	Name	Porosity ϵ	D_H	κ_s	κ_f	Drag	α
1	Pebble bed	0.39	0.06	k_s^a	linear Peclet model	KTA	KTA PBR correlation
2	Outlet cone	0.39	0.06	k_s^a	linear Peclet model	KTA	KTA PBR correlation
3	Outlet chute	0.39	0.06	k_s^a	linear Peclet model	KTA	KTA PBR correlation
4	Upper cavity	1	0.67	—	Gap model	—	—
5	Upper reflector	0.3	0.2	k_{Gr}	k_f	Churchill†	D-T
6	Cold plenum*	0.2	1	k_{Gr}	k_f	$F = 0.063$	5×10^3W/m^3-K
7	Lower reflector	0.3	0.2	k_{Gr}	k_f	Churchill†	—
8	Hot plenum*	0.2	1	k_{Gr}	k_f	$F = 0.063$	5×10^3W/m^3-K
9	Riser	0.32	0.1875	k_{Gr}	k_f	Churchill	D-T
10	Bypass channel	0.32	0.15	k_{Gr}	k_f	Adjusted	D-T
11	Side reflector	0	—	k_{Gr}	—	—	—
12	Carbon brick	0	—	k_{Gr}	—	—	—
13 & 15	Gas gap	0	—	Gap model	—	—	—
14	Core barrel	0	—	$k_s = 17$W/m-K	—	—	—
15	Reactor pressure vessel	0	—	$k_s = 38$W/m-K	—	—	—

k_s^a Radiation: Breitbach-Barthels, Conduction: ZBS, Fluid conduction: ZBS
$k_{Gr} = 26$ W/m-K is the assumed thermal conductivity of graphite
k_f is the molecular thermal conductivity of helium
† Churchill correlation in the vertical direction, very large pressure drop coefficient in the radial direction
D-T is the Dittus–Boelter heat transfer correlation converted to a volumetric heat transfer coefficient
Gap model: the effective conductivity in gaps is defined in Section 2.2.1 in Reference [35]
* The authors do not have reliable information for the hot and cold plenum so the selected parameters are likely unrealistic
Drag coefficient in the bypass channel is adjusted to yield a mass flow rate of 1 kg/s

Table 11. Modeling parameters and closure relations used in the Pronghorn HTR-PM reference plant model, where D_H is the characteristic length of each region in m, κ_s is the effective solid thermal conductivity, κ_f is the effective fluid thermal conductivity, α is the volumetric heat transfer coefficient, and F is the Forchheimer coefficient. Regions with a porosity of zero have no defined flow variable.

2.4. Primary Loop And Secondary Side Modeling Approach And Assumptions

In this work, the primary loop and the RCCS of the HTR-PM are modeled using the SAM 0D/1D component system. Given the lack of design details in the open domain, the dimensions and geometric information used in this work for the primary loop and the RCCS were largely obtained through a rough visual estimation of publicly available CAD figures of the reactor [3, 36]. Schematics of the SAM primary loop and RCCS models are shown in Figure 9. The primary circuit is modeled using a series of 1D fluid components ($PBOneDFluidComponent$) that are connected to each other using branch components ($PBVolumeBranch$). The blower is modeled with the $PBPump$ component. The pump head and the loss coefficients of the blower are tuned to reach a steady-state mass flow rate of 96 kg/s, as stated in Table 1. The HTR-PM has a once-through helical coil steam generator, which is currently not available in SAM. As a result, the steam generator is instead modeled using a counter-current heat exchanger component ($PBHeatExchanger$). Adjustments are applied to the heat exchanger component to capture key thermal fluid parameters, such as primary and secondary flow areas and heat transfer surface area densities. A reference pressure of the primary loop is set using the $PBTDV$ component. The pipe wall between the inner and outer channels of the coaxial duct is modeled using the $PBCoupledHeatStructure$ component to capture the heat transfer between the helium flows entering and exiting the core.

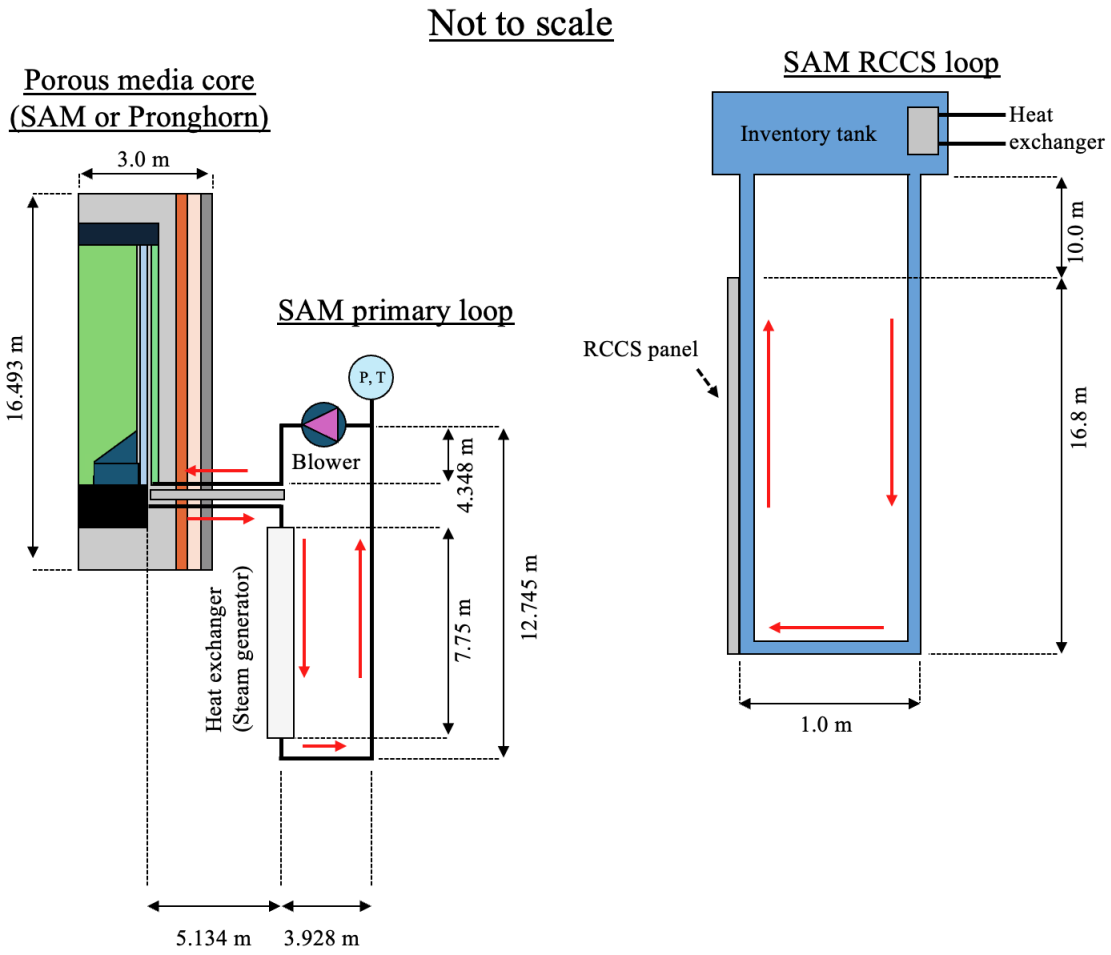

Figure 9. Schematic of the SAM 0D/1D primary loop and RCCS models.

The design information of the RCCS loop was obtained primarily from the work by Roberto et al. [37]. Similar to the primary loop, the $PBOneDFluidComponent$ and $PBVolumeBranch$ components are used to model the circuit of the RCCS loop. The cooling panel is modeled with the $PBCoupledHeatStructure$ component. The inner surface of the panel receives heat from the RPV through thermal radiation, while the outer surface is coupled to the riser channel of the RCCS loop. This allows water in the RCCS loop to remove heat from the panel through convection. Downstream of the riser channel is the unheated chimney channel. An inventory tank, modeled using the $PBLiquidVolume$ component, is located downstream of the unheated chimney. A $PBHeatExchanger$ component is connected to the inventory tank to remove the heat from the water in the RCCS loop. A downcomer channel is added to connect the inventory tank to the inlet of the riser channel.

2.5. Coupling Approach And Assumptions

2.5.1. Pronghorn Thermal Fluids Coupling with Griffin Neutronics

The developed multiphysics coupling scheme for performing equilibrium core calculations of the coupled Griffin-Pronghorn code system is shown in Figure 10. Griffin is the main application, and it solves the neutron diffusion equation for steady-state and transient neutronics calculations along with the streamline pebble depletion-advection problem, establishing the transfer system to exchange coupling variables with sub-applications. Pronghorn solves the porous media approximation for fluids and the conjugate heat conduction problem to obtain reactor thermal fields. Additionally, BISON solves the pebble and TRISO conduction problem for each pebble type and burnup group in the active core region. In Griffin, the scaled neutron flux obtained from diffusion calculations is used to compute the reaction rates and perform the streamline pebble depletion-advection calculations to obtain number densities and volume fractions for each pebble type and burnup group to reconstruct the cross sections in each reactor region. The calculated power density by Griffin is transferred to Pronghorn as a heating source for the thermal fluids calculations, which in turn transfer back the pebble surface temperature and reflector temperature to Griffin. The pebble fraction, power density, and surface temperatures are transferred from Griffin to BISON to obtain the fuel and moderator temperatures needed for updating cross sections, along with the reflector temperature.

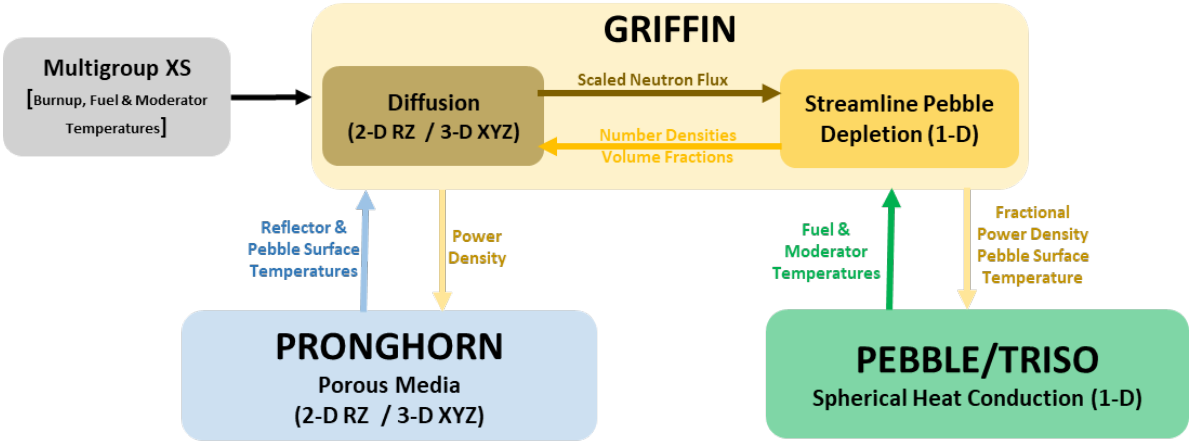

Figure 10. Multiphysics coupling scheme of Griffin and Pronghorn for equilibrium core calculations and transient analysis.

2.5.2. SAM Thermal Fluids Coupling with Griffin Neutronics

The coupling of the SAM/Griffin multiphysics model is discussed in this section. The coupling between the models is shown in Figure 11. The coupling between the Griffin neutronics and SAM thermal fluids models follows the same approach discussed in Section 2.5.1. The Griffin model is the $MainApp$ that controls the execution of the entire coupled simulation. The Griffin model calculates power density and transfers it to the SAM 2D model as a heating source for the thermal fluids calculations, which in turn transfer back the pebble surface temperature and reflector temperature to Griffin.

Similarly, the SAM thermal fluids model also utilizes the MOOSE $MultiApp$ system to couple the 2D core model, the primary loop model, and the RCCS model, as shown in Figure 9. As depicted in Figure 11, the SAM 2D model is the primary application ($MultiApp - 1$) that controls the execution and information exchange on the thermal fluids side of the coupled simulation, while the primary loop and RCCS models are two separate $SubApps$. The 2D core model transfers the core outlet temperature, velocity, and pressure drop across the core to the primary loop $SubApp$, and in return it receives the inlet velocity and temperature. Furthermore, fluid temperatures, heat transfer coefficients, and wall temperatures in the riser and control rod (bypass) channel are exchanged between the two models to capture convective heat transfer due to flow in the riser and control rod channels. On the other hand, for the coupling between the SAM 2D model and the RCCS model, the 2D model transfers layer-averaged heat flux to the RCCS to be applied on the inner surface of the RCCS panel. In return, the RCCS model transfers layer-averaged panel temperature to be used as T_∞ for the radiative boundary condition on the surface of the RPV. Picard iterations are performed to ensure that converged solutions are obtained.

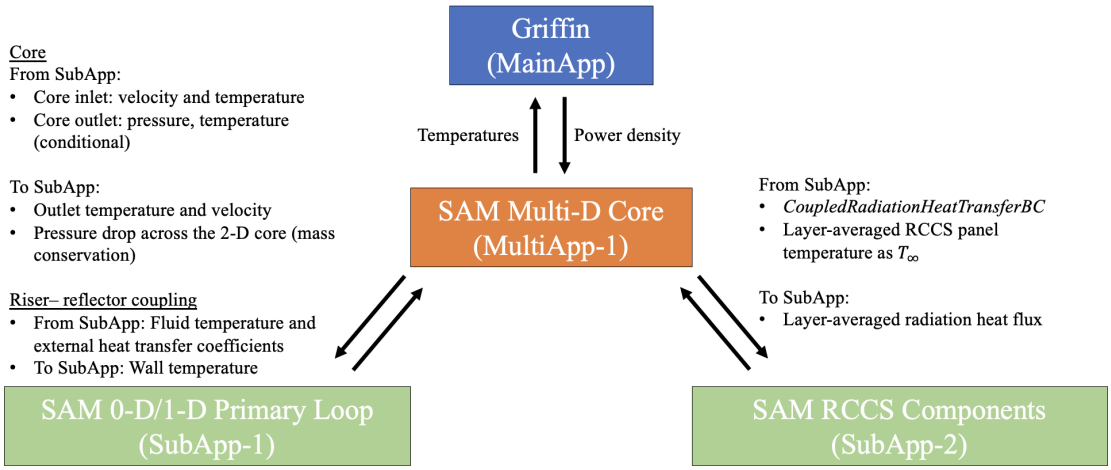

Figure 11. Coupling between the SAM 2D and 0D/1D models.

The so-called domain overlapping approach is used to couple the SAM 2D core model and the 0D/1D primary loop model. The domain overlapping approach was chosen because it has been shown to be more numerically stable than the conventional domain decomposition approach [38]. The schematic of the SAM domain overlapping approach is shown in Figure 12. In this approach, a surrogate channel is used to represent the 2D core in the primary loop model. The surrogate channel is separated from the rest of the primary loop, but boundary conditions are exchanged between the two entities through SAM's $PPSTDJ$ and $PPSTDV$ components. In the 2D model, the frictional pressure drop experienced by the fluid in the core is calculated and transferred to the primary loop model, which is then imposed on the surrogate channel. At the same time, velocity is obtained from the outlet of the primary loop and set as the inlet velocity of the surrogate channel. Based on the inlet velocity and the frictional pressure drop imposed on the surrogate channel, the

outlet velocity of the surrogate channel can then be calculated. This outlet velocity is then used to set the inlet velocity of the primary loop. Furthermore, the outlet temperature is obtained from the 2D core model and set as the inlet temperature of the primary loop. Lastly, the outlet velocity and temperature from the primary loop are used as the inlet velocity and temperature of the 2D core model. Picard iteration is performed during the coupling of these different models to ensure the convergence of the solutions. It should be noted that another coupling approach, the so-called single-solve approach, has been developed in SAM to couple the 2D core to the primary loop within a single model without the need for $MultiApp$ and Picard iterations. This improves the computational speed and the numerical robustness of the model. This coupling approach has been demonstrated in the SAM model for a fluoride-cooled high-temperature pebble-bed reactor (PB-FHR) [39].

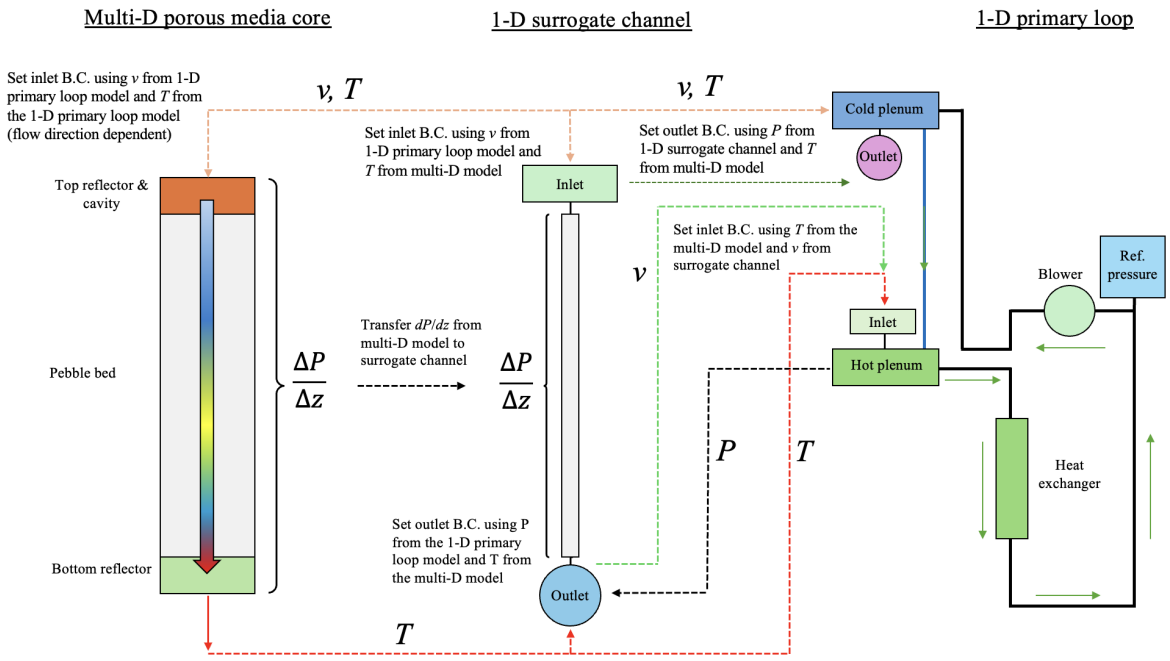

Figure 12. Domain overlapping scheme in the SAM thermal fluids model.

2.5.3. Pronghorn Thermal Fluids Coupling with Griffin PKE

A PKE model was developed using Griffin to replace the higher-fidelity Griffin 2D and 3D models while performing control rod withdrawal events with Pronghorn. The coupling scheme of the Griffin-PKE and Pronghorn model for transient analysis is shown in Figure 13. The steps to develop an accurate PKE model of the HTR-PM based on the a higher-fidelity multiphysics model can be summarized as follows:

- Step 1: Develop a 3D or 2D fully coupled model of the equilibrium core.
- Step 2: Establish the steady-state solution of the equilibrium core.
- Step 3: Perform a reactor characterization study to evaluate:
  - Temperature feedback coefficients
  - Control rod worth
  - Kinetics parameters
  - Power peaking.
- Step 4: Develop the PKE model based on the 3D or 2D fully coupled core characterization.
- Step 5: Adjust the control rod reactivity as needed.

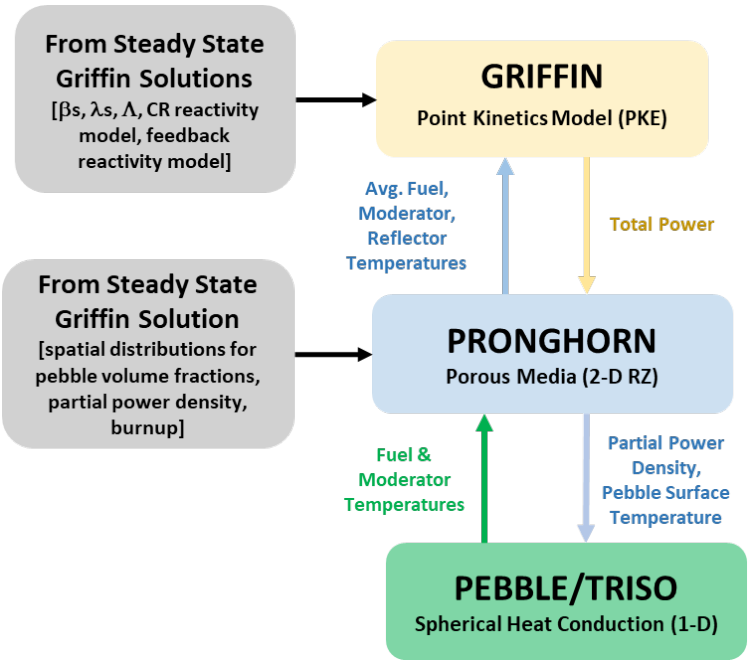

Figure 13. Multiphysics coupling scheme of Griffin-PKE and Pronghorn for transient analysis of equilibrium core.

2.5.4. SAM PKE and Thermal Fluids Model

The modeling approach of the SAM PKE model is discussed in this section, in which SAM's internal PKE model is used for neutronics calculations instead of Griffin. The PKE parameters and feedback coefficients are obtained from the 2D Griffin model, as tabulated in Tables 12 and 13. The mean generation time, Λ, is 0.001348 seconds.

Table 12. Delayed neutron fractions and delayed neutron precursor decay constants.

Groups	β	λ (1/s)
1	0.000174	0.013336
2	0.000993	0.032739
3	0.000884	0.12078
4	0.001949	0.30278
5	0.000855	0.84949
6	0.000338	2.853

Table 13. Reactivity feedback temperature coefficients at 900 K from the 2D Griffin model.

Regions	Coefficients at 900 K (pcm/K)
Fuel	-4.30
Moderator	-1.85
Reflector	1.45

Several assumptions and simplifications are adopted by the model. First, it only considers the total

feedback coefficients for the fuel, moderator, and reflector, where the spatial distributions of these coefficients are ignored. As a result, the volume-averaged fuel, moderator, and reflector temperatures are used to calculate reactivity feedback. We made this simplification due to the lack of available reactivity coefficients, even though the SAM PKE model is capable of modeling reactivity feedback using spatially dependent feedback coefficients and temperatures [40]. Additionally, the local fuel and moderator temperatures are calculated based only on the total local power density; no distinctions are made between burnup groups. The PKE model also assumes a constant power density distribution for steady-state and transient scenarios. For consistency, the solution from the SAM/Griffin/SAM coupled model is used to set the power density distribution for the SAM PKE model. Furthermore, the model only considers fission power, ignoring decay power. This means that during the transient, the core power is scaled with respect to the steady-state equilibrium power based on reactivity changes. In this work, the SAM PKE model was only used to demonstrate the over-cooling transient, which is relatively short, so the effects of decay heat are largely negligible. However, it should be pointed out that the SAM PKE model is capable of including decay heat through its internal model or a user-provided decay heat curve.

3. ANALYSIS AND RESULTS

This section presents the simulation results for the steady-state equilibrium core and transient analysis results of the protected depressurized loss of forced cooling (DLOFC), protected pressurized loss of forced cooling (PLOFC), unprotected over-cooling (UOC) accident, and reactivity insertion accident (RIA) via control rod movement, along with detailed s of the Pronghorn/Griffin and SAM/Griffin/SAM results obtained with the 2D model. Additionally, transient analysis results of the RIA due to localized perturbation (few rod ejections) using the 3D model are presented and compared to the reduced-order model results of the 2D equivalent model and the PKE model to explore the validity of these models compared to the higher-fidelity model.

Section 3.1 presents the equilibrium core calculations using the Pronghorn/Griffin multiphysics model of the HTR-PM and compares the results of the 2D and 3D models. It also presents a detailed steady-state of standalone SAM and Pronghorn and those coupled to Griffin in 2D geometry. Sections 3.2, 3.3, 3.4, and 3.5 present results of the SAM/Griffin and Pronghorn/Griffin 2D models for the DLOFC, PLOFC, UOC, and RIA, respectively. Section 3.6 presents results of the Pronghorn/Griffin 3D, 2D, and PKE models for a delayed and prompt supercritical RIA.

3.1. Equilibrium Core

This section presents the steady-state equilibrium core calculation results of the HTR-PM using the 2D and 3D models of coupled Pronghorn/Griffin. A comparison of the steady-state global parameter values for the equilibrium core calculation results obtained by the 2D and 3D models is presented in Tables 14, 15, and 16. Prior to this work, the equilibrium core results of the 2D Pronghorn/Griffin model were verified against Very Superior Old Programs (VSOP), as presented in References [19, 20].

Table 14 compares the eigenvalue, neutron leakage fraction, peak power, average power density, and average and maximum temperatures of the fuel, moderator, and solid temperatures. In general, the results show good agreement between the two models. The eigenvalue is higher by about 34 pcm in the 2D model, and the neutron leakage fraction of the 2D model is about 0.36% lower than in the 3D model. This is attributed to differences in the surface area of the outer regions due to approximations for the cylindrical geometry in the XYZ geometry in the 3D model, which enhances the neutron leakage and reduces the eigenvalue. Additionally, the explicit modeling of the control rods in the 3D model might slightly perturb the neutron flux distribution and enhance the neutron leakage through the KLAK region, where there is no absorbing material. The average and maximum temperatures are consistent in both models, with differences within 1.5% of each other. The average power density is the same in both models, with a small variation in power peaking of about 0.62% due to the explicit modeling of the control rods in the 3D model, which might slightly perturb the power distribution. Figures 14 and 15 show the power density, peak power, fast, and thermal neutron flux distributions obtained from 2D and 3D Pronghorn/Griffin calculations, while Figures 16 and 17 show the average fuel, average moderator, solid, and fluid temperature profiles obtained from 2-D and 3-D Pronghorn/Griffin calculations.

The core kinetics parameters are compared in Table 15 for each delayed neutron group effective fraction (β_{eff}) and the neutron mean generation time (Λ), with no major differences observed between the two models. The kinetics parameters are obtained from improved quasi-static (IQS) calculations in Griffin and weighted with the adjoint-neutron flux solution. The calculated kinetics parameters and isothermal temperature feedback coefficients are used to develop the PKE models discussed later in this section.

Also, a comparison of the isothermal temperature feedback coefficients of reactivity for the equilibrium core is provided in Table 16. The temperature coefficients were calculated by perturbing the temperature of the fuel, moderator, or reflector by 50 K steps from 500 K to 2000 K, as shown in Figure 18. The results of the 2D and 3D models match very well, with a maximum difference of 0.5%.

Table 14. Comparison of 2D and 3D equilibrium core main parameters obtained from Pronghorn/Griffin.

Parameter	Unit	2D	3D	Diff. (% or pcm)
Eigenvalue	pcm	0.99201	0.99167	-34.0
Leakage fraction	–	0.05216	0.05235	0.36
Fuel avg. temp.	K	907.0	907.2	0.02
Fuel max. temp.	K	1134.8	1126.4	-0.74
Moderator avg. temp.	K	893.0	893.2	0.02
Moderator max. temp.	K	1124.1	1123.5	-0.06
Solid avg. temp.	K	671.7	662.1	-1.43
Solid max. temp.	K	1115.7	1115.0	-0.06
Control rod position	m	13.386	13.386	0.00
Avg. power density	MW/m^3	3.215	3.215	0.00
Power peaking	–	1.994	2.007	0.62

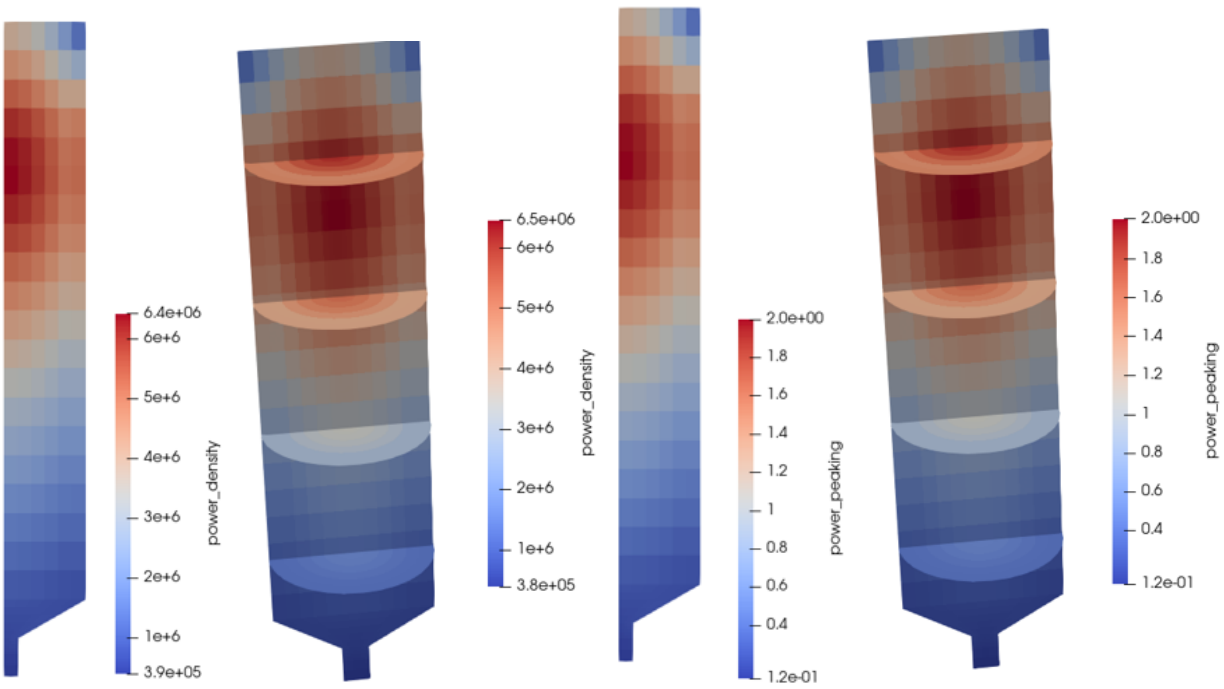

(a) 2D Power Density (b) 3D Power Density (c) 2D Peak Power (d) 3D Peak Power

Figure 14. 2D and 3D power density and peak powers of the equilibrium core obtained by the Pronghorn/Griffin models.

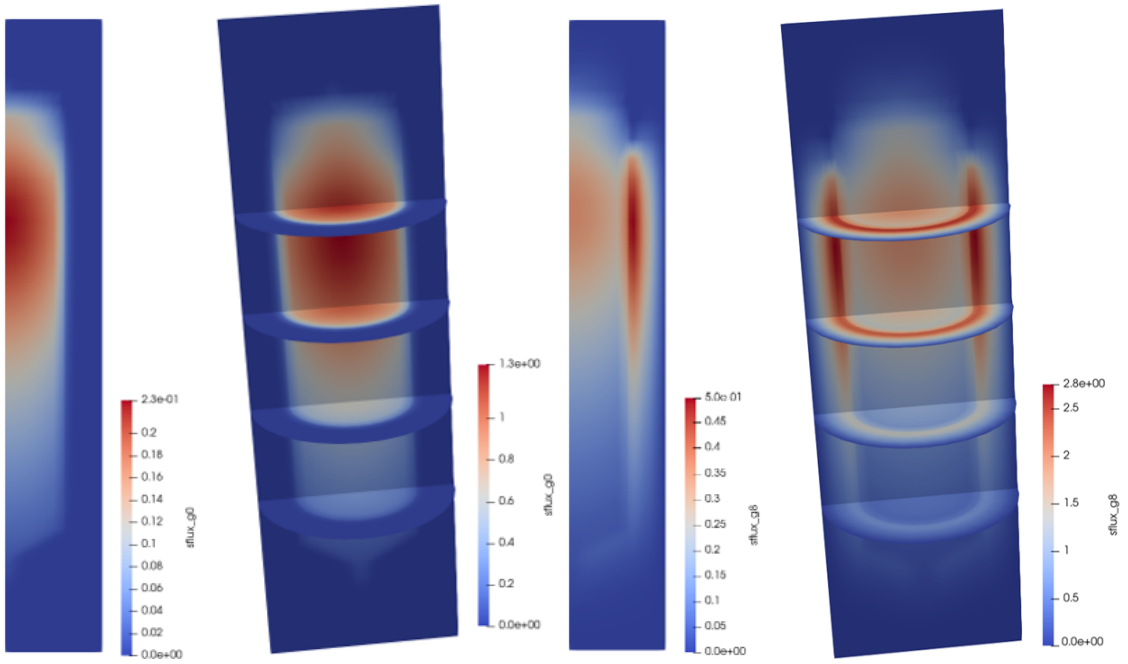

(a) 2D Fast (b) 3D Fast (c) 2D Thermal (d) 3D Thermal

Figure 15. 2D and 3D fast and thermal neutron fluxes of the equilibrium core obtained with the Pronghorn/Griffin models.

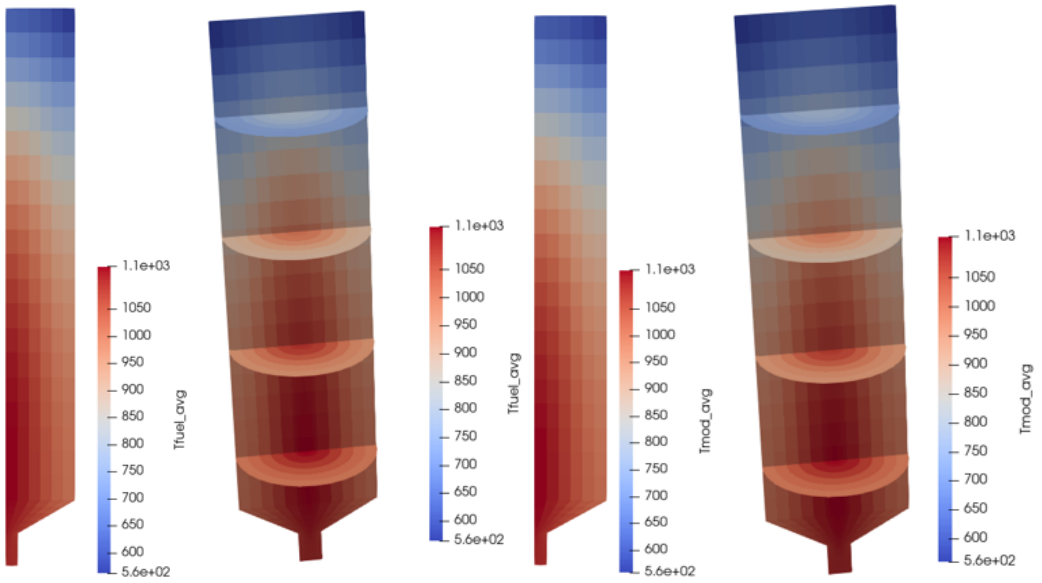

(a) 2D Fuel (b) 3D Fuel (c) 2D Moderator (d) 3D Moderator

Figure 16. 2D and 3D average fuel and moderator temperatures of the equilibrium core obtained with the Pronghorn/Griffin models.

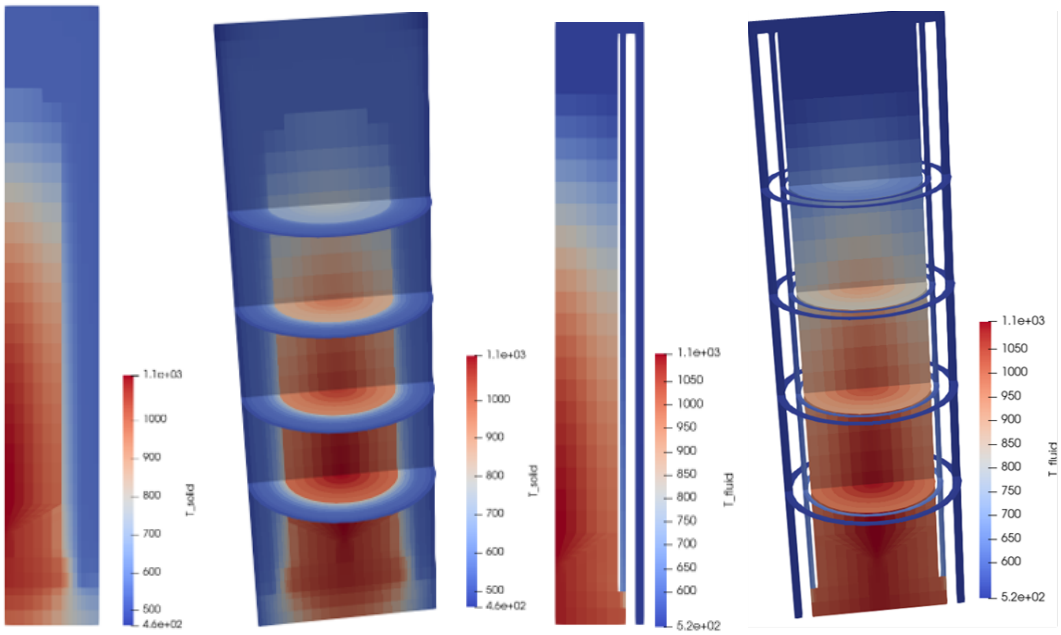

(a) 2D Solid (b) 3D Solid (c) 2D Fluid (d) 3D Fluid

Figure 17. 2D and 3D solid and fluid temperatures of the equilibrium core obtained by the Pronghorn/Griffin models.

Table 15. Comparison of 2D and 3D equilibrium core kinetic parameters obtained with the Pronghorn/Griffin models.

β_{eff}	Unit	3D	2D	Diff. (pcm or %)
1	pcm	17.38	17.37	-0.007
2	pcm	99.29	99.29	-0.005
3	pcm	88.42	88.41	-0.007
4	pcm	194.85	194.84	-0.007
5	pcm	85.48	85.47	-0.007
6	pcm	33.76	33.75	-0.008
Total	pcm	519.17	519.14	-0.007
Lambda	ms	1.348	1.347	-0.018

Table 16. Comparison of 2D and 3D equilibrium core isothermal temperature feedback coefficients at 900 K obtained by Pronghorn/Griffin.

Feedback Coef.	Unit	3D	2D	Diff. (%)
Fuel	pcm/K	-4.32	-4.30	-0.46
Moderator	pcm/K	-1.85	-1.85	-0.18
Reflector	pcm/K	1.44	1.45	0.09

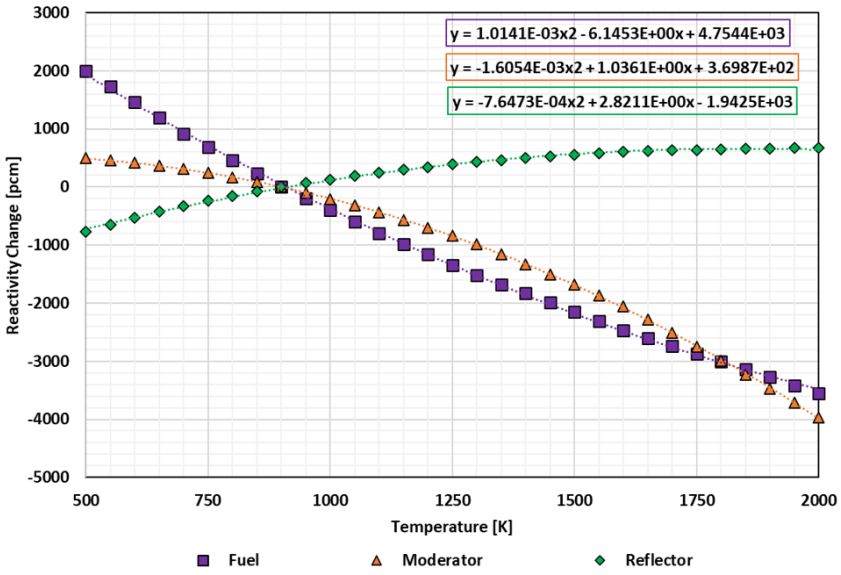

Figure 18. Fuel, moderator, and reflector isothermal temperature feedback coefficients.

3.1.1. Steady-State Comparison of Standalone SAM and Pronghorn 2D Porous Media Models

In this section, a comparison of standalone SAM and Pronghorn 2D porous media models for steady-state calculations is performed. Because the purpose of this analysis is to compare and contrast the two 2D porous media models without the influence of the primary loop and RCCS models, neither were included. To ensure a one-to-one comparison, several restrictions were applied, namely the use of identical meshes, porosities, boundary conditions on the external RPV surface, uniform power density, and correlations for frictional pressure drop, heat transfer coefficients, and effective thermal conductivity. A summary of the correlations is provided in Table 9.

Several key parameters predicted by the standalone 2D SAM and Pronghorn models are tabulated in Table 17 where excellent agreement is observed. Note that the total mass flow rate and inlet temperature are boundary conditions set at the core inlet. For further comparison, the axial profiles of key parameters were obtained from six radial locations in the pebble-bed region, and the radial profiles of the same parameters were obtained from six axial locations across the core, as shown in Figure 19. These parameters are solid temperature, fluid temperature, and velocity, a shown in Figures 20 to 22. Furthermore, the distributions of solid temperature, fluid temperature, and velocity along with the streamlines of the flow are compared in Figure 23.

Table 17. Comparison of the standalone 2D SAM and Pronghorn porous media models during steady-state equilibrium condition.

	SAM	Pronghorn
Total mass flow rate (kg/s)	96.0	96.0
Core mass flow rate (kg/s)	94.9	95.0
Bypass mass flow rate (kg/s)	1.1	1.0
Inlet temperature (K)	523.2	523.2
Outlet temperature (K)	1023.8	1023.7
Pressure drop in the pebble bed (kPa)	79.9	79.9

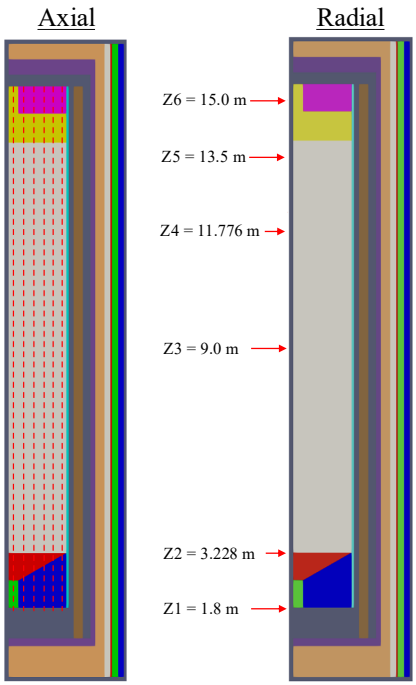

Figure 19. Locations of axial and radial profiles for comparing the SAM and Pronghorn 2D porous media models.

Figure 20 compares the axial and radial profiles of the solid temperatures of the standalone SAM and Pronghorn porous media models. For the axial profiles, detailed comparisons are obtained for the top cavity, the top reflector, and the pebble bed regions. However, in the cone, chute, and lower reflector regions, the two models deviate because the core outlet is located differently in the models. In SAM, the outlet of the porous media model is located at the bottom surface of the bottom plenum, whereas in Pronghorn it is located at the right surface of the bottom plenum. As a result, the flow patterns in the bottom plenum are different between the two models. As shown in the streamlines in Figure 23, helium flows straight down at the bottom plenum in the SAM model. However, in the Pronghorn model, the helium flow changes direction in the bottom plenum to exit the core on the right surface. Consequently, the differences in flow pattern in the bottom plenum likely lead to differences in heat removal, which in turn cause the the discrepancies in the temperature distribution. The same observation can also be made for the solid temperature radial profiles. Good agreement between the SAM and Pronghorn models is obtained at all axial locations other than z = 1.8 m, which is the top boundary of the bottom plenum for the reason explained above. Outside the pebble bed, in the reflector, carbon brick, core barrel, and RPV, both models show good agreement.

Figure 21 compares the axial and radial profiles of fluid temperatures of the SAM and Pronghorn standalone porous media models. Similar to the solid temperature, good agreement is obtained for the fluid temperature of both models in the cavity, top reflector, and pebble-bed regions. However, in the cone, chute, bottom reflector, and bottom plenum, some disagreements are observed due to the different flow patterns caused by the outlet locations. For the radial profiles, good agreement between the two models is observed for all axial locations other than z = 1.8 m, where the Pronghorn model shows a fluid temperature that is roughly 60 K higher than the SAM model shows in the innermost region. This is likely because the flow direction changes from downward to outward at the region in the Pronghorn model, which leads to a poorer heat removal rate. The temperature profiles for the pebble-bed region are relatively uniform in the radial direction for both models.

Figure 22 compares the axial and radial velocity profiles of the standalone SAM and Pronghorn models.

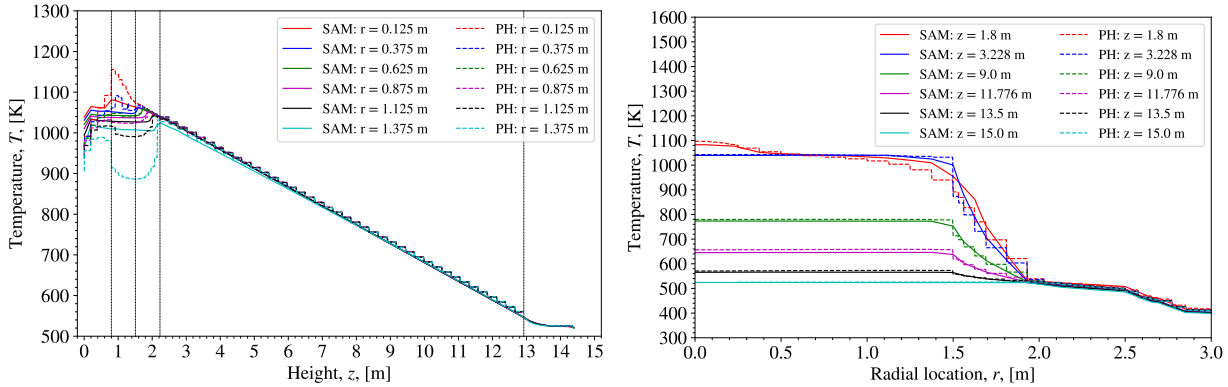

(a) Axial (b) Radial

Figure 20. Comparison of axial and radial solid temperature profiles for the standalone 2D SAM and Pronghorn porous media models.

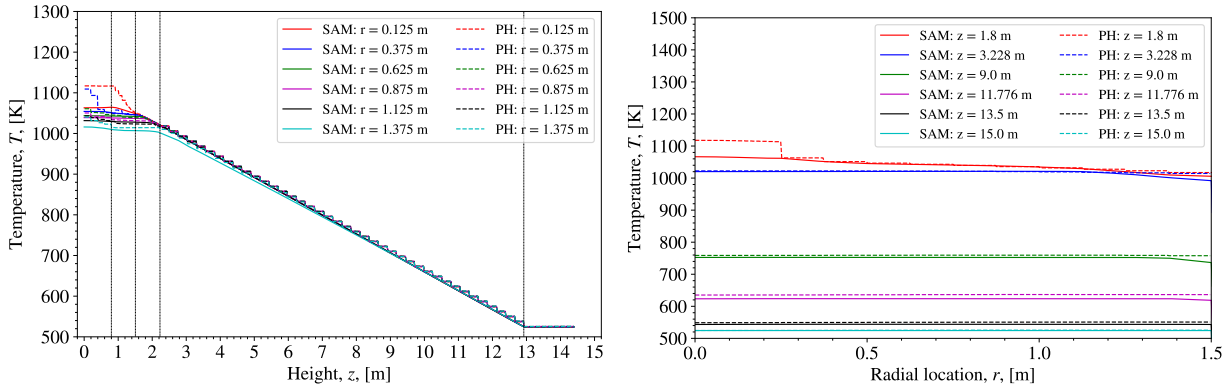

(a) Axial (b) Radial

Figure 21. Comparison of axial and radial fluid temperature profiles for the standalone 2D SAM and Pronghorn porous media models.

Note that only axial velocity (v_y) is shown here because during the steady state radial velocity (v_x) is several magnitudes smaller and thus negligible. The axial profiles show good agreement between the two models in the pebble-bed region. However, some differences in the regions above and below the pebble bed are observed. In the Pronghorn model, the top plenum is explicitly meshed and is a part of the fluid flow. However, in the SAM model, the top plenum is not explicitly meshed and so is modeled using a 0D component as part of the primary loop. This means that the inlet in the 2D SAM model is set as the top surface of the cavity and top reflector. As a result, the Pronghorn model captures the change in flow direction in the top region while the SAM model shows that helium flows straight down across the top region into the pebble bed. The velocity radial profiles also show good agreement for the pebble bed, namely at z = 3.228 m, 9.0 m, 11.776 m, and 13.5 m. Conversely, at z = 1.8 m and 3.228 m, due to different flow patterns more disagreements are observed. The differences in flow patterns in the regions above and below the pebble bed are shown in the streamlines in Figure 23.

The distributions for solid temperature, fluid temperature, and velocity along with streamlines from both models are shown in Figure 23. The solid temperature distributions show that heat is primarily contained within the pebble-bed region where the external components, such as the reflectors, core barrel, carbon brick,

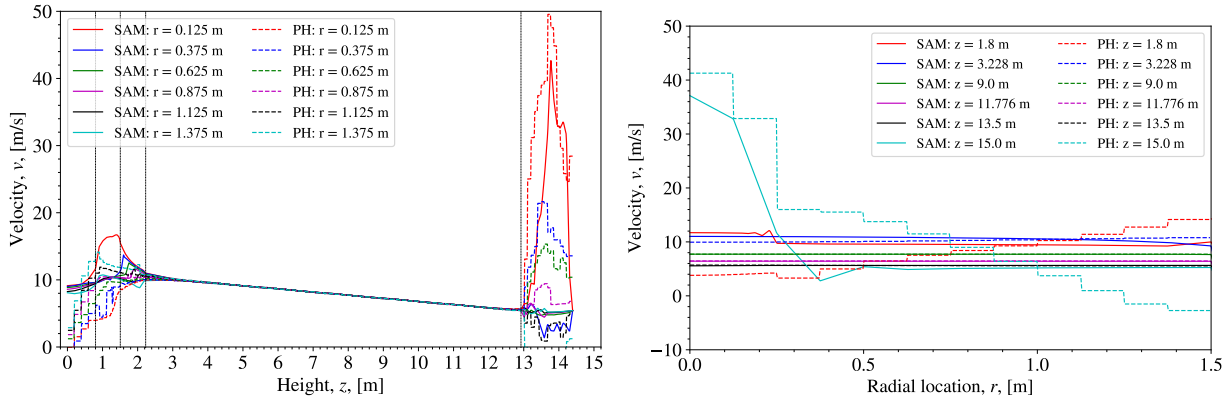

(a) Axial (b) Radial

Figure 22. Comparison of axial and radial fluid velocity (v_y) profiles for the standalone 2D SAM and Pronghorn porous media models.

and RPV, remain at a significantly lower temperature. This indicates that heat is primarily removed through forced convection, in which only a small amount of heat escapes to the surrounding structures. However, an exception is observed in the region directly below the hot plenum, which experiences a significantly higher temperature as a large amount of heat is deposited in this region. The fluid temperature distributions of both models are largely the same as the solid temperature profiles. As cold helium flows downward from the top of the pebble bed, it continues to remove heat from the pebbles and increases in temperature. The velocity profiles from both models are largely comparable, especially those for the pebble-bed regions. However, due to the differences in the locations of the inlet and outlet, the regions above and below the pebble bed show different flow patterns.

Generally, the standalone 2D SAM and Pronghorn porous media models show a good agreement, especially in the pebble bed. The core-wide parameters of the two models such as temperature increase and pressure drop are almost identical. The axial and radial profiles of the temperatures and velocities in the pebble bed also show good agreement between both models. However, due to the differences in the flow pattern at the hot plenum and bottom reflector region, which stem from the different modeling approaches, some differences between the models are observed.

3.1.2. Steady-State Comparison of Coupled SAM/Griffin/SAM and Coupled Pronghorn/Griffin Media Models

In this section, the performance of the SAM/Griffin/SAM and Pronghorn/Griffin coupled models in the steady state is compared. Identical meshes, boundary conditions, and correlations (as summarized in Table 9) were used for the SAM and Pronghorn 2D porous media models. The porous media models were coupled to the 2D equilibrium core Griffin model described in the previous section for neutronics and power density calculations. Furthermore, the SAM primary loop and the RCCS loop were included in the coupled model.

Several key parameters of the two coupled models are compared in Table 18. Overall, good agreement for the two models is obtained. Note that in the coupled models, the blower head determines the total mass flow rate, and the heat removal rate of the heat exchanger in the primary loop controls the inlet temperature. The mass flow rate predicted by the SAM/Griffin/SAM model is slightly higher than that of the Pronghorn/Griffin model. This in turn leads to a slightly lower outlet temperature and a marginally higher pressure drop in the pebble bed. Nevertheless, the two coupled models generally agree well with each other.

Figures 24 to 27 compare the axial and radial profiles for power density, solid temperature, fluid

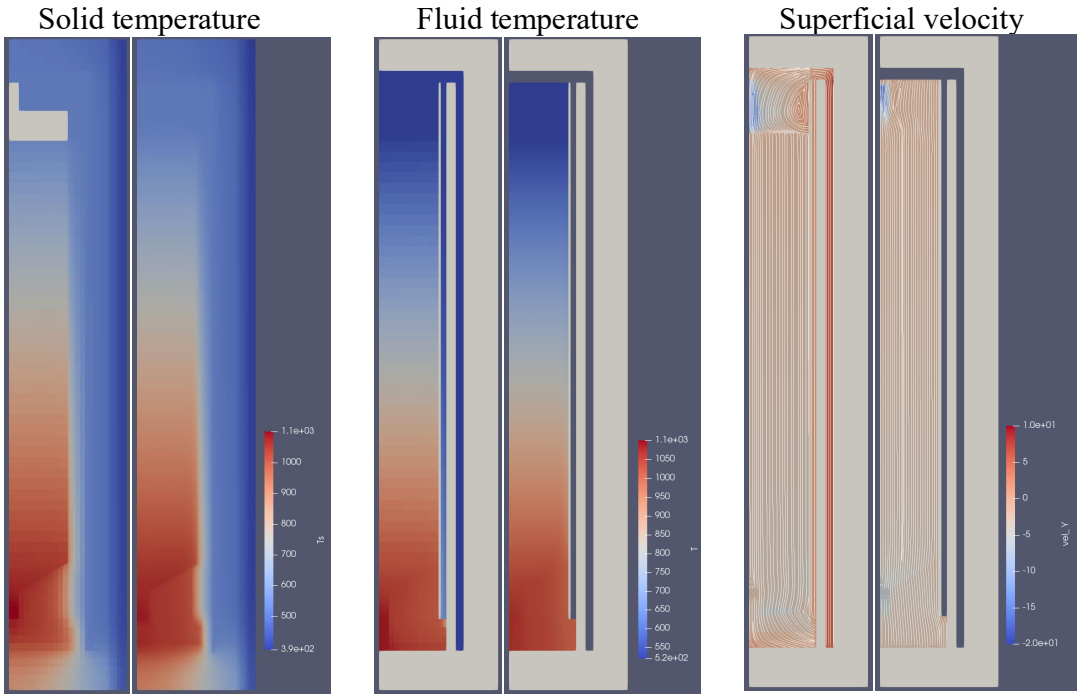

Figure 23. Comparison of solid temperature, fluid temperature, and superficial velocity profiles of the standalone Pronghorn (*left*) and 2D SAM (*right*) porous media models.

Table 18. Comparison of the 2D SAM/Griffin/SAM and Pronghorn/Griffin coupled models during steady-state equilibrium condition.

	SAM/Griffin/SAM	Pronghorn/Griffin
Total mass flow rate ([])kg/s)	96.1	95.7
Core mass flow rate (kg/s)	95.0	94.5
Bypass mass flow rate (kg/s)	1.1	1.2
Inlet temperature (K)	523.9	523.9
Outlet temperature (K)	1027.3	1027.6
Pressure drop in the pebble bed (kPa)	89.5	88.4

temperature, and velocity of the SAM/Griffin/SAM and Pronghorn/Griffin coupled models. Solid lines represent results from the SAM/Griffin/SAM model and dashed lines the results from the Pronghorn/Griffin model. The radial and axial locations at which the profiles were obtained are shown in Figure 19. Figure 24 compares the axial and radial power density profiles of the SAM/Griffin/SAM and the Pronghorn/Griffin models. The overall trends of both coupled models are similar. The power density peaks at the inner, upper half of the pebble bed region and drops quickly from the peak to the bottom of the core. However, it can be seen from the axial profiles that the SAM/Griffin/SAM model predicts a higher power density for the upper half of the core, especially the inner region. The trend inverts for the lower half of the core at approximately z = 8 m, for which the Pronghorn/Griffin model shows larger values for power densities than the SAM/Griffin/SAM model. Similar observations are made for the radial profiles; the SAM/Griffin/SAM model consistently predicts a higher power density at z = 11.776 and 13.5 m, whereas the Pronghorn/Griffin model predicts a higher power density at z = 3.228 and 9.0 m. It is also observed that the discrepancies between the predictions of the two models are higher at z = 13.5 m compared to the other two axial locations.

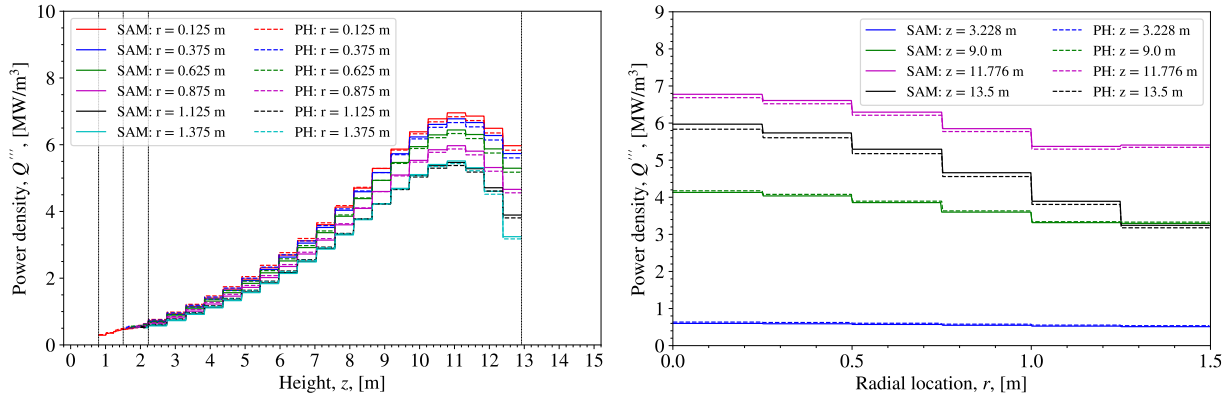

(a) Axial (b) Radial

Figure 24. Comparison of axial and radial power density profiles of the coupled SAM/Griffin/SAM and Pronghorn/Griffin models.

Figures 25 and 26 compare the axial and radial solid and fluid temperature profiles of the SAM/Griffin/SAM and Pronghorn/Griffin coupled models. For both solid and fluid temperatures, the general trends predicted by both coupled models are similar. The temperatures increase non-linearly from the top to the bottom of the pebble bed due to the non-uniform power density distributions. In the top half of the pebble bed, the agreement between the two coupled models is relatively good. However, at the bottom half of the core, deviations are observed; the SAM/Griffin/SAM model shows a larger spread from the inner to the outer region of the core compared to the Pronghorn/Griffin model. The discrepancies at the bottom half of the core are likely caused by differences in the power density distributions. As shown in the axial power density distribution in Figure 24, at the top half of the core where power density is highest, the SAM/Griffin/SAM model predicts a higher power density at the inner region than the Pronghorn/Griffin model. And because helium predominantly flows downward axially in the core with very little flow in the radial direction, this means that in the SAM/Griffin/SAM model the helium in the inner region of the core carries more heat than the helium in the Pronghorn/Griffin model. This causes the temperature in the inner region to be higher in the SAM/Griffin/SAM model than in the Pronghorn/Griffin model.

As shown in the of the standalone SAM and Pronghorn porous media models comparison in the previous section, when uniform power density distributions are applied to both models, excellent agreement for the solid and fluid temperatures in the pebble-bed region is obtained. Comparatively, when the power density distributions of the two coupled models are not identical, discrepancies in the predicted temperatures are observed. Moreover, the differences in temperature are likely exacerbated by the differences in the flow patterns in the lower plenum due to the different outlet locations of the SAM and Pronghorn models. Similarly, the radial profiles of the solid and fluid temperatures from the two coupled models share similar general trends. At z = 1.8 and 3.228 m, the SAM/Griffin/SAM coupled model shows higher temperatures at the inner region of the pebble bed, whereas the Pronghorn/Griffin model shows a higher temperature at the outer region, which is consistent with the observation from the axial plots. Outside the pebble bed, the temperatures of the side reflector, carbon brick, core barrel, and RPV show good agreement between both models.

Figure 27 compares the axial and radial profiles of velocity (v_y) between the SAM/Griffin/SAM and Pronghorn/Griffin coupled models. For the pebble bed, the axial profiles predicted by both coupled models are largely similar. Nevertheless, the SAM/Griffin/SAM shows a larger spread in the radial direction compared to the Pronghorn/Griffin, which is consistent with the bigger spread in fluid temperatures predicted by the SAM/Griffin/SAM model. Conversely, larger differences are observed between the two coupled models for the regions above and below the pebble bed due to different flow patterns caused by the different inlet

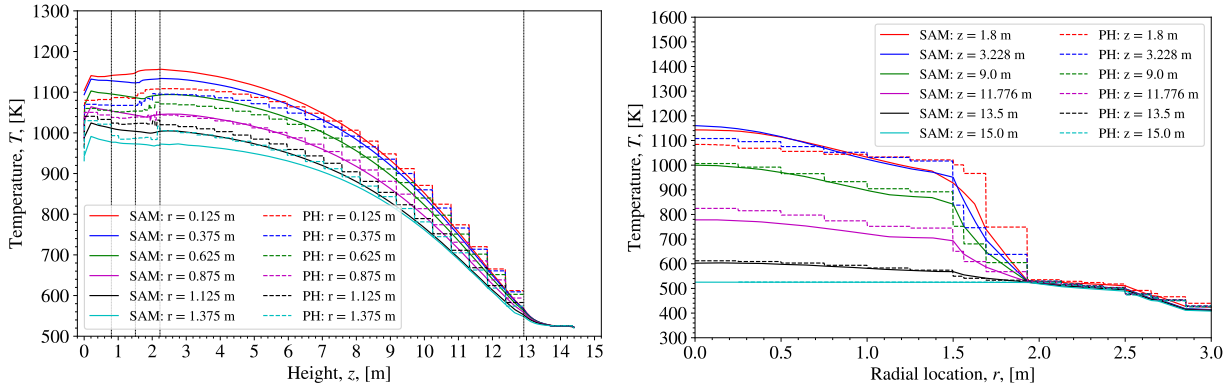

(a) Axial (b) Radial

Figure 25. Comparison of axial and radial solid temperature profiles of the coupled SAM/Griffin/SAM and Pronghorn/Griffin models.

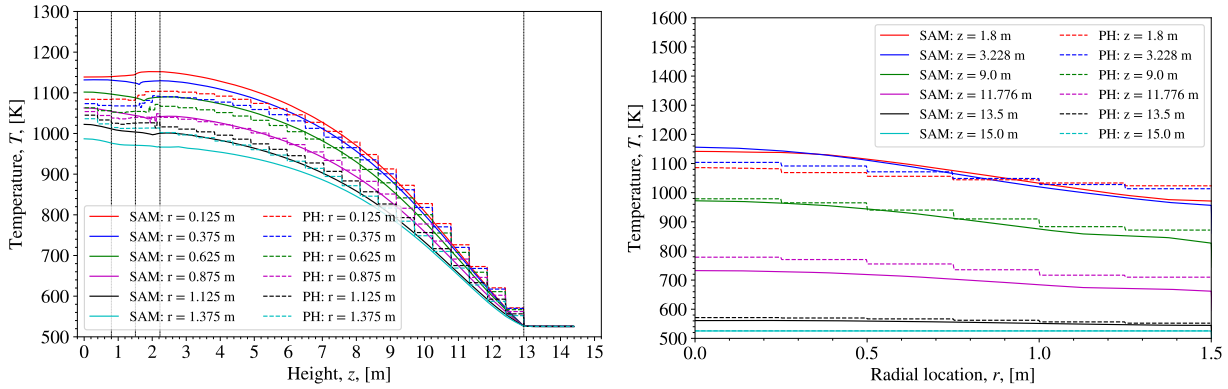

(a) Axial (b) Radial

Figure 26. Comparison of axial and radial fluid temperature profiles of the coupled SAM/Griffin/SAM and Pronghorn/Griffin models.

and outlet locations of the models. From the radial profiles it can be observed that both models show better agreement for the pebble-bed region (z = 3.228, 9.0, 11.776, and 13.5 m) compared to the regions z = 1.8, 15.0 m. The velocity profiles for the pebble bed are also much more uniform compared to those for the region above it, which shows a steep drop from the inner to the outer wall. This is because the inner region is a part of the cavity while the outer region is the top reflector, which has a porosity of 0.3 and thus provides greater flow resistance. Consequently, most of the flow rushes into the low-resistance cavity and in turn results in higher local flow velocities.

Figure 28 shows the solid temperature, fluid temperature, power density, and velocity profiles of the SAM/Griffin/SAM and Pronghorn/Griffin coupled models. As was observed in the axial profiles, the SAM/Griffin/SAM coupled model shows slightly higher solid and fluid temperatures and power density in the inner regions of the core. Furthermore, the streamlines show the differences in flow patterns at the top and bottom regions of the core due to the different inlet and outlet locations of the models.

Generally, the overall trends of the temperature, velocity, and power density profiles of the 2D SAM/Griffin/SAM and Pronghorn/Griffin coupled models are similar and show good agreement. Some differences are observed. For example, compared to the Pronghorn/Griffin model, the SAM/Griffin/SAM

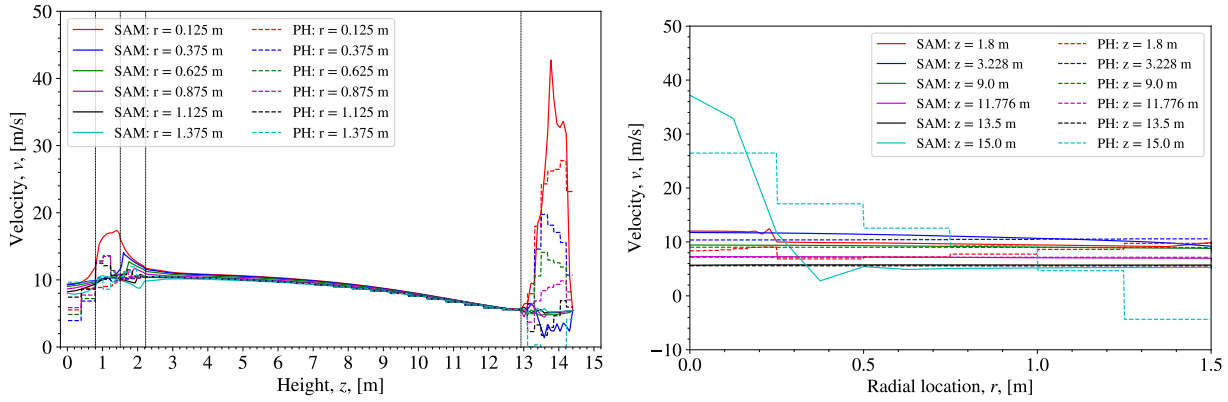

(a) Axial (b) Radial

Figure 27. Comparison of axial and radial fluid velocity (v_y) profiles of the coupled SAM/Griffin/SAM and Pronghorn/Griffin models.

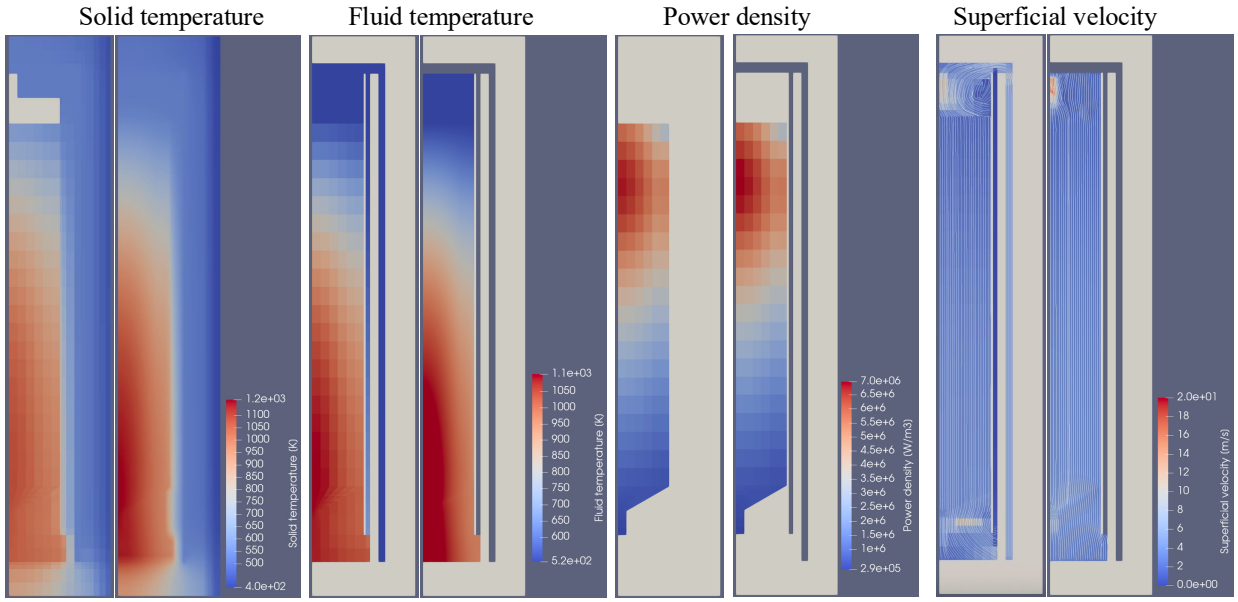

Figure 28. Comparison of solid temperature, fluid temperature, power density, and superficial velocity profiles of the coupled Pronghorn/Griffin (*left*) and SAM/Griffin/SAM models (*right*).

model predicts a larger temperature difference between the inner and outer regions of the core, which stems from the power density distribution differences between the models. Similar to the standalone model comparison, due to the difference in flow patterns, the temperature and velocity distributions in the hot plenum and bottom reflector region are somewhat different. Nevertheless, the core-wide parameters of the two models, such as core mass flow rate, pressure drop, and outlet temperature, agree well.

3.2. Depressurized Loss Of Forced Cooling Scenario

3.2.1. 2D SAM/SAM Results

In this section, the simulation of the protected DLOFC transient using the SAM model is discussed. The sequence of events for the DLOFC is summarized in Table 19. The sequence recommendations of the OECD-NEA benchmark exercise report for the PBMR-400 reactor [9] were modified for this simulation. Prior to initiating the transient, equilibrium steady-state conditions are first achieved. For this simulation, a simplification was made where the reactor is scrammed instantly at the beginning of the transient, reducing the reactor power to the decay heat level. The decay heat curve from the OECD-NEA report is applied to dictate the reactor power. From t = 0–13 seconds, the flow rate is reduced linearly from 96 kg/s to 0 kg/s, and the pressure is reduced from 7 MPa to 0.1 MPa (1 atm). The transient is simulated for 700,000 seconds.

Table 19. Sequence of events for the DLOFC simulated by the SAM model.

Time (s)	Events
< 0	Steady-state equilibrium is achieved.
0	Reactor is assumed to scram instantly.
	Decay heat curve is enabled.
0–13	Flow rate is reduced linearly to zero.
	System pressure is reduced linearly to 1 atm.
13–700,000	Simulate until the end of the transient.

Similar to the SAM DLOFC transient discussed in Section 3.2.1, the SAM model was simplified. Given that this is a protected transient in which the reactor is scrammed, the Griffin model was removed, and instead a decay heat curve dictates the decay heat level of the reactor during the transient. However, to ensure the accuracy of the model, the power density distribution during the transient is obtained from the steady-state results of the SAM/Griffin/SAM coupled model. Additionally, a simplified primary loop is used; both the blower and heat exchanger were removed and replaced with inlet and outlet boundary conditions. The primary loop model was developed based on the information available in the open literature. Therefore, the full primary loop model may introduce model-specific uncertainties that may not be accurate in the actual reactor. During the transient, the density of helium at 1 atm is significantly lower than the density of helium during normal operating conditions of 7 MPa. As a result, the effects of natural convection in the core can be neglected, as was done by Zheng et al. [3] in their simulation of the HTR-PM with TINTE code. This means that this is a conservative approach that represents the upper bound of the transient. In this approach, decay heat is removed from the core radially through conduction and thermal radiation. The correlations used in the SAM 2D model are summarized in Table 9.

Figure 29 shows the maximum and core-averaged pebble surface temperatures predicted by the SAM model during the DLOFC transient. The maximum pebble surface temperature rises sharply from approximately 1140 K to 1822.5 K within 24 hours from the start of the transient. The maximum pebble surface temperature remains below the safety limit of TRISO fuel, which is 1900 K [3]. Once the maximum temperature reaches its peak value, it decreases steadily for the remainder of the transient. The average pebble surface temperature has a trend that is similar to the maximum temperature in the first 25 hours. However, once the average temperature reaches its peak value, it remains relatively constant for the next 75 hours. At roughly t = 100 hours, the average pebble temperature starts to decrease steadily until the end of the simulation. The general trends of the maximum and average pebble temperatures agree with those reported by Zheng et al. [3], who simulated the DLOFC of the HTR-PM with TINTE and SPECTRA codes.

Figure 30 shows the maximum and volume-averaged temperatures of the side reflectors. The maximum temperature drops in the early stage of the transient after the reactor is scrammed and the power of the reactor

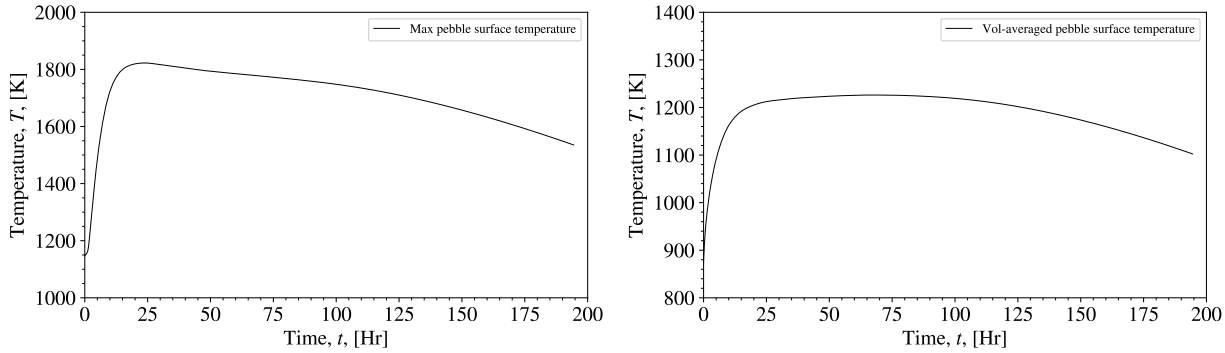

(a) Maximum (b) Volume Averaged

Figure 29. Maximum and volume-averaged pebble surface temperatures predicted by the SAM/SAM model during the DLOFC.

is reduced to the decay heat level. However, as the transient progresses and decay heat is transferred radially from the pebble bed to the surrounding reflectors, the maximum temperature increases until it reaches a peak value of approximately 1375 K at approximately t = 97 hours, after which it decreases steadily until the end of the simulation. On the other hand, the average reflector temperature does not drop initially. Instead, it increases continuously until approximately t = 100 hours before decreasing for the remainder of the simulation. The maximum and volume-averaged core barrel temperatures are shown in Figure 31. The overall trends of the core barrel temperatures are similar to the trends of the reflector temperatures. However, the peak maximum and average core barrel temperatures are 840.2 K and 626.4 K, respectively, which are lower than the peak maximum and average reflector temperatures. The maximum and volume-averaged RPV temperatures are shown in Figure 32; their trends are similar to those of the core barrel maximum and average temperatures. As expected, the RPV has lower maximum and average temperatures of 591 K and 505.6 K, respectively. Table 20 summarizes the time each region reaches peak temperature along with the maximum and volume-averaged temperatures. As the heat from the core moves mainly in the radial direction, each region attains its peak relatively soon after the region prior to it.

Table 20. Peak temperature of various reactor regions during the DLOFC simulated with the SAM/SAM model. Note the average temperatures of each region are the volume-averaged temperatures at the time when each region reached its peak temperature.

Region	Time to Peak (hr)	Avg. Temperature (K)	Max. Temperature (K)
Pebble surface	23.7	1210.9	1822.5
Reflector	97.3	840.2	1375.7
Core barrel	120.9	626.4	804.9
RPV	125.1	505.6	591.0

Figure 33 compares the RCCS heat removal rate with the decay heat produced by the reactor during the DLOFC transient. During steady-state conditions, the RCCS removes approximately 0.3 MW of heat, equivalent to roughly 0.1% of the total power. During the transient, as heat is transferred radially from the pebble bed to the side reflectors, the core barrel, the RPV, and eventually the RCCS, the RCCS heat removal rate increases substantially to a peak value of about 0.83 MW at approximately t = 125 hours. At the same time, the heat removal rate exceeds the decay heat of the core at about t = 100 hours, after which the temperatures of the pebble bed and other components of the reactor start to decrease. It should again be

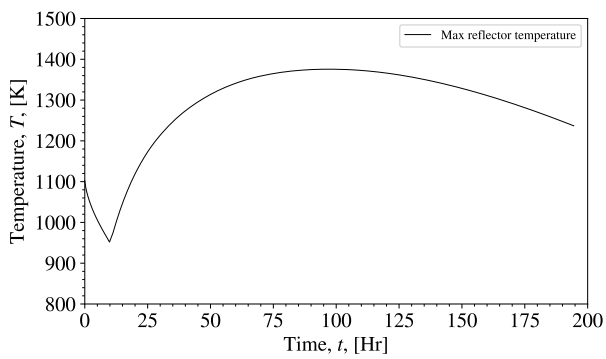

(a) Maximum

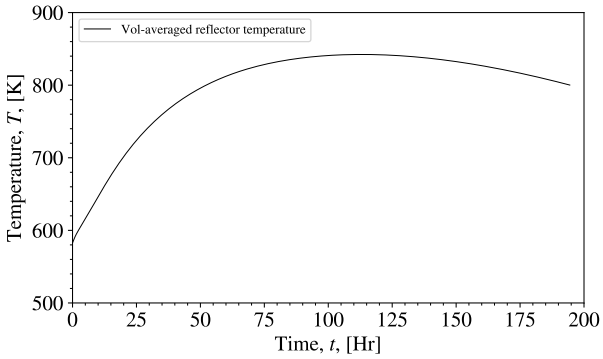

(b) Volume Averaged

Figure 30. Maximum and volume-averaged reflector temperature predicted by the SAM/SAM model during the DLOFC.

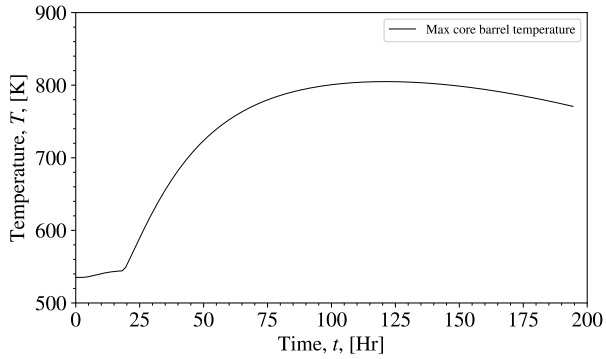

(a) Maximum

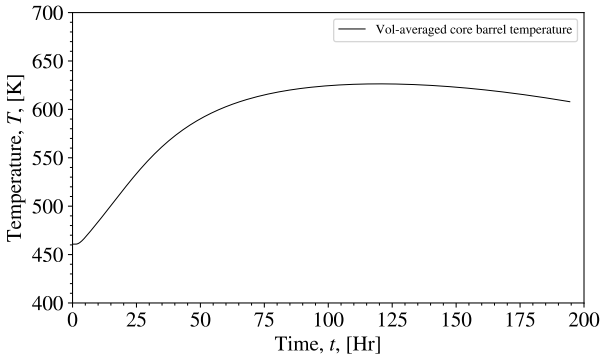

(b) Volume Averaged

Figure 31. Maximum and volume-averaged core barrel temperature predicted by the SAM/SAM model during the DLOFC.

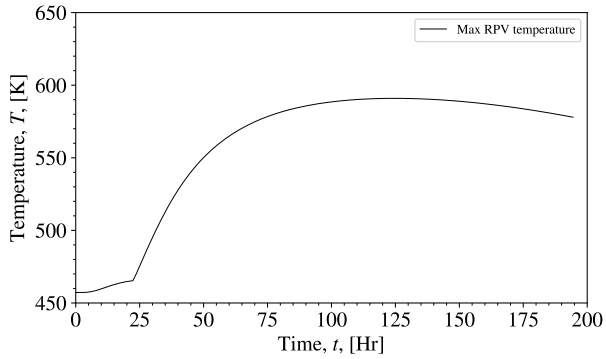

(a) Maximum

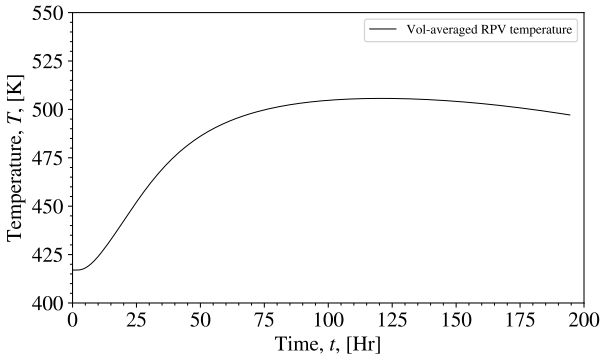

(b) Volume Averaged

Figure 32. Maximum and volume-averaged RPV temperature predicted by the SAM/SAM model during the DLOFC.

stressed that the RCCS model used here is based primarily on publicly available design information [37] and may not reflect the actual RCCS of the HTR-PM, which means that the heat removal rate of the actual RCCS

may differ from the results shown here. Nevertheless, the RCCS used in this work sufficiently removes decay heat during the DLOFC transient and keeps the pebble temperature below the safety limit.

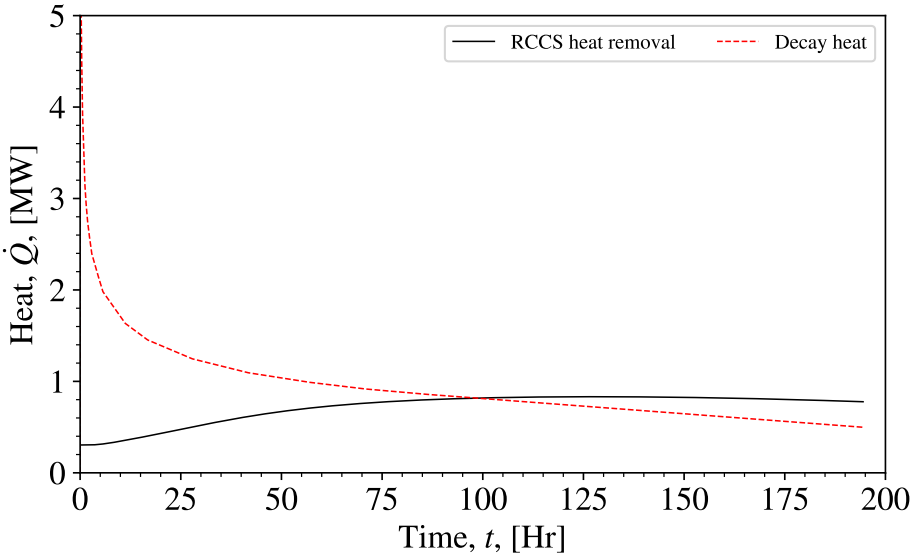

Figure 33. RCCS decay heat removal rate predicted by the SAM/SAM model during the DLOFC.

Figure 34 shows the distributions of solid temperature during the DLOFC transient. During steady-state equilibrium conditions, the hottest zone in the core is located at the bottom region. During the DLOFC, the hottest zone shifts upward to the inner upper region of the core. This is consistent with the power density distribution of the reactor during steady-state normal operating conditions. As the transient progresses, the temperature of the hot zone increases to its peak value of 1822.5 K at roughly t = 23.7 hours. Heat continuously dissipates radially from the pebble to the external structures through thermal radiation and conduction, causing the temperatures of these structures to rise. Conversely, heat dissipation in the axial direction in the core appears to be lower, as the temperature distribution of the core in the axial direction remains largely unchanged for most of the transient. Eventually, heat is transferred from the RPV external surface to the RCCS panel through thermal radiation.

Figure 35 shows the axial and radial solid temperature profiles of the reactor during peak pebble temperature at t = 23.7 hours. Based on the axial profiles, it can be seen that temperature rises sharply from the bottom to the top half of the core, following the same trend as the power density distribution. The radial profiles show a significant drop in temperature from the pebble bed to the surrounding structures during peak pebble temperature. Due to heat generation, the radial temperature profiles of the pebble bed have a parabolic shape, while the profiles for regions outside it show a linear trend. Both axial and radial profiles show that the pebble surface temperature peaks at about 1800 K. From the radial profiles it is observed that the RPV temperatures at all elevations are fairly uniform due to heat slowly dissipating from the pebble bed to the outer structures.

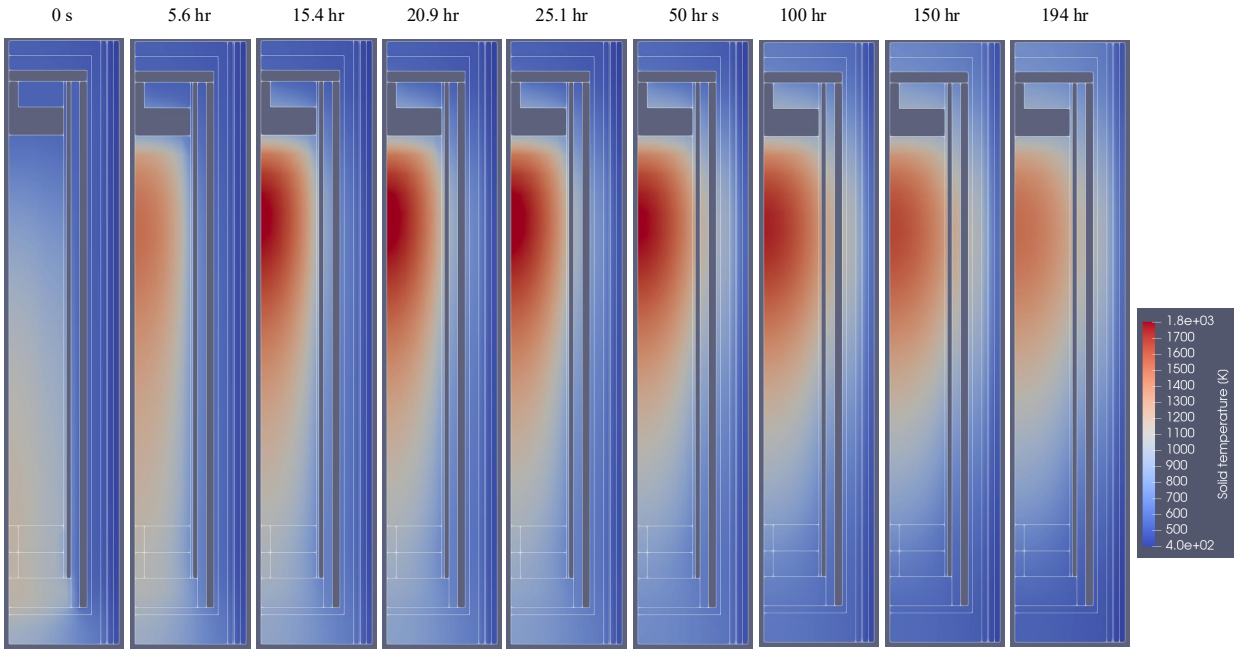

Figure 34. Distributions of solid temperature predicted by the SAM/SAM model during the DLOFC.

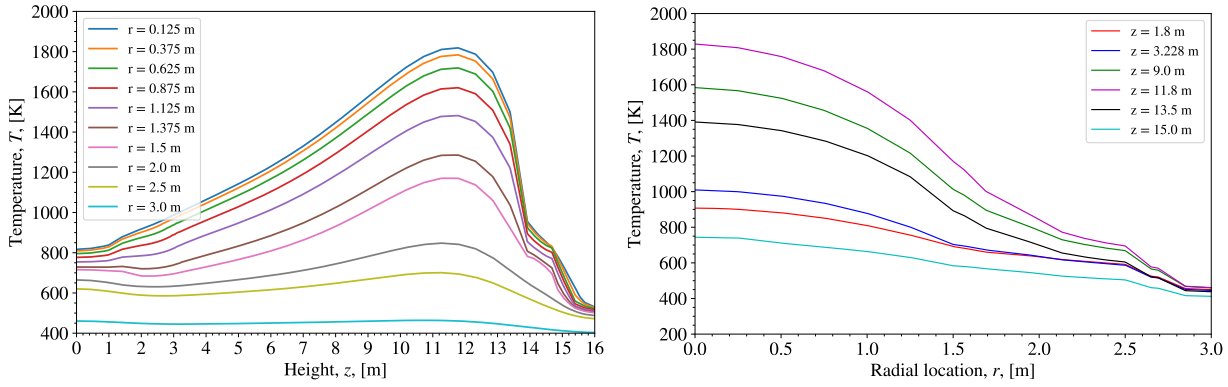

(a) Axial (b) Radial

Figure 35. Axial and radial solid temperature profiles predicted by the SAM/SAM model during the DLOFC during peak pebble temperature at t = 23.7 hours.

3.2.2. 2D Pronghorn/Griffin Results

This section presents the protected DLOFC accident scenario simulated with the Pronghorn/Griffin coupled code system.

For this scenario, it is assumed that the coolant completely leaks out of the RPV due to a large break in the coaxial duct, resulting in a fast reduction of the helium inventory in the system, followed by a depressurization of the reactor and flow coast-down. Natural circulation contributes minimally in extracting heat from the fuel due to the low coolant density at atmospheric pressure. Instead, the heat is extracted from the fuel via conduction and radiation heat transfer through the reflector, core barrel, RPV, and RCCS. The main objective of simulating the DLOFC is to examine whether the maximum fuel temperature exceeds the safety limits and whether the reactor is able to remove heat efficiently from the fuel. Preliminary verification test results of the DLOFC are presented in Reference [41].

The DLOFC transient simulation was initiated by reducing the mass flow rate of the coolant from its nominal (96.0 kg/s) operational value to zero while reducing the system pressure (7.0 MPa) to atmospheric pressure (0.101 MPa) over 13 seconds, and it was assumed that these changes behaved linearly. Therefore, after initiating the accident, the control rods were fully inserted (SCRAM) to shut down the reactor after the coolant mass flow rate reduction and system depressurization. Beyond that, there were no changes to the system's main parameters, and the simulation was performed for 200 hours. The sequence of events for the protected DLOFC transient is listed in Table 21.

Table 21. Sequence of events for the protected DLOFC simulated by Pronghorn/Griffin.

Time (s)	Event
< 0	Equilibrium steady state complete.
0–13	Reducing outlet pressure linearly to 0.1 MPa and mass flow rate linearly to 0 kg/s.
13	Mass flow rate and pressure ramps completed and control rods SCRAM is initiated.
13–16	Control rods fully inserted and power level is determined by decay heat until the end of the transient.
720,000	Transient simulation end time.

Initially, the equilibrium core steady-state solution was established with the Pronghorn/Griffin coupled code system. During the transient simulation the time-dependent reactor power was determined from the decay heat curve after reactor shutdown, taken from Reference [9], and was used to scale the power density distribution of the steady-state solution. The decay power is the main driving heat source during the transient since the prompt power goes to zero after the control rod are inserted. Figure 36 shows the average and maximum pebble surface temperature evolutions during the DLOFC transient. The average and maximum pebble surface temperatures increase and attain their maximum values at approximately 35 hours, with values of 1233.2 K and 1809.8 K, respectively. Beyond that point, the pebble surface temperature decreases as the heat dissipates radially through the reflector region to the RPV. Additionally, Figures 37, 38, and 39 show the maximum and average temperatures of the reflector, core barrel, and RPV, respectively. Since the heat generated moves mainly in the radial direction, each region attains its peak relatively soon after the region prior to it. The maximum and average temperature peaks of each region are provided in Table 22. Generally, the temperature profiles of the three regions are similar, except for the maximum reflector temperature. The reflector temperature drops significantly and then starts increasing at approximately 12 hours. This could be related to the change in the location of the peak pebble surface temperature after the transient is initiated

The reactor power evolution and the heat removed by the RCCS during the DLOFC transient are shown in Figure 40. Initially, 0.25 MW is removed by the RCCS at a steady-state rate, and the removal rate increases as the transient progresses, exceeding the reactor power generated from decay heat of about 1.0 MW at 62 hours, peaking at 1.026 MW after 82 hours of the transient. Beyond that, the heat removed by the RCCS

Table 22. Peak temperature of various reactor regions during the DLOFC simulated with Pronghorn/Griffin. Note that the average temperatures of each region are the averaged temperatures at the time when each region reaches its peak temperature.

Region	Time to Peak (hr)	Avg. Temperature (K)	Max. Temperature (K)
Pebble surface	35	1233.2	1809.8
Reflector	64	790.7	1274.5
Core barrel	78	630.6	777.1
RPV	81	530.2	639.8

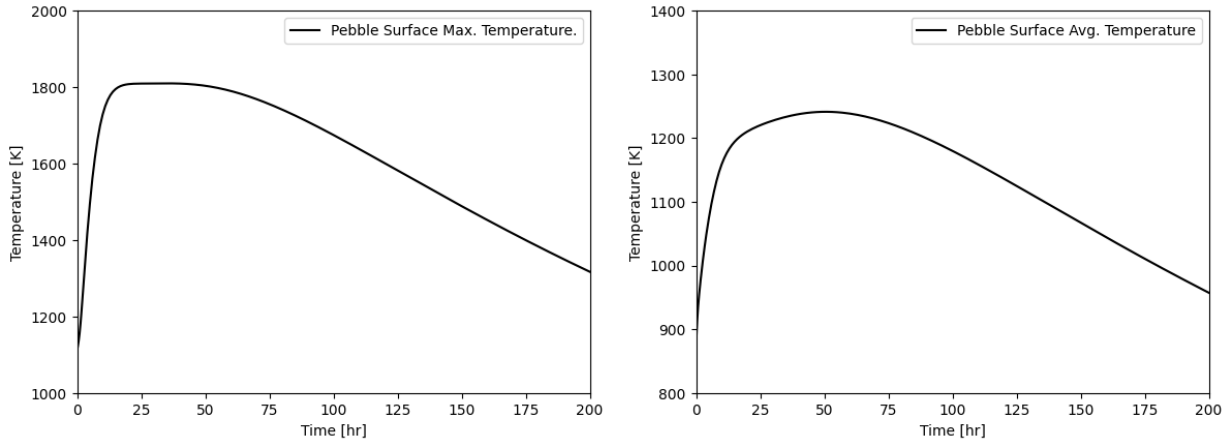

(a) Maximum (b) Average

Figure 36. Maximum and average pebble surface temperatures during the DLOFC obtained by the Pronghorn/Griffin model.

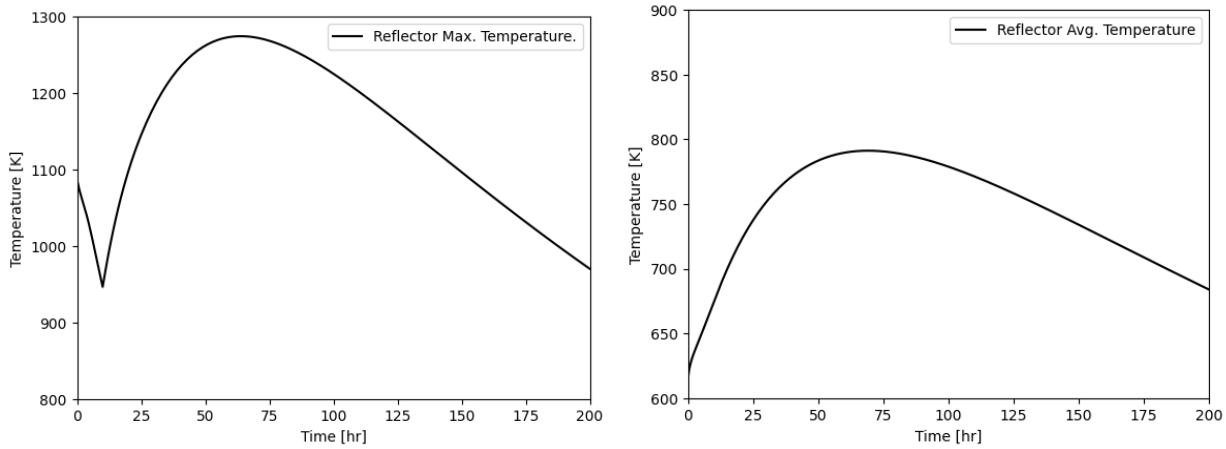

(a) Maximum (b) Average

Figure 37. Maximum and average reflector temperatures during the DLOFC obtained by the Pronghorn/Griffin model.

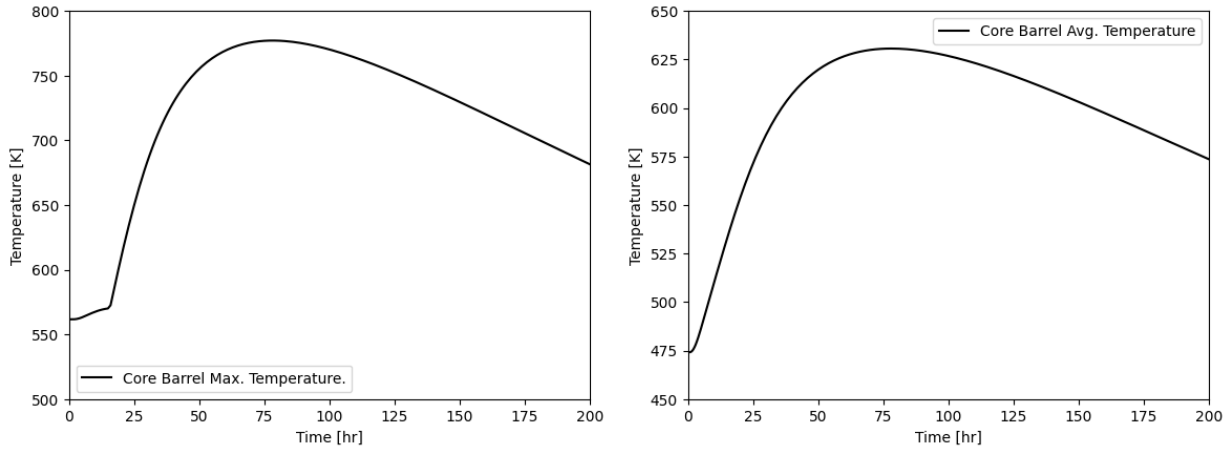

(a) Maximum (b) Average

Figure 38. Maximum and average core barrel temperatures during the DLOFC obtained by the Pronghorn/Griffin model.

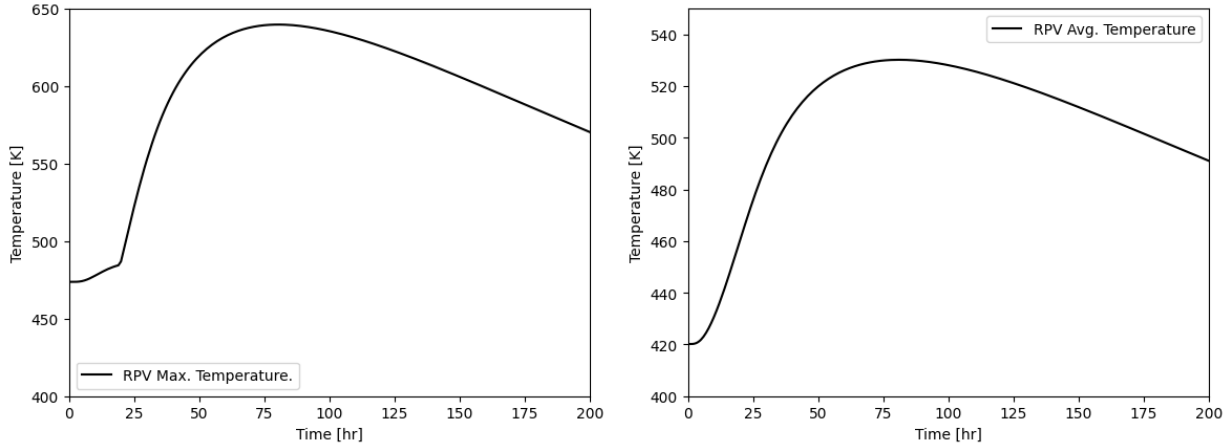

(a) Maximum (b) Average

Figure 39. Maximum and average RPV temperatures during the DLOFC obtained by the Pronghorn/Griffin model.

decreases monotonically. Additionally, Figure 41, which shows the solid temperature distribution during the DLOFC transient, illustrates the shift in the solid peak temperature location after the transient is initiated. The maximum solid temperature transitions from the bottom of the core toward the top region of the core under the cavity, where the core power density peaks. The temperature increases until it reaches a maximum value of approximately 1800 K, then it decreases as the heat dissipates radially toward the RPV region. The axial and radial solid temperature profiles at 35 hours, when the pebble temperature peaks, are shown in Figure 42. The temperature profile peaks at 1800 K at position 11.0 m and toward the center of the core, and there is significant variation in the radial direction toward the outer core regions. The discontinuities in the solid temperature profile observed in Figure 42 occur at the cavity above the pebble-bed region.

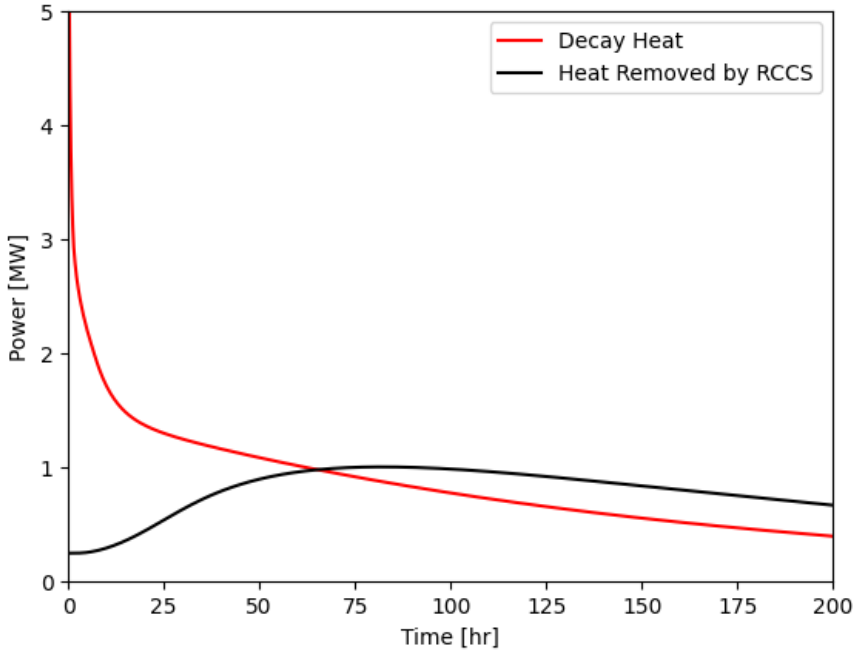

Figure 40. Decay heat and heat removed by the RCCS during the DLOFC obtained by the Pronghorn/Griffin model.

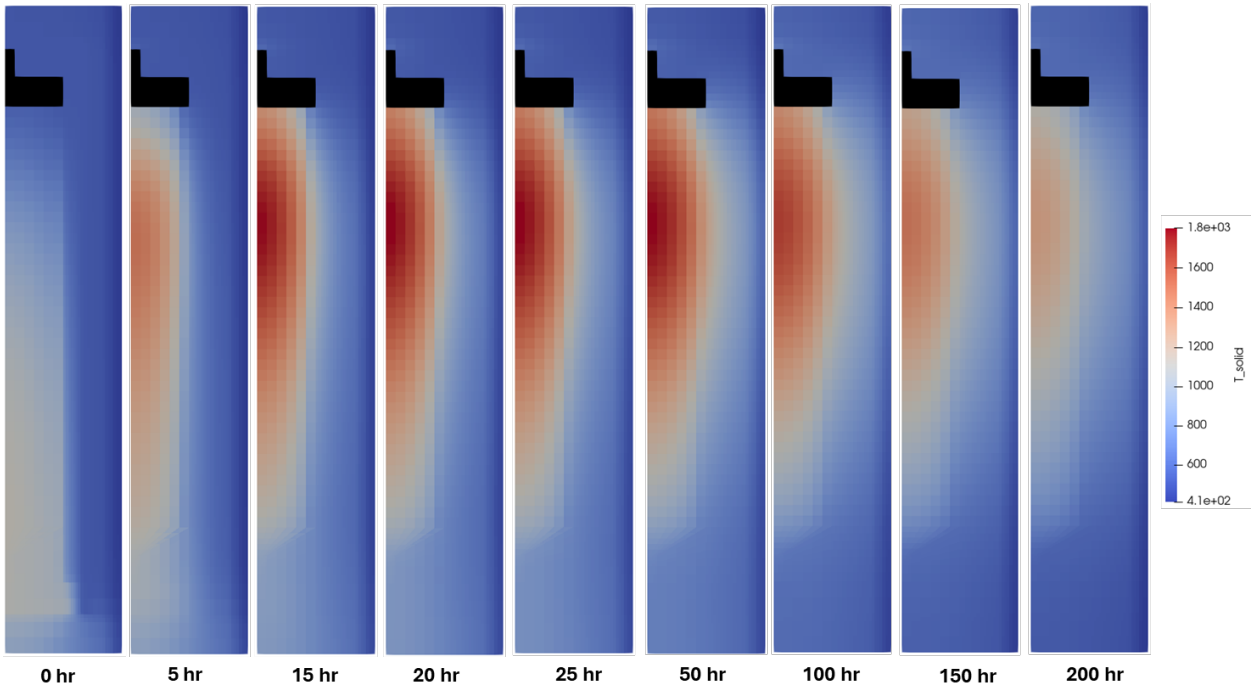

Figure 41. Solid temperature distribution during the DLOFC obtained by the Pronghorn/Griffin model.

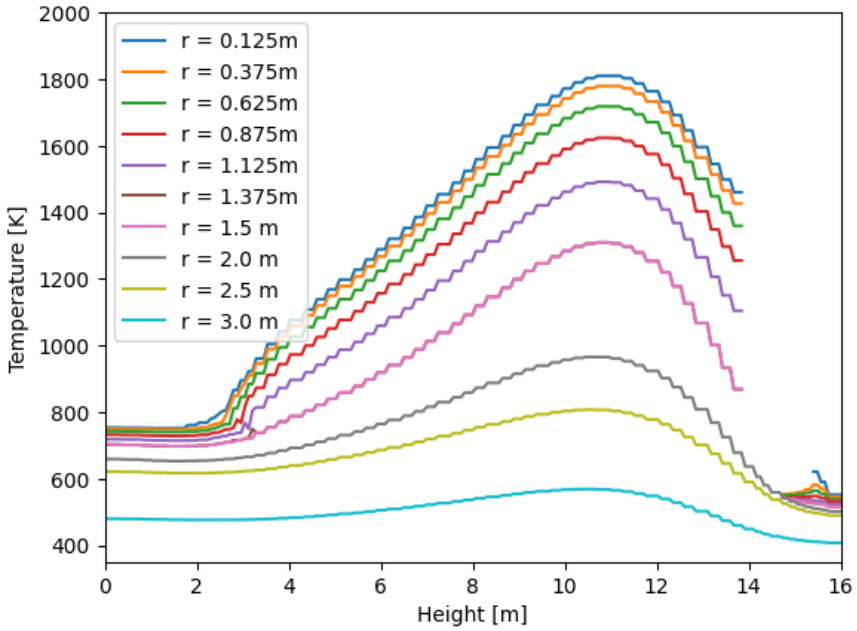

(a) Axial

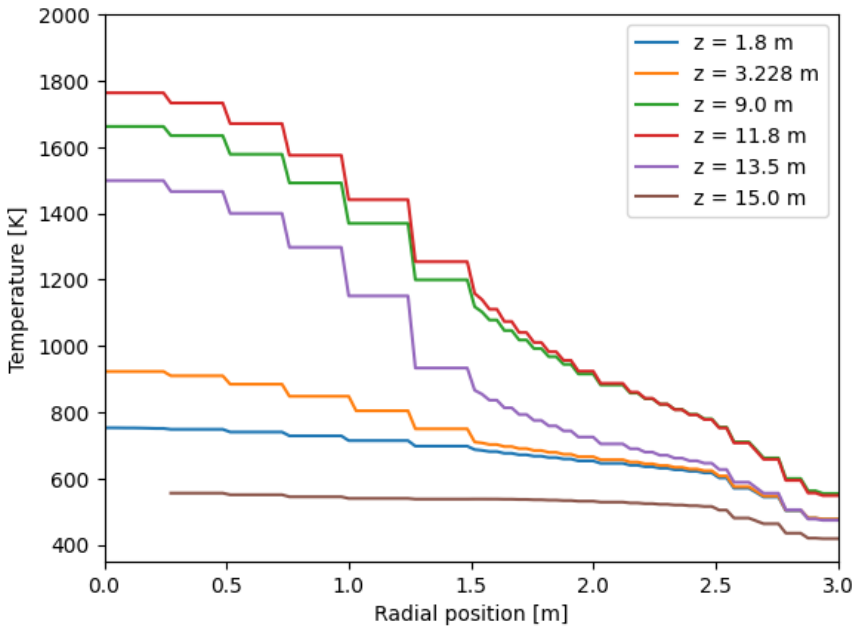

(b) Radial

Figure 42. Axial and radial solid temperature profiles during the DLOFC obtained by the Pronghorn/Griffin model during peak temperature of the pebble surface at 35 hours of the transient.

3.2.3. Comparison

As discussed previously, decay heat generated in the pebble-bed region is removed to the surrounding reflectors almost entirely through conduction and thermal radiation due to the minimal convective effects caused by the low density of helium at atmospheric pressure. Hence, it is important to ensure that calculations of the effective thermal conductivity in the pebble-bed region are accurate.

A comparison of the effective thermal conductivity between the 2D SAM and 2D Pronghorn models shows that during steady-state conditions, the 2D SAM model has a maximum effective thermal conductivity of 12.2 W/mK, while the 2D Pronghorn model has a higher value of 15.5 W/mK. This is due to the differences in the correlations the models use to calculate the effective thermal conductivity of the pebble bed. In the 2D SAM model, as summarized in Table 9, the ZBS correlation is used to calculate the contributions from three mechanisms, namely solid-solid conduction, solid-solid radiation, and solid-fluid conduction. On the other hand, the 2D Pronghorn model uses the ZBS correlation for solid-solid conduction and solid-fluid conduction, and the Breitbach–Barthels [42] correlation for solid-solid radiation.

In this section, we discuss the findings of the sensitivity analysis we performed to investigate how effective thermal conductivity affects the prediction of the SAM/SAM model during a DLOFC. The DLOFC simulation was repeated with different approaches to calculate the effective thermal conductivity of the pebble bed, namely the ZBS correlation, the International Atomic Energy Agency (IAEA correlation [43], and a modified ZBS correlation in which a multiplicative factor of 1.3 is applied only to the radiation portion of the correlation. The value of the multiplicative factor is selected based on the differences in the effective thermal conductivities calculated by the 2D SAM and Pronghorn models during the steady-state equilibrium condition.

Figure 43 compares the maximum and volume-averaged pebble surface temperatures during the DLOFC predicted by the SAM/SAM model using different approaches to calculate the pebble-bed effective thermal conductivity. The three sets of results essentially share the same overall trend. However, as tabulated in Table 43, the SAM/SAM model predicts the highest pebble surface temperature with the ZBS correlation, followed by the IAEA correlation, and lastly the modified ZBS correlation. This analysis highlights the sensitivity of the pebble temperature to the effective thermal conductivity during a DLOFC, where conduction and radiation are the dominant heat removal mechanisms in the pebble bed. Finally, it should be pointed out that the impacts of effective thermal conductivity are practically non-existent during steady-state normal operating conditions because heat is removed almost entirely by forced convection.

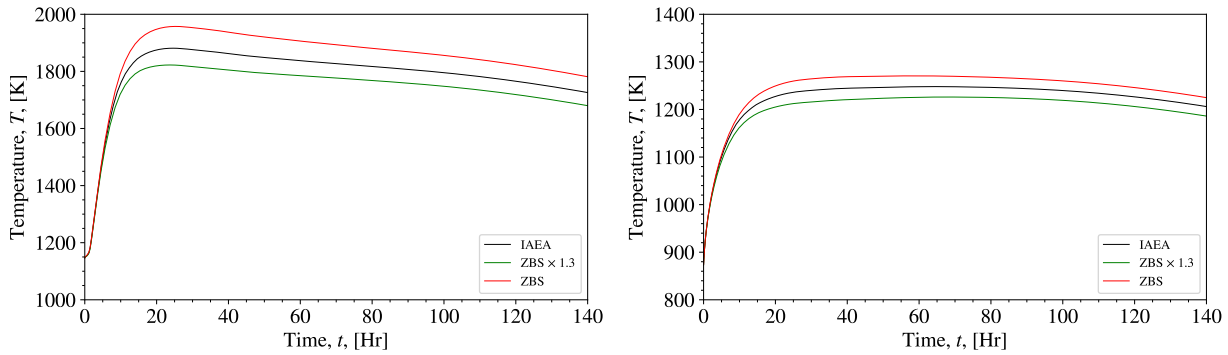

(a) Maximum

(b) Volume Averaged

Figure 43. Comparison of the maximum and volume-averaged pebble surface temperatures during the DLOFC predicted by the SAM/SAM model with different effective thermal conductivity correlations. Note the multiplicative factor of 1.3 is only applied to the radiation portion of the ZBS correlation.

Table 23. Comparison of maximum pebble surface temperature predicted by the SAM/SAM model with different effective thermal conductivity models. Note the multiplicative factor of 1.3 is only applied to the radiation portion of the ZBS correlation.

Correlations	Max. Pebble Surface Temperature (K)
ZBS	1957.5
IAEA	1881.2
ZBS×1.3	1822.5

With a multiplicative factor of 1.3 applied to the radiation portion of the ZBS correlation, the effective thermal conductivity predicted by the SAM/SAM model matches the effective thermal conductivity predicted by the Pronghorn/Griffin model the best. Hence, its results are presented in Section 3.2.1 and this section for comparison with the Pronghorn/Griffin results. The remainder of this section compares and contrasts the DLOFC predictions of the SAM/SAM and Pronghorn/Griffin models presented in Sections 3.2.1 and 3.2.2, respectively.

Generally, the DLOFC predictions from the SAM/SAM and Pronghorn/Griffin models show decent agreement. As shown in Figure 44, the predicted peak temperatures from both models are close, with the SAM/SAM model predicting 1822.5 K and the Pronghorn/Griffin model predicting 1809.8 K. The general trends of the maximum and average pebble surface temperatures from both models are similar; the maximum temperature increases drastically from less than 1200 K to roughly the peak value within 25 hours from the start of the transient. The pebble surface temperatures predicted by both models agree well up to approximately t = 75 hours, after which Pronghorn/Griffin predicts a sharper drop. The discrepancy is likely because the Pronghorn/Griffin model imposes radiative and convective boundary conditions on the external surface of the RPV to simulate heat loss to the RCCS, whereas the SAM/SAM model includes the RCCS model. This likely results in a different heat removal rate on the surface of the RPV, as shown in Figure 45. The SAM/SAM model predicts the crossover point between decay heat and heat removal rate at approximately 100 hours, while the Pronghorn/Griffin model predicts the crossover at approximately 62 hours. The SAM/SAM model also predicts a lower peak heat removal rate of 0.83 MW, while the Pronghorn/Griffin model predicts a peak removal rate of about 1.0 MW. Additionally, the decay heat level of the Pronghorn/Griffin model is also slightly lower than that of the SAM/SAM model after about t = 100 hours, which further contributes to the differences between the predicted pebble surface temperatures.

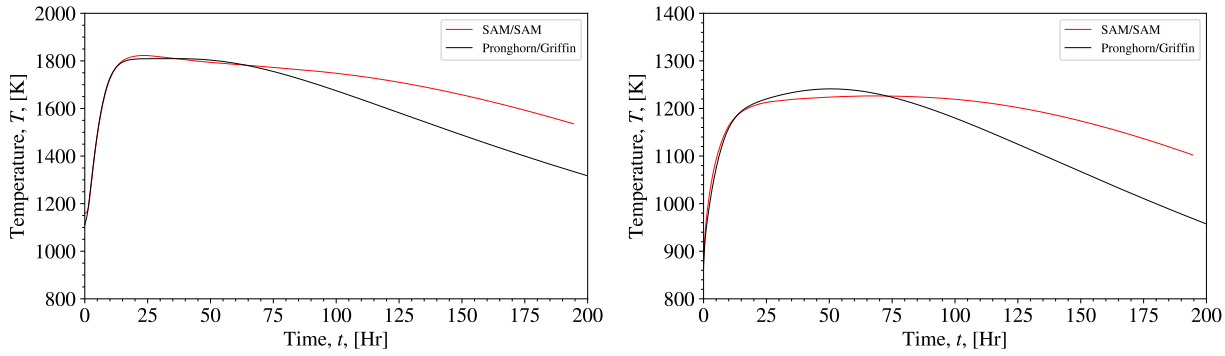

(a) Maximum

(b) Volume Averaged

Figure 44. Comparison of the maximum and volume-averaged pebble surface temperatures during the DLOFC predicted by the SAM/SAM and Pronghorn/Griffin models.

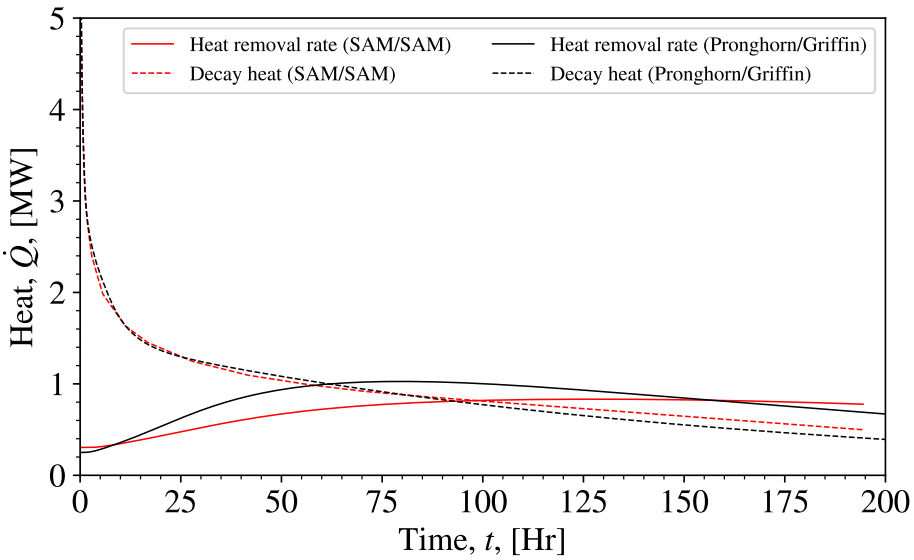

Figure 45. Comparison of the RCCS heat removal rate during the DLOFC predicted by the SAM/SAM and Pronghorn/Griffin models.

Furthermore, the maximum and average temperatures of the reflectors and core barrel predicted by both models also show good agreement, as shown in Figures 46 and 47. Similar to the pebble surface temperatures, the reflector and core barrel temperatures between the two models show decent comparison initially but diverge later in the transient. The SAM/SAM model also predicts higher temperatures than the Pronghorn/Griffin model, likely due to the difference in how the heat removal mechanism is modeled for the RPV. The maximum and average temperatures of the RPV are shown in Figure 48. Compared to the SAM/SAM model, the temperature increase in the Pronghorn/Griffin model is steeper in the initial stage of the transient, followed by a steeper temperature drop in the later stage. This indicates that decay heat is being removed in the Pronghorn/Griffin model at a faster rate than in the SAM/SAM model.

Overall, the SAM/SAM and Pronghorn/Griffin models predicted similar reactor behavior during the DLOFC transient. Despite some differences in the RCCS heat removal rate, both models showed that the maximum pebble temperature, which is one of the primary safety concerns during a DLOFC, remains below the safety limit. The trends of the average and maximum pebble surface, reflector, core barrel, and RPV temperatures produced by both models are similar. For all regions, agreement is good early in the transient, but there are differences in the latter part of the transient due to the modeling of the RCCS and the differences in decay heat between the two models. Both models also predicted a similar time evolution for the temperature distributions, in which the hottest region in the core shifts from the bottom of the core upward to the top of the core as the transient progresses. All in all, both the SAM/SAM and Pronghorn/Griffin models demonstrate that they can model the DLOFC transient well.

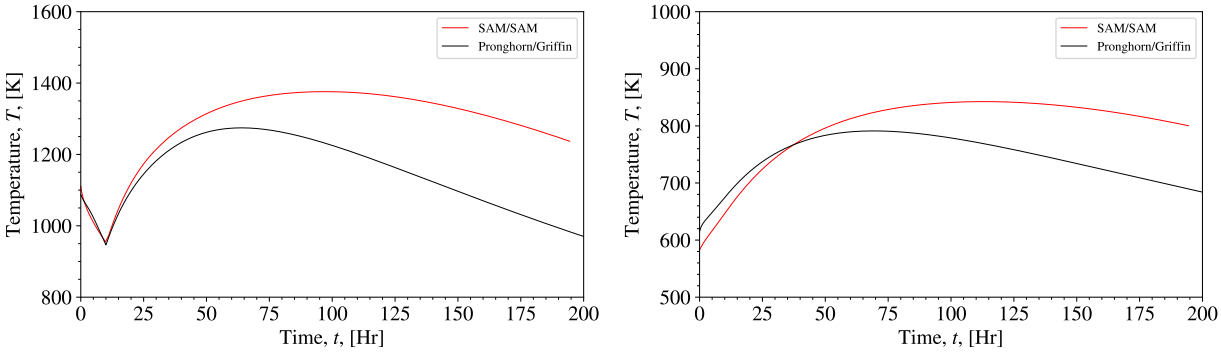

(a) Maximum (b) Volume Averaged

Figure 46. Comparison of the maximum and volume-averaged reflector temperatures during the DLOFC predicted by the SAM/SAM and Pronghorn/Griffin models.

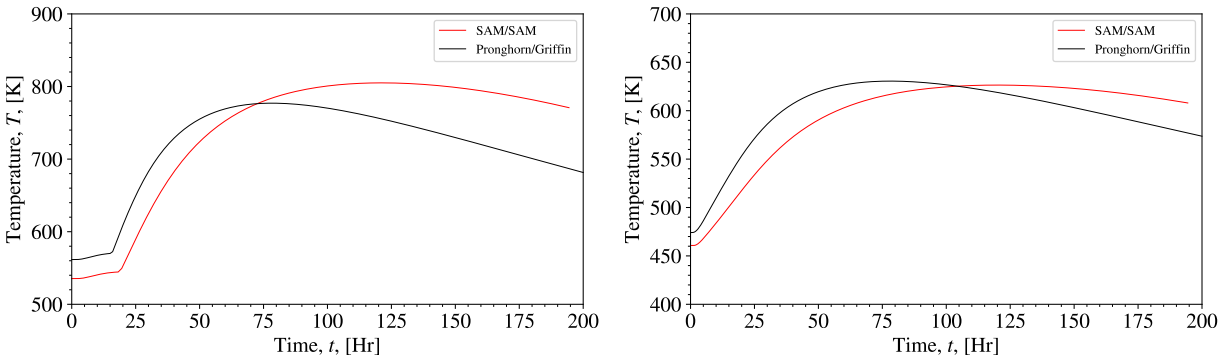

(a) Maximum (b) Volume Averaged

Figure 47. Comparison of the maximum and volume-averaged core barrel temperatures during the DLOFC predicted by the SAM/SAM and Pronghorn/Griffin models.

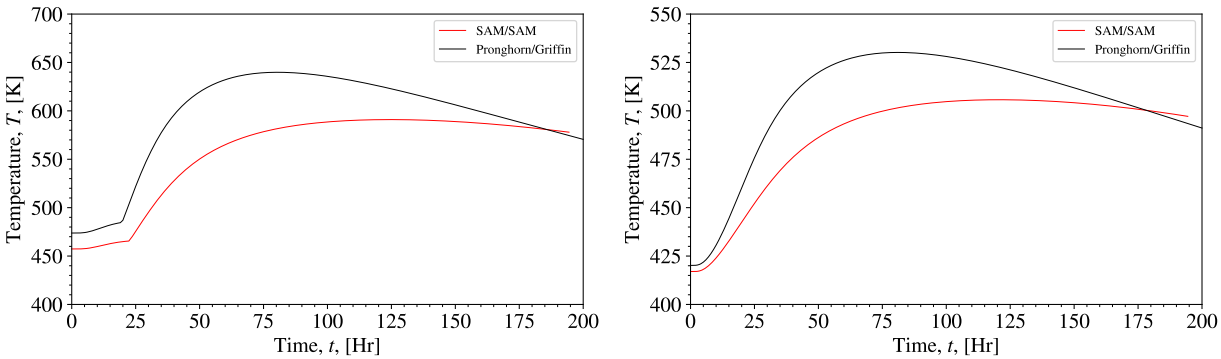

(a) Maximum (b) Volume Averaged

Figure 48. Comparison of the maximum and volume-averaged RPV temperatures during the DLOFC predicted by the SAM/SAM and Pronghorn/Griffin models.

3.3. Pressurized Loss Of Forced Cooling Scenario

3.3.1. 2D SAM/SAM Results

In this section, we discuss the protected PLOFC transient simulated by the SAM model. The sequence of events during the PLOFC transient, summarized in Table 24, was modified from the recommendations of the OECD-NEA benchmark exercise report for the PBMR-400 reactor [9]. Prior to the transient, equilibrium steady-state conditions are first achieved. For this simulation, a simplification was made where the reactor is scrammed instantly at the beginning of the transient, reducing the reactor power to the decay heat level. The decay heat curve obtained from the OECD-NEA report is applied to dictate the reactor power. From t = 0–13 seconds, the flow rate is reduced linearly from 96 kg/s to 0 kg/s, and the pressure is maintained at 7 MPa throughout the transient. The transient is simulated for 700,000 seconds.

Table 24. Sequence of events for the PLOFC simulated by the SAM model.

Time (s)	Events
< 0	Steady-state equilibrium is achieved.
0	Reactor is assumed to scram instantly.
	Decay heat curve is enabled.
0–13	Flow rate is reduced linearly to zero.
	System pressure is maintained at 7 MPa.
13–700,000	Simulate until the end of the transient.

Similar to the SAM DLOFC transient discussed in Section 3.2.1, the SAM model was simplified. Given that this is a protected transient in which the reactor is scrammed, the Griffin model was removed, and instead a decay heat curve dictated the decay heat level of the reactor during the transient. However, to ensure the accuracy of the model, the power density distribution during the transient was obtained from the steady-state results of the SAM/Griffin/SAM coupled model. Additionally, a simplified primary loop was used where the blower and heat exchanger were removed and replaced with inlet and outlet boundary conditions. Given that the design information of the primary loop was obtained from rough estimates based on sources in the public domain, including the full primary loop model, it introduced model-specific uncertainties that may not be accurate in the actual reactor. Furthermore, this approach is consistent with the procedure of the HTR-PM reactor protection system during a PLOFC, in which the helium blower, feed-water pump, and steam generators are halted and isolated from the core [44].

The correlations used by the 2D SAM model are summarized in Table 25. The effective thermal conductivity of the pebble bed is calculated using the ZBS correlation without the multiplicative factor discussed in Section 3.2.3. This is because convective heat transfer plays a dominant role in heat removal during a PLOFC due to natural circulation in the core. As a result, the impact of effective thermal conductivity is significantly smaller in a PLOFC than in a DLOFC. A separate PLOFC simulation was conducted with the same multiplicative factor applied to the radiation portion of the ZBS correlation, and it was found that the maximum and average pebble surface temperatures only decrease by approximately 20 K and 10 K, respectively, while maintaining the same trends. Hence, for the PLOFC simulation, the ZBS correlation was not modified. Additionally, the frictional pressure drop correlation for the upper reflector, lower reflector, hot plenum, and top cavity was switched to the KTA correlation from the Churchill correlation. This modification was needed due to convergence difficulties in the original model, likely due to numerical instability stemming from the low-flow condition in these regions during a PLOFC. Work is currently underway to address this issue.

Figures 49 show the maximum and volume-averaged pebble surface temperatures predicted by the SAM model during the PLOFC transient. The maximum pebble surface temperature increases sharply from

Table 25. Correlations used in the 2D SAM model for the PLOFC.

Regions	HTC	Wall HTC	Friction	Effective Thermal Conductivity
Pebble bed, chute, cone	KTA	KTA	KTA	ZBS
Upper and lower reflector, hot plenum, top cavity	Dittus–Boelter	Dittus–Boelter	KTA	ZBS

approximately 1140 K to approximately 1335 K in the first 5 hours of the transient. After that, the maximum temperature decreases gradually for the remainder of the transient. A similar trend is observed in the average pebble surface temperature during the early phase of the transient. As forced convection is lost, the average surface temperature rises from approximately 860 K to approximately 980 K within roughly 5 hours from the start of the transient. As natural circulation is established within the core, heat dissipates throughout the core, thus bringing the average pebble surface temperature down. However, at approximately t = 20 hours, the average pebble surface temperature starts to increase again, eventually reaching a peak value of roughly 950 K at approximately t = 65 hours. The second peak observed in the average pebble surface temperature is due to heat being distributed in the pebble bed by natural circulation, which causes the overall temperature of the pebble bed to rise even though the maximum temperature is decreasing. Once it peaks, the average pebble temperature remains relatively constant for approximately 25 hours before decreasing more rapidly from roughly t = 90 hours. The effects of natural circulation can also be seen in the trend of maximum pebble temperature after its peak. From roughly t = 5 to 20 hours, the maximum pebble temperature shows a relatively large decrease due to natural circulation in the core. However, from approximately t = 20 to 90 hours, the rate of the maximum pebble temperature decrease slows due to heat being redistributed within the pebble bed by natural circulation. From t = 90 hours onward, the rate of decrease once again picks up as heat dissipates from the pebble to the surrounding structures and eventually to the RCCS.

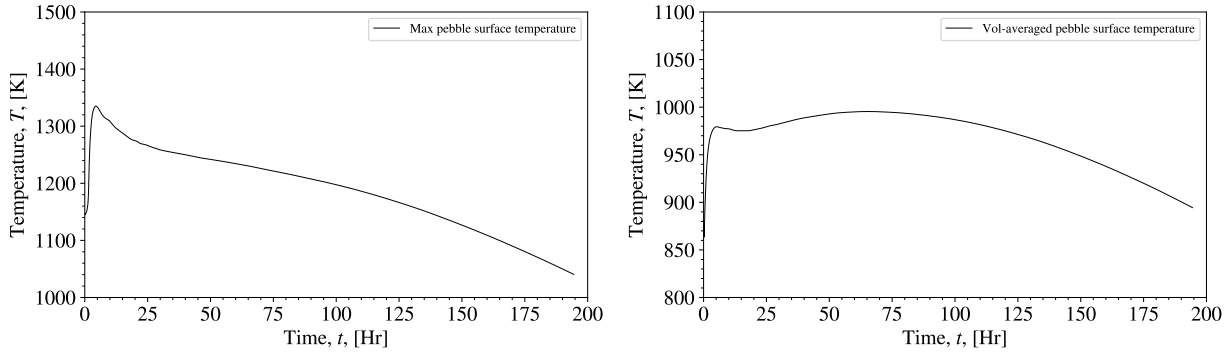

(a) Maximum (b) Volume Averaged

Figure 49. Maximum and volume-averaged pebble surface temperature predicted by the SAM/SAM model during the PLOFC.

Figures 50 to 52 show the maximum and volume-averaged temperatures for the reflector, core barrel, and RPV. The maximum reflector temperature drops in the early stage of the transient after the reactor is scrammed and the power of the reactor is reduced to the decay heat level. However, as the transient progresses and decay heat is transferred radially from the pebble bed to the surrounding reflectors, the maximum temperature starts to increase until it reaches a second peak of about 1009 K at approximately t = 64.5 hours, after which it decreases steadily until the end of the simulation. On the other hand, the average reflector temperature does not show an initial drop. Instead, it increases continuously until roughly t = 100 hours before it decreases for

the remainder of the simulation. The maximum and volume-averaged core barrel temperatures are shown in Figure 51. The overall trends of the core barrel temperatures are similar to the trends of the reflector temperatures. However, the peak maximum and average core barrel temperatures are about 665 K and 602 K, respectively, which are lower than the peak maximum and average reflector temperatures. The maximum and volume-averaged RPV temperatures are shown in Figure 52; their trends are similar to those of the core barrel maximum and average temperatures. As expected, the RPV has lower maximum and average temperatures of roughly 530 K and 496 K, respectively. Similar to the average pebble surface temperature and due to the distribution of heat from the pebble bed to the external structures, the average temperatures of the reflector, core barrel, and RPV remain relatively constant for an extended period before dropping significantly.The times of peak temperature for each region are tabulated in Table 26. As the heat from the core moves mainly in the radial direction, each region attains its peak relatively soon after the region prior to it.

Figure 53 compares the RCCS heat removal rate with the decay heat produced by the reactor during the PLOFC transient. During steady-state conditions, the RCCS removes about 0.3 MW of heat, the equivalent to roughly 0.1% of the total power. During the transient, as heat is transferred radially from the pebble bed to the side reflectors, the core barrel, the RPV, and eventually the RCCS, the RCCS heat removal rate increases substantially to a peak value of about 0.75 MW at approximately t = 110 hours. At the same time, the heat removal rate exceeds the decay heat of the core at roughly t = 125 hours, after which the temperatures of the pebble bed and other components of the reactor start to decrease. It should again be stressed that the RCCS model used here is based primarily on publicly available design information [37] and may not reflect the actual RCCS of the HTR-PM, which means that the heat removal rate of the actual RCCS may differ from the results shown here. Nevertheless, the RCCS used in this work sufficiently removed decay heat during the PLOFC transient and kept the pebble temperature below the safety limit.

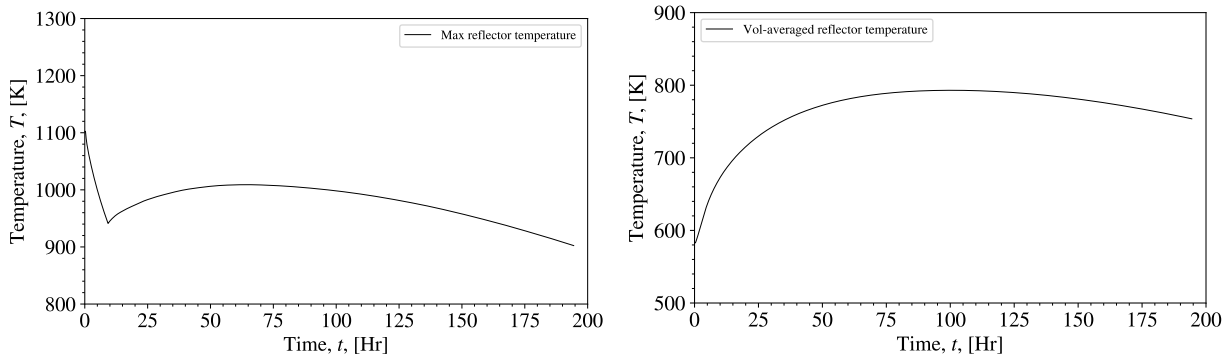

(a) Maximum (b) Volume Averaged

Figure 50. Maximum and volume-averaged reflector temperature predicted by the SAM/SAM model during the PLOFC.

Figure 54 shows the evolution of the solid temperature distribution, and Figure 55 shows the fluid temperature distribution along with the streamlines of the flow in the core during the PLOFC. At the beginning of the transient, heat is concentrated at the bottom region of the reactor due to the coolant flowing from the top to the bottom. As the transient progresses and natural circulation forms in the core, the top half of the core starts to heat up following the distribution of power density. The formation of natural circulation is evident from the streamlines in Figure 55, where helium is observed to flow upward in the hotter inner region of the core and downward in the colder outer region. At the same time, natural circulation improves the distribution of heat from the hotter region to the colder region in the core, which then helps to dissipate heat from the pebble bed to the side reflectors. Compared to the temperature distributions during the DLOFC shown in Figure 34, the solid temperature is more uniform across the pebble bed due to the improved distribution of

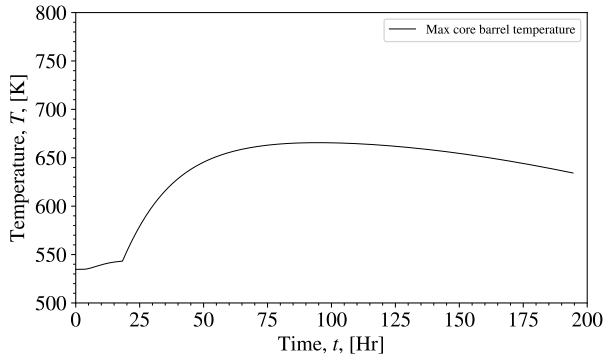

(a) Maximum

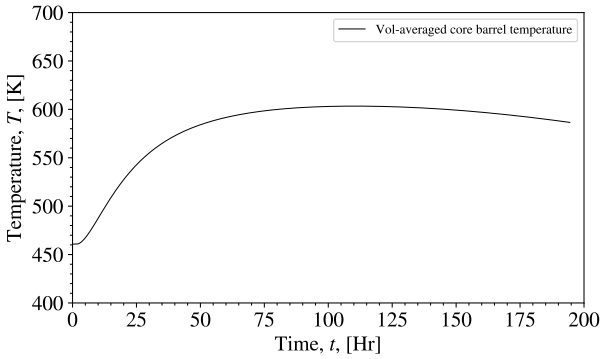

(b) Volume Averaged

Figure 51. Maximum and volume-averaged core barrel temperature predicted by the SAM/SAM model during the PLOFC.

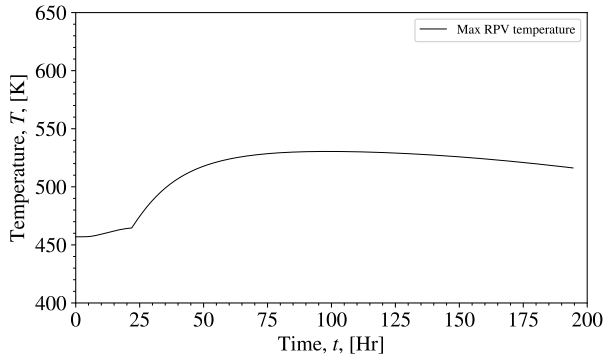

(a) Maximum

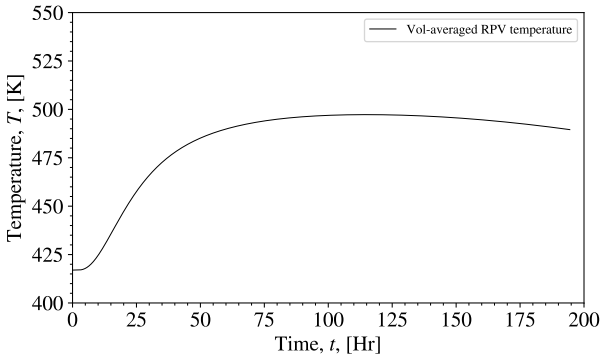

(b) Volume Averaged

Figure 52. Maximum and volume-averaged RPV temperature predicted by the SAM/SAM model during the PLOFC.

Table 26. Peak temperature of various reactor regions during the PLOFC simulated with the SAM/SAM model. Note that the average temperatures of each region are the volume-averaged temperatures at the time when each region reaches its peak temperature.

Region	Time to Peak (hr)	Avg. Temperature (K)	Max. Temperature (K)
Pebble	4.4	978.5	1335.3
Reflector	64.5	783.9	1009.0
Core barrel	94.6	602.5	665.6
RPV	98.7	496.8	530.4

heat by natural circulation in the core. As heat is continuously transferred radially outward from the pebble bed, the temperatures of the surrounding structures start to heat up, and the temperature of the pebble bed eventually decreases as the RCCS heat removal rate exceeds the decay heat.

Figure 56 shows the axial and radial profiles of the solid temperature during peak pebble temperature at t = 4.4 hours. In the pebble bed, represented by r = 0.125 m to 1.5 m, the axial profiles show two major peaks: one smaller peak at the lower region of the core and a larger peak at the upper region. The larger peak is due

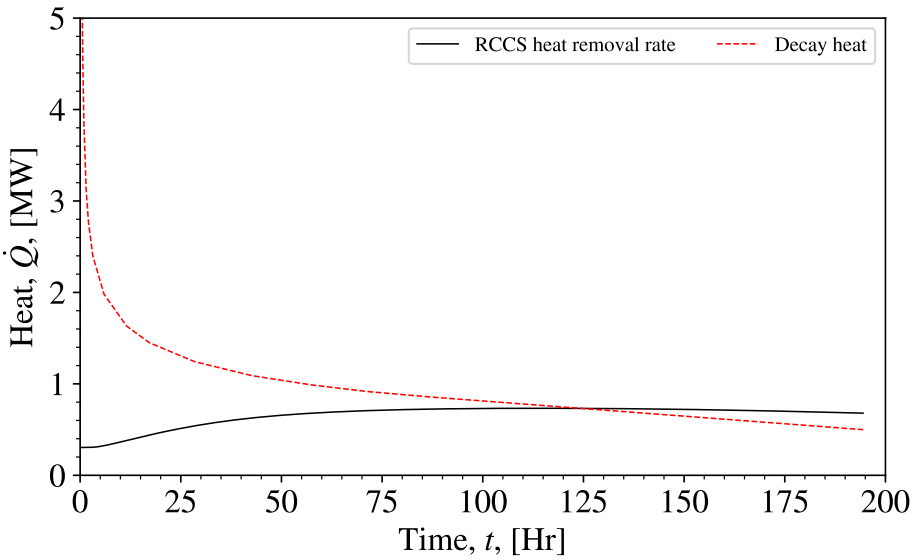

Figure 53. RCCS decay heat removal rate predicted by the SAM/SAM model during the PLOFC.

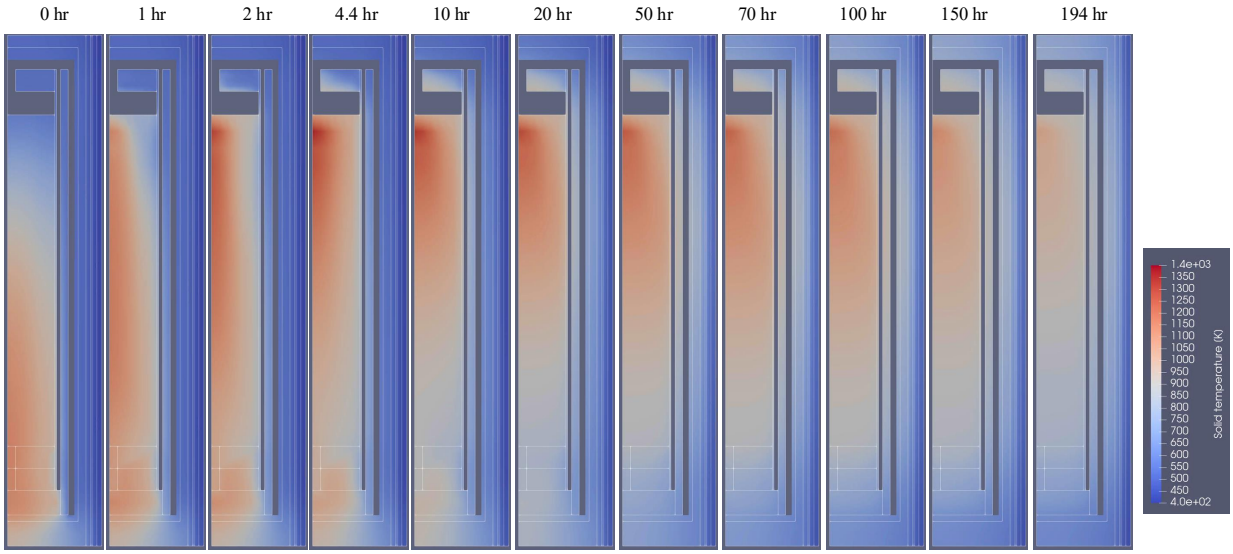

Figure 54. Distributions of solid temperature predicted by the SAM/SAM model during the PLOFC.

to the shape of the power density distribution, while the smaller peak is likely due to convective heat transfer from the hot helium to the colder region below the pebble bed. On the other hand, the radial temperature profiles show a steeper and more linear drop across the pebble bed compared to the parabolic profiles of the DLOFC shown in Figure 35, highlighting the improved heat transfer within the pebble bed caused by in-core natural circulation. Outside the pebble bed, the temperatures of the reflectors, core barrel, and RPV are relatively uniform due to slow radial heat transfer from the pebble bed to the external structures.

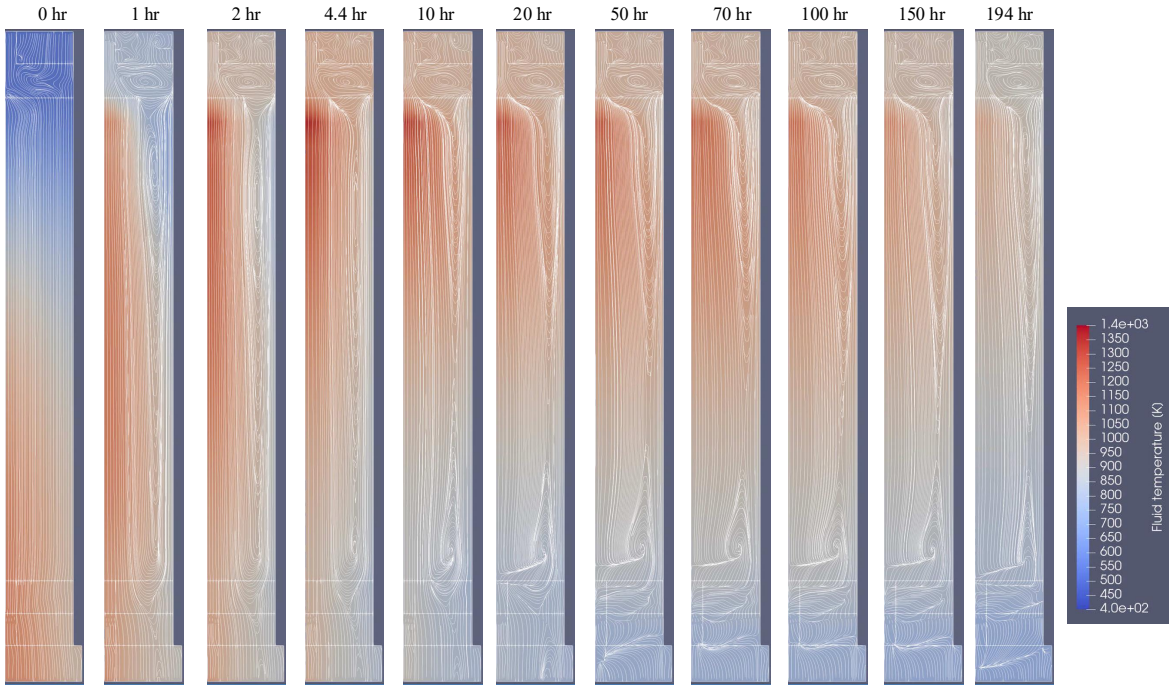

Figure 55. Streamline and fluid temperature predicted by the SAM/SAM model during the PLOFC.

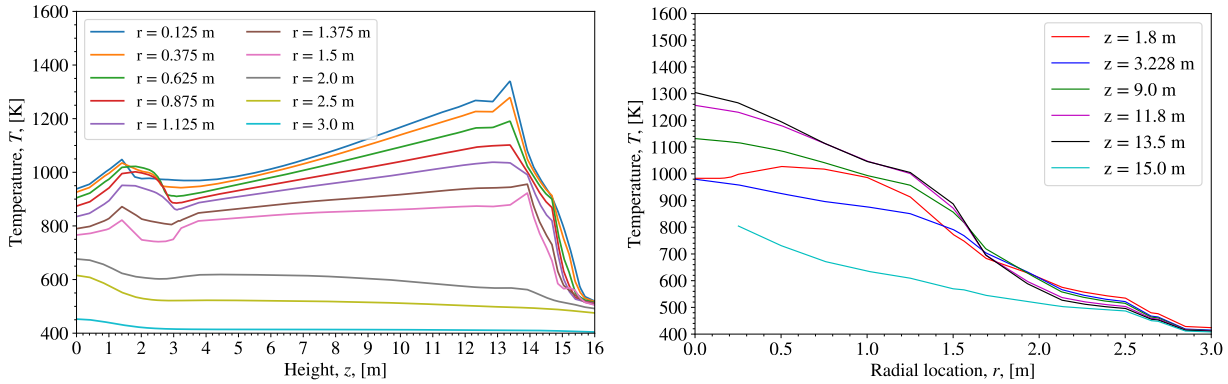

(a) Axial

(b) Radial

Figure 56. Axial and radial solid temperature profiles predicted by the SAM/SAM model during the PLOFC during peak pebble temperature at t = 4.4 hours.

3.3.2. 2D Pronghorn/Griffin Results

This section presents the protected PLOFC accident scenario simulated by the Pronghorn/Griffin coupled code system. The initial model developed to simulate the PLOFC is presented in Reference [35]. In this scenario, it is assumed that the forced circulation coast-down occurs due to failure of the helium blower, station blackout, or loss of power supply. As a protected transient, it is assumed that the reactor protection system inserts the control rods and closes the flap valves immediately after triggering the change in coolant mass flow rate, and the pressure control system maintains the reactor at an operating pressure condition of 7.0 MPa. Also, the top and bottom of the carbon bricks are assumed to be thermally insulated to prevent RPV damage due to elevated temperatures. The natural circulation of the pressurized coolant has a significant impact on the temperature redistribution during the PLOFC transient; it lowers the maximum temperature and achieves a more uniform distribution compared to that of the DLOFC transient, and it expedites the heat dissipation toward the outer regions of the core. The main objective of simulating the PLOFC is to examine whether the maximum pebble surface temperature exceeds the safety limits and whether the reactor can remove heat from the fuel efficiently.

The PLOFC transient simulation was initiated by reducing the mass flow rate of the coolant linearly from its nominal (96.0 kg/s) operational value to zero over 13 seconds, while maintaining the system pressure at 7.0 MPa. Therefore, after the initiation of the accident, the control rods were fully inserted (SCRAM) to shut down the reactor after the coolant mass flow rate coast-down. Beyond that, there were no changes to the system's main parameters, and the simulation was performed for 200 hours. The sequence of events for the protected PLOFC transient is listed in Table 27.

Table 27. Sequence of events for the protected PLOFC simulated by Pronghorn/Griffin.

Time (s)	Event
< 0	Equilibrium steady state completed.
0–13	Mass flow rate reduced linearly to 0 kg/s while system pressure is maintained at 7.0 MPa.
13	Mass flow rate ramp completed and control rods SCRAM initiated.
13–16	Control rods fully inserted and power level determined by decay heat until end of transient.
720,000	Transient simulation end time.

Initially, the equilibrium core steady-state solution was established with the Pronghorn/Griffin coupled code system. During the transient simulation, the time-dependent reactor power was determined from the decay heat curve after reactor shutdown, which was taken from Reference [45], and it was used to scale the power density distribution of the steady-state solution. The decay heat is the main driving heat source during the transient as the prompt power goes to zero after control rod insertion.

Figure 57 shows the average and maximum pebble surface temperatures during the PLOFC transient. The average and maximum pebble surface temperatures start increasing and attain their first peak at approximately 5 hours, with values of 976 K and 1322 K, respectively. Then the pebble surface temperature starts decreasing as the natural circulation of the helium transfers the heat toward the upper regions of the reflector. At approximately 25 hours of the transient, the pebble surface temperature starts increasing again until it reaches its second peak at roughly 61 hours, with average and maximum pebble surface temperatures of 1008 K and 1303 K, respectively. This is mainly caused by energy redistribution due to natural convection. Beyond that point, the pebble surface temperature starts decreasing as the heat dissipates radially through the reflector region toward the RPV.

Figures 58, 59, and 60 show the maximum and average temperatures of the reflector, core barrel, and

RPV, respectively. As the generated heat moves mainly in a radial direction, each region attains its peak relatively soon after the region prior to it. The maximum and average temperature peaks of each region are provided in Table 28. Generally, the three regions behave similarly, except for the maximum reflector temperature. Initially it drops and then starts increasing at approximately 1.5 hours, showing an evolution similar to that of the pebble surface temperature, which has an early peak followed by a second peak.

Table 28. Peak temperature of various reactor regions during the PLOFC simulated with Pronghorn/Griffin. Note that the average temperatures of each region are the averaged temperatures at the time when each region reaches its peak temperature.

Region	Peak No.	Time to Peak (hr)	Avg. Temperature (K)	Max. Temperature (K)
Pebble surface	1	5.1	976.4	1322.4
	2	60.9	1007.9	1303.3
Reflector	1	6.3	689.8	1235.2
	2	67.4	823.6	1255.9
Core barrel	1	76.3	642.3	757.7
RPV	1	80.0	535.1	621.1

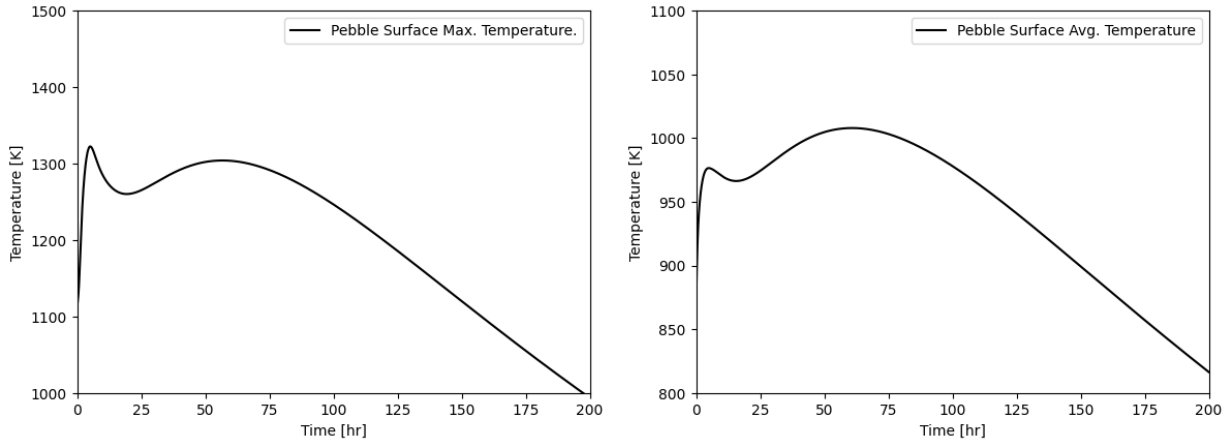

(a) Maximum (b) Average

Figure 57. Maximum and average pebble surface temperatures during the PLOFC obtained by the Pronghorn/Griffin model.

The reactor power evolution and the heat removed by the RCCS during the PLOFC transient are shown in Figure 61. Initially, 0.25 MW is removed by the RCCS at the steady-state rate, and the removal rate increases as the transient progresses, exceeding the reactor power generated from decay heat (about 0.96 MW) after 68 hours and peaking at 0.98 MW after 82 hours of the transient. Beyond that, the amount of heat removed by the RCCS starts decreasing monotonically.

Figure 62 shows the solid and fluid temperature distributions with streamlines during the PLOFC transient. It illustrates how, after the transient is initiated, the peak temperature location shifts to the upper regions of the pebble bed and the upper reflector as heat moves in a radial direction. The maximum temperature location switches from the core's bottom to its top region under the cavity, where core power density peaks in that

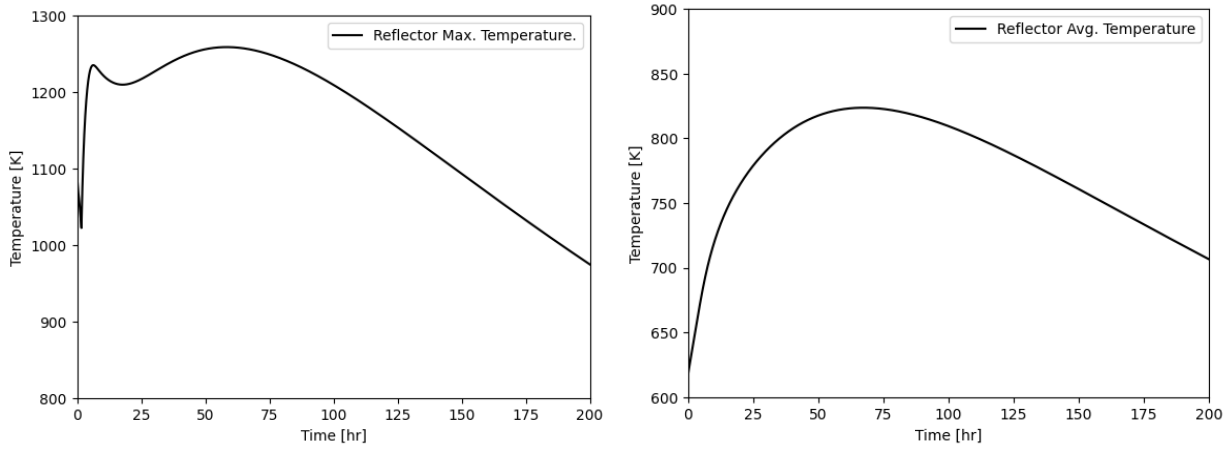

(a) Maximum (b) Average

Figure 58. Maximum and average reflector temperatures during the PLOFC obtained by the Pronghorn/Griffin model.

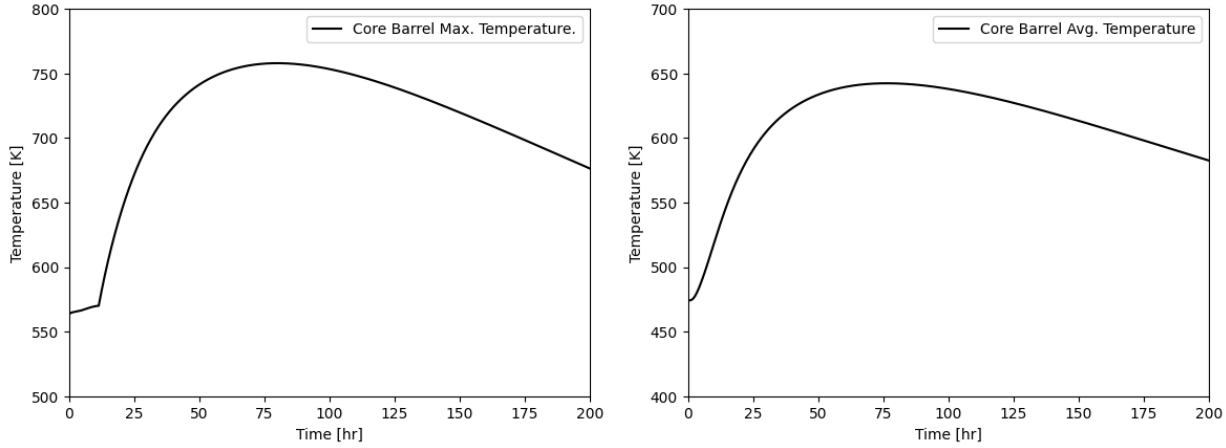

(a) Maximum (b) Average

Figure 59. Maximum and average core barrel temperatures during the PLOFC obtained by the Pronghorn/Griffin model.

region. Additionally, the temperature peaks in the upper reflector region as the heat dissipates axially due to natural convection and the circulation of the helium in the cavity.

Compared to the DLOFC transient, the PLOFC solid temperature peaks at a much lower value and has a more uniform temperature distribution in the upper core later in the transient as heat dissipates radially toward the RPV region. The axial and radial solid temperature profiles at 5.1 hours, when the pebble temperature peaks, are shown in Figure 63. The temperature peaks at 1322 K at position 13.0 m and toward the center of the core, and there is significant variation in the radial direction toward the outer core regions. The discontinuities in the solid temperature profile observed in Figure 63 occur at the cavity above the pebble-bed region.

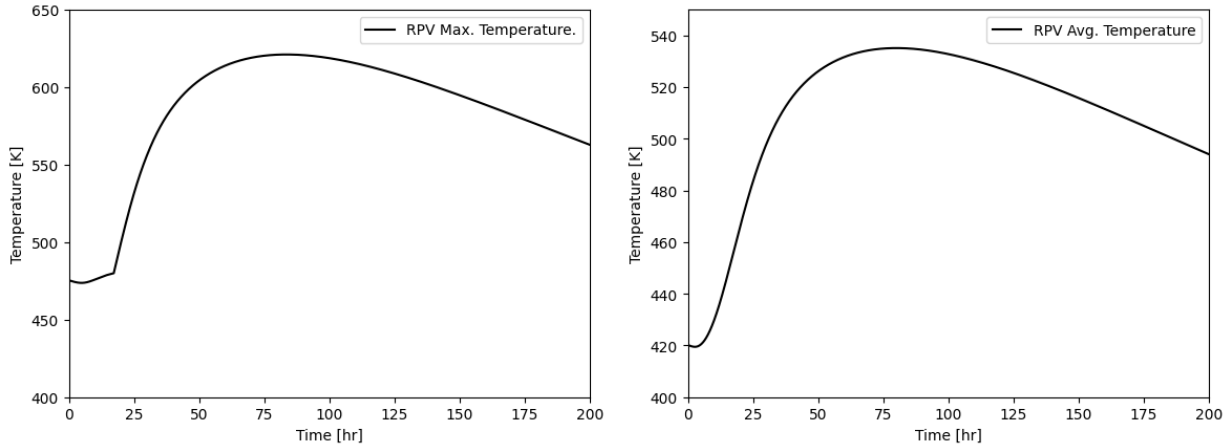

(a) Maximum (b) Average

Figure 60. Maximum and average RPV temperatures during the PLOFC obtained by the Pronghorn/Griffin model.

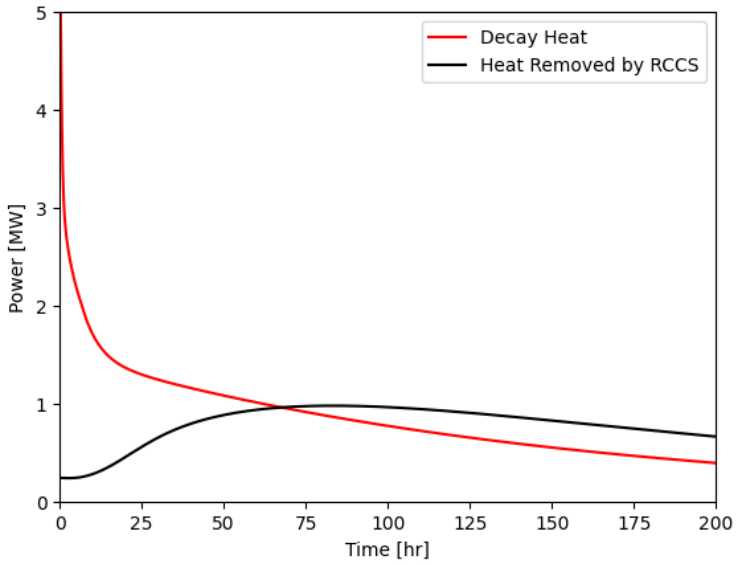

Figure 61. Decay heat and heat removed by the RCCS during the PLOFC obtained by the Pronghorn/Griffin model.

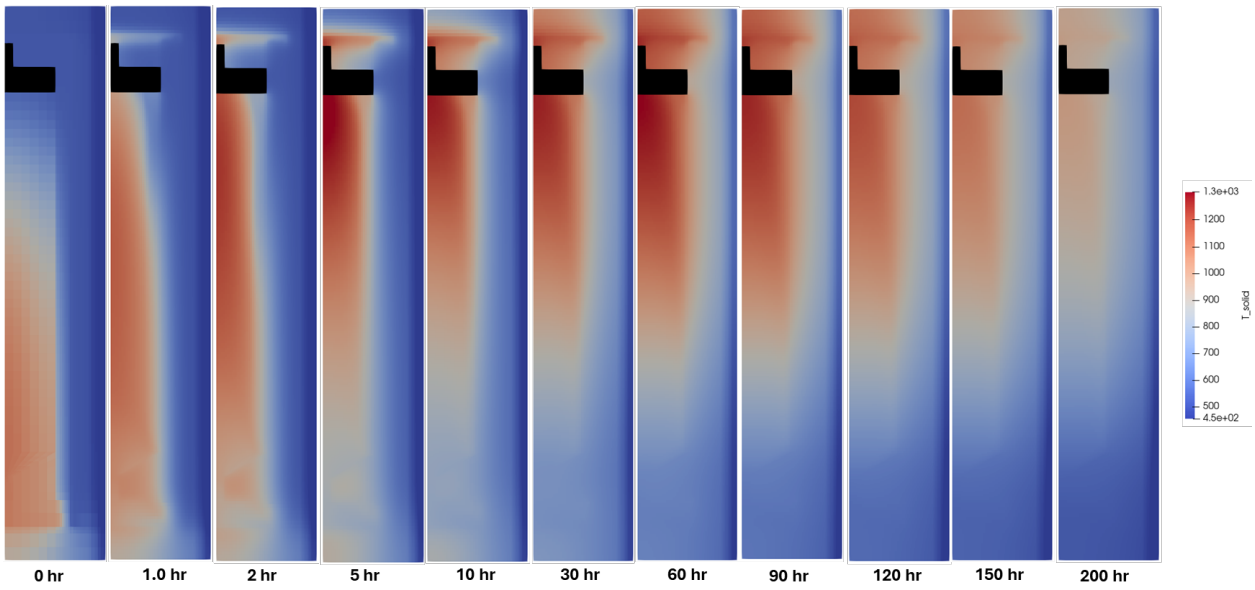

(a) Solid

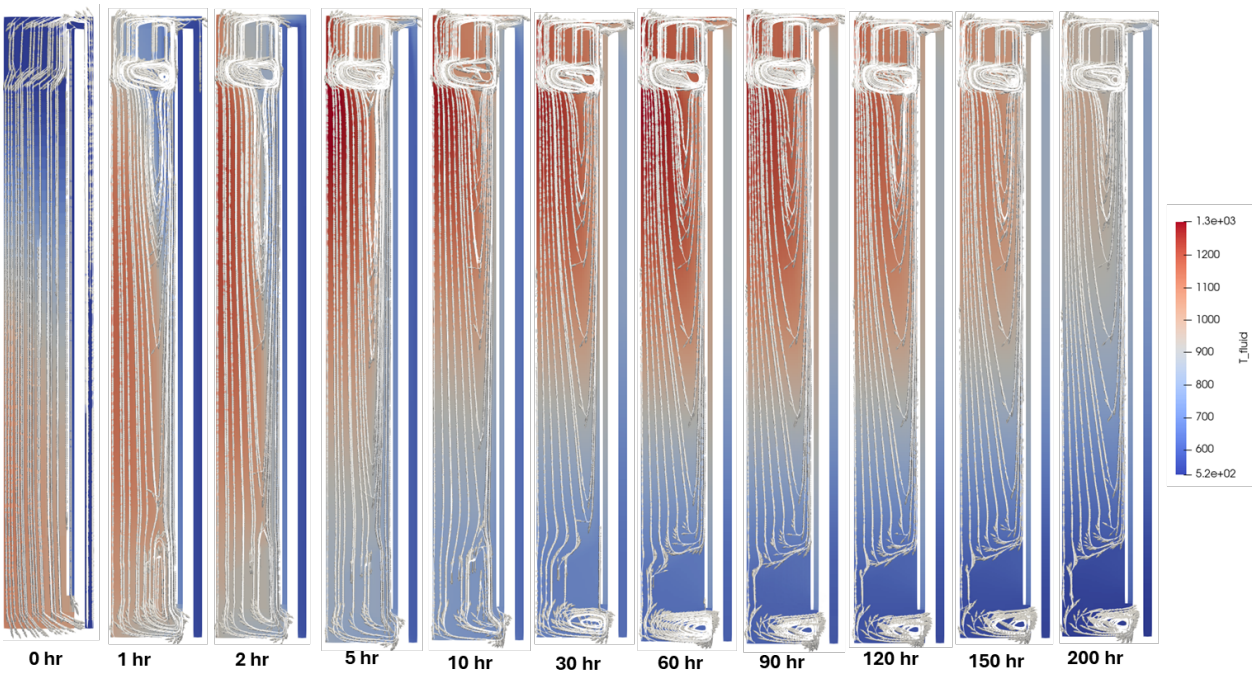

(b) Fluid

Figure 62. Solid and fluid temperature distributions during the PLOFC obtained by the Pronghorn/Griffin model.

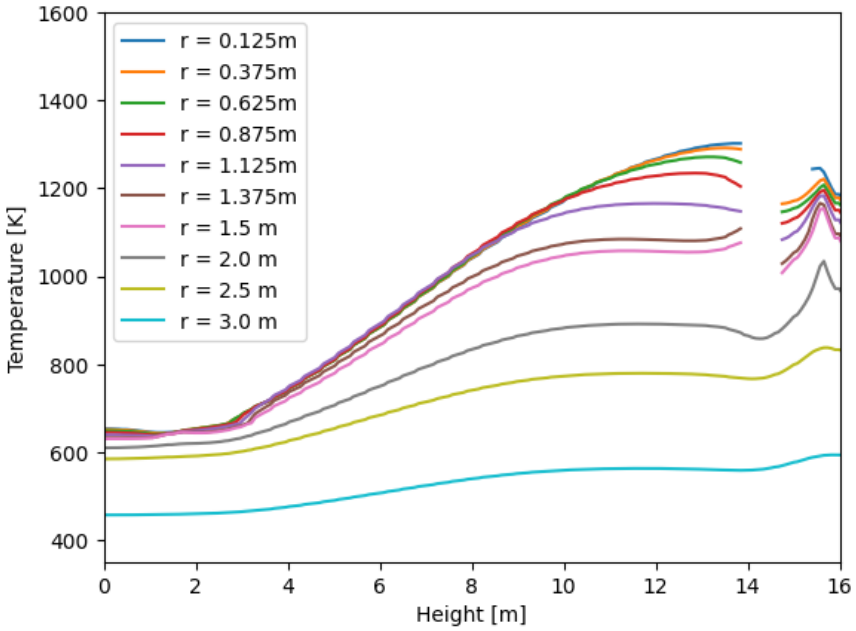

(a) Axial

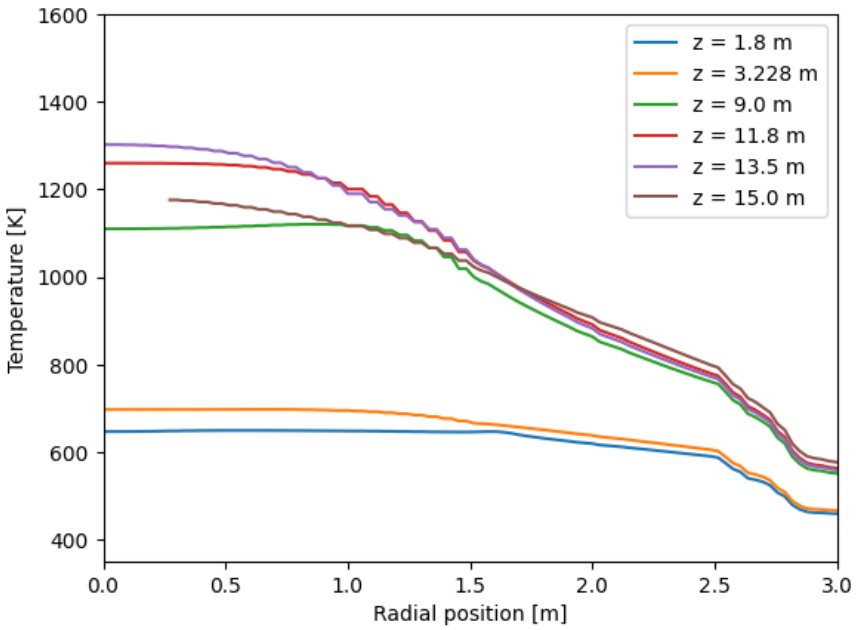

(b) Radial

Figure 63. Axial and radial solid temperature profiles during the PLOFC obtained by the Pronghorn/Griffin model during peak temperature of the pebble surface at 5.1 hours of the transient.

3.3.3. Comparison

The PLOFC predictions from the SAM/SAM and Pronghorn/Griffin models are compared in this section. Both models demonstrate in-core natural circulation, as shown by the streamlines in Figures 55 and 62. In both models, helium flows upward in the inner core and downward in the outer core due to buoyancy effects caused by temperature differences. However, some differences are observed between the solid temperature distributions, particularly at the upper part of the reactor around the top (cold) plenum. The Pronghorn/Griffin model shows that the top cavity gets increasingly hotter as the transient progresses, almost reaching the same temperature as the pebble bed. Conversely, in the SAM/SAM model the same region remains at a much lower temperature throughout the transient. The difference is due to how the top plenum is modeled. In SAM/SAM, fluid flow in the top plenum is not modeled by the 2D model and is instead modeled with a 0D volume branch as part of the primary loop. This means that convective heat transfer between the fluid and solid in that top plenum is not captured. Although conduction in the top plenum is included in the 2D model, due to the dominance of convection during the PLOFC conduction alone is not able to capture the increase in temperature in this region. A different modeling approach capable of capturing the convective heat transfer in the top plenum will be implemented in the 2D SAM model in the future.

Both models show that the maximum and average pebble surface temperatures rise quickly at the beginning of the transient, as seen in Figure 64. The peak maximum temperatures predicted by both models are close, with the SAM/SAM model showing a peak value of 1335 K and the Pronghorn/Griffin model showing a peak value of 1322 K. The peak times are also similar, at 4.4 hours for SAM/SAM and 5.1 hours for Pronghorn/Griffin. Both models show that the maximum temperature starts to decrease shortly after reaching the peak value. However, the SAM/SAM model predicts a continuous decrease of the maximum temperature, whereas the Pronghorn/Griffin model predicts a secondary peak that reaches a temperature of 1303 K at $t = 60$ hours. The difference likely stems from the difference in the modeling approach for the top plenum. Based on the temperature distributions, the Pronghorn/Griffin model predicts more heat retention and a hotter top region than the SAM/SAM model. This then leads to an increase in the maximum pebble temperature again after the initial drop. However, much better agreement is obtained for the average pebble surface temperatures, where two peaks of similar values are observed in the results from both the SAM/SAM and Pronghorn/Griffin models. Similar to the observation from the DLOFC transient, the Pronghorn/Griffin model predicts a steeper drop in pebble temperature, likely due to the difference in the heat removal rate at the RPV surface. In the SAM/SAM model, the RPV surface is coupled to the RCCS model, whereas in the Pronghorn/Griffin model heat removal at the RPV surface is achieved through convective and radiative boundary conditions. The difference in the heat removal rates at the RPV surface is evident in Figure 65, where the Pronghorn/Griffin model predicts a higher value and an earlier crossover point than the SAM/SAM model. Furthermore, the decay heat of the Pronghorn/Griffin model is slightly higher than that of the SAM/SAM model after $t = 100$ hours, which leads to further differences in the pebble temperatures.

Outside the pebble bed, the maximum reflector temperatures predicted by both models are also slightly different, as shown in Figure 66. The SAM/SAM model shows a drop in the maximum reflector temperature in the first stage of the transient, followed by an increase as heat gradually flows into the reflectors. On the other hand, the maximum reflector temperature predicted by the Pronghorn/Griffin model has a trend similar to that of the maximum pebble surface temperature, in which two distinct peaks are observed. Moreover, the Pronghorn/Griffin model also predicts a higher maximum reflector temperature of more than 1200 K, while the maximum reflector temperature predicted by the SAM/SAM model does not exceed 1100 K. However, better agreement is observed for the overall trend of the average reflector temperature. Nonetheless, the Pronghorn/Griffin model predicts a higher peak average reflector temperature of 823 K compared to the 783 K predicted by the SAM/SAM model. The difference in the reflector temperatures is likely caused by the SAM/SAM model underpredicting the temperature in the top region of the core due to the different modeling approaches the models use for the top plenum.

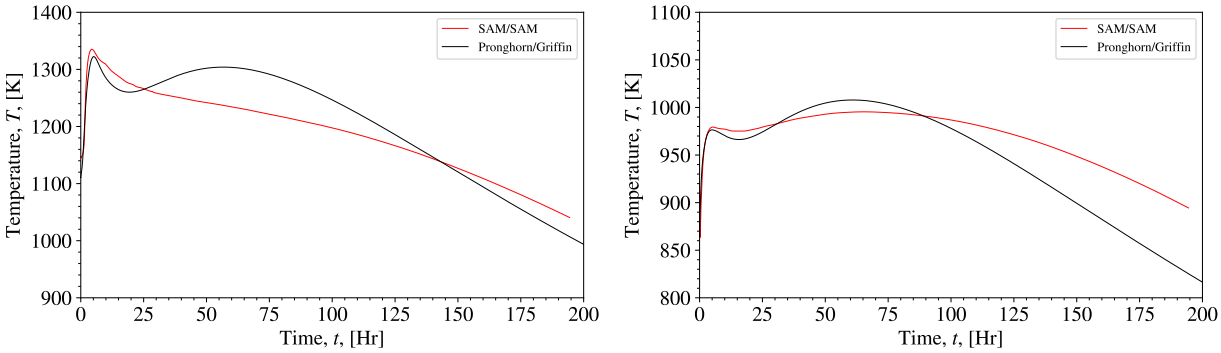

(a) Maximum (b) Volume Averaged

Figure 64. Comparison of the maximum and volume-averaged pebble surface temperatures during the PLOFC predicted by the SAM/SAM and Pronghorn/Griffin models.

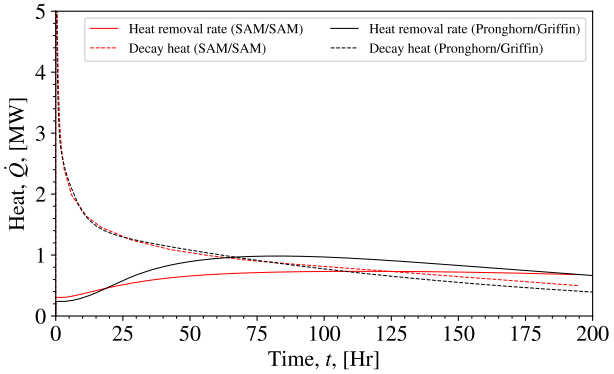

Figure 65. Comparison of the RCCS heat removal rate during the PLOFC predicted by the SAM/SAM and Pronghorn/Griffin models.

For the core barrel and RPV, as shown in Figures 67 and 68, both models predict similar overall trends for maximum and average temperatures, but the Pronghorn/Griffin model consistently predicts higher temperatures than the SAM/SAM model for the same reason mentioned above. Due to the higher heat removal rate on the RPV surface, the Pronghorn/Griffin model consistently predicts a faster drop in temperatures in the reflector, core barrel, and RPV than does the SAM/SAM model.

Overall, the SAM/SAM and Pronghorn/Griffin models predict largely comparable reactor behavior during the PLOFC transient. In-core natural circulation, which plays an important role in the redistribution and removal of decay heat, is predicted by both models. Despite some differences in the trend of the maximum pebble temperatures, the peak values predicted by both models are close. The SAM/SAM model does not predict a secondary peak in the maximum pebble surface temperature due to the use of a 0D component to model the top plenum. On the other hand, both models predict similar average pebble temperatures in terms of the overall trend and the peak values. Outside the core, the trends of the reflector, core barrel, and RPV temperatures from both models are similar. However, due to differences in the modeling of the heat removal at the RPV surface and in the decay heat levels, the Pronghorn/Griffin model consistently predicts higher temperatures in these regions than the SAM/SAM model. All in all, both the SAM/SAM and Pronghorn/Griffin models demonstrate that they can model the PLOFC transient in a way that key features and behaviors of the core behave as expected.

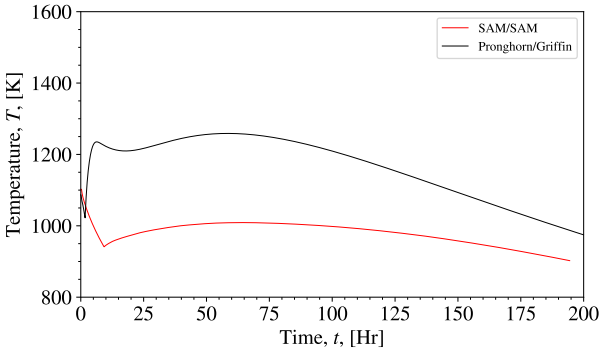

(a) Maximum

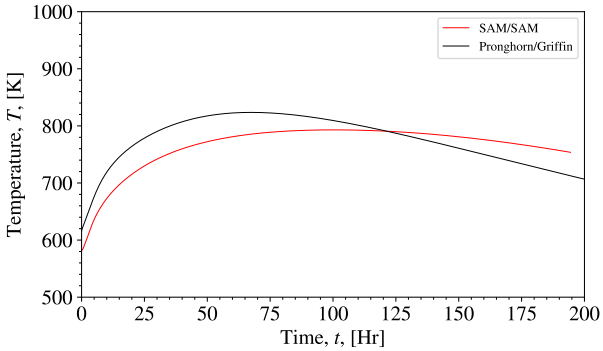

(b) Volume Averaged

Figure 66. Comparison of the maximum and volume-averaged reflector temperatures during the PLOFC predicted by the SAM/SAM and Pronghorn/Griffin models.

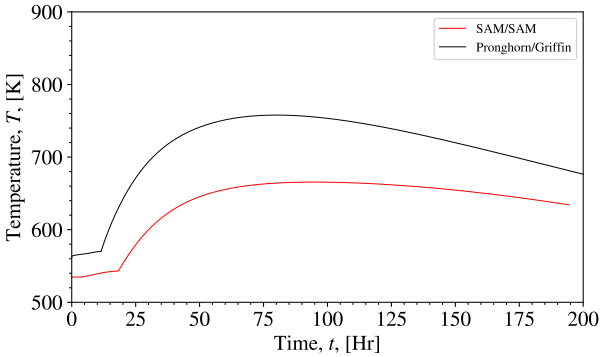

(a) Maximum

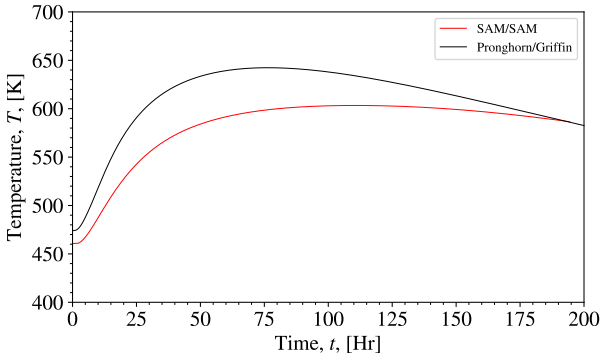

(b) Volume Averaged

Figure 67. Comparison of the maximum and volume-averaged core barrel temperatures during the PLOFC predicted by the SAM/SAM and Pronghorn/Griffin models.

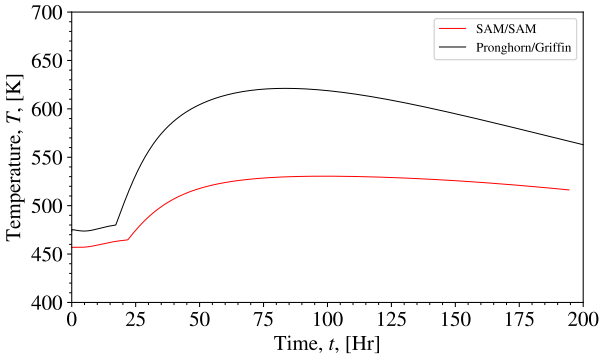

(a) Maximum

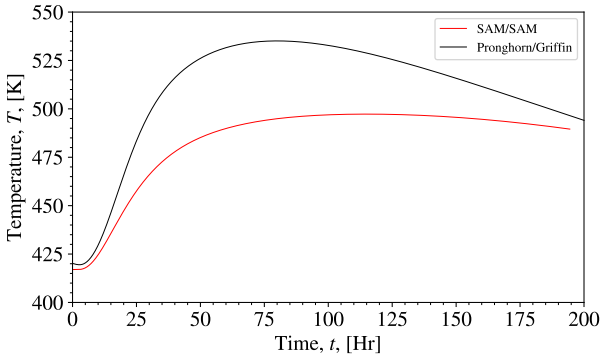

(b) Volume Averaged

Figure 68. Comparison of the maximum and volume-averaged RPV temperatures during the PLOFC predicted by the SAM/SAM and Pronghorn/Griffin models.

3.4. Unprotected Over-Cooling Scenario

3.4.1. 2D SAM/Griffin/SAM Results

The UOC transient simulated with the SAM/Griffin/SAM coupled model is discussed in this section. The transient is one of the exercises recommended by the OECD-NEA PBMR-400 benchmark report [9]. It is intended to simulate the injection of cold helium into the core due to the opening of a bypass valve. In this model, the temperature of the secondary side of the heat exchanger is lowered to achieve the decrease of core inlet temperature. This transient is suitable for testing the reactivity feedback as well as the thermal fluids response of the reactor. The correlations used in the 2D SAM model are summarized in Table 9.

The sequence of events of the UOC transient is shown in Table 29. Prior to the transient, a steady-state equilibrium condition is first achieved with the coupled model. At t = 1,000 seconds, the transient is initiated by lowering the inlet temperature on the secondary side of the heat exchanger by 50 K, from 523.15 K to 473.15 K over a span of 10 seconds, which causes the inlet temperature of the core to drop by the same amount. From t = 1,010 to 1,310 seconds, the input parameters are held constant. Then, from t = 1,310 to 1,320 seconds, the secondary side heat exchanger temperature is raised linearly back to the steady-state value of 523.15 K over 10 seconds, after which the transient is simulated until t = 2,000 seconds, at which point it is terminated.

Table 29. Sequence of events for UOC transient simulated by the SAM model.

Time (s)	Events
$<$ 1,000	Steady-state equilibrium is achieved.
1,000–1,010	Secondary side heat exchanger temperature is lowered linearly by 50 K from 523.15 K to 473.15 K.
1,010–1,310	No change in operating condition.
1,310–1,320	Secondary side heat exchanger temperature is raised linearly by 50 K from 473.15 K to 523.15 K.
1,320–2,000	Simulate runs until end of transient.

Figure 69 shows the coolant temperature at the riser inlet and the cold plenum. For the first 1,000 seconds in which the system is in a steady-state equilibrium condition, the cold plenum temperature is slightly higher than the riser inlet temperature. This happens because as the coolant travels upward along the riser into the cold plenum, it removes heat from the surrounding reflectors and experiences a small increase in temperature. During the transient, the riser inlet temperature is first reduced by 50 K, then held constant for 300 seconds, and then raised back up by 50 K to its steady-state value of 523.15 K. At the same time, the cold plenum temperature also experiences similar changes. However, due to the large volume of existing helium in the cold plenum, its temperature drops less and more gradually during the transient. Similarly, the cold plenum temperature also takes longer to recover to the steady-state value once the inlet temperature is raised back to 523.15 K. The system mass flow rate is shown in Figure 70. During the transient, the system mass flow rate increases from 96 kg/s to around 98.2 kg/s. This happens because the model assumes a constant pump head for the blower throughout the simulation, and the helium density increases due to the temperature drop, which means that more helium is pumped through the system.

Figure 71 shows the total power during the UOC transient. At the beginning of the transient, the total power initially increases sharply and then gradually before reaching a peak value of roughly 290 MW. Once the inlet coolant temperature is brought back to 523.15 K, the total power decreases sharply and stabilizes at roughly 252 MW. Figure 72 compares the maximum and average temperatures of the different components of the reactor. During the transient, the maximum fluid, pebble, fuel, and moderator temperatures follow similar trends in which they experience a large increase due to a power increase. The same is also observed for the

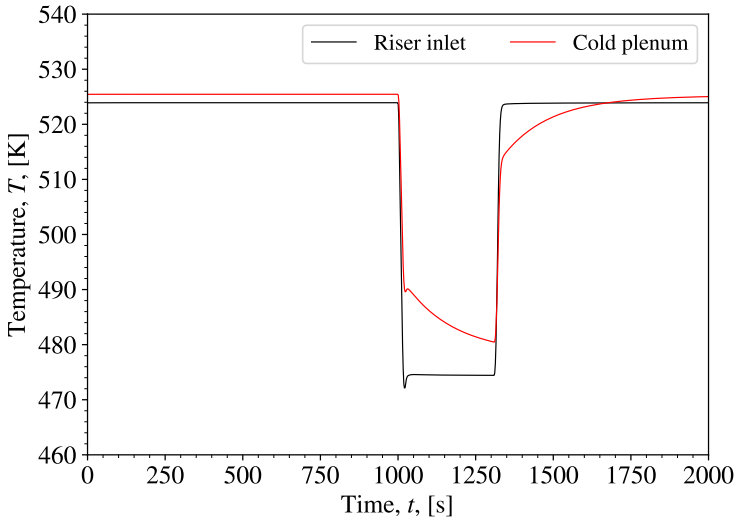

Figure 69. Inlet temperatures predicted by the SAM/Griffin/SAM model during the UOC transient.

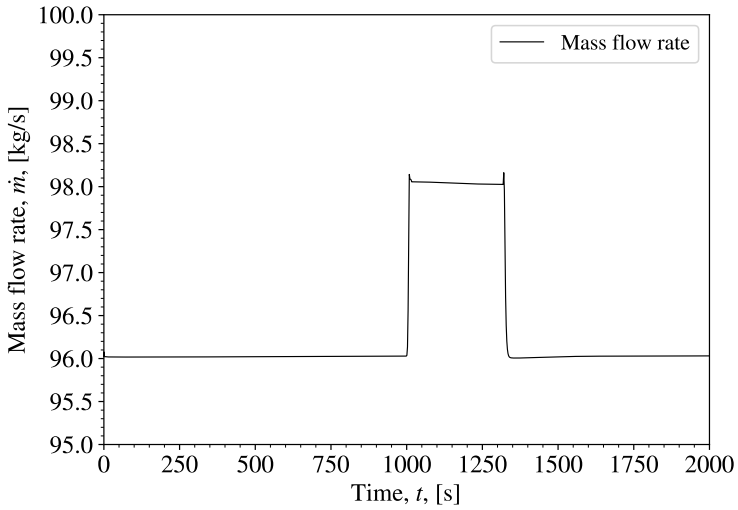

Figure 70. System mass flow rate predicted by the SAM/Griffin/SAM model during the UOC transient.

average pebble, fuel, and moderator temperatures; they experience an overall increase during the transient. Conversely, the average fluid temperature decreases during the same time due to the introduction of cold helium in the core.

To better compare the trends of the total power and average temperatures, normalized values of these parameters are plotted in Figure 73. These parameters are normalized with their respective steady-state values. The solid lines are the normalized temperatures and the dashed pink line represents the normalized power whose y-axis is on the right side of the figure. Note that the plot is cropped to show only the transient portion of the simulation. At the beginning of transient at t = 1,000 seconds, the average fluid temperature decreases sharply due to the introduction of cold helium into the core. This in turn causes the pebble, moderator, and fuel temperatures to drop. At the same time, the decrease in temperature leads to the increase in power due to reactivity feedback as the overall reactivity coefficient of the core is negative. The power increase then causes the fuel, moderator, pebble, and fluid temperatures to increase. A delay is observed between the times

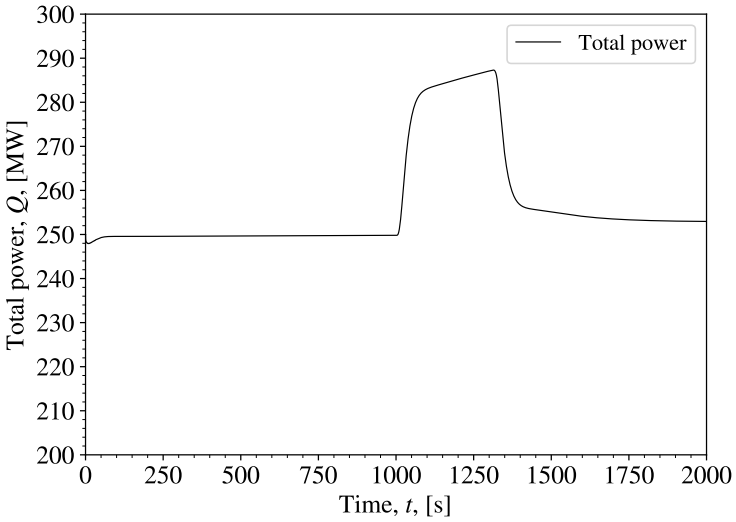

Figure 71. Total power predicted by the SAM/Griffin/SAM model during the UOC transient.

when the fuel, moderator, and pebble temperatures start to increase. This is because heat is generated in the fuel particles, which then has to travel through the moderator in the pebble before reaching the pebble surface and the fluid. At about t = 1,025 seconds, the power increase starts to taper off due to negative reactivity coefficients. At the same time, the fuel, moderator, pebble, and fluid continue to experience a temperature increase. At t = 1,310 seconds, when the helium temperature is raised back to the steady-state value of 523.15 K, the fuel, moderator, pebble, and fluid temperatures experience a sudden spike. Once again due to a negative reactivity coefficient, the total power initially decreases sharply followed by a gradual decay. After the initial spike, the decrease in power then causes the fuel, moderator, pebble, and fluid temperatures to decrease. The simulation is terminated at t = 2,000 seconds, when the total power is still approximately 1% higher than the steady-state value. This is also reflected in the fuel, moderator, pebble, and fluid temperatures, which are observed to be roughly 0.5% higher than their respective steady-state values.

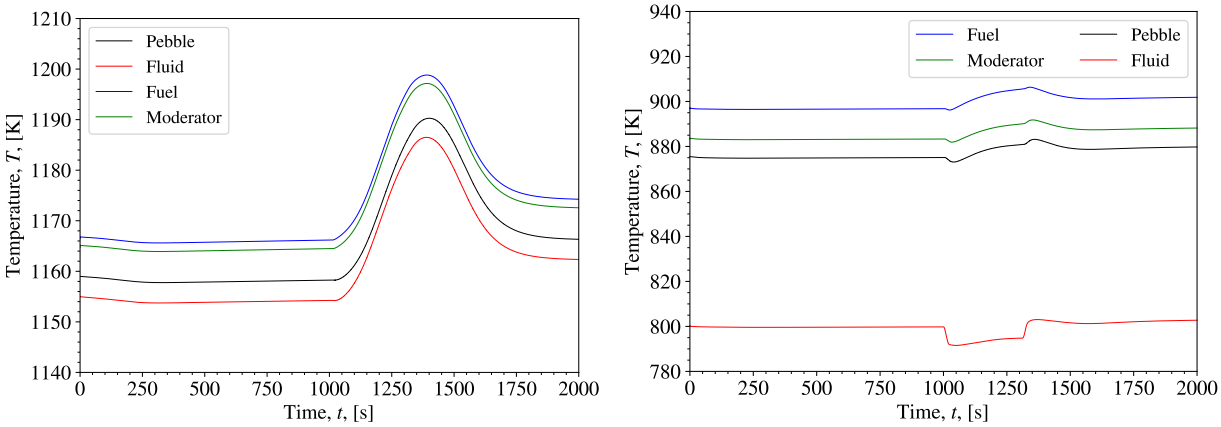

(a) Maximum

(b) Volume Averaged

Figure 72. Maximum and volume-averaged temperatures predicted by the SAM/Griffin/SAM model during the UOC transient.

Figure 74 shows the solid temperature axial and radial profiles during the peak fuel temperature at t

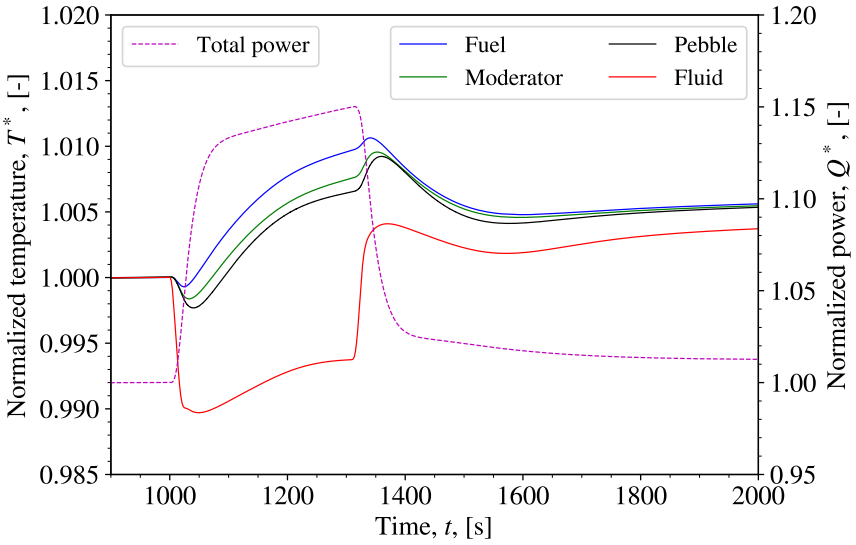

Figure 73. Comparison of the normalized temperatures and power level predicted by the SAM/Griffin/SAM model during the UOC transient. Note the secondary y-axis on the right for normalized power.

= 1,391 seconds. The transient temperature profiles (solid lines) are compared to the steady-state profiles (dashed lines). During the steady-state and peak fuel temperatures, the axial and radial profiles share the same trend at all locations. However, due to the higher total power, the peak fuel temperatures are higher at all axial and radial locations in the pebble-bed region by approximately 10–20 K. Outside the pebble bed, no significant differences are observed, indicating that the additional heat generated by the power increase is removed almost entirely by the helium through forced convection.

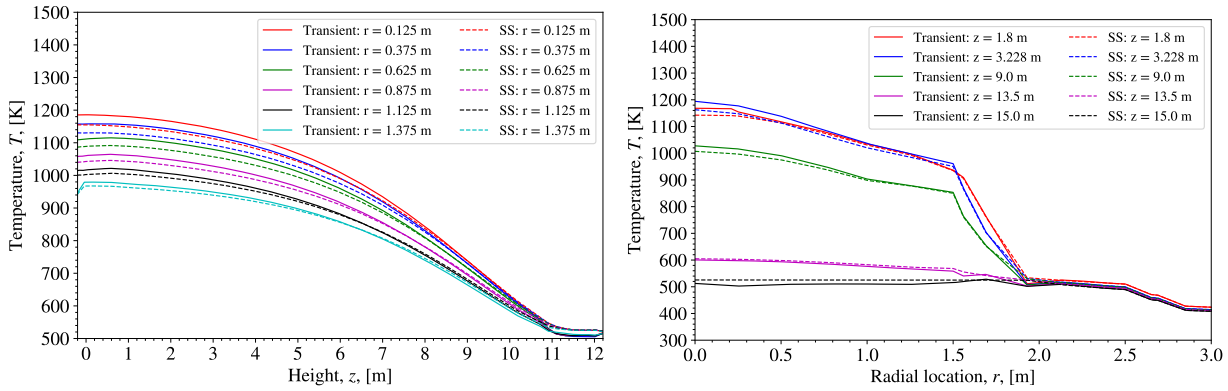

(a) Axial (b) Radial

Figure 74. Axial and radial temperatures predicted by the SAM/Griffin/SAM model during the UOC transient during the peak fuel temperature at t = 1,391 seconds.

3.4.2. 2D SAM/PKE/SAM Results

In this section, the UOC transient simulated with the 2D SAM/PKE/SAM model is discussed. The sequence of events is the same as that summarized in Table 29. In this model, SAM's internal PKE capability is used for neutronics and feedback calculations instead of the Griffin model. It should be noted that the

model was simplified so that it only considers prompt fission power and ignores decay power. This means that during the transient the core power is scaled with respect to the steady-state equilibrium power based on reactivity changes. However, it should be pointed out that the SAM PKE model is capable of including decay heat through its internal model or a user-provided decay heat curve.

Figure 75 compares the total power predictions of the SAM/PKE model and the SAM/Griffin/SAM model. Their general trends are similar in that the power increases suddenly at the beginning of the transient, followed by a gradual increase, before it decreases again as the helium temperature is increased back to 523.15 K. However, the increase in total power predicted by the SAM/PKE model is lower than that of the SAM/Griffin/SAM model, with the former reaching a peak value of approximately 284 MW and the latter 290 MW. During the final phase of the transient, after the helium temperature has been raised back to 523.15 K, the SAM/PKE model predicts a slower decrease in power after the initial sharp drop.

Figures 76 and 77 compare the maximum and volume-averaged temperatures of the fuel, moderator, pebble, and fluid of the two models. Overall, the maximum temperatures have similar trends, with the SAM/Griffin/SAM model predicting higher maximum values due to higher power. However, the models predict opposite trends for the average temperatures. Despite the power increase, the SAM/PKE model shows that the average fuel, moderator, pebble, and fluid temperatures decrease over the same period of time. Figure 78 compares the maximum and average reflector temperatures of the two models. The results are generally agreeable, with the SAM/Griffin/SAM model showing a slightly higher maximum temperature. This is because almost all the heat is removed from the core by helium during this transient, which means the temperature trends of the pebble bed may not be reflected by the trend of the surrounding reflectors.

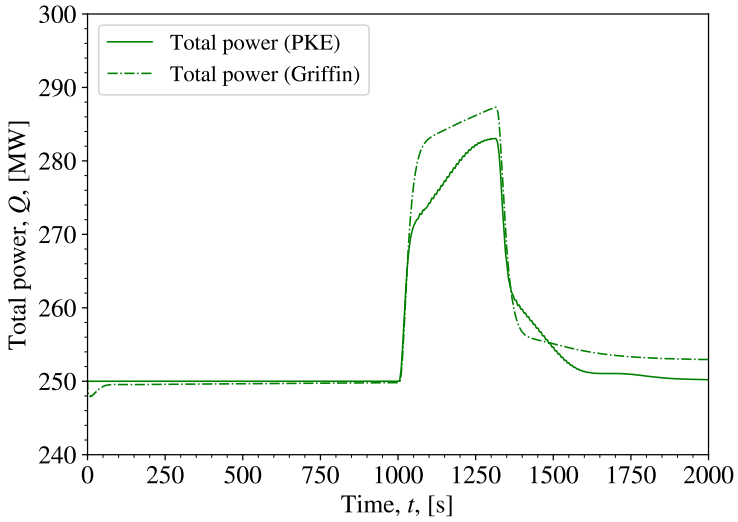

Figure 75. Comparison of the total power level predicted by the SAM/Griffin/SAM model and the SAM-standalone PKE model during the UOC transient.

The opposite trends of the average temperatures predicted by the two models, shown in Figures 76 and 77, can be explained with the following analysis. Figures 79 and 80 show the local temperature increase experienced by the pebble bed during the transient predicted by the SAM/PKE and SAM/Griffin/SAM models, respectively. The temperature increase is calculated with respect to the steady-state temperature. For visualization purposes, the temperature distributions are filtered to show only a temperature increase. Note that the range of values of each figure's legend is different. At the beginning of the transient at t = 1,000 seconds, both models show a negligible increase. As the transient progresses, due to the introduction of "cold" helium, the top of the pebble bed decreases in temperature while the remainder of the core increases in

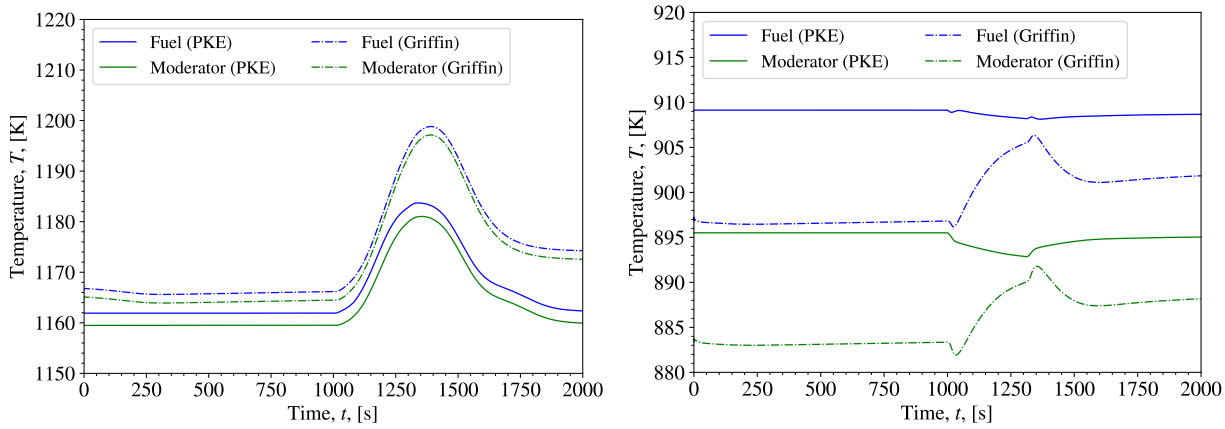

(a) Maximum (b) Volume Averaged

Figure 76. Comparison of the maximum and volume-averaged fuel and moderator temperatures predicted by the SAM/Griffin/SAM model and the SAM-standalone PKE model during the UOC transient.

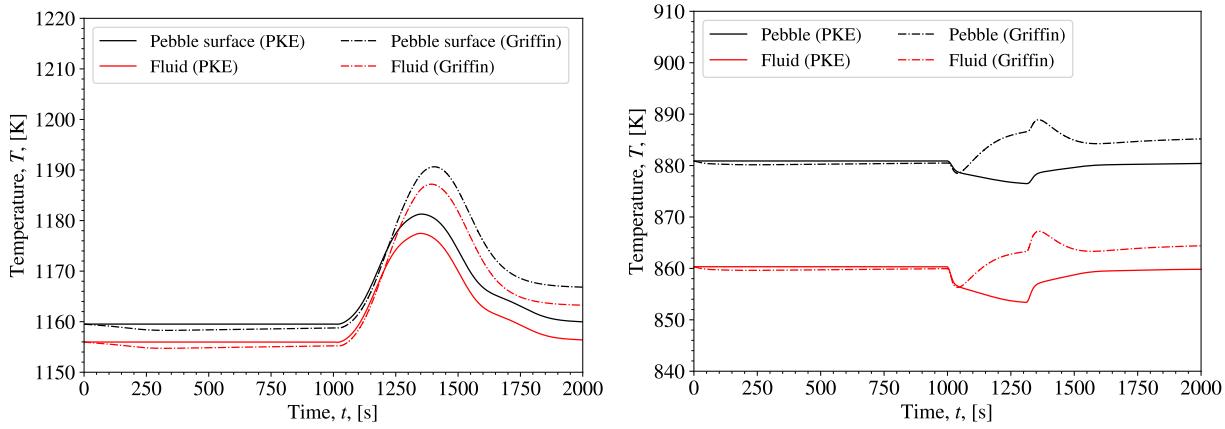

(a) Maximum (b) Volume Averaged

Figure 77. Comparison of the maximum and volume-averaged pebble and fluid temperatures predicted by the SAM/Griffin/SAM model and the SAM-standalone PKE model during the UOC transient.

temperature. The SAM/Griffin/SAM temperature profile shows that the region that decreases in temperature remains largely constant throughout the transient and is confined to roughly the top region of the pebble bed. Conversely, the SAM/PKE model shows that the region that decreases in temperature continues to expand throughout the transient to where it covers almost half of the pebble bed at approximately t = 1,297 seconds. Additionally, comparing the range of values of the legends, it is seen that the SAM/Griffin/SAM model predicts a larger temperature increase, reaching a maximum value of 31 K at t = 1,297 seconds, whereas the SAM/PKE model predicts a maximum temperature increase of only 21 K.

Figures 81 and 82 show the local power increase experienced by the pebble bed during the transient predicted by the SAM/PKE and SAM/Griffin/SAM models, respectively. Similarly, the figures are filtered to show only a power increase. Both models show that the entire pebble bed experiences a power increase during the transient. However, in comparing the range of values of the legends, it is observed that the SAM/Griffin/SAM model predicts a significantly higher power increase than the SAM/PKE model at all time steps. For example, the increase predicted by the SAM/Griffin/SAM model at t = 1,297 seconds has

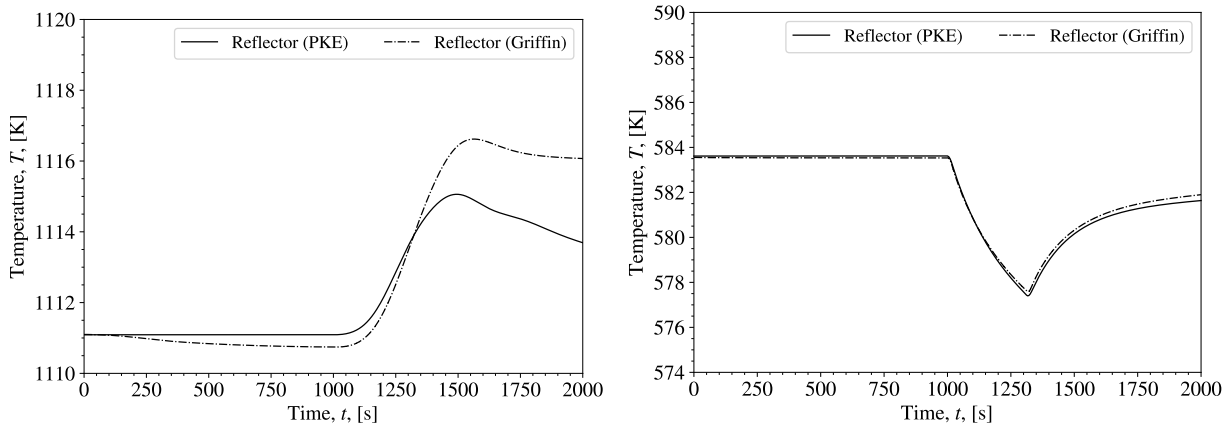

(a) Maximum

(b) Volume Averaged

Figure 78. Comparison of the maximum and volume-averaged reflector temperatures predicted by the SAM/Griffin/SAM model and the SAM-standalone PKE model during the UOC transient.

a maximum value of 1.4×10^6 W/m^3, whereas the SAM/PKE model only shows a maximum increase of 9.5×10^5 W/m^3. The analysis shows that the increase in local power predicted by the SAM/PKE model is unable to overcome the local temperature drop caused by the introduction of "cold" helium into the pebble bed. As a result, the average temperature of the pebble bed (fuel, moderator, pebble surface, and fluid temperatures) decreases despite an increase in reactor power. The analysis highlights a potential inaccuracy that the PKE model may introduce, as the local changes of temperature may not be captured by a core-wide average temperature. Furthermore, spatially dependent reactivity feedback coefficients may also be needed to more accurately capture the effects of feedback mechanisms.

3.4.3. 2D SAM/SAM PKE Sensitivity Demonstration

Dakota [46] is an optimization and uncertainty quantification analysis code developed by Sandia National Laboratories and is of interest to support sensitivity and uncertainty studies. Dakota has the flexibility to support these types of analysis with any desired simulation code via black box interfaces. In this structure, Dakota supplies parameter values (e.g., steps in a parameter study or sets of random samples from input distributions) and then receives response values back for summary and statistical processing with no knowledge of the simulation code or underlying physics. The functions of preprocessing Dakota-supplied parameters for a simulation code, executing the simulation, and post-processing/returning responses to Dakota can be accomplished by analysis driver scripts. An analysis driver script was previously developed to interface Dakota with the SAM code [47] and was modified in this work to demonstrate applying Dakota to support analyses within the BlueCRAB framework. Within this scope, a basic parameter sensitivity study was carried out using the SAM-standalone PKE UOC transient model with a version of SAM built within the BlueCRAB code suite.

Figure 83 shows a portion of the results of a parameter study carried out with BlueCRAB/SAM and Dakota to investigate the sensitivity of the SAM-standalone PKE model's maximum fuel temperature to perturbations in pebble-bed porosities. Figure 84 shows the peak temperature values calculated for the fluid, moderator, and fuel regions at different porosities. Each perturbed version of the model was generated and executed by Dakota in parallel to similar studies of other input parameters.

Figure 85 shows a portion of the results from the parameter study investigating the sensitivity of the SAM-standalone PKE model's maximum fuel temperature to perturbations in the secondary inlet temperature.

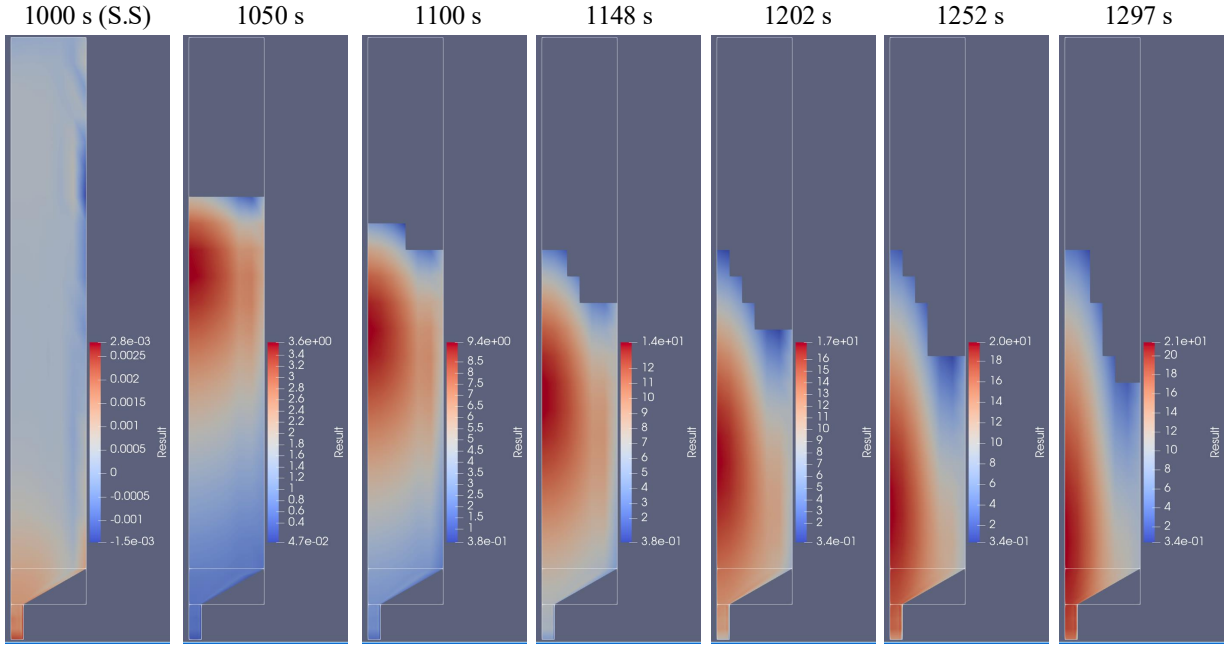

Figure 79. Temperature change in the core predicted by the SAM-standalone PKE model during the UOC transient. Only temperature increase is displayed.

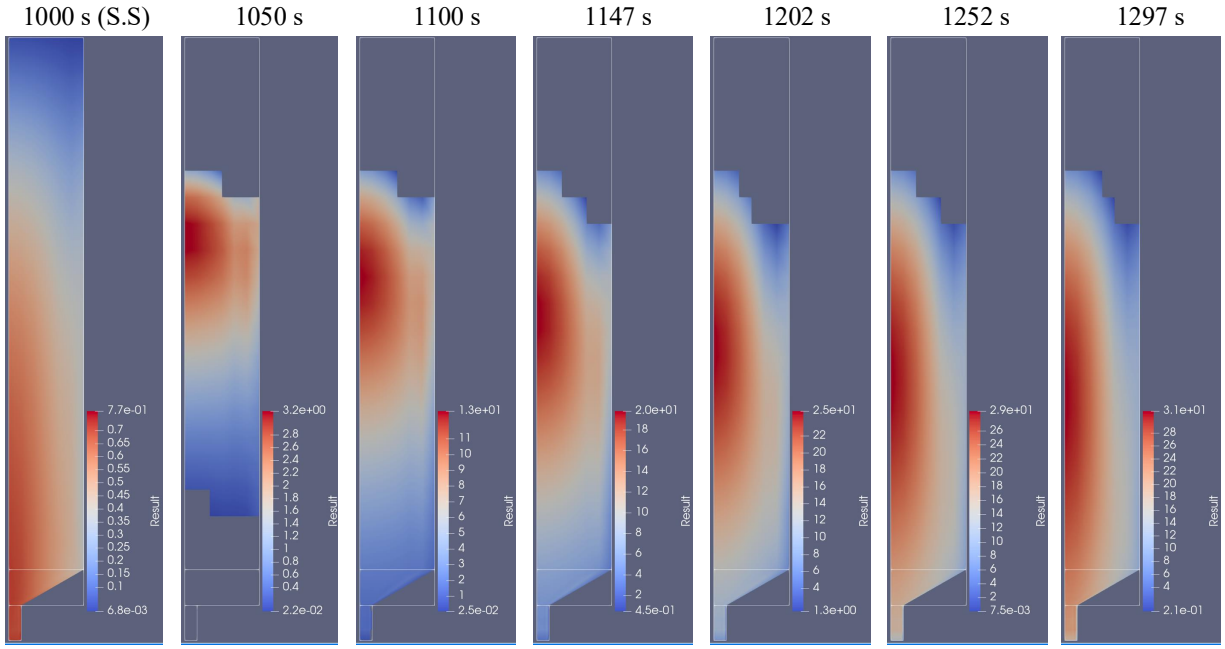

Figure 80. Temperature change in the core predicted by the SAM/Griffin/SAM model during the UOC transient. Only temperature increase is displayed.

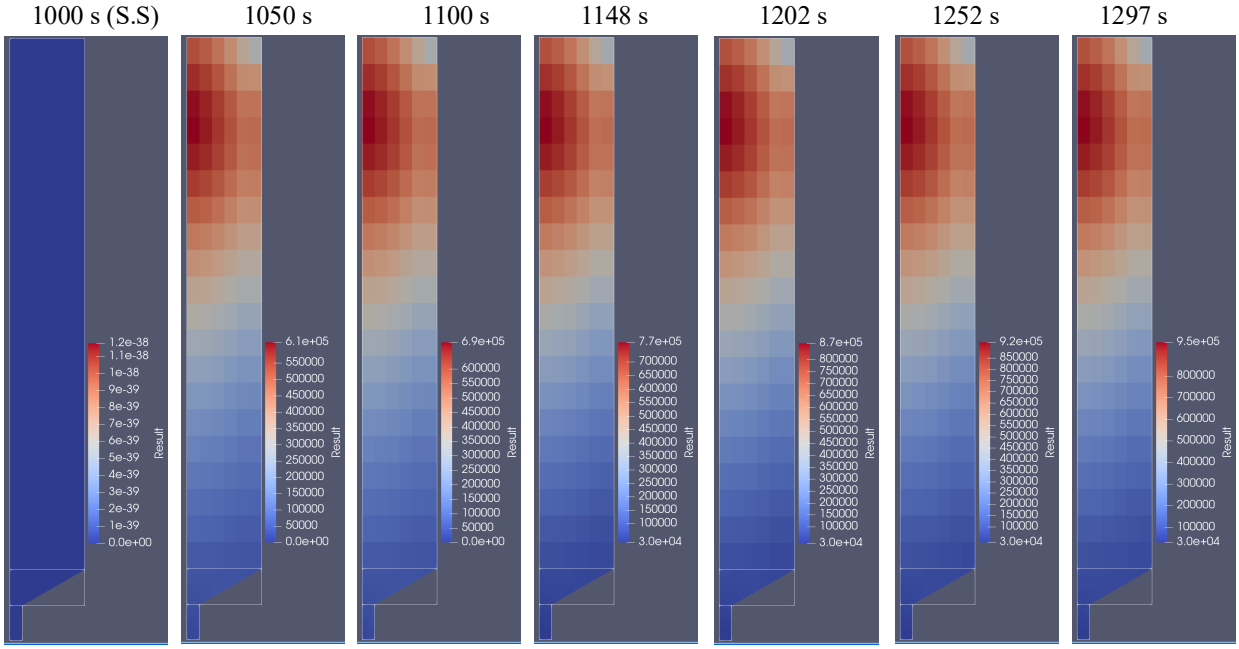

Figure 81. Power density change in the core predicted by the SAM-standalone PKE model during the UOC transient. Only power density increase is displayed.

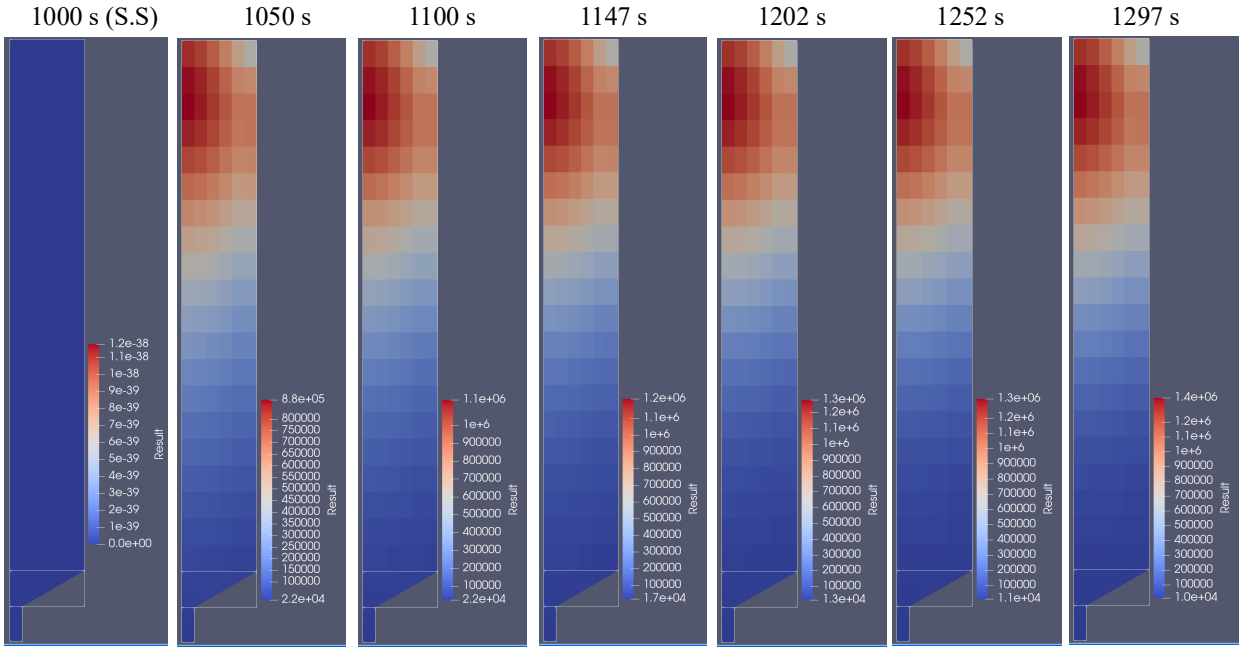

Figure 82. Power density change in the core predicted by the SAM/Griffin/SAM model during the UOC transient. Only power density increase is displayed.

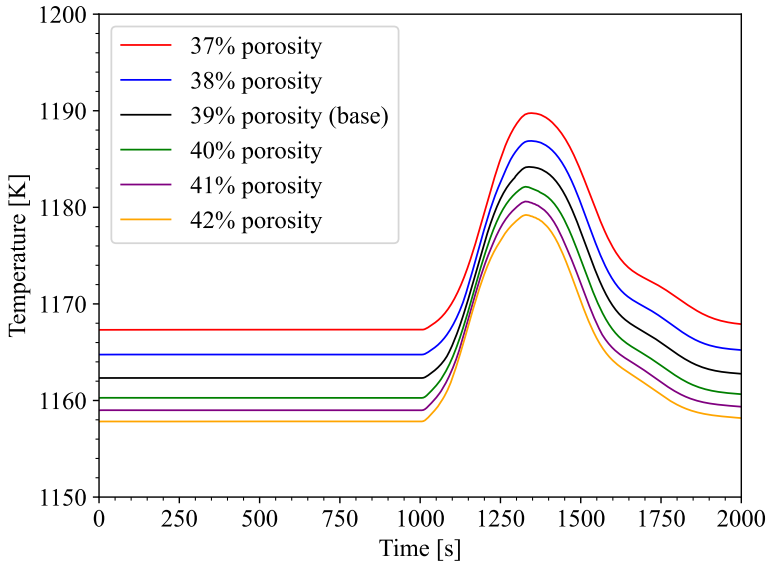

Figure 83. Maximum fuel temperatures for a porosity parameter study using the Dakota/SAM-standalone PKE model during the UOC transient.

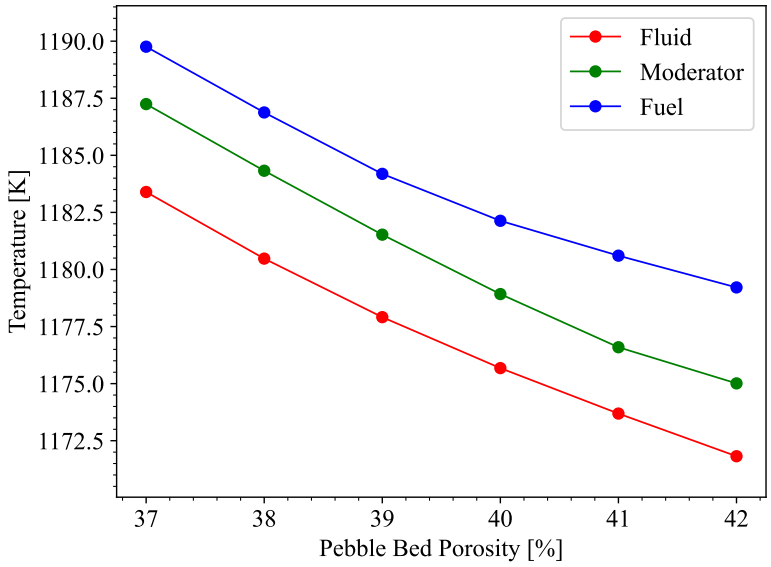

Figure 84. Peak fluid, moderator, and fuel temperature values for a porosity parameter study using the Dakota/SAM-standalone PKE model during the UOC transient.

In this case, the secondary inlet transient temperature was uniformly shifted for the duration of the transient. Figure 86 shows the peak temperature values calculated for the fluid, moderator, and fuel regions at different initial secondary inlet temperatures.

Additional studies can be carried out with any parameter accessible through the model inputs, including, for example, reactivity coefficients, material properties, boundary conditions, and built-in sensitivity coefficients for correlations. Beyond assessing sensitivity to individual parameters, as demonstrated here, Dakota provides

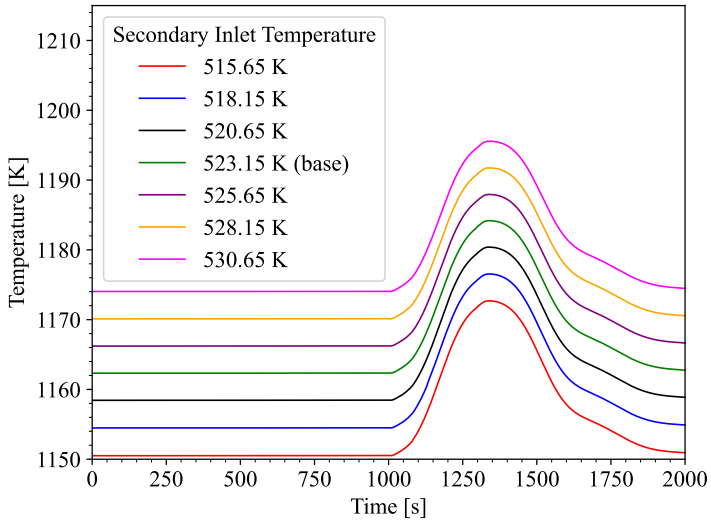

Figure 85. Maximum fuel temperatures for a secondary inlet temperature parameter study using the Dakota/SAM-standalone PKE model during the UOC transient.

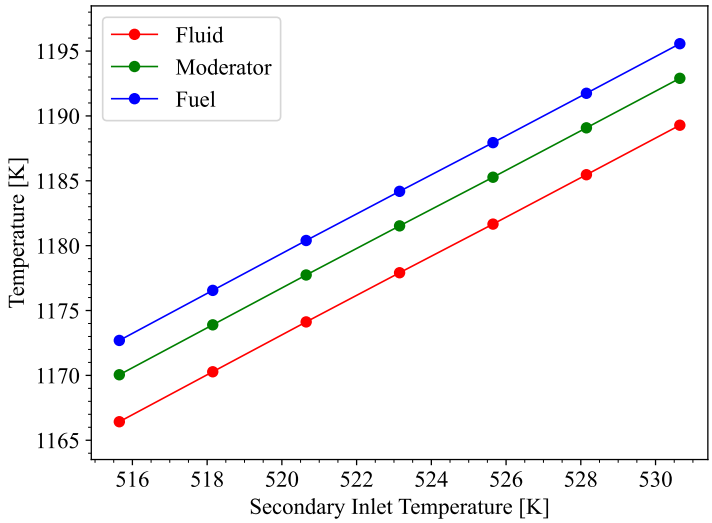

Figure 86. Peak fluid, moderator, and fuel temperature values for a secondary inlet temperature study using the Dakota/SAM-standalone PKE model during the UOC transient.

other analysis methods such as multivariate sensitivity analysis and uncertainty propagation using random sampling. These other analysis methods can be applied using the same analysis driver scripts without further modification.

Future work in this area may further explore and demonstrate practical applications of interfacing with Dakota, as well as a generalization of interface scripts for other codes in the BlueCRAB suite. The long-term goal of this effort is to provide analysts with a framework that will support diverse BlueCRAB analyses ranging from individual parameter sensitivity studies to multiphysics uncertainty propagation.

3.4.4. 2D Pronghorn/Griffin Results

The UOC transient simulated with the 2D Pronghorn/Griffin and 2D Pronghorn/PKE coupled models is discussed in this section. In this transient, the injection of cold helium into the core is simulated. Knowing the impact of the temperature feedback of the fuel and moderator, it is expected the power level of the reactor to increase as the cold helium starts flowing into the core. The transient was simulated by adjusting the coolant inlet temperature and inlet mass flow rate provided by SAM as boundary conditions during the transient. The sequence of events for the UOC transient is shown in Table 30. Prior to starting the transient, steady-state equilibrium conditions were achieved with the coupled model. During the first 1,000 seconds of the transient, the transient calculations were conducted with no change in system parameters (null transient). The inlet coolant temperature was reduced from 523.15 K to approximately 473.15 K over 10 seconds, while the inlet mass flow rate was increased from 96.0 kg/s to roughly 98.0 kg/s, as shown in Figure 87. After that, there were no changes to system parameters up to 1,310 seconds. Then, the coolant inlet temperature and mass flow rate were restored to their initial values over 10 seconds. The transient simulation was continued up to 2,000 seconds.

Table 30. Sequence of events for the UOC transient simulated with Pronghorn/Griffin.

Time (s)	Event
0–1,000	Equilibrium steady state completed.
1,000–1,010	Coolant inlet temperature reduced and inlet mass flow rate increased considering the values provided by SAM at the core inlet.
1,010–1,310	No change in operating conditions.
1,310–1,320	Coolant inlet temperature and mass flow rate returned to normal operation conditions.
2,000	Transient simulation end time.

Figure 88 compares the total power, peak power, and reactivity change predicted by Pronghorn coupled to the Griffin and PKE neutronics models. During the first 1,000 seconds of the transient, the system's main parameters were not changed to ensure steady-state conditions were well established. Once the inlet temperature starts decreasing and the inlet mass flow rate starts increasing, which will enhances the heat transfer from the pebbles and introduces a positive reactivity insertion. The power increases sharply and continues increasing at a lower rate due to the reduced feedback reactivity. Once the inlet coolant temperature and mass flow rate return to their nominal steady-state conditions, the power starts decreasing due to the negative thermal feedback. Both models show consistent results for power and reactivity evolutions, while the PKE model underestimates the power peaking.

Figure 89 compares the maximum and average fuel and moderator temperatures, and Figure 90 compares the reflector maximum and average temperatures of both models. The maximum temperatures of the fuel, moderator, and reflector increase 17 K, 16 K, and 6 K, respectively. The 2D and PKE models result in slightly different trends for the average fuel and moderator temperatures. Initially, temperatures decrease in both models, then the PKE solution shows a slight increase, followed by a decrease, and then an increase as the inlet conditions return to normal. The average temperatures predicted by the 2D model continue to increase as the power increases and then return to the steady-state value. The average temperature change is within 3 K for both the fuel and moderator. The average reflector temperature results are consistent between the two models and show a decreasing trend during the temperature and flow rate ramps; their temperature changes are within 6 K.

Figure 91 provides radial and axial solid temperature profiles at various locations at 1,391 seconds. Figures 92 and 93 display the steady-state power density and solid temperature and their relative change during the transient from both the 2D and PKE models.

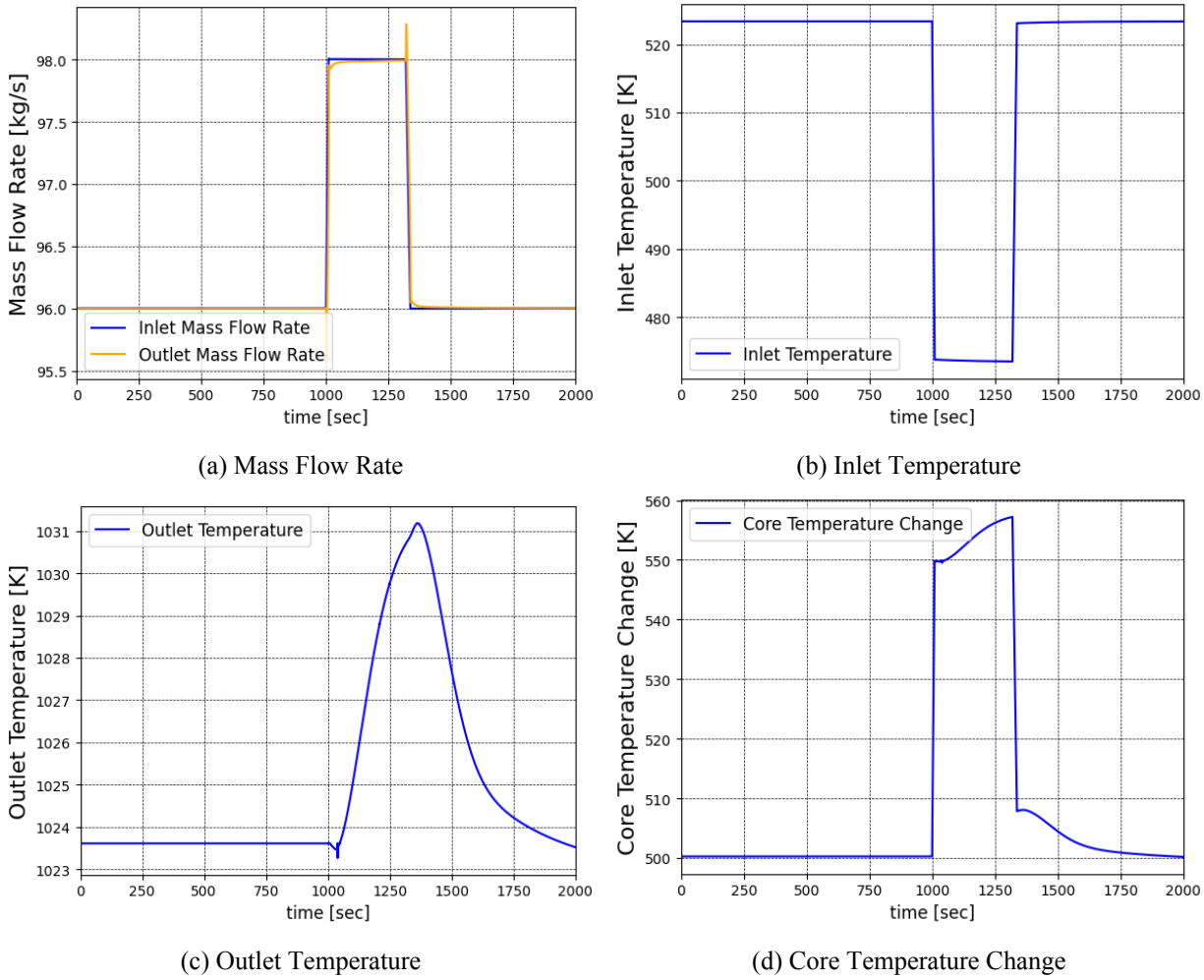

(a) Mass Flow Rate

(b) Inlet Temperature

(c) Outlet Temperature

(d) Core Temperature Change

Figure 87. Inlet and outlet mass flow rates and coolant temperatures and core temperature change obtained with the Pronghorn/Griffin model during the UOC transient.

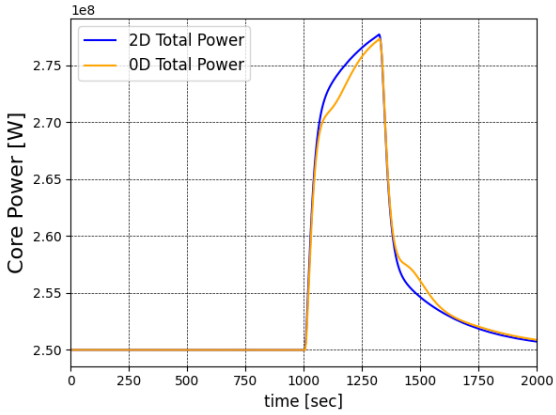

(a) Total Power

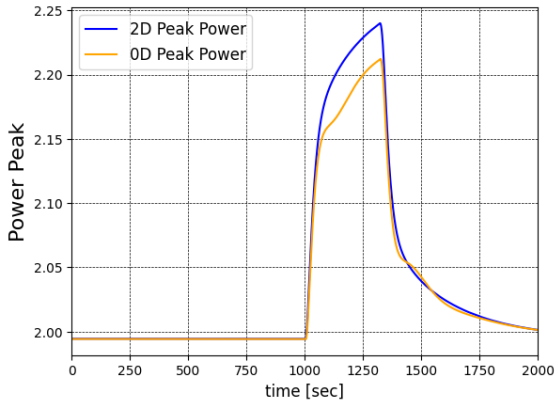

(b) Peak Power

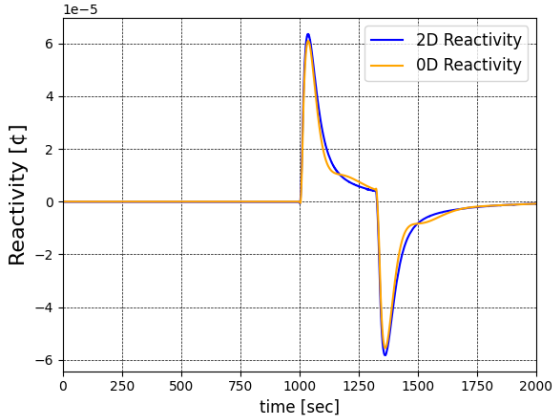

(c) Reactivity

Figure 88. Reactor total power, peak power ratio, and reactivity change obtained by the Pronghorn/Griffin model during the UOC transient.

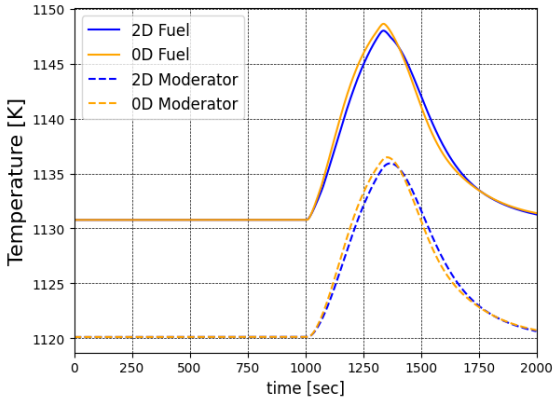

(a) Maximum

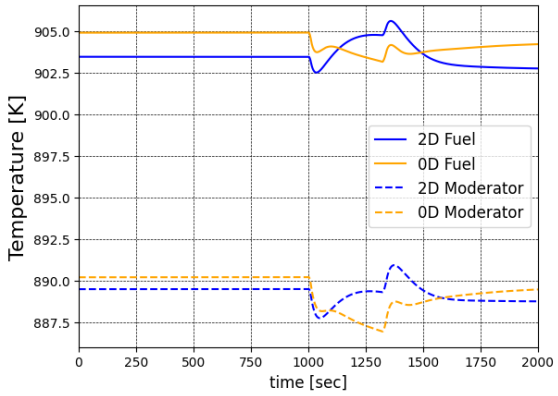

(b) Average

Figure 89. Maximum and average fuel and moderator temperatures obtained by the Pronghorn/Griffin model during the UOC transient.

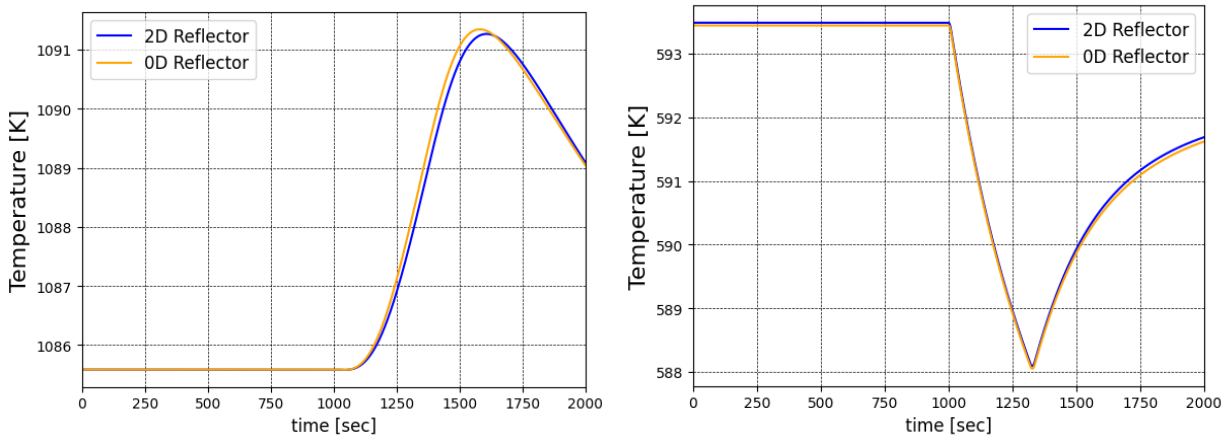

(a) Maximum (b) Average

Figure 90. Maximum and average reflector temperatures obtained by the Pronghorn/Griffin model during the UOC transient.

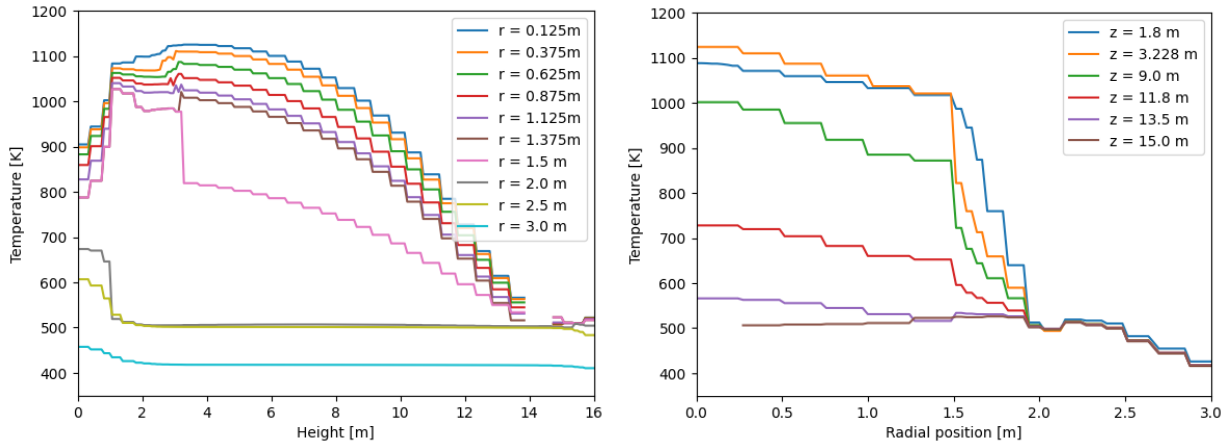

(a) Axial (b) Radial

Figure 91. Axial and radial solid temperature profiles obtained by the Pronghorn/Griffin model at 1,391 seconds of the UOC transient.

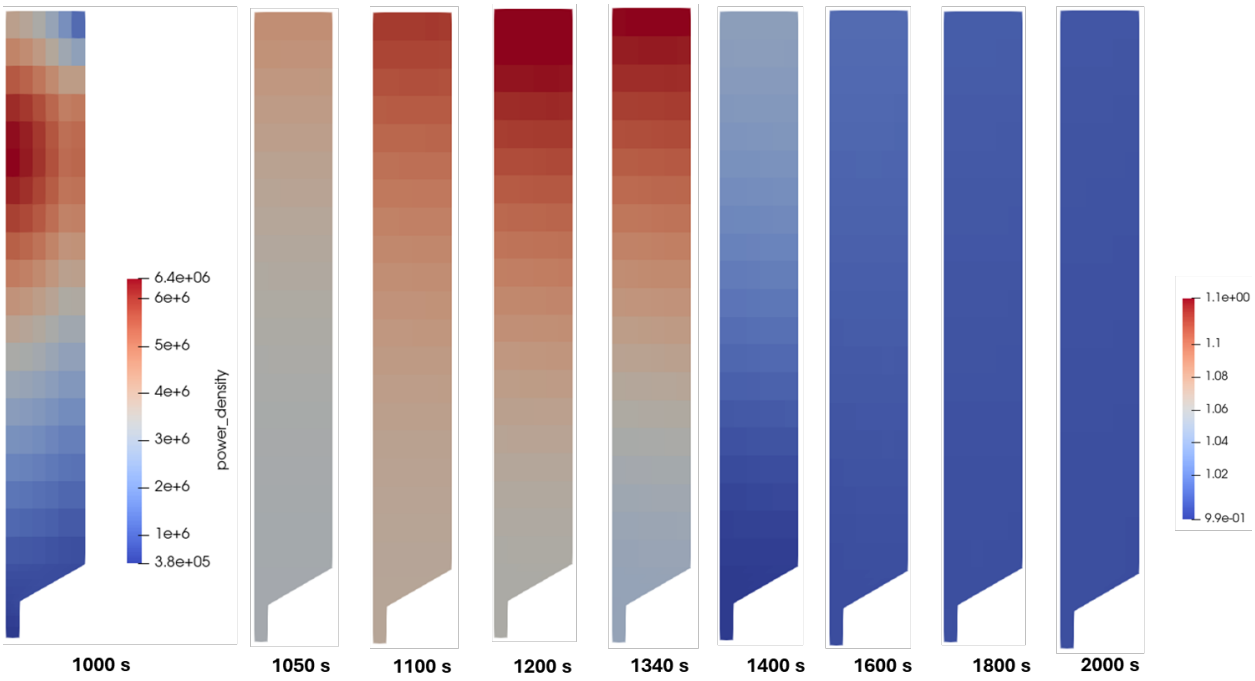

(a) 2D

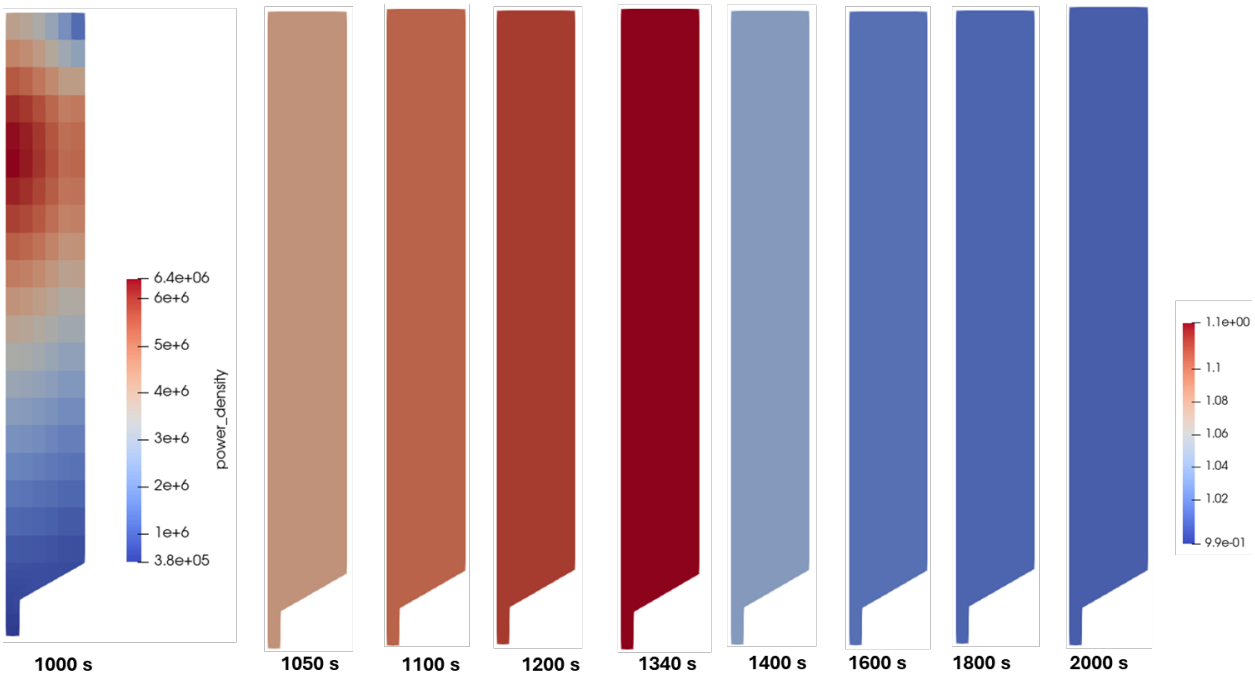

(b) 0D/PKE

Figure 92. Power density ratio relative to the steady-state power density obtained by the Pronghorn/Griffin model during the UOC transient.

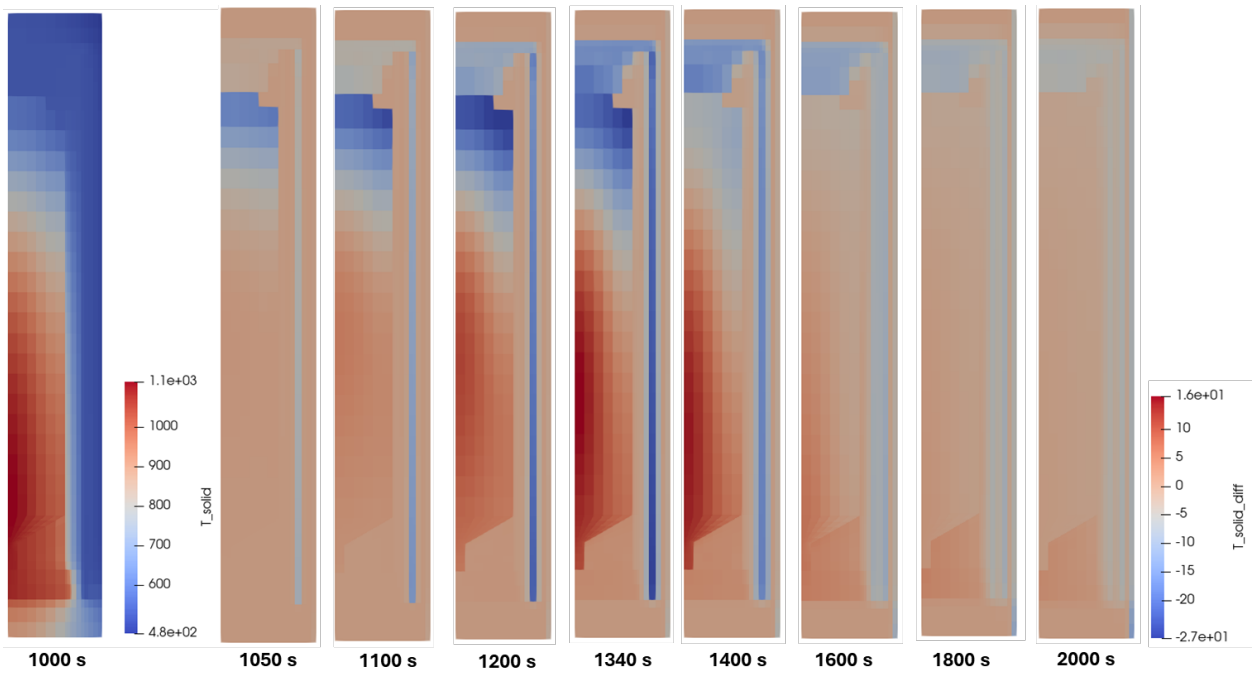

(a) 2D

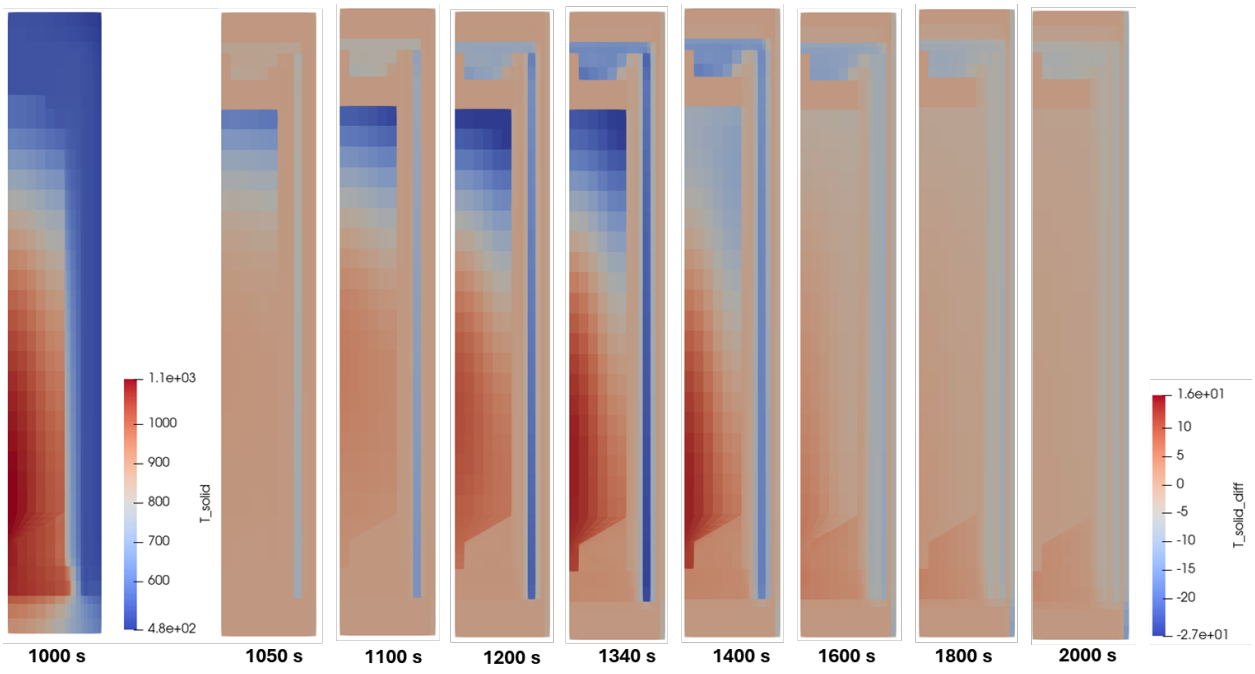

(b) 0D/PKE

Figure 93. Solid temperature change relative to the steady-state solid temperature obtained by the Pronghorn/Griffin model during the UOC transient.

3.4.5. Comparison

The results of the UOC transient predicted by the 2D SAM/Griffin/SAM and the 2D Pronghorn/Griffin models are compared in this section. Note that the Pronghorn/Griffin model uses the inlet mass flow rate and temperature from the SAM/Griffin/SAM model as the inlet boundary conditions. The overall trends of the major parameters predicted by both models are largely similar. As seen in Figure 94, both models show that the total core power increases sharply at the beginning of the transient, after which the total power continues to increase but at a slower rate. However, the peak total powers predicted by the models are slightly different, with the SAM/Griffin/SAM model predicting a peak power of about 290 MW and the Pronghorn/Griffin model a slightly lower peak power of about 278 MW. As a result, the peak fuel and moderator temperatures predicted by the SAM/Griffin/SAM model are higher than the those predicted by the Pronghorn/Griffin model at roughly 1200 K and 1147 K, respectively. Furthermore, due to the greater power increase, the SAM/Griffin/SAM model predicts a greater increase in fuel temperature, as shown in Figure **??**, where the temperature change is defined with respect to the steady-state equilibrium temperature.

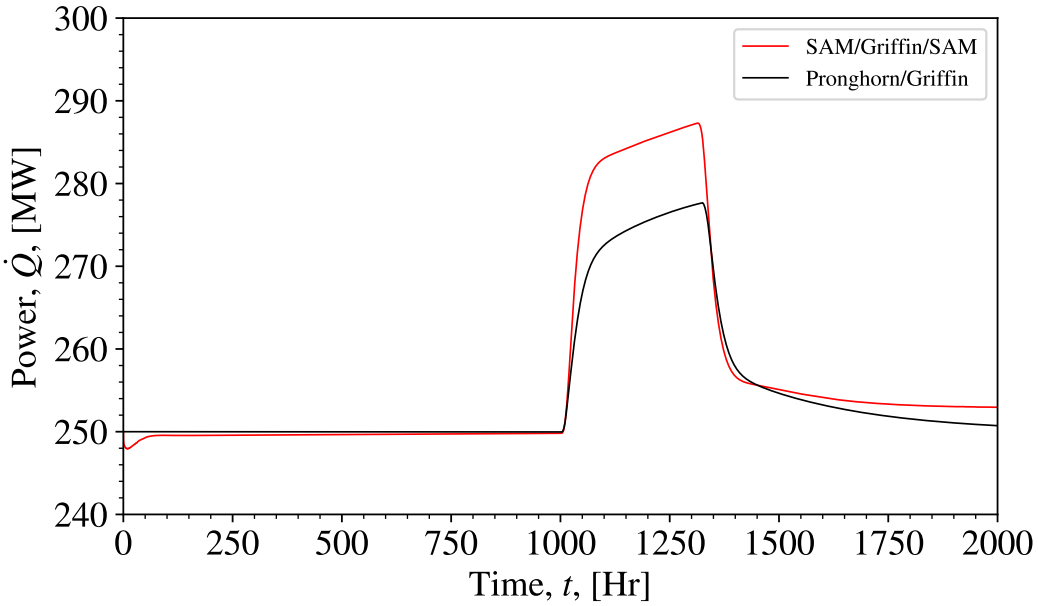

Figure 94. Comparison of the total power predicted by the SAM/Griffin/SAM and Pronghorn/Griffin models during the UOC transient.

Figure 96 shows the change in maximum and volume-averaged moderator temperatures from both models. Overall, the changes in moderator temperatures essentially follow the same trend as the fuel temperatures. The differences between the two models' predictions for the UOC transient are consistent with the comparison observed during steady-state equilibrium conditions; the 2D SAM/Griffin/SAM model predicts higher fuel and moderator temperatures than the Pronghorn/Griffin model. The changes in maximum and volume-averaged reflector temperatures are shown in Figure 97. The reflector temperatures from both models essentially share the same trend. The maximum reflector temperatures are largely unchanged with a maximum increase of only about 6 K. This is because forced convection remains the dominant heat removal mechanism in the core, and it transfers only a small amount of power to the reflectors. On the other hand, the volume-averaged reflector temperatures from both models decrease during the transient due to improved cooling, the result of colder helium flowing upward in the riser. However, as the helium temperature is increased back to its nominal value, the volume-averaged reflector temperatures from both models also increase.

Overall, the SAM/Griffin/SAM and Pronghorn/Griffin models agree relatively well qualitatively with each other for the UOC transient. The differences observed in this transient are consistent with the differences observed in the steady-state equilibrium conditions. As discussed in Section 3.1.2, differences are seen in the power density distributions predicted by both models during steady-state equilibrium conditions. It is also likely that the power density distributions of the two models are different for the UOC transient. This, in turn, leads to different local reactivity feedback responses, ultimately causing the power and temperature changes between the two models to differ. Nevertheless, despite the differences, both models respond as expected with respect to core temperature changes.

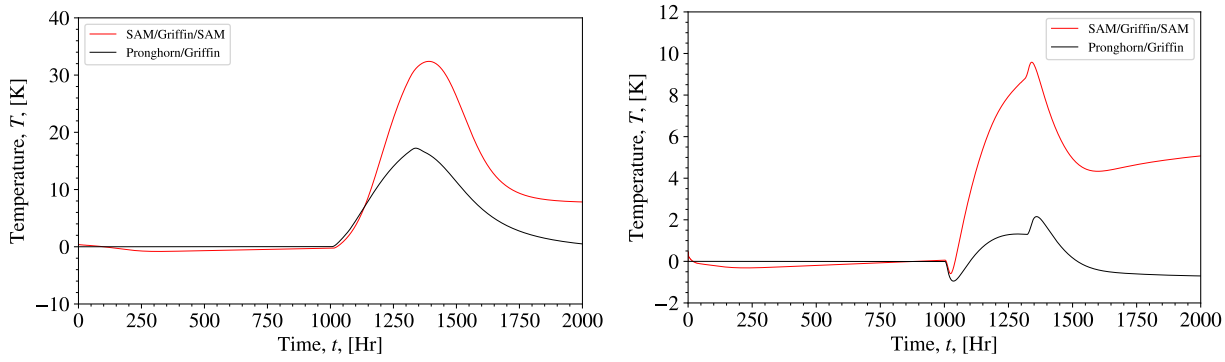

(a) Maximum (b) Average

Figure 95. Comparison of the change in maximum and average fuel temperatures predicted by the SAM/Griffin/SAM and Pronghorn/Griffin models during the UOC transient.

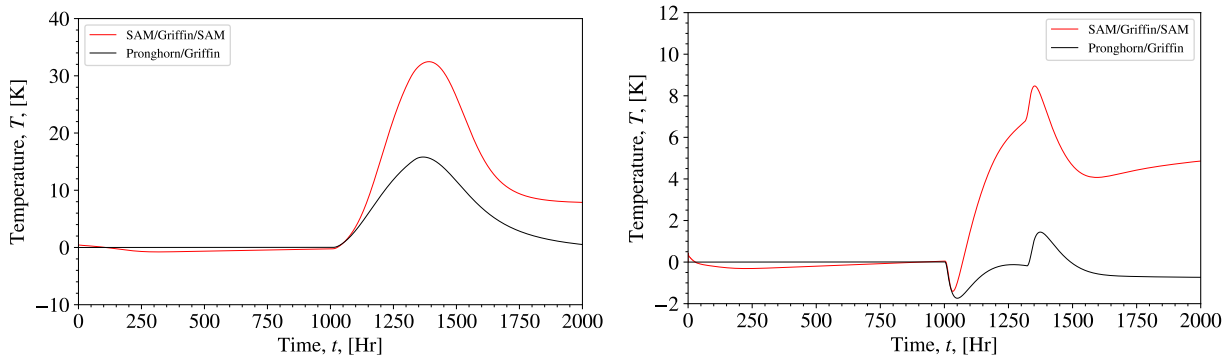

(a) Maximum (b) Average

Figure 96. Comparison of the change in maximum and average moderator temperatures predicted by the SAM/Griffin/SAM and Pronghorn/Griffin models during the UOC transient.

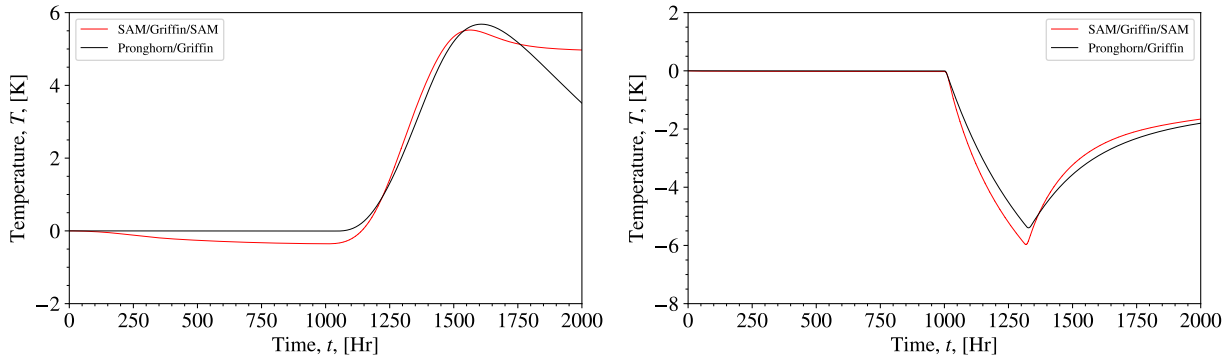

(a) Maximum (b) Average

Figure 97. Comparison of the change in maximum and average reflector temperatures predicted by the SAM/Griffin/SAM and Pronghorn/Griffin models during the UOC transient .

3.5. CONTROL ROD MOVEMENT ACCIDENT SCENARIOS—2D SIMULATION

This section presents the results of the RIA obtained using 2D models of SAM/Griffin/SAM and Pronghorn/Griffin, as well as a comparison of the two solutions. In this transient scenario, all control rods were moved together to introduce about 0.3$ of reactivity.

3.5.1. 2D SAM/Griffin/SAM Results

The results of the control rod movement scenario predicted by the 2D SAM/Griffin/SAM model are presented in this section. The correlations used in the 2D SAM model are summarized in Table 9. The sequence of events for this transient is summarized in Table 31. In this simulation steady-state equilibrium conditions were first achieved with the coupled model. During the transient, the control rods were moved from their initial position of 12.317 m to 12.852 m from t = 10 to 20 seconds. The position of the control rods was then held constant until t = 200 seconds, at which point the control rods were moved back to the initial position over 10 seconds. The simulation was terminated at t = 400 seconds. The position of the control rods is shown in Figure 98. Note that the position represents the elevation of the control rods in the reactor.

Table 31. Sequence of events for the control rod withdrawal event.

Time (s)	Event
0.0–10.0	No change in system parameters and the system runs for 10.0 seconds to confirm steady-state conditions are well established with all control rods at 12.317 m.
10.0–20.0	All control rods are withdrawn from position 12.317 m to position 12.852 m in 10 seconds.
20.0–200.0	The control rods stay at the 12.852 m position.
200.0–210.0	The control rods are reinserted to their initial position in 10 seconds.
210.0–400.0	There are no changes to the system's main parameters.

The total power and the maximum power peaking are shown in Figure 99. Power peaking is defined as the ratio of the local power density to the core-average power density. At the beginning of the transient, due to the withdrawal of the control rod, the total power experiences a massive surge from 250 to approximately 640 MW. The increase in power is followed by an increase in the maximum fuel and moderator temperatures

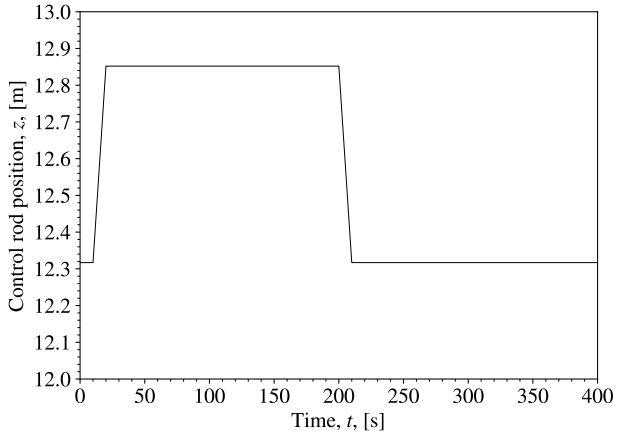

Figure 98. Control rod position during the control rod movement accident.

of roughly 75 K, as shown in Figures 100 and 101. Similarly, the average fuel and moderator temperatures also increase suddenly by approximately 20 K. As the temperature increases, negative reactivity causes the total power to rapidly decrease, eventually settling at roughly 300 MW. At the same time, since the total power remains higher than the steady-state power, the fuel and moderator temperatures continue to increase even though the power level remains relatively flat.

At t = 200 seconds, when the control rod is reinserted back to its original position, the total power decreases sharply due to increased neutron absorption by the control rod. The decreased power level causes the maximum fuel and moderator temperatures to decrease significantly, approaching the steady-state values. The decrease in temperatures, in turn, leads to positive reactivity in the core, which causes the power level to increase and return to the steady-state level of 250 MW. At the same time, the average fuel and moderator temperatures also slowly decrease.

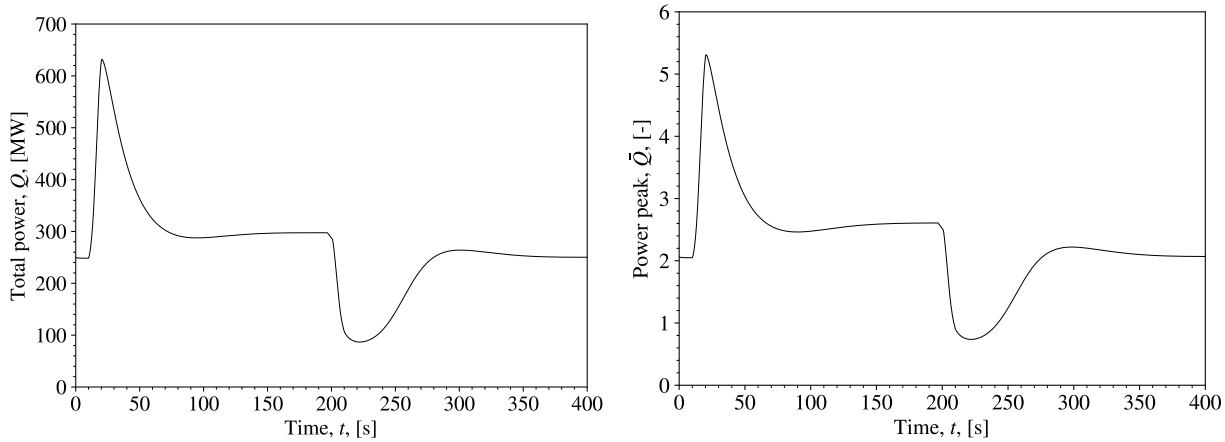

(a) Total Power (b) Maximum Power Peaking

Figure 99. Total power and power peak predicted by the SAM/Griffin/SAM coupled model for the control rod movement accident.

Figure 102 compares the axial and radial temperature profiles during peak temperature with the temperature profiles during steady-state equilibrium conditions. Despite the higher values, the axial and radial profiles during peak temperature are largely similar to the steady-state profiles. The radial profiles show that

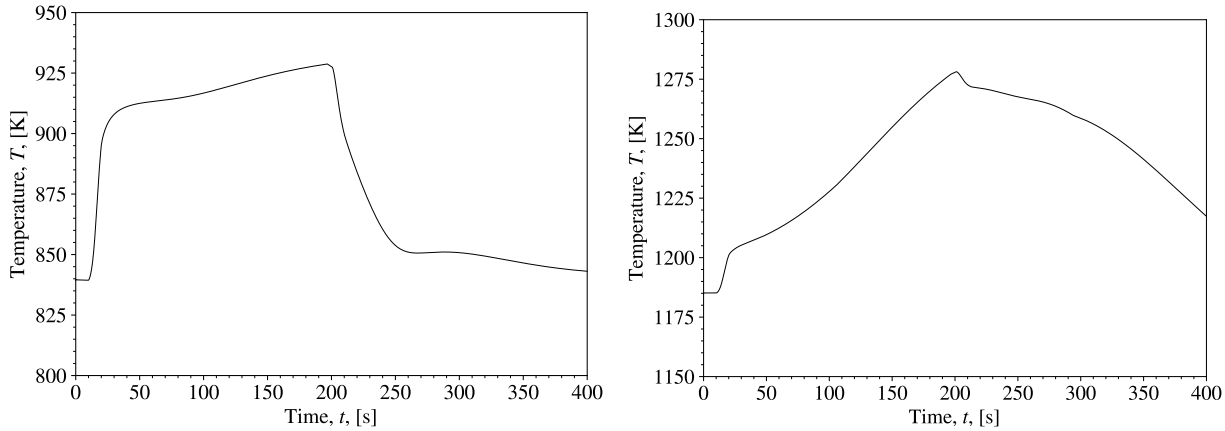

(a) Volume Averaged (b) Maximum

Figure 100. Volume-averaged and maximum fuel temperatures predicted by the SAM/Griffin/SAM coupled model for the control rod movement accident.

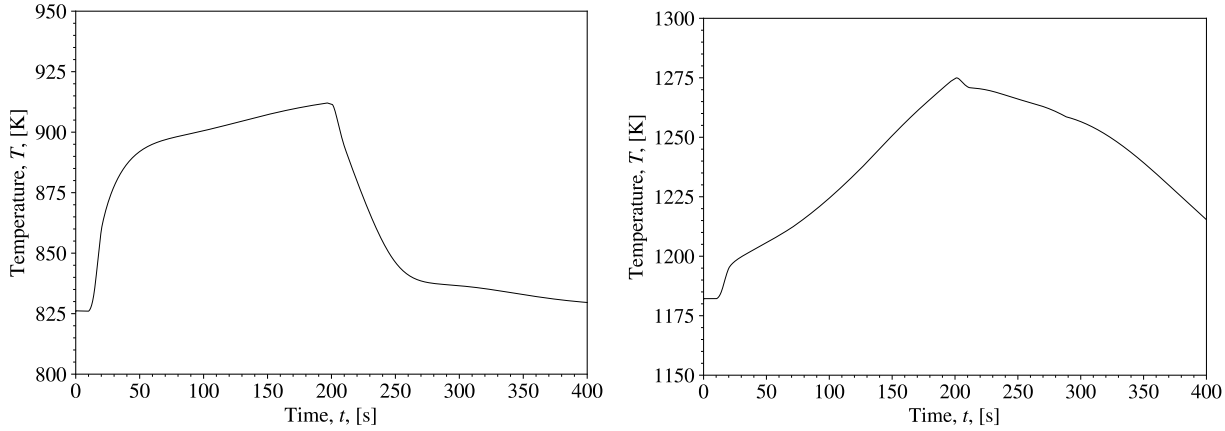

(a) Volume Averaged (b) Maximum

Figure 101. Volume-averaged and maximum moderator temperatures predicted by the SAM/Griffin/SAM coupled model for the control rod movement accident.

temperatures outside the pebble bed are effectively unchanged from the steady-state values during the transient. This is because the heat generated from the core is removed almost entirely by the coolant. The comparison of the axial and radial profiles of the power density is shown in Figure 103. As expected, during peak temperature, the power densities are significantly higher than the power densities during steady-state equilibrium conditions. During the power peak, z = 7 m experiences a greater increase in power density compared to the top and bottom of the core. This results in steeper slopes from the peak location to the top and bottom of the core. Similarly, the radial profiles also show steeper slopes from the inner to the outer core during peak temperature than during steady-state equilibrium.

The evolutions of power density and solid temperature distributions in the core during the transient are shown in Figures 104 and 105, respectively. The inner region of the core experiences a greater increase in power density than the outer region. Because helium in the core predominantly flows straight downward, the inner region of the core experiences a greater temperature increase than the outer region. Furthermore, the location of peak power density shifts upward from t = 50 seconds to 200 seconds and back down to the

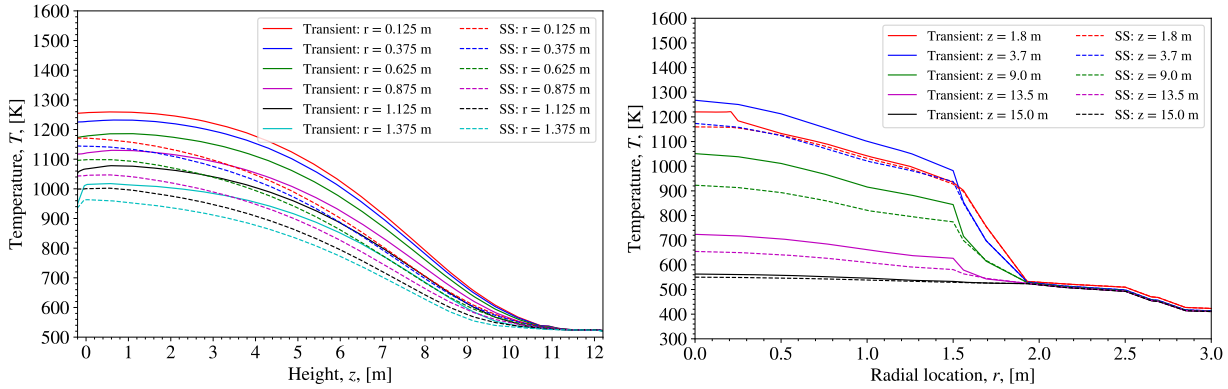

(a) Axial (b) Radial

Figure 102. Axial and radial solid temperature profiles predicted by the SAM/Griffin/SAM coupled model during peak temperature for the control rod movement accident.

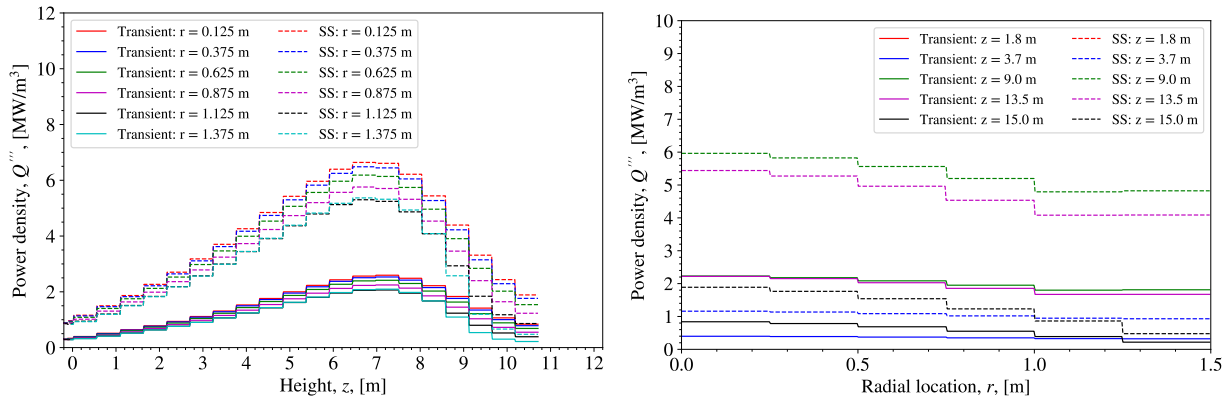

(a) Axial (b) Radial

Figure 103. Axial and radial power density profiles predicted by the SAM/Griffin/SAM coupled model during peak temperature for the control rod movement accident.

steady-state location from t = 300 seconds onward.

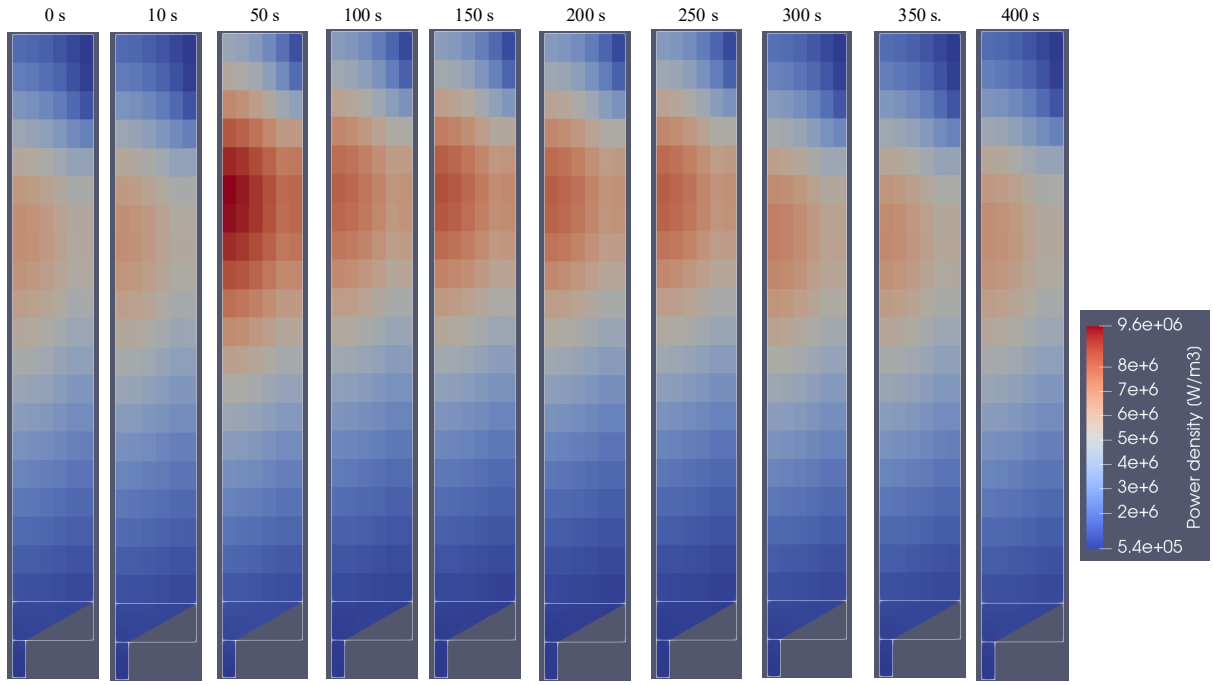

Figure 104. Evolution of power density distribution in the core predicted by the SAM/Griffin/SAM coupled model during the control rod movement accident.

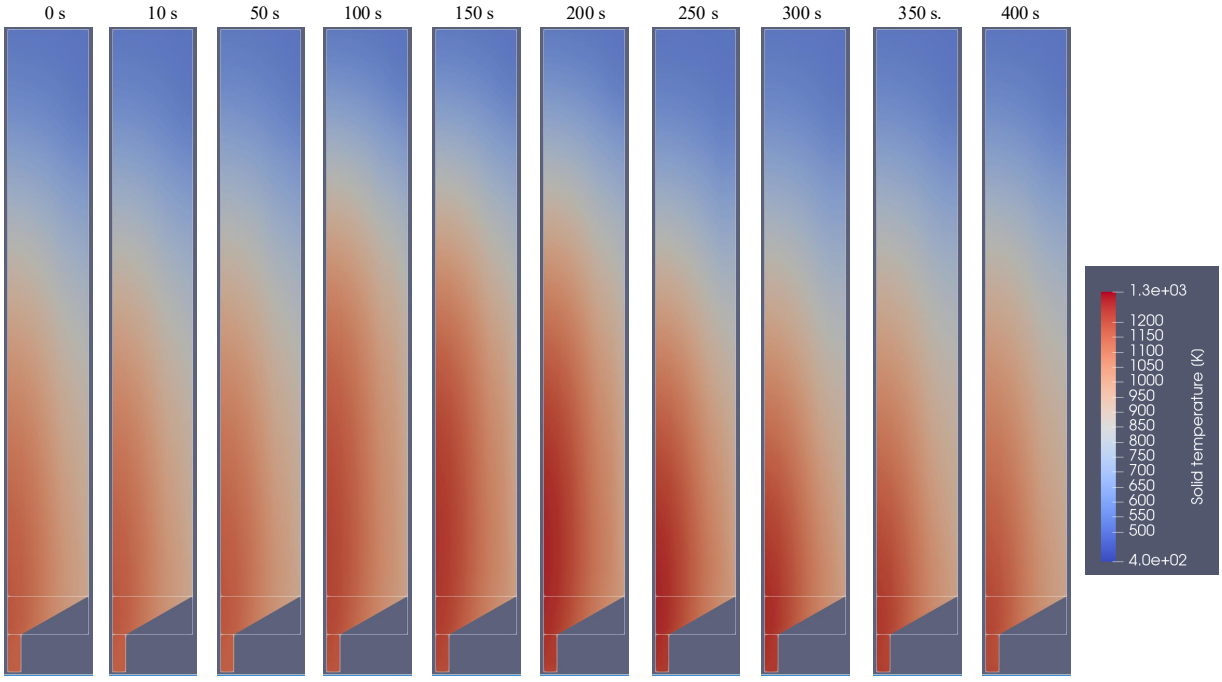

Figure 105. Evolution of solid temperature in the core predicted by the SAM/Griffin/SAM coupled model during the the control rod movement accident.

3.5.2. 2D Pronghorn/Griffin Results

This subsection presents control rod movement transient results obtained from the 2D Griffin/Pronghorn model. Steady-state equilibrium core conditions were established prior to the start of the transient. Then, the control rods were moved from their initial position of 12.317 m to 12.852 m in 10 seconds. They were held in that position for 180 seconds. At t = 200 seconds the control rods were moved back to their initial position over 10 seconds. The control rods remained at that position until the end of the transient simulation. Table 32 provides the sequence of events for the control rod withdrawal scenario.

Table 32. Sequence of events for the control rod withdrawal event.

Time (s)	Event
0.0–10.0	No change in system parameters; the system runs for 10.0 seconds to confirm steady-state conditions are well established with all control rods at 12.317 m.
10.0–20.0	All control rods are withdrawn from position 12.317 m to position 12.852 m in 10 seconds.
20.0–200.0	The control rods remain at position 12.852 m.
200.0–210.0	The control rods are reinserted to their initial position in 10 seconds.
210.0–400.0	No changes made to the system's main parameters. The simulation runs for 400 seconds.

Figure 106 shows the time-evolution of the reactor total power, peak power, and dynamic reactivity, and it illustrates the change in control rod position during the transient. During the initial 10 seconds of the transient we verify that the initial steady-state conditions are well established and no change is made to the system's main parameters. As the control rods are withdrawn, the reactor power starts increasing and peaks at 637 MW after 20.4 seconds due to the induced reactivity from the control rod movement. The power peak increases from about 2.02 to 5.22 following the evolution of the reactor power. After that, the thermal feedback dominates, resulting in a power decrease to a level higher than the 250 MW steady-state power by 37 MW at 200 seconds. Once the control rods are reinserted to their initial position, the power starts decreasing due to the negative reactivity insertion, and it starts increasing again as the positive feedback of the fuel and moderator cooling down begins to dominate. Approximately 350 seconds into the transient, the reactor total power returns to its initial steady-state value.

Figures 107 and 108 show the maximum and average fuel and moderator temperature evolution during the transient. The fuel and moderator average temperatures increase by about 65 and 60 K, respectively, within the first 30 seconds and then slowly increase until reaching roughly 950 and 934 K at 200 seconds, respectively. As the reactor power decreases, both the fuel and moderator temperatures decrease until they return to nominal steady-state values. The fuel and moderator reach maximum temperatures of 1215 and 1210 K at 200 seconds, respectively. Figure 109 shows the reflector temperature, which increases slightly by about 1.5 K, while Figure 110 provides radial and axial solid temperature profiles at various locations. Finally, Figure 111 presents the steady-state power density and fuel average temperature and their relative change during the transient. It can be clearly seen that the significant change in the power distribution occurs in the region where the control rod is moved, while the fuel temperature change follows the change in the reactor power at the beginning of the transient and then dissipates toward the lower part of the core as the transient proceeds.

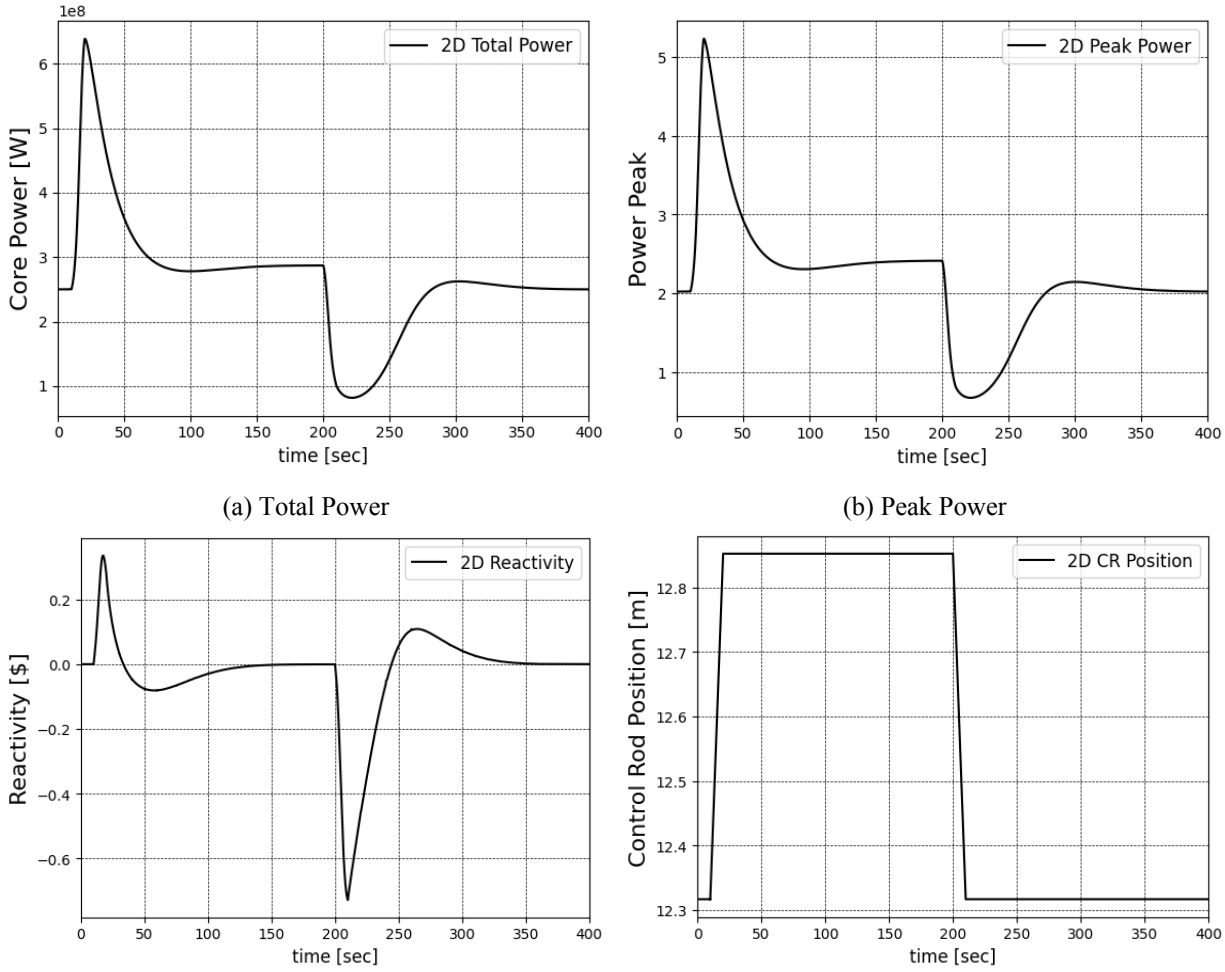

(a) Total Power

(b) Peak Power

(c) Reactivity

(d) Control Rod Axial Position

Figure 106. Reactor total power, peak power ratio, reactivity change, and control rod axial position obtained with the Pronghorn/Griffin model during the reactivity insertion transient.

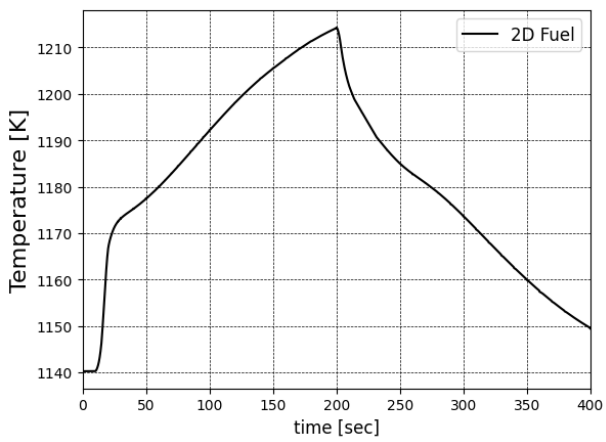

(a) Maximum

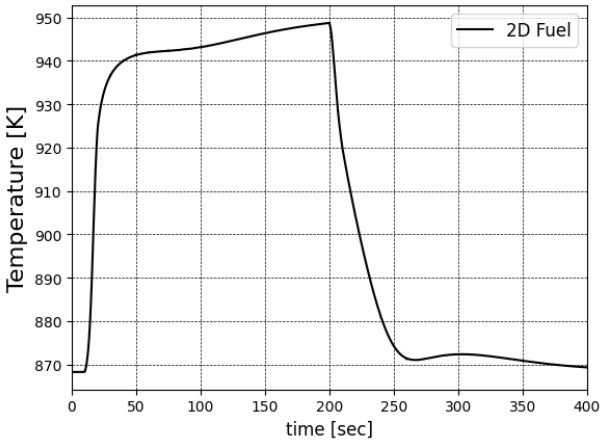

(b) Average

Figure 107. Maximum and average fuel temperatures obtained with the Pronghorn/Griffin model during the reactivity insertion transient.

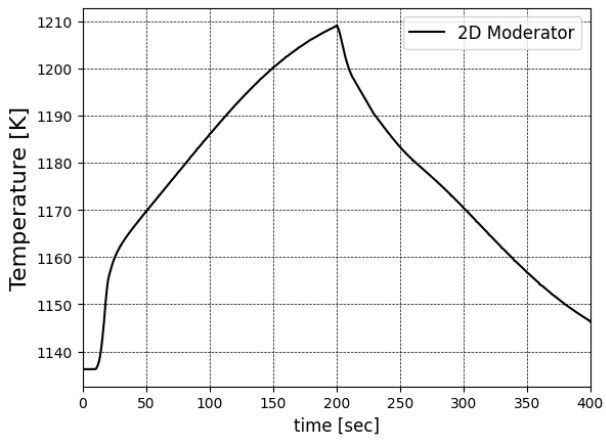

(a) Maximum

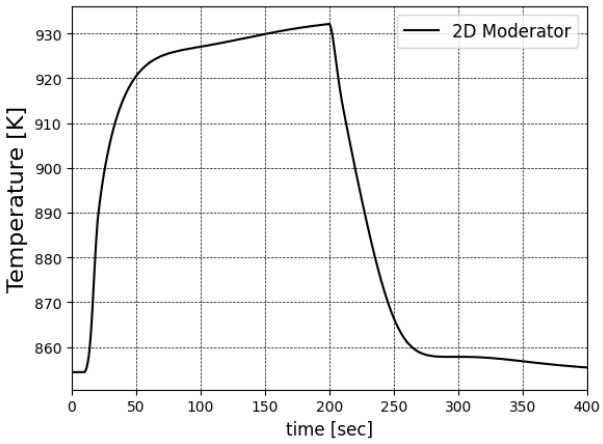

(b) Average

Figure 108. Maximum and average moderator temperatures obtained with the Pronghorn/Griffin model during the reactivity insertion transient.

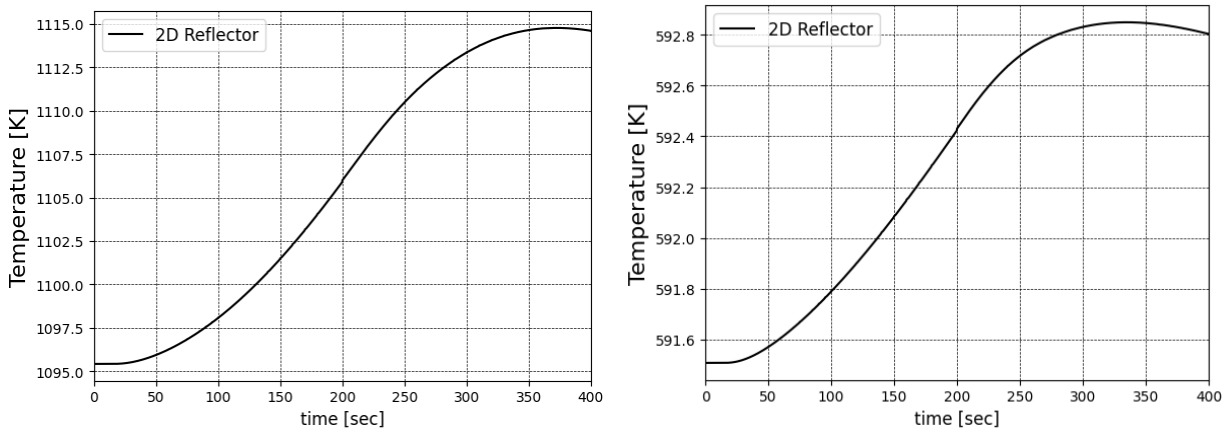

(a) Maximum (b) Average

Figure 109. Maximum and average reflector temperatures obtained with the Pronghorn/Griffin model during the reactivity insertion transient.

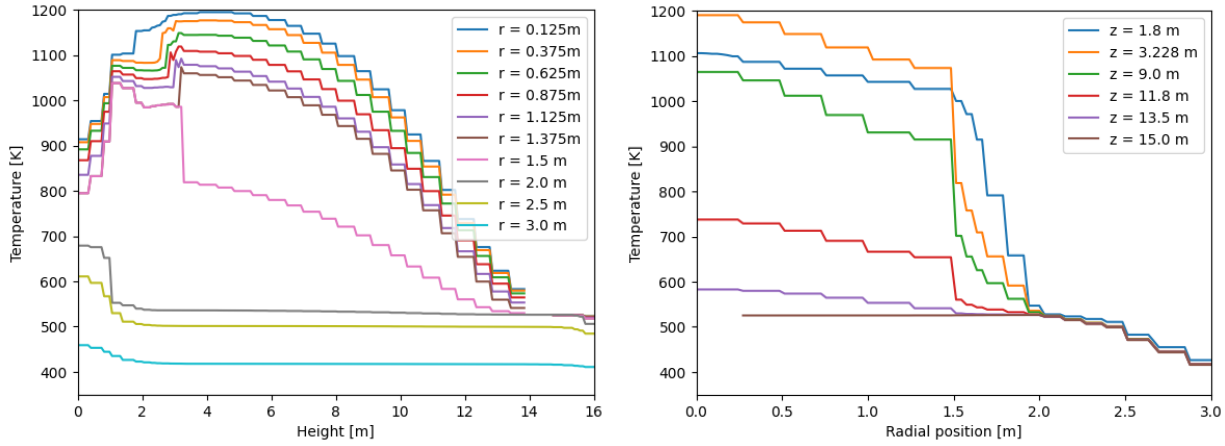

(a) Axial (b) Radial

Figure 110. Axial and radial solid temperature profiles obtained with the Pronghorn/Griffin model during the reactivity insertion transient during peak temperature of the pebble surface at 200 seconds.

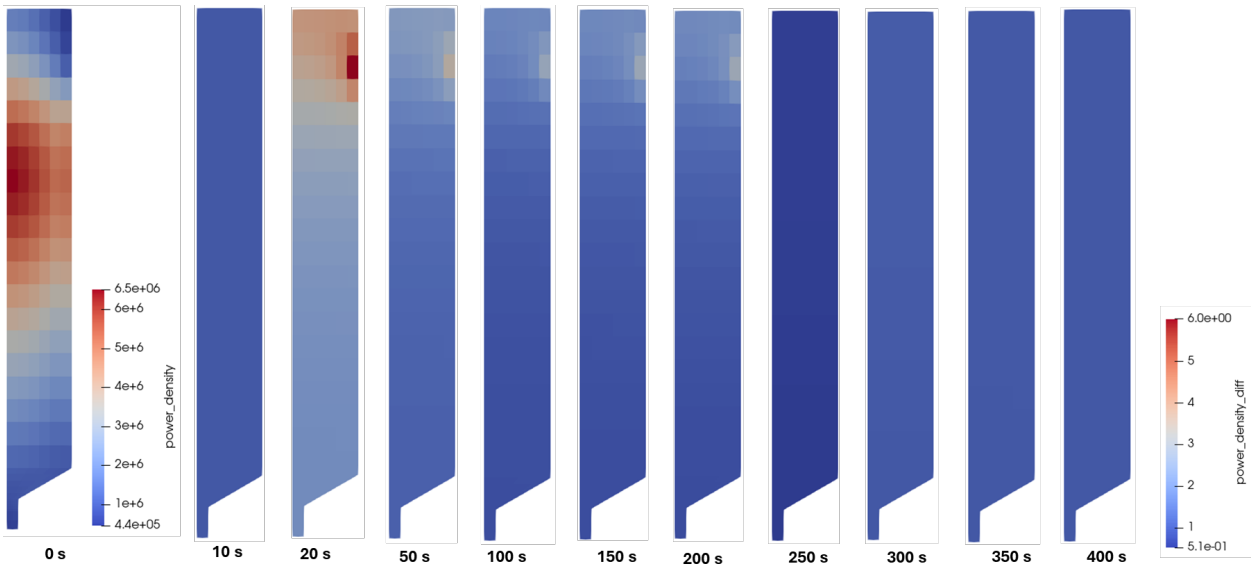

(a) Power Density

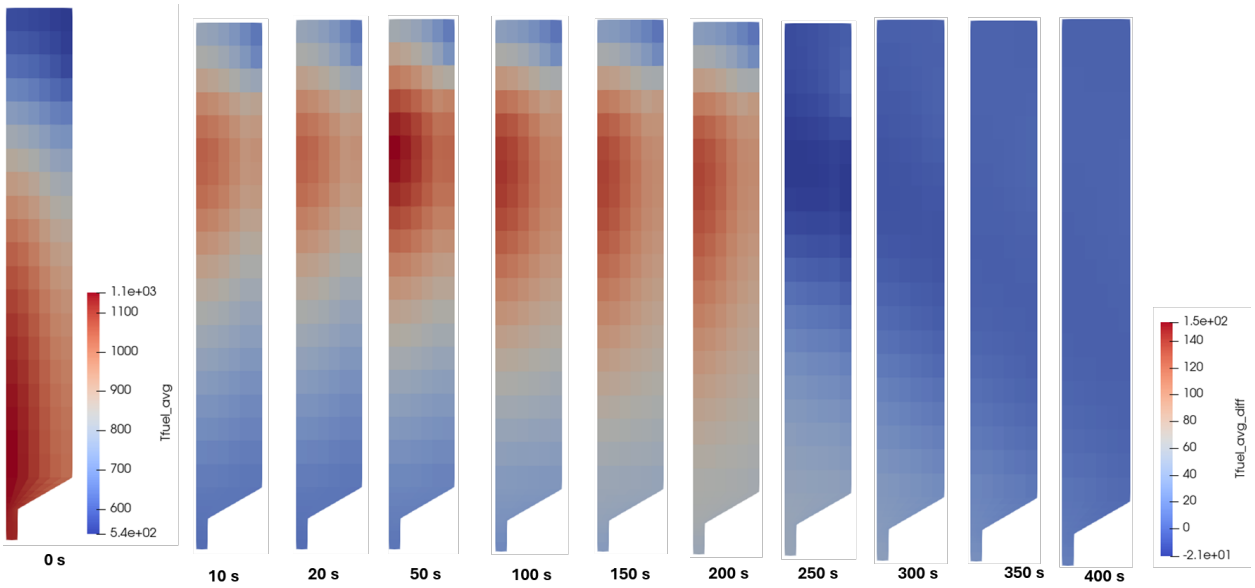

(b) Fuel Avg. Temperature

Figure 111. Power density and fuel average temperature changes obtained withduring the reactivity insertion transient relative to the steady-state power solution.

3.5.3. Comparison

The results of the RIA transient predicted by the 2D SAM/Griffin/SAM and the 2D Pronghorn/Griffin models are compared in this section. The overall trends of the major parameters predicted by both models are similar. Both code systems predicted very similar power evolution, as shown in Figure 112, with minor differences for both the total power and the power peak shown in the same figure. The solutions reach a maximum power value of approximately 640 MW, and a similar power peaking occurs at approximately 20 seconds during the transient. The average and maximum fuel and moderator temperature evolutions are shown in Figures 113 and 114. In general, the trends of the temperature evolution are very similar; however, the codes predict different magnitudes. Pronghorn/Griffin predicts higher average fuel and moderator temperatures than SAM/Griffin/SAM, while SAM/Griffin/SAM predicts higher maximum fuel and moderator temperatures than Pronghorn/Griffin. Additionally, differences in the equilibrium core steady-state maximum and average temperatures are observed during the first 10 seconds of the transient. Table 33 compares the peak values obtained by SAM/Griffin/SAM and Pronghorn/Griffin for power and temperatures of the fuel and moderator.

Table 33. Comparison of the peak values of the main core parameters obtained from 2D simulations of the SAM/Griffin/SAM and Pronghorn/Griffin codes during the RIA.

Parameter		SAM/Griffin/SAM	Pronghorn/Griffin
Power	Total (MW)	631.8	637.3
	Peak (-)	5.31	5.22
Fuel	Avg. (K)	928.8	948.7
	Max. (K)	1278.1	1214.2
Moderator	Avg. (K)	912.1	932.2
	Max. (K)	1275.0	1209.0

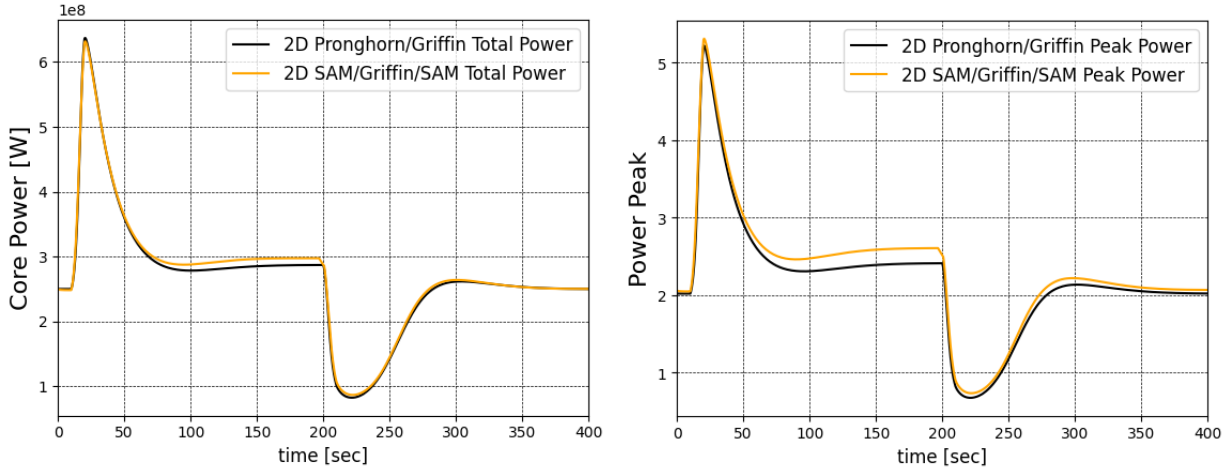

(a) Total Power

(b) Peak Power

Figure 112. Comparison of the total and peak powers predicted by the SAM/Griffin/SAM and Pronghorn/Griffin models during the RIA.

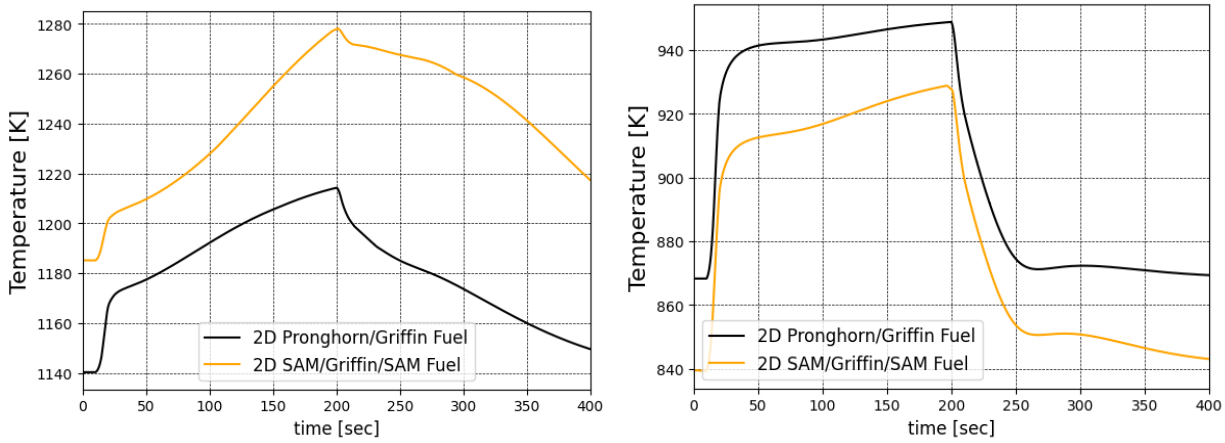

(a) Maximum (b) Average

Figure 113. Comparison of the maximum and average fuel temperatures predicted by the SAM/Griffin/SAM and Pronghorn/Griffin models during the RIA.

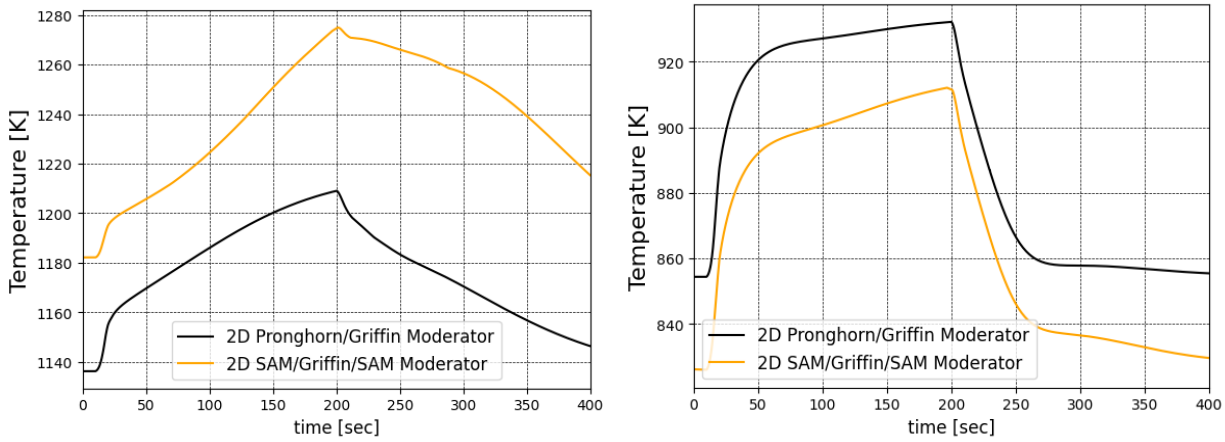

(a) Maximum (b) Average

Figure 114. Comparison of the maximum and average moderator temperatures predicted by the SAM/Griffin/SAM and Pronghorn/Griffin models during the RIA.

3.6. CONTROL ROD MOVEMENT ACCIDENT SCENARIOS—3D SIMULATION

This section presents the results of the reactivity insertion accident (RIA) for the delayed supercritical and prompt supercritical transients obtained using Pronghorn/Griffin 3D, 2D, and PKE models. The equivalent 2D model was developed to match the effect of single or two control rod movements by splitting the homogenized control rod region in the baseline 2D model into two regions and adjusting the boron concentration in one region to match the effect of the desired control rod. Figure 115 shows a comparison of the integral and differential reactivity worth of Control Rod 3 and combined Control Rods 3 and 4 as numbered in the mesh file.

The PKE model was developed using the point kinetics solver of Griffin, and it uses the kinetics parameters provided in Table 15 and utilizes a linear reactivity model that combines the thermal feedback reactivity components of the fuel, moderator, and reflector average temperatures provided in Table 16. For an accurate estimation of the inserted reactivity in the PKE model, the reactivity worth of the simulated control rods is obtained from the integral worth presented in Figure 115.

In the following subsections, the results of four reduced-order models are presented and compared to the reference solution of the 3D model. The models are listed as follows:

- 3D: Provide the reference solution of the simulated transient with the 3D model.
- 2D Same CR: Model the same axial movement of the control rod with no adjustments to the initial or final positions using the 2D model.
- 2D Same ρ: Model the same reactivity of the control rod by adjusting the initial control rod position of the 2D model to match the 3D model reactivity insertion.
- 0D/PKE Same CR: Model the same axial movement of the control rod with no adjustments to the initial or final positions using the PKE model and utilizing integral worth obtained from coupled calculations.
- 0D/PKE Same ρ: Model the same reactivity of the control rod by adjusting the integral worth used in the PKE model to match the 3D model reactivity insertion.

3.6.1. 3D Pronghorn/Griffin: Delayed Supercritical

This subsection presents the delayed supercritical RIA via control rod withdrawal with the Pronghorn/Griffin 3D, 2D, and PKE models. Steady-state equilibrium core conditions were established prior to the start of the transient. Then, the delayed supercritical RIA was initiated by moving a single rod from its initial position of 10.178 to 14.111 m in 2 seconds, resulting in an insertion of 0.8$ based on the control rod integral worth, as shown in Figure 115. The control rod then remained in the same position for 188 seconds. At t = 200 seconds, the control rod was moved back to the initial position over 2 seconds. The control rod remained at the same location until the end of the transient simulation. Table 34 provides the sequence of events for the control rod withdrawal scenario. However, due to differences in the 3D and 2D integral control rod worth, a slight difference in the inserted reactivity was observed. As a result, the control rod position in the 2D model was adjusted to 9.83 m instead of 10.178 m to match the reactivity insertion of the 3D model.

Figure 116 shows the time-evolution of the reactor total power, peak power, and reactivity, and the change in control rod position, during the transient for all models. Table 35 compares the total power, power peaking, and reactivity peak values obtained from different models. No change was made to the system's main parameters during the initial 10 seconds of the transient to verify that the initial steady-state conditions were well established. As the control rod is withdrawn, the reactor power starts increasing and peaks at 652 MW after 14.6 seconds due to the induced reactivity from the control rod movement simulated by the 3D model. The power peak increases from about 1.84 to 5.13 following the evolution of the reactor power. After that, thermal feedback dominates, resulting in a power decrease to a level higher than the 250 MW steady-state power by 44 MW at 200 seconds. Once the control rod is reinserted to its initial position, the power starts

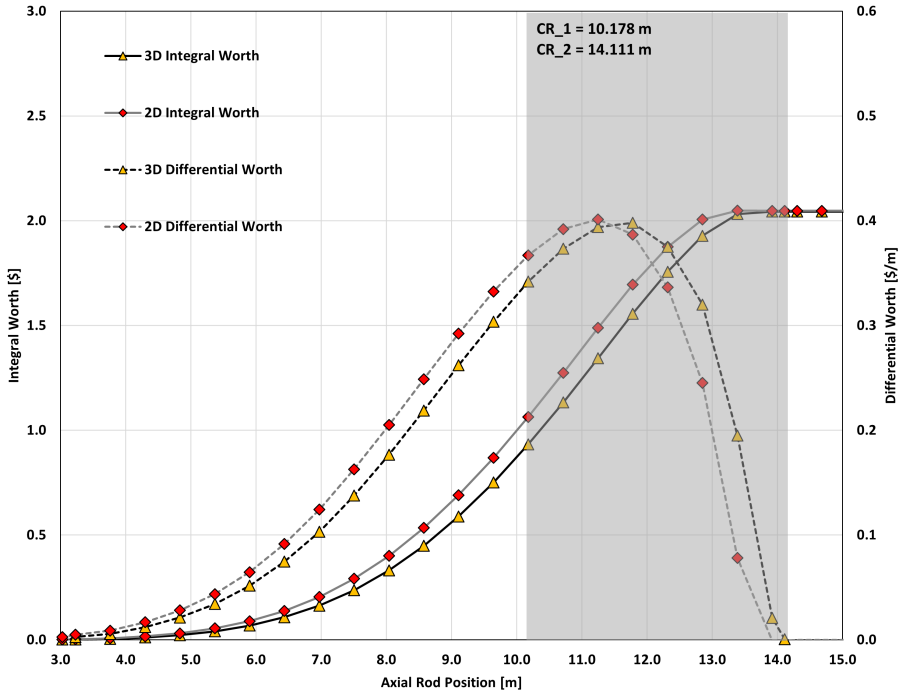

(a) Control Rod 3

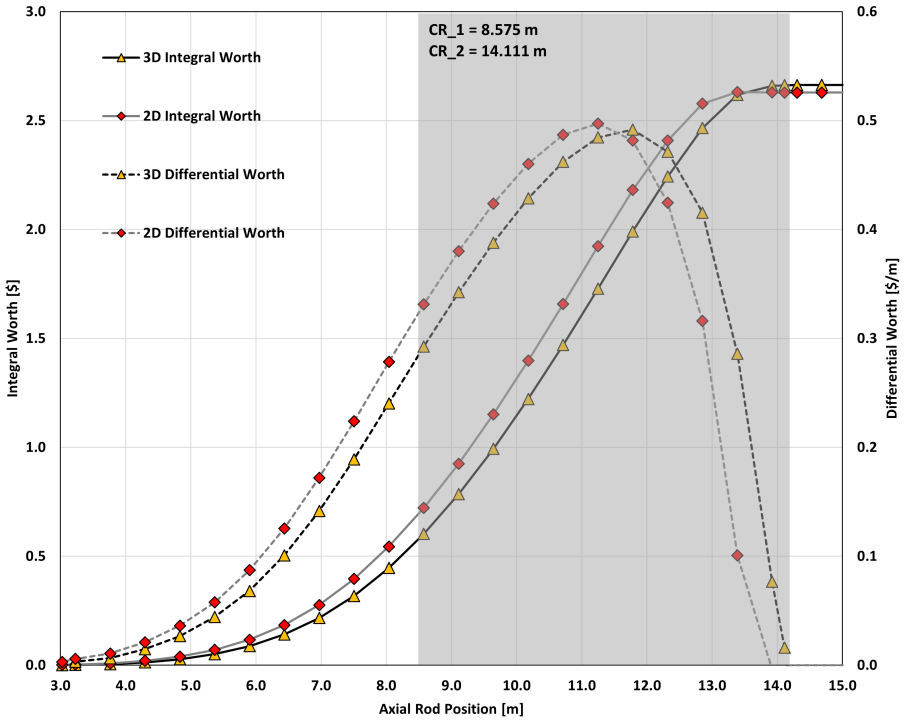

(b) Control Rods 3 & 4

Figure 115. Integral and differential control rod worth of the 3D and 2D models.

Table 34. Sequence of events for the control rod withdrawal event (delayed supercritical).

Time (s)	Event
0.0–10.0	No change in system parameters. The system runs for 10.0 seconds to confirm steady-state conditions are well established with Control Rod 3 at 10.178 m and the remaining rods at 13.386 m.
10.0–12.0	Control Rod 3 is withdrawn from position 10.178 m to position 14.111 m in 2 seconds.
12.0–200.0	The control rod remains at position 14.111 m.
200.0–202.0	The control rod is reinserted to the initial position in 2 seconds.
202.0–400.0	No change to the system's main parameters. The simulation runs for 400 seconds.

decreasing due to the negative reactivity insertion caused by the control rod, and it starts increasing again as the positive feedback of the fuel and moderator cooling down begins to dominate. Approximately 370 seconds into the transient, the reactor total power returns to its initial steady-state value.

Comparing the 2D solutions to the 3D reference solution, the 2D model with the same control rod movement resulted in less reactivity insertion and, as a result, had a lower peak power (-9%), while the 2D model with corrected reactivity insertion was an excellent match with the 3D power solution (-0.4%). The corrected reactivity was estimated from two static eigenvalue calculations of the 3D model with initial and final control rod positions. Knowing the correct static reactivity of the control rod resulted in very close dynamic reactivities for the 3D and 2D models. The 2D model with the same control rod movements resulted in -0.04$ lower reactivity, while with the same static reactivity it was 0.01$ higher.

Comparing the PKE solutions to the 3D reference solution, the PKE model with the same control rod movement, using the control rod integral worth obtained from 3D static calculations, showed a significant increase in total power (30.87%), while the PKE model with corrected reactivity insertion was a better match with the 3D power solution, with a relative error of -4.79%. In terms of reactivity, the PKE model with the same control rod movement significantly overestimated the reactivity by 0.11$, while the reactivity predicted by the PKE model with the same reactivity insertion is 0.07$ lower. There is a significant difference between the reactivity inserted by the two models of 0.18$, which is mainly due to not considering the impact of spectral changes on the thermal feedback effects while calculating the control rod worth. Figure 117 shows the reactivity components of the control rod, fuel, moderator, and reflector along with total reactivity obtained from the linear summation of all the reactivity components for both PKE models. The predicted control rod reactivity component with the PKE model with the same control rod movement is about 1.3$, while the model with corrected reactivity shows 0.8$. Both models resulted in very similar reactivity evolutions for the thermal feedback components but with different magnitudes, causing different total reactivity insertions.

Table 35. Peak power and reactivity of the delayed supercritical RIA simulated with Pronghorn/Griffin.

Model	Power (GW)	Diff. [%]	Time to Peak (s)	Power Peak	Diff. (%)	Time to Peak (s)	Reactivity ($)	Diff. ($)	Time to Peak (s)
3D	0.6524	–	14.60	5.13	–	14.30	0.576	–	11.30
2D Same CR	0.5937	-9.00	14.90	4.65	-9.31	14.70	0.532	-0.04	11.30
2D Same ρ	0.6498	-0.40	14.60	5.07	-1.12	14.40	0.581	0.01	11.30
PKE Same CR	0.8537	30.87	14.84	6.19	20.71	14.84	0.686	0.11	11.43
PKE Same ρ	0.6211	-4.79	16.00	4.50	-12.18	16.00	0.503	-0.07	11.68

Figure 118 shows the evolutions of the fuel and moderator average and maximum temperatures during the transient for all models. Additionally, Table 36 compares the average and maximum fuel, moderator, and reflector peak values obtained from the different models. As the power starts increasing, the fuel and moderator temperatures increase sharply and then at a much slower rate as the power starts decreasing to a new steady-state level. Once the control rod is reinserted, the temperature decreases significantly to a lower value than its steady-state level and starts increasing again until it returns to the steady-state level. The peak average and maximum fuel temperatures obtained from the 3D model are 977 and 1236 K, respectively.

Comparing the 2D solutions to the 3D reference solution, the 2D model with the same control rod movement results in a lower temperature increase and peaks at 966.8 and 1222.2 K for average and maximum fuel temperatures, respectively, while the 2D model with the same reactivity insertion shows an excellent match with the 3D solution for both average and maximum temperatures, peaking at 976.6 and 1236.7 K, respectively. However, the PKE model shows a very different average temperature evolution for both fuel and moderator, while it shows a similar maximum temperature evolution but with different magnitudes. The PKE model with the same control rod movement peaks at 1006.7 and 1334.9 K for average and maximum fuel temperatures, respectively, and the PKE model with the same reactivity insertion peaks at 969.2 and 1271.6 K for average and maximum fuel temperatures, which are much closer to the reference solution results.

Table 36. Peak temperatures of the delayed supercritical RIA simulated with Pronghorn/Griffin.

Model	Fuel		Moderator		Reflector	
	Avg.	Max.	Avg.	Max.	Avg.	Max.
3D	977.4	1236.4	960.3	1219.2	595.1	1113.3
2D Same CR	966.8	1222.2	950.1	1205.7	595.4	1108.2
2D Same ρ	976.6	1236.7	959.4	1219.5	595.5	1112.2
PKE Same CR	1006.7	1334.9	985.0	1311.6	596.6	1134.6
PKE Same ρ	969.2	1271.6	949.8	1252.0	595.6	1119.5

Figures 119 and 120 compare the profiles of the averaged power density in the radial and axial directions of the 3D and reactivity-corrected 2D and PKE models at different time points. Both the 3D and 2D models show very similar power shapes averaged radially and axially, while significant differences in shape and magnitude are observed throughout the transient, except for the beginning and end of the transient. This is mainly due to the reduced-order model of the PKE not capturing the local perturbation effect of moving the control rod.

Figures 121 and 122 compare the profiles of the averaged fuel temperature in the radial and axial directions of the 3D and reactivity-corrected 2D and PKE models at different time points. Both the 3D and 2D models show very similar temperature profiles averaged radially and axially, while significant differences in shape and magnitude are observed during the transient, except for the beginning and end of the transient. This is mainly due to the reduced-order model of the PKE not capturing the local perturbation effect of moving the control rod.

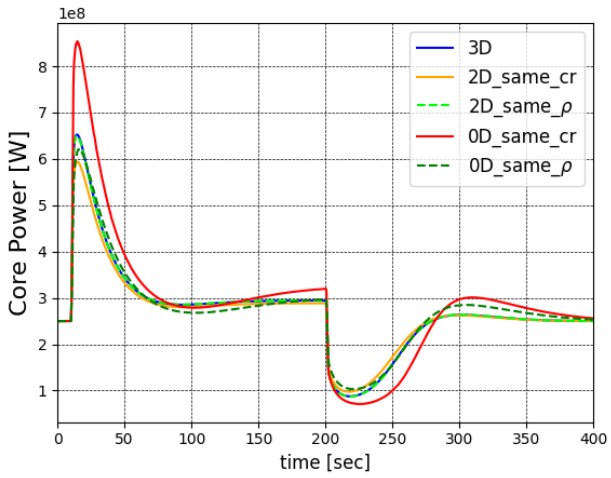

(a) Total Power

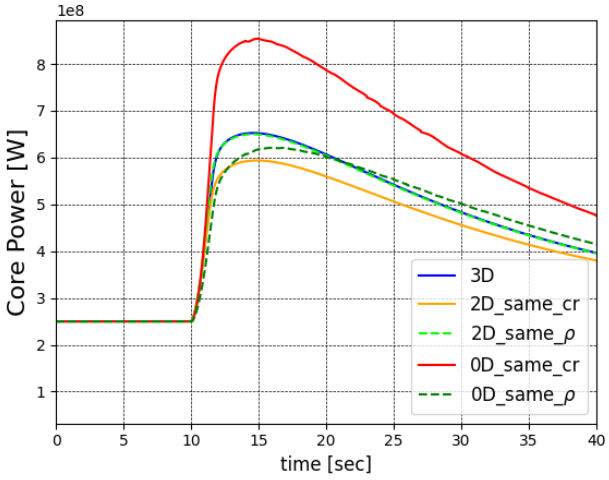

(b) Total Power First 40 Seconds

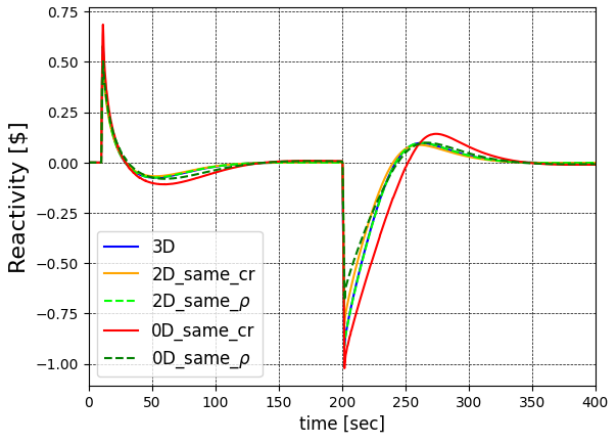

(c) Reactivity

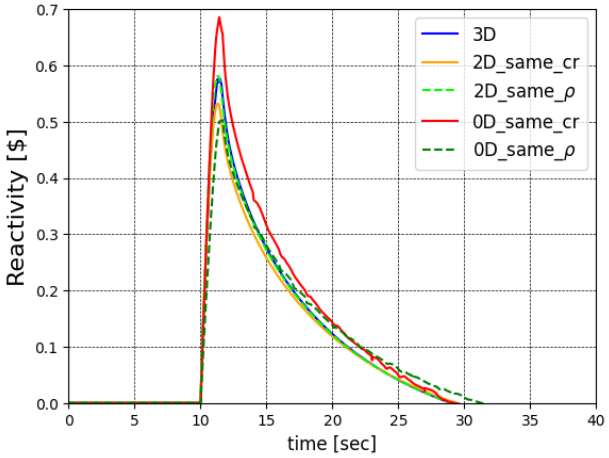

(d) Reactivity First 40 Seconds

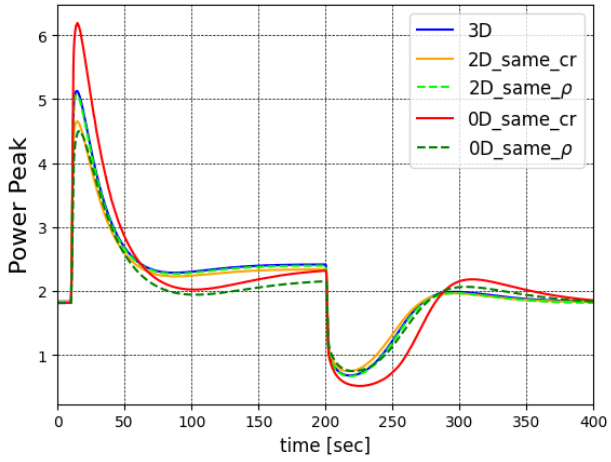

(e) Power Peaking

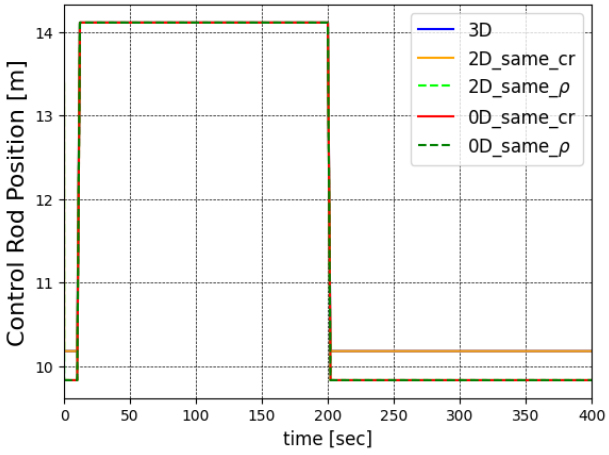

(f) Control Rod Position

Figure 116. Total power, peak power, reactivity, and control rod position evolution during the delayed supercritical control rod withdrawal.

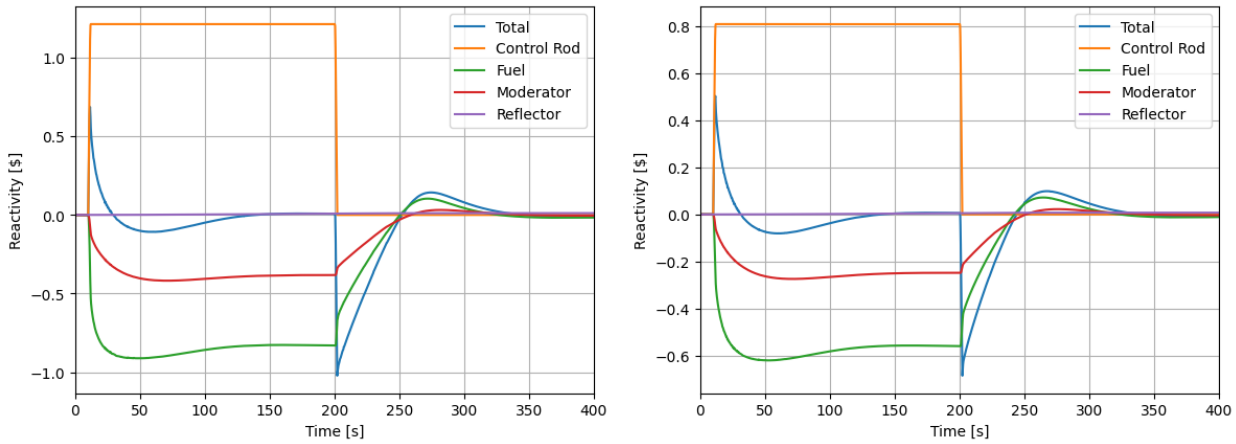

(a) Nominal (b) Corrected

Figure 117. PKE model reactivity component evolution during the delayed supercritical control rod withdrawal.

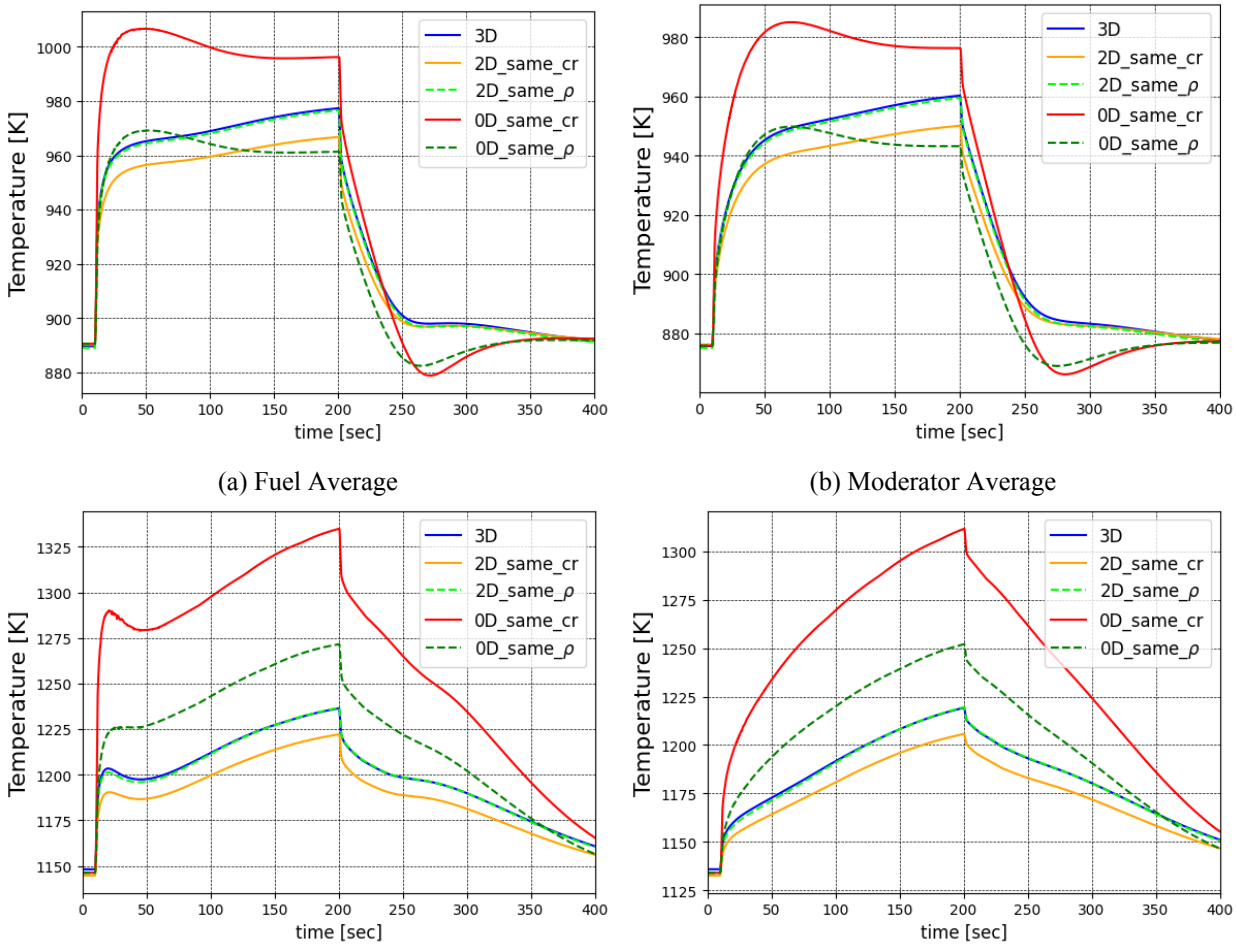

(a) Fuel Average (b) Moderator Average

(c) Fuel Maximum (d) Moderator Maximum

Figure 118. Fuel and moderator temperature evolution during the delayed supercritical control rod withdrawal.

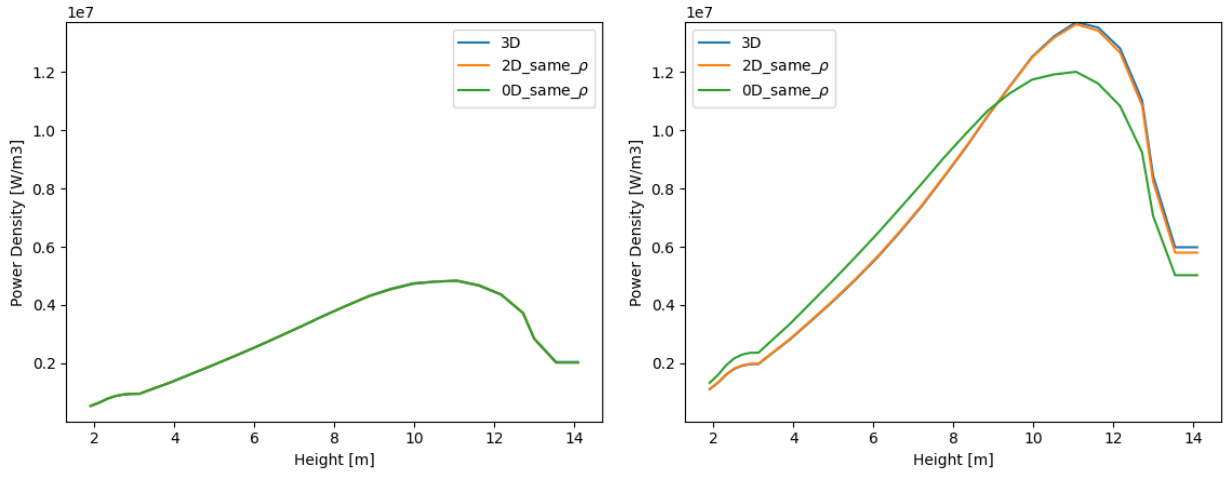

(a) t = 0 s

(b) t = 17 s

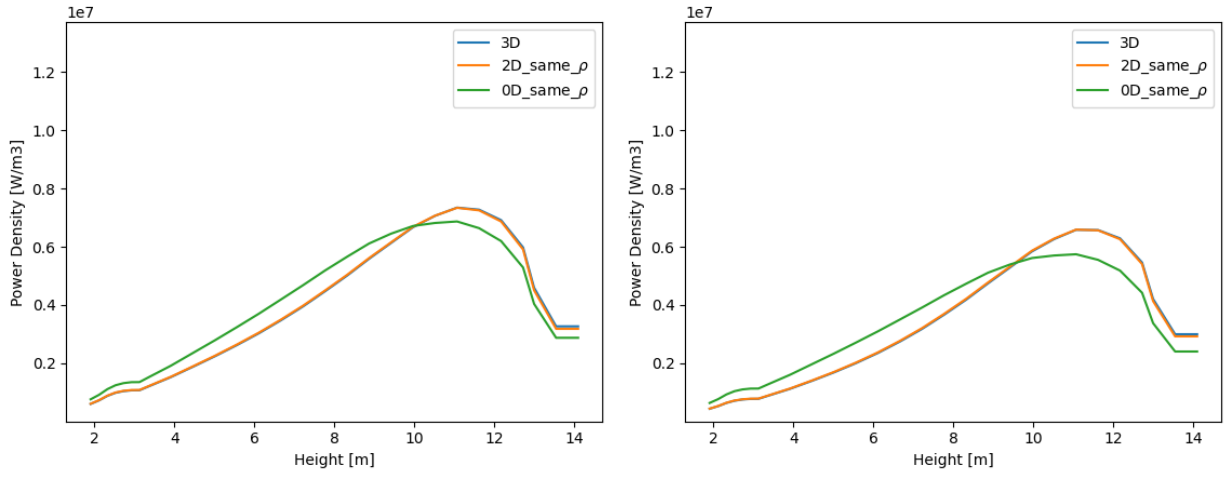

(c) t = 50 s

(d) t = 200 s

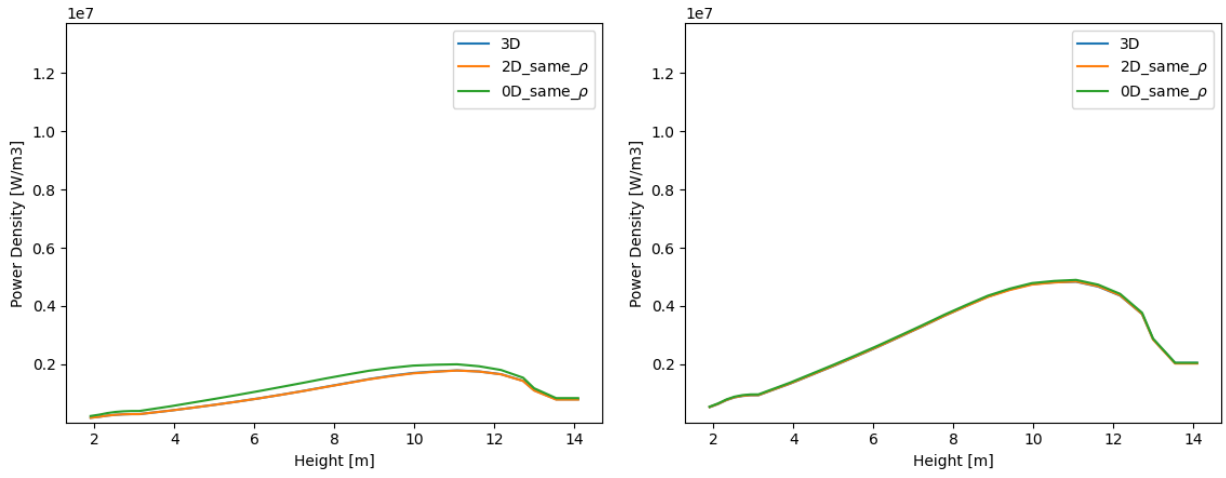

(e) t = 220 s

(f) t = 400 s

Figure 119. Radially averaged power density during the delayed supercritical control rod withdrawal.

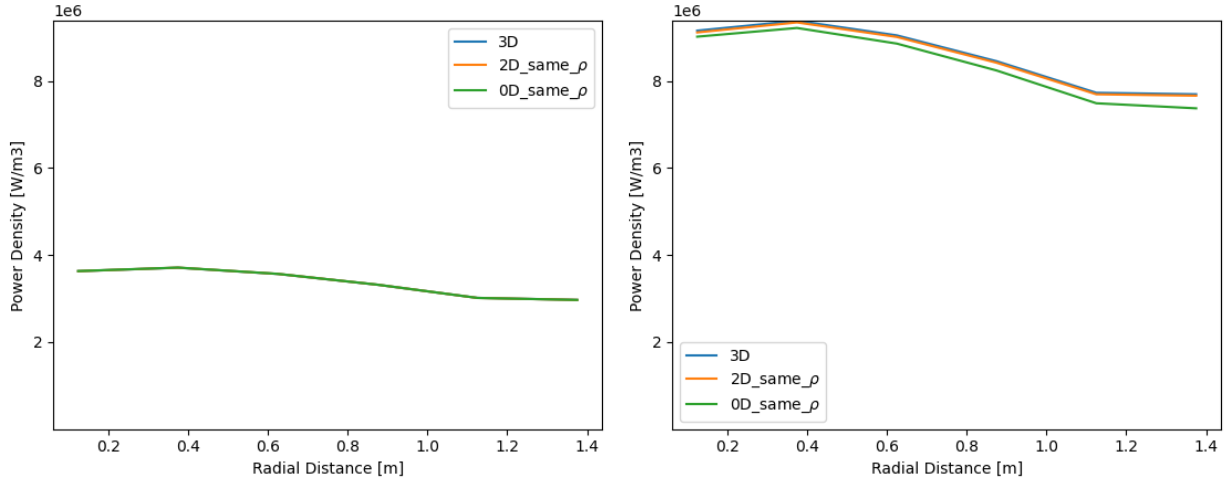

(a) t = 0 s

(b) t = 17 s

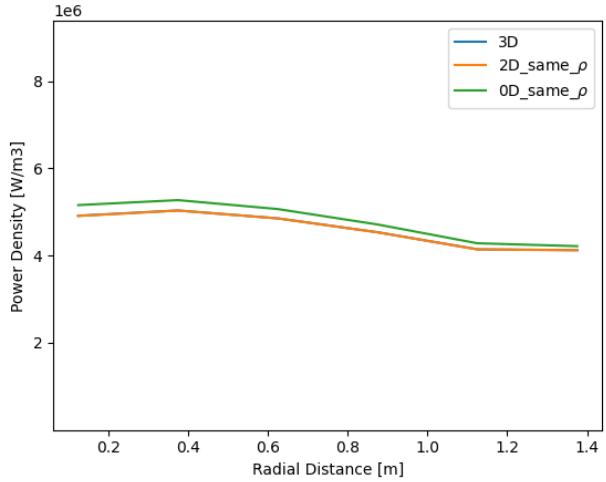

(c) t = 50 s

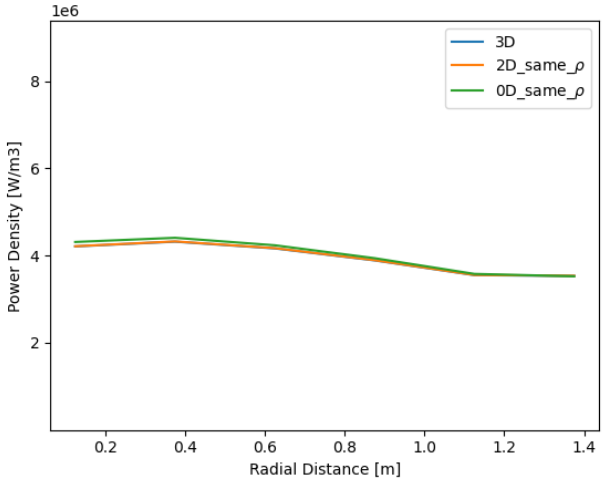

(d) t = 200 s

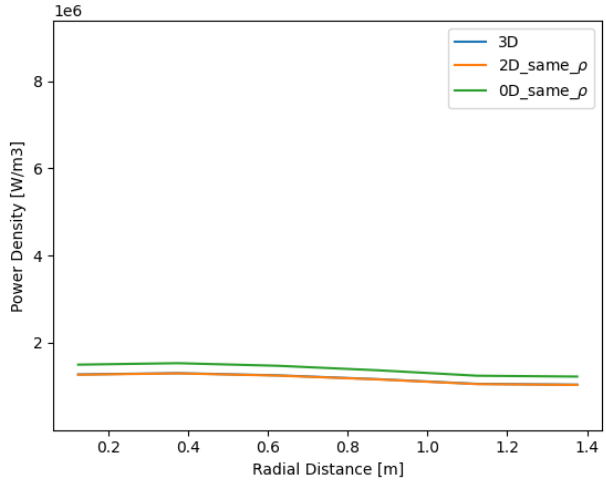

(e) t = 220 s

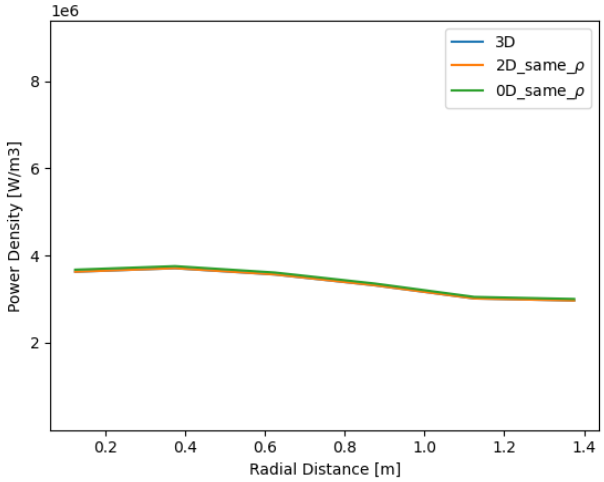

(f) t = 400 s

Figure 120. Axially averaged power density during the delayed supercritical control rod withdrawal.

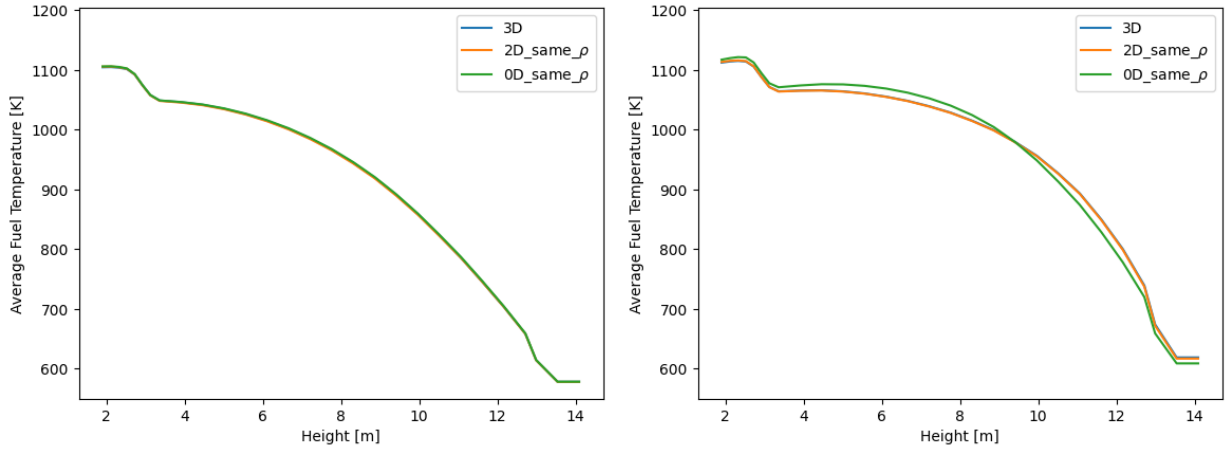

(a) t = 0 s

(b) t = 17 s

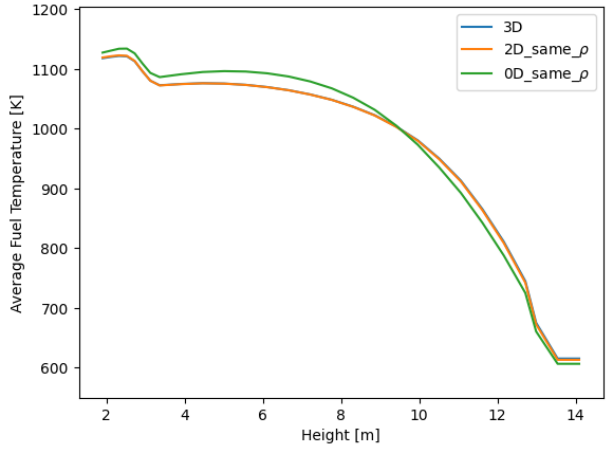

(c) t = 50 s

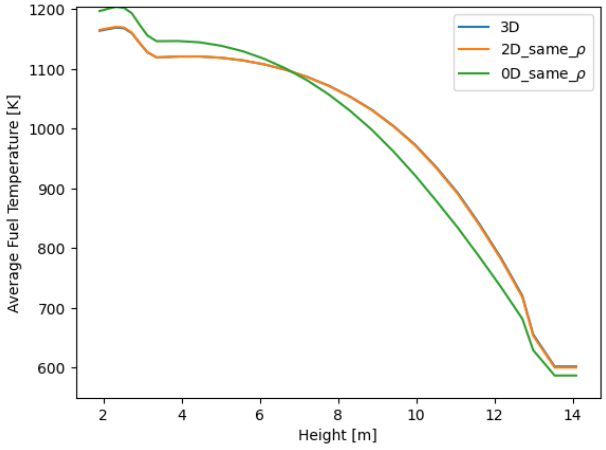

(d) t = 200 s

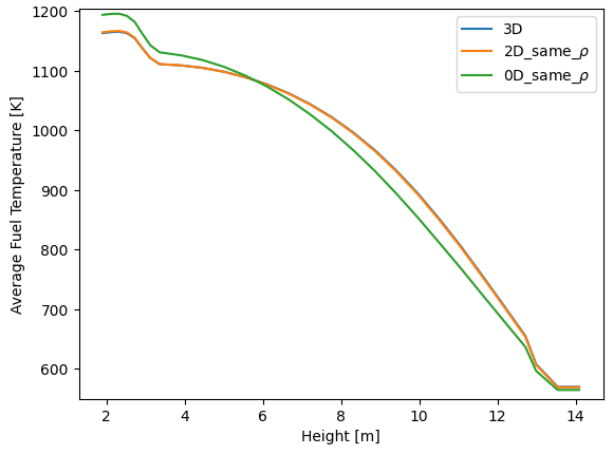

(e) t = 220 s

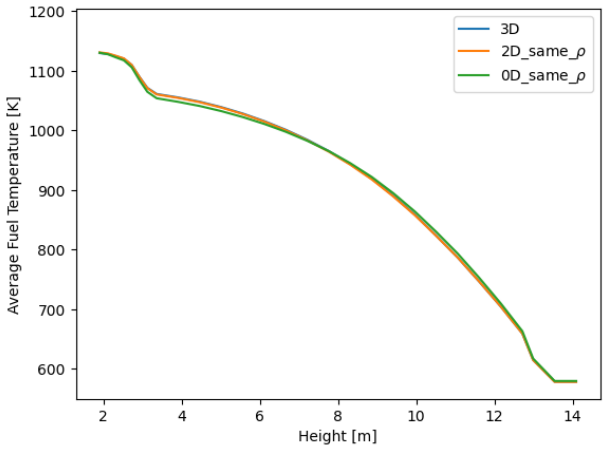

(f) t = 400 s

Figure 121. Radially averaged fuel temperature during the delayed supercritical control rod withdrawal.

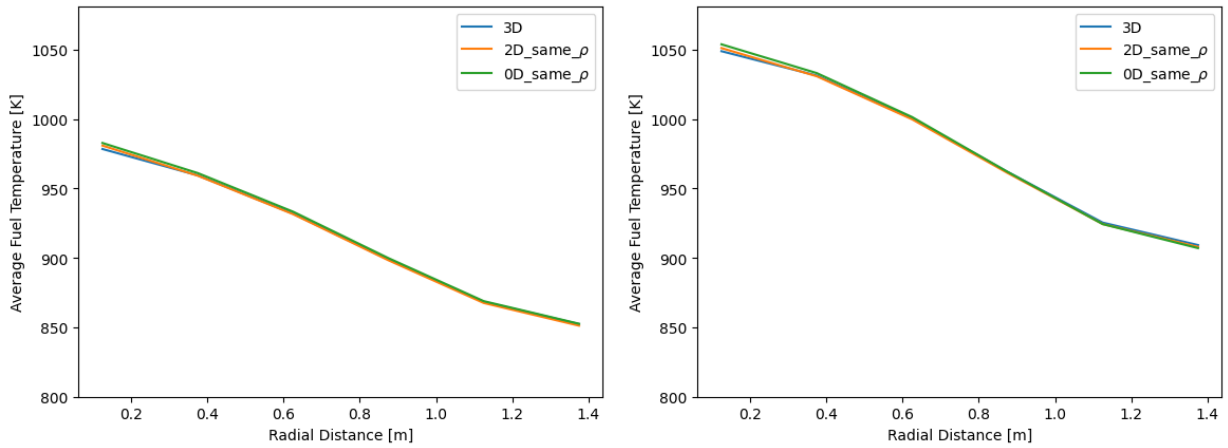

(a) t = 0 s

(b) t = 17 s

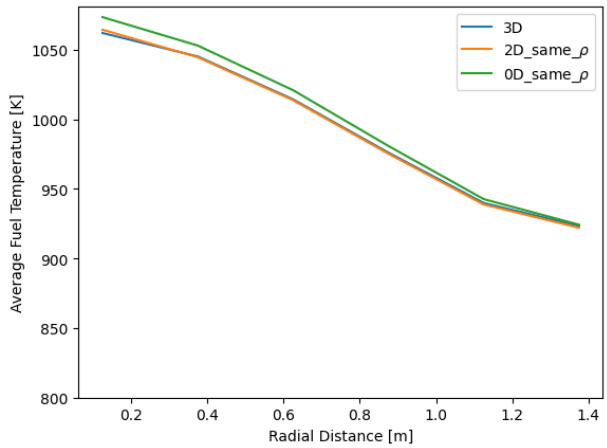

(c) t = 50 s

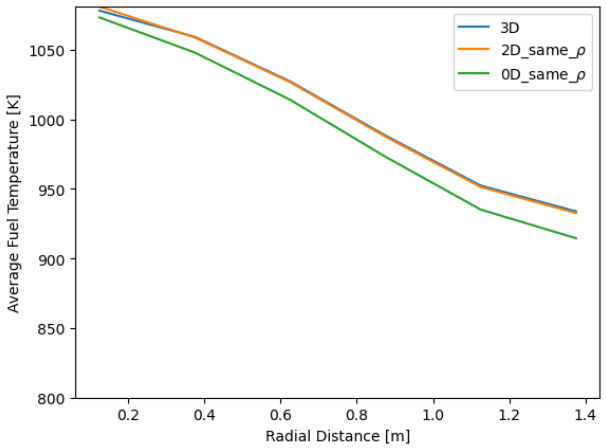

(d) t = 200 s

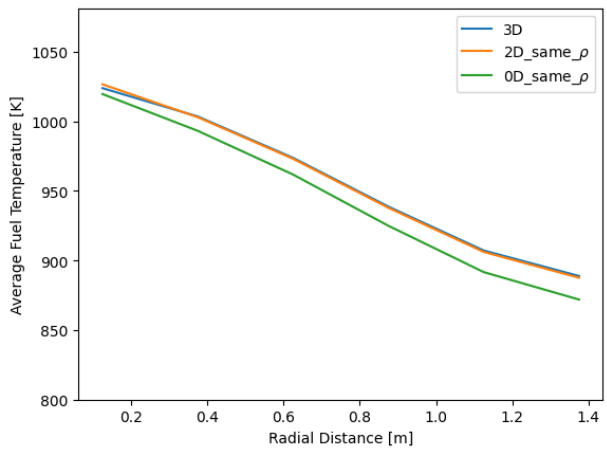

(e) t = 220 s

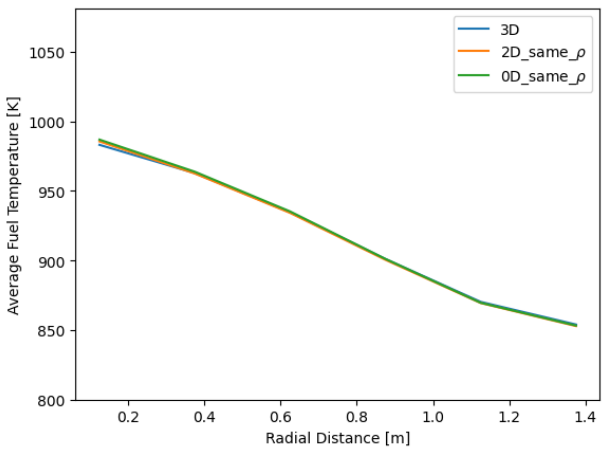

(f) t = 400 s

Figure 122. Axially averaged fuel temperature during the delayed supercritical control rod withdrawal.

3.6.2. 3D Pronghorn/Griffin: Prompt Supercritical

This subsection presents the prompt supercritical RIA via control rod withdrawal with the Pronghorn/Griffin 3D, 2D, and PKE models. Similar to the delayed supercritical RIA, steady-state equilibrium core conditions were established prior to the start of the transient. Then, the prompt supercritical RIA was initiated by moving a single rod from its initial position of 8.575 to 14.111 m in 2 seconds, resulting in an insertion of 1.7$, where it was held in the same position for 188 seconds. At t = 200 seconds, the control rod was moved back to the initial position over 2 seconds. Beyond that, the control rod remained at the same location until the end of the transient simulation. Table 37 provides the sequence of events for the control rod withdrawal scenario. However, due to differences in the 3D and 2D integral control rod worth, a slight difference in the inserted reactivity was observed, and the control rod position was adjusted to 8.08 m instead of 8.575 m in the 2D model to match the reactivity insertion of the 3D model.

Table 37. Sequence of events for the control rod withdrawal event (prompt supercritical).

Time (s)	Event
0.0–10.0	No change in system parameters and the system runs for 10.0 seconds to confirm steady-state conditions are well established with Control Rods 3 and 4 at 8.5745 m and the remaining rods at 13.386 m.
10.0–12.0	Control Rods 3 and 4 are withdrawn from position 8.5745 m to position 14.111 m in 2 seconds.
12.0–200.0	The control rods remain at position 14.111 m.
200.0–202.0	The control rods are reinserted to the initial position in 2 seconds.
202.0–400.0	No change to the system's main parameters. The simulation runs for 400 seconds.

Figure 123 shows the evolutions of the reactor total power, peak power, and reactivity, and the change in control rod position, during the transient for all models. Additionally, Table 38 compares the total power, power peaking, and reactivity peak values obtained from the different models. During the initial 10 seconds of the transient, to verify that the initial steady-state conditions are well established no change is made to the system's main parameters. As the control rod is withdrawn, the reactor power starts increasing and peaks at 1.134 GW after 13.61 seconds due to the induced reactivity from the control rod movement simulated by the 3D model. The power peak increases from approximately 1.79 to 8.65 following the evolution of the reactor power. After that, the thermal feedback dominates, resulting in a power decrease to a level higher than the 250 MW steady-state power by 92 MW at 200 seconds. Once the control rod is reinserted to its initial position, the power starts decreasing due to the negative reactivity insertion by the control rod, and it starts increasing again as the positive feedback of the fuel and moderator cooling down begins to dominate. Around 360 seconds into the transient, the reactor total power returns to its initial steady-state value.

Comparing the 2D solutions to the 3D reference solution, the 2D model with the same control rod movement resulted in less reactivity insertion and, as a result, lower peak power (-8.80%), while the 2D model with corrected reactivity insertion shows an excellent match with the 3D power solution (-1.31%). The corrected reactivity was estimated from two static eigenvalue calculations of the 3D model with initial and final control rod positions. Knowing the correct static reactivity of the control rod resulted in very close dynamic reactivities for the 3D and 2D models. The 2D model with the same control rod movements resulted in a reactivity that is 0.04$ lower, while the same static reactivity is almost the same as that of the reference.

Comparing the PKE solutions to the 3D reference solution, the PKE model with the same control rod movement, using control rod integral worth obtained from 3D static calculations, shows a significant increase in total power (28.70%), while the PKE model with corrected reactivity insertion shows a better match with the 3D power solution, with a relative error of -0.08%. In terms of reactivity, the PKE model with the same

control rod movement significantly overestimated the reactivity by 0.1$, while the reactivity predicted by the PKE model with the same reactivity insertion is 0.02$ lower. There is a significant difference between the reactivity inserted by the two models of 0.12$, which is mainly due to not considering the impact of spectral changes on the thermal feedback effects while calculating the control rod worth. Figure 124 shows the reactivity components of the control rod, fuel, moderator, and reflector along with total reactivity obtained from the linear summation of all the reactivity components for both PKE models. The predicted control rod reactivity component with the PKE model with the same control rod movement is about 2.2$, while the model with corrected reactivity shows 1.7$. Both models resulted in very similar reactivity evolutions for the thermal feedback components but with different magnitudes, which caused different total reactivity insertions.

Table 38. Peak power and reactivity of the prompt supercritical RIA simulated with Pronghorn/Griffin.

Model	Power (GW)	Diff. (%)	Time to Peak (s)	Power Peak	Diff. (%)	Time to Peak (s)	Reactivity ($)	Diff. ($)	Time to Peak (s)
3D	1.134	–	13.10	8.65	–	12.90	0.850	–	11.30
2D Same CR	1.034	-8.80	13.20	7.88	-9.01	13.00	0.814	-0.04	11.30
2D Same ρ	1.119	-1.31	13.10	8.46	-2.24	12.90	0.850	0.00	11.30
PKE Same CR	1.459	28.70	13.00	10.36	19.69	13.00	0.949	0.10	11.34
PKE Same ρ	1.133	-0.08	13.87	8.04	-7.08	13.87	0.830	-0.02	11.45

Figure 125 shows the evolutions of the fuel and moderator average and maximum temperatures during the transient for all models. Table 39 compares the average and maximum fuel, moderator, and reflector peak values obtained from different models. As the power starts increasing, the fuel and moderator temperatures increase sharply and then at a much slower rate as the power starts dropping to a new steady-state level. Once the control rods are reinserted, the temperature decreases significantly to a value lower than its steady-state level and starts increasing again until it returns to the steady-state level. The peak average and maximum fuel temperatures obtained from the 3D model are 1056.5 and 1352.2 K, respectively.

Comparing the 2D solutions to the 3D reference solution, the 2D model with the same control rod movement results in a lower temperature increase and peaks at 1038.7 and 1328.5 K for average and maximum fuel temperatures, respectively, while the 2D model with the same reactivity insertion shows an excellent match with the 3D solution for both the average and maximum temperatures, peaking at 1056.1 and 1354.5 K, respectively. However, the PKE model shows a very different average temperature evolution for both fuel and moderator, and it shows a similar maximum temperature evolution but with different magnitudes. The PKE model with the same control rod movement peaks at 1090.0 and 1501.4 K for average and maximum fuel temperatures, respectively, and the PKE model with the same reactivity insertion peaks at 1043.6 and 1419.7 K for average and maximum fuel temperatures, which are much closer to the reference solution results.

Figures 126 and 127 compare the profiles of the averaged power density in the radial and axial directions of the 3D and reactivity-corrected 2D and PKE models at different time points. Both the 3D and 2D models show very similar power shapes averaged radially and axially, while significant differences in shape and magnitude are observed during the transient, except for the beginning and end of the transient. This is mainly due to the reduced-order model of the PKE not capturing the local perturbation effect of moving the control rod.

Figures 128 and 129 compare the profiles of the averaged fuel temperature in the radial and axial directions of the 3D and reactivity-corrected 2D and PKE models at different time points. Both the 3D and 2D models show very similar temperature profiles averaged radially and axially, while significant differences in shape and magnitude are observed during the transient, except for the beginning and end of the transient. This is

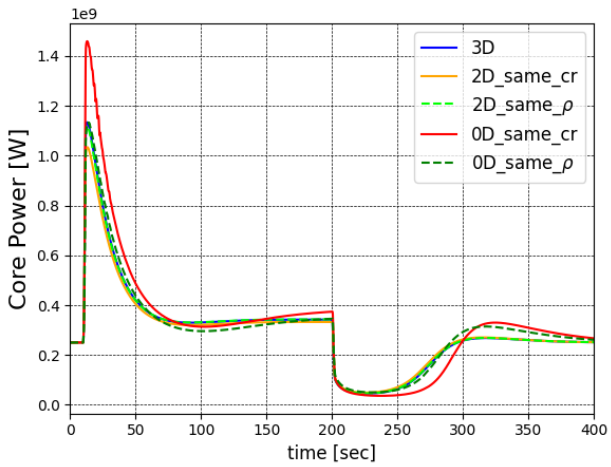

(a) Total Power

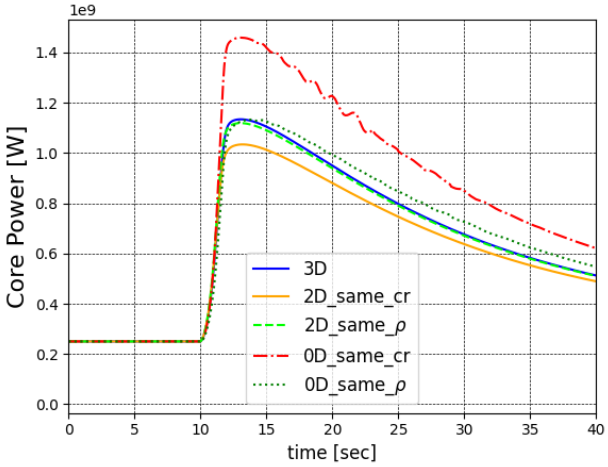

(b) Total Power First 40 Seconds

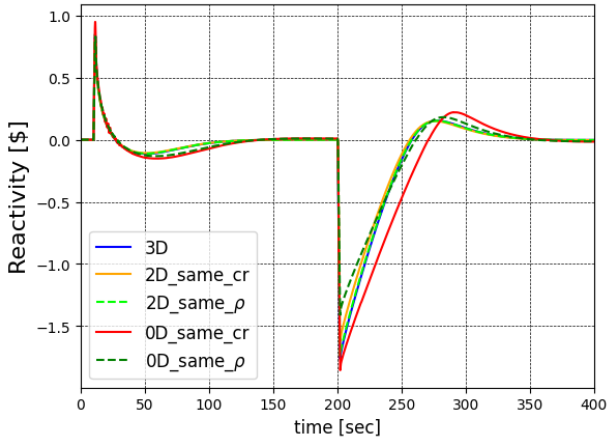

(c) Reactivity

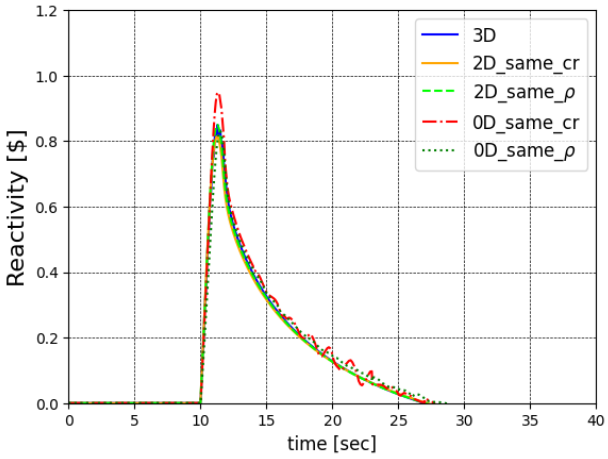

(d) Reactivity First 40 Seconds

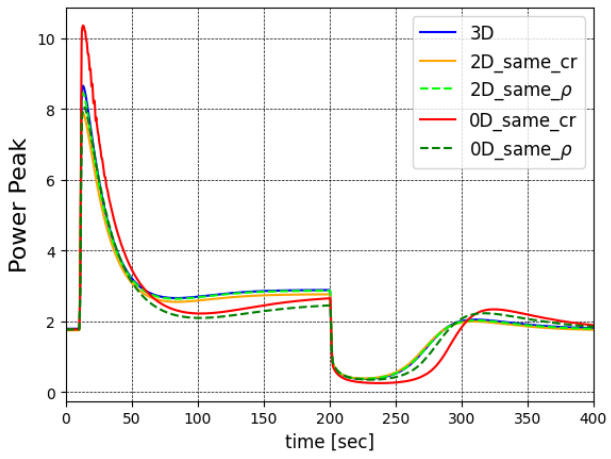

(e) Power Peaking

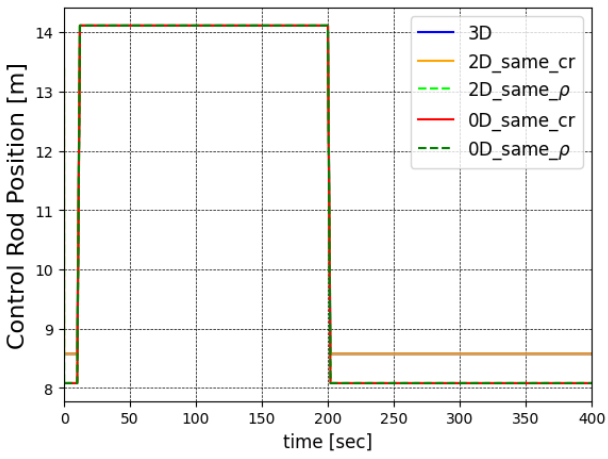

(f) Control Rod Position

Figure 123. Total power, peak power, reactivity, and control rod position evolution during the prompt supercritical control rod withdrawal.

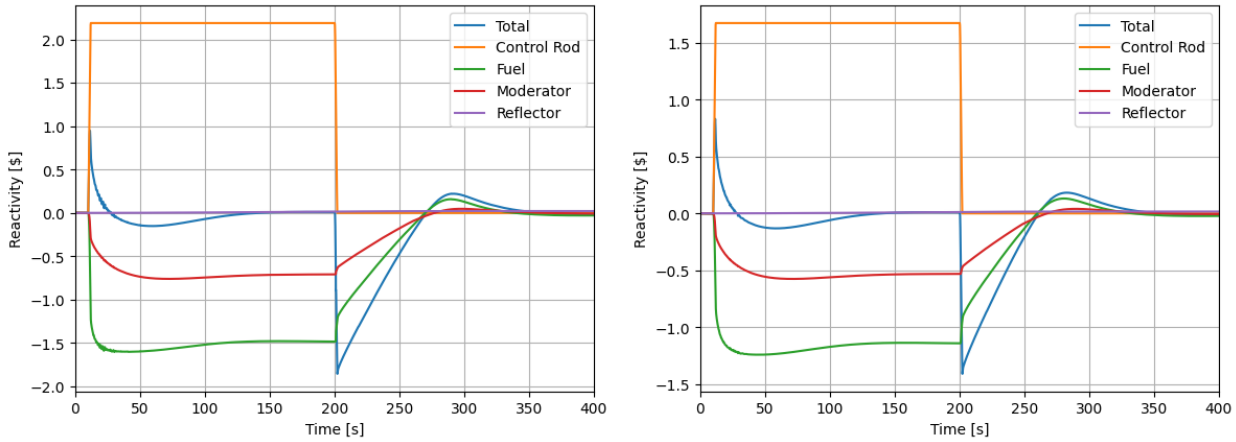

(a) Nominal (b) Corrected

Figure 124. PKE model reactivity component evolution during the prompt supercritical control rod withdrawal.

Table 39. Peak temperatures of the prompt supercritical RIA simulated with Pronghorn/Griffin.

Model	Fuel		Moderator		Reflector	
	Avg.	Max.	Avg.	Max.	Avg.	Max.
3D	1056.5	1352.2	1035.8	1328.7	596.6	1152.8
2D Same CR	1038.7	1328.5	1018.8	1306.2	596.3	1138.1
2D Same ρ	1056.1	1354.5	1035.3	1330.9	596.8	1145.5
PKE Same CR	1090.0	1501.4	1062.2	1467.2	598.3	1179.7
PKE Same ρ	1043.6	1419.7	1019.0	1390.9	597.1	1159.2

mainly due to the reduced-order model of the PKE not capturing the local perturbation effect of moving the control rod.

Detailed visualizations of the distributions of the main field variables, obtained from the 3D and reactivity-corrected 2D and PKE models at different time points during the transient, are provided in Figures 130 (thermal neutron flux), 131 (power density), 132 (peak power), 133 (average fuel temperature), 134 (maximum fuel temperature), and 135 (solid temperature). Except for Figure 130, all figures show the steady-state distribution in the leftmost subfigure, while the subfigures next to it show the relative change (ratio) for power density and peak power, and the relative difference for fuel and solid temperatures. These figures provide a visual aid for capturing local perturbations using high- and low-fidelity models.

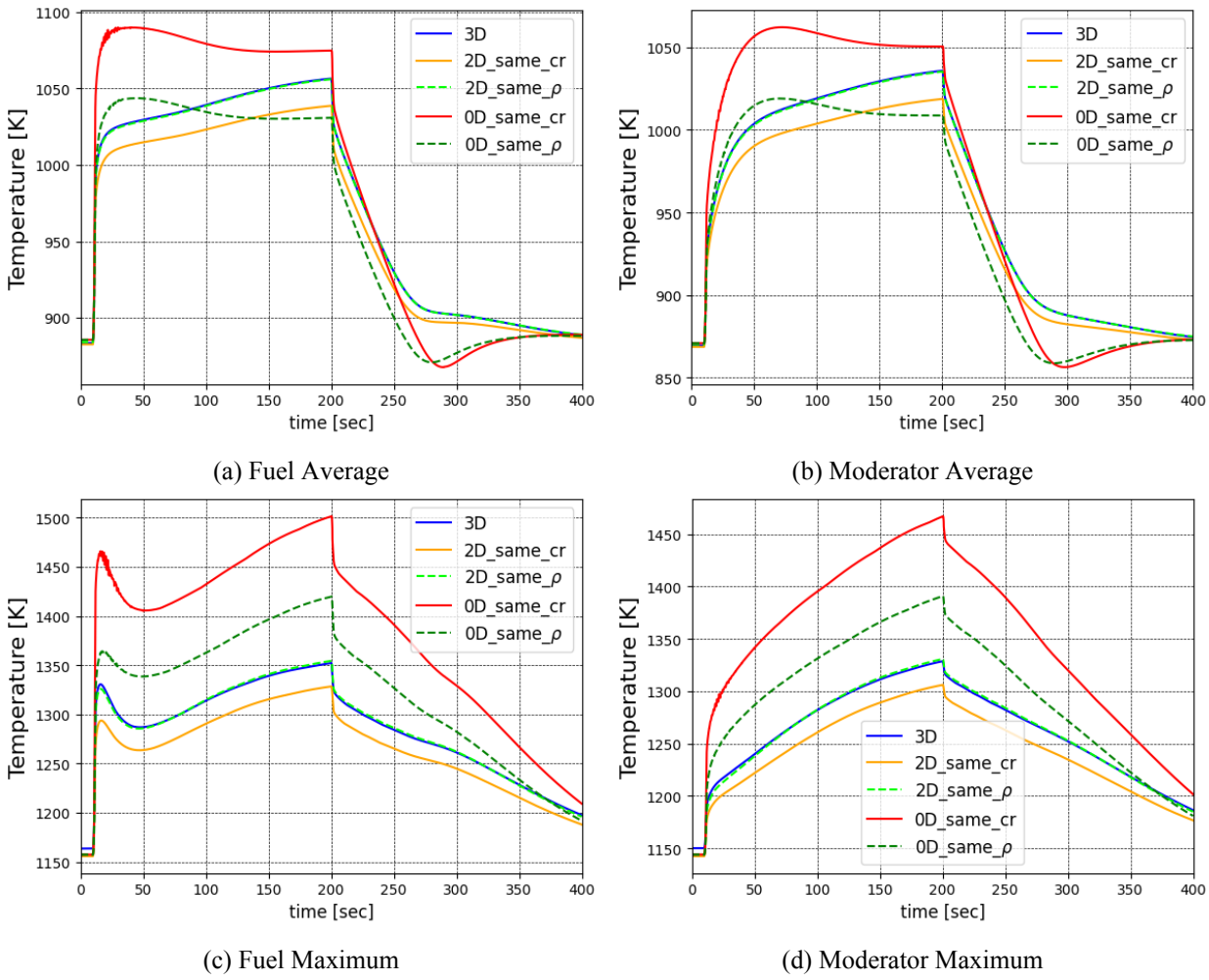

(a) Fuel Average

(b) Moderator Average

(c) Fuel Maximum

(d) Moderator Maximum

Figure 125. Fuel and moderator temperature evolution during the prompt supercritical control rod withdrawal.

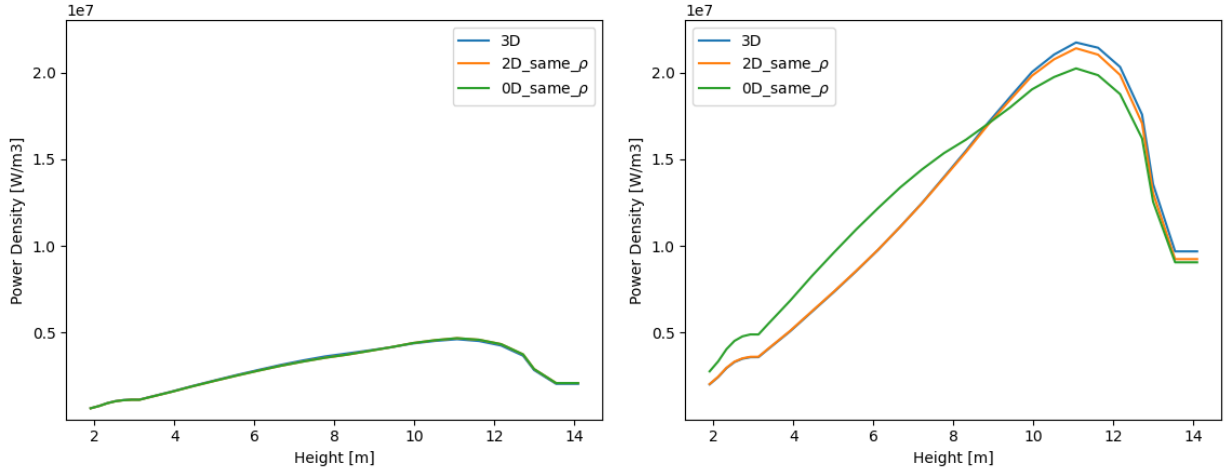

(a) t = 0 s

(b) t = 17 s

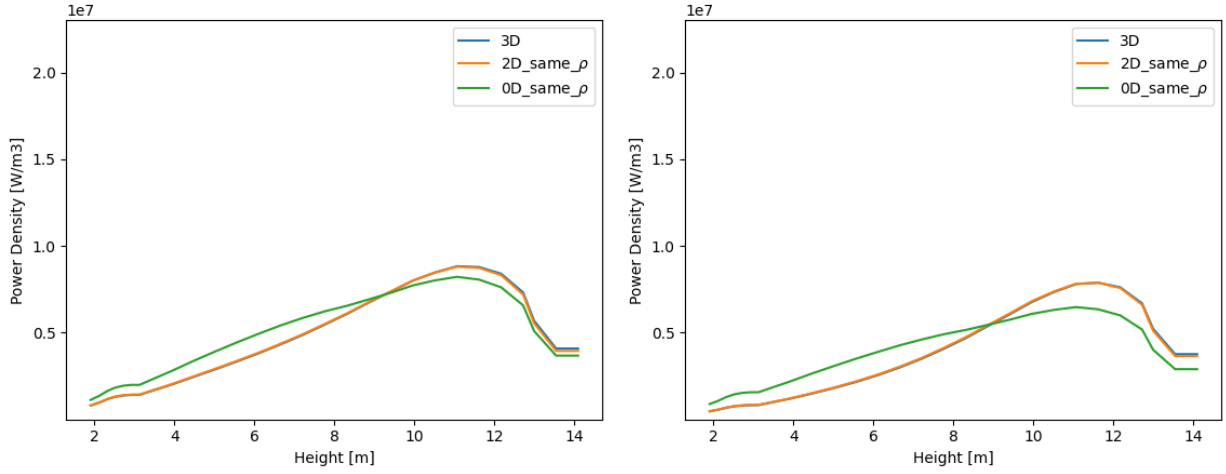

(c) t = 50 s

(d) t = 200 s

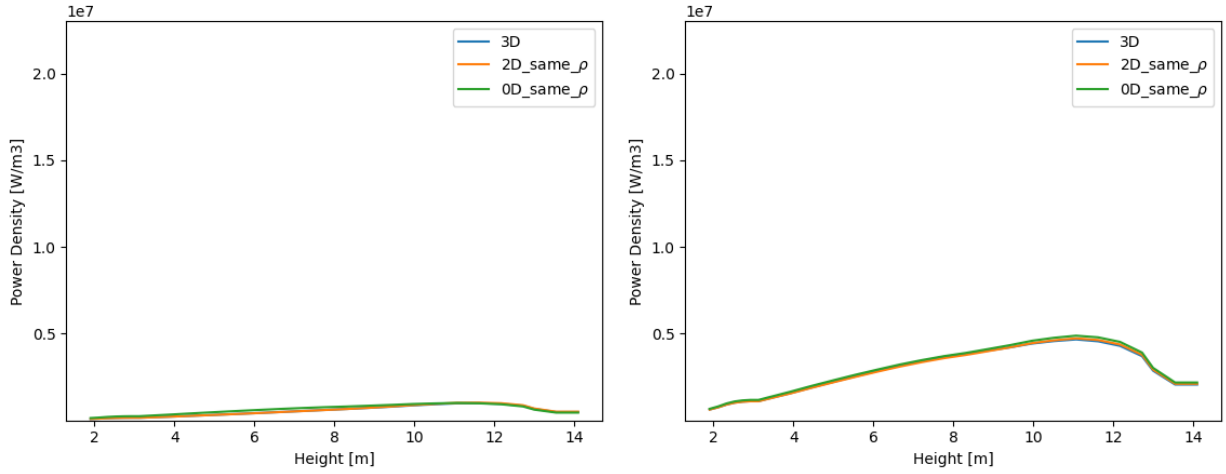

(e) t = 220 s

(f) t = 400 s

Figure 126. Radially averaged power density during the prompt supercritical control rod withdrawal.

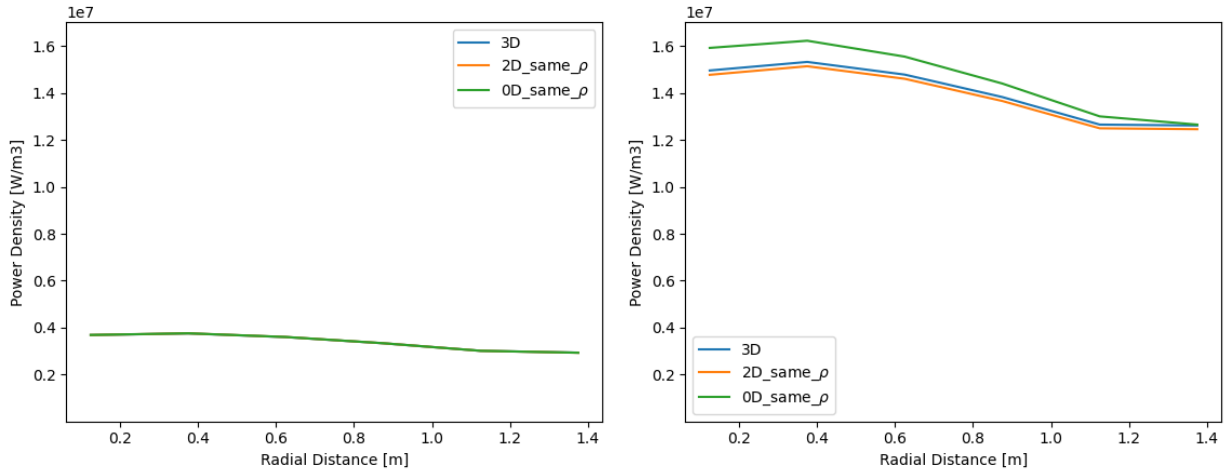

(a) t = 0 s

(b) t = 17 s

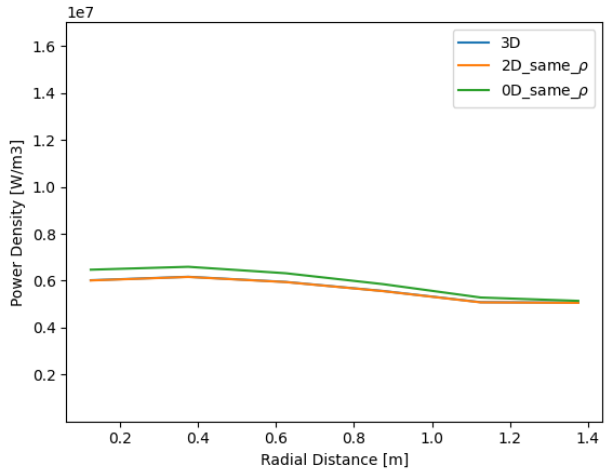

(c) t = 50 s

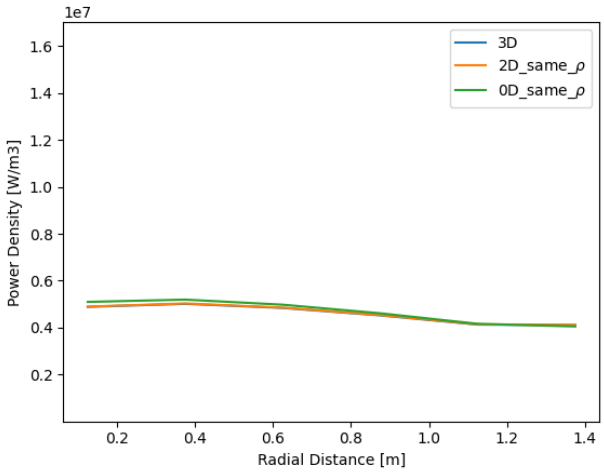

(d) t = 200 s

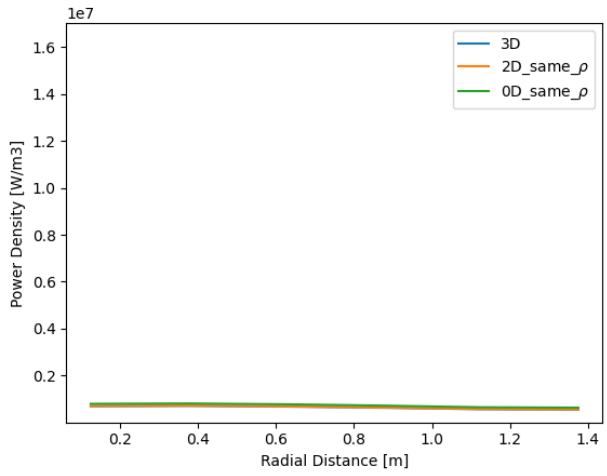

(e) t = 220 s

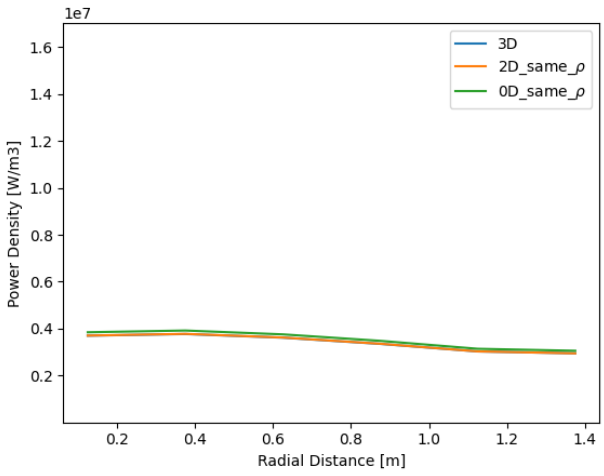

(f) t = 400 s

Figure 127. Axially averaged power density during the prompt supercritical control rod withdrawal.

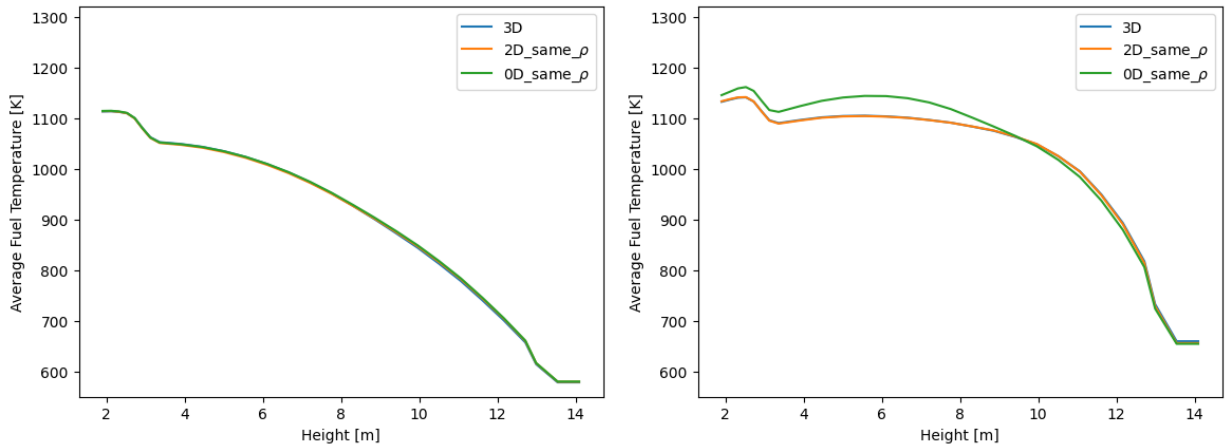

(a) t = 0 s

(b) t = 17 s

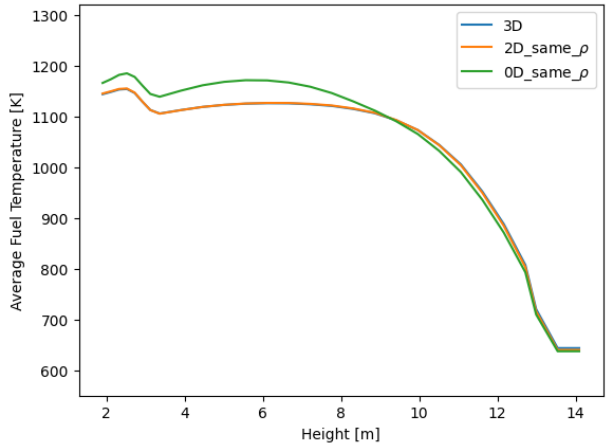

(c) t = 50 s

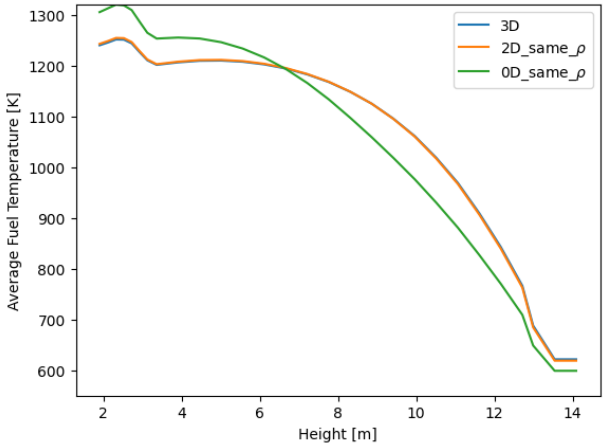

(d) t = 200 s

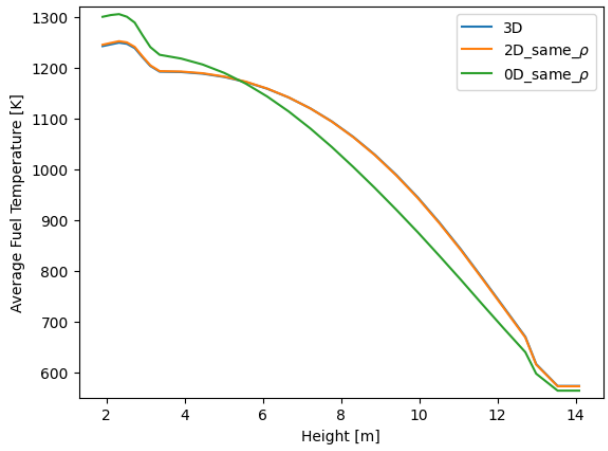

(e) t = 220 s

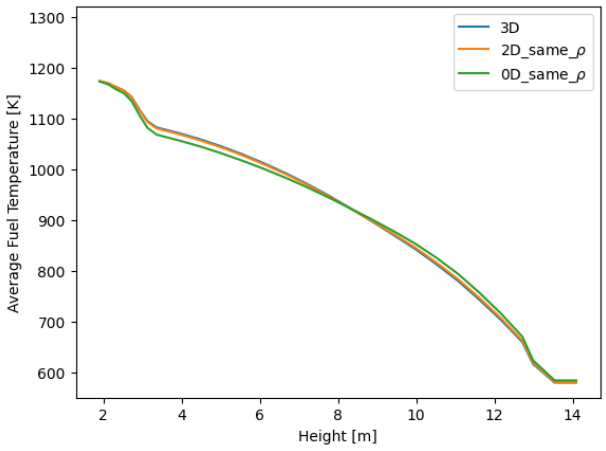

(f) t = 400 s

Figure 128. Radially averaged fuel temperature during the prompt supercritical control rod withdrawal.

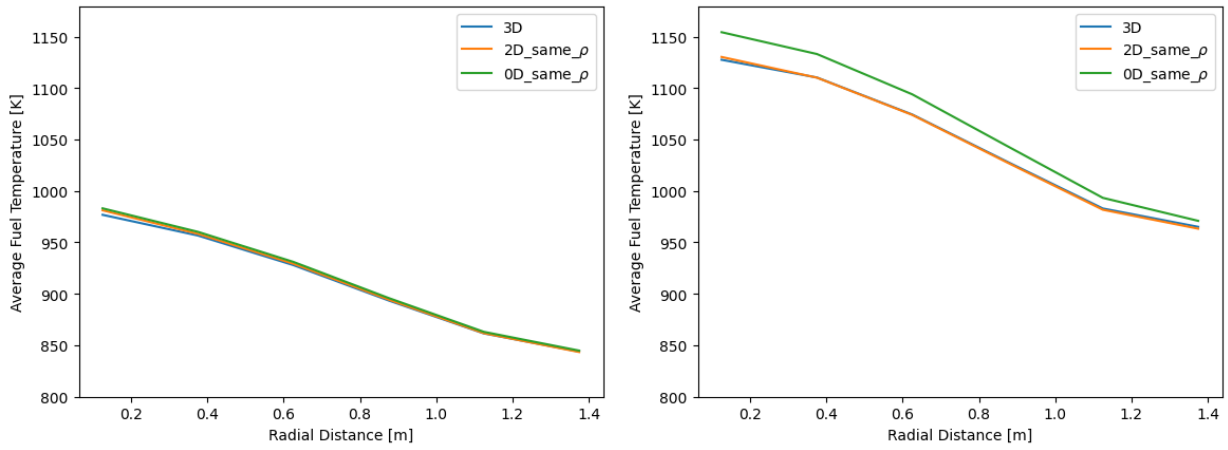

(a) t = 0 s

(b) t = 17 s

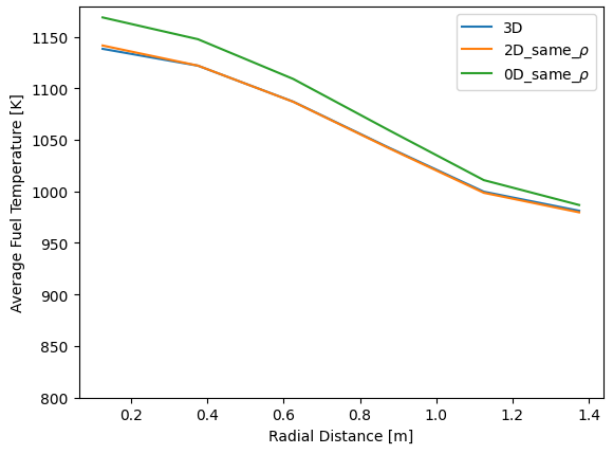

(c) t = 50 s

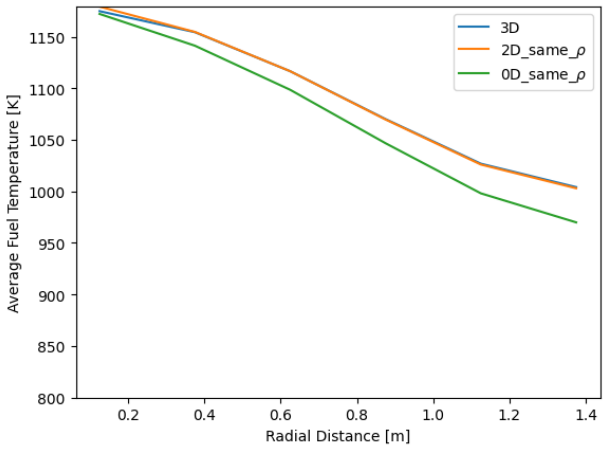

(d) t = 200 s

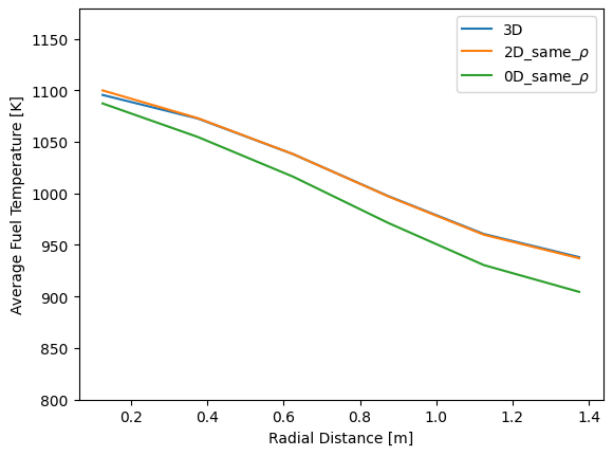

(e) t = 220 s

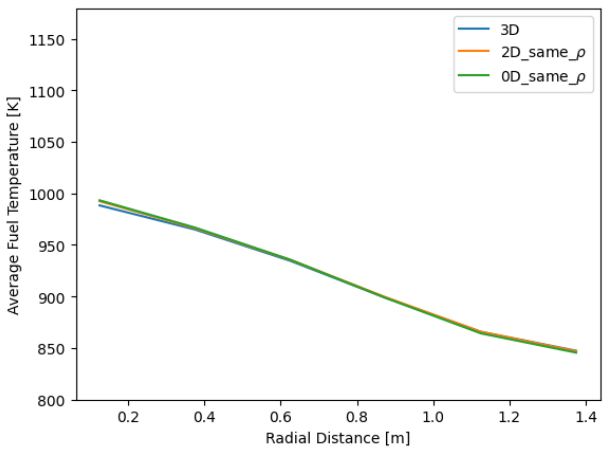

(f) t = 400 s

Figure 129. Axially averaged fuel temperature during the prompt supercritical control rod withdrawal.

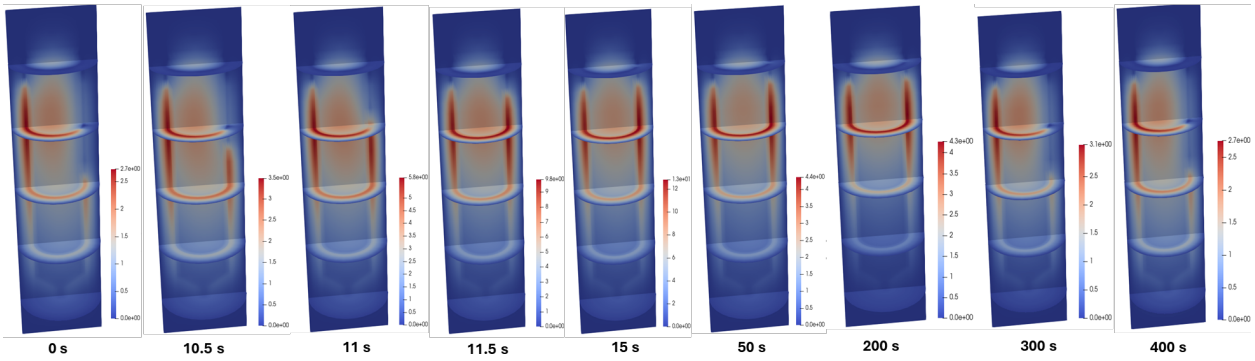

(a) 3D

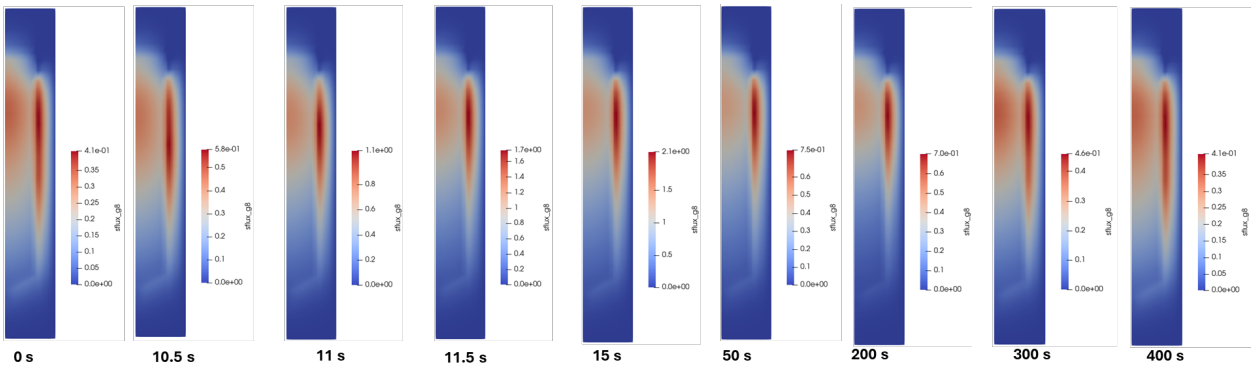

(b) 2D

Figure 130. Thermal neutron flux distribution during the prompt supercritical control rod withdrawal.

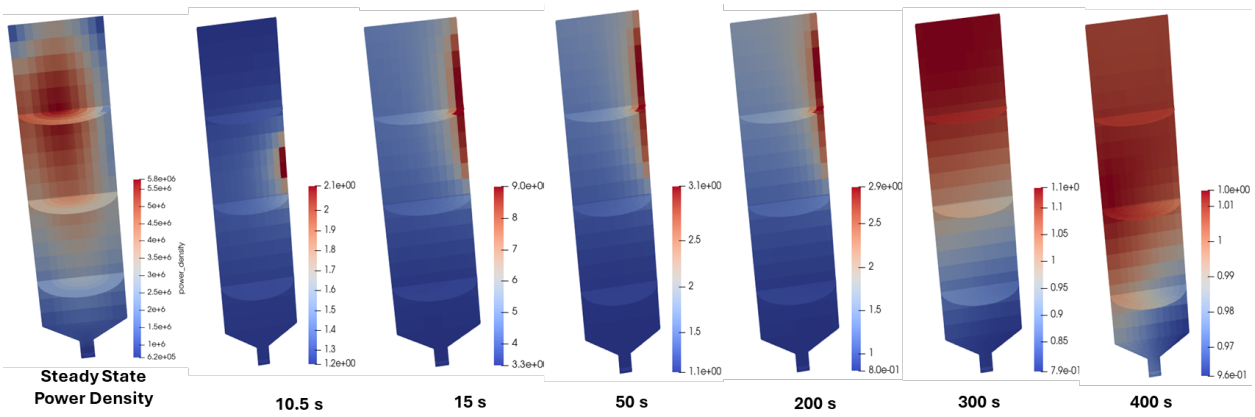

(a) 3D

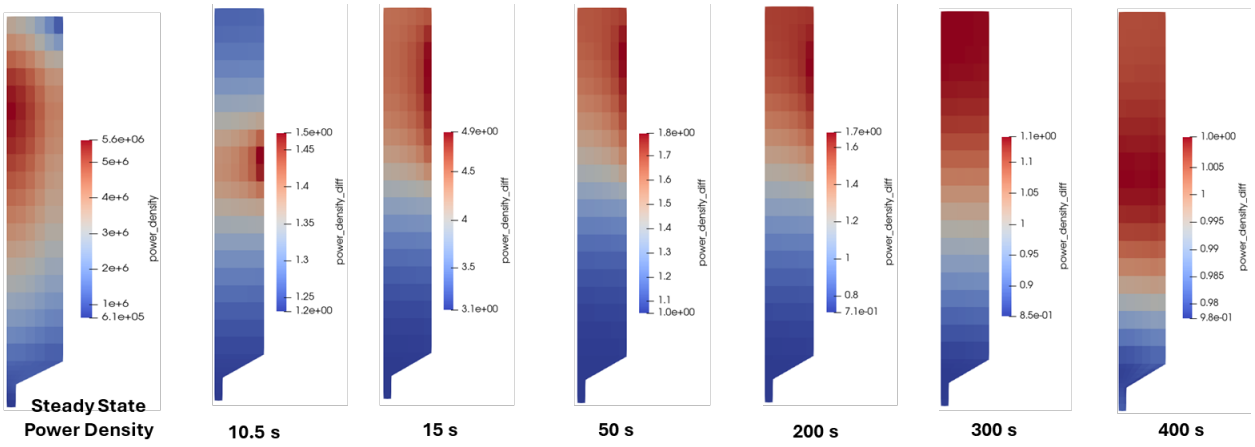

(b) 2D

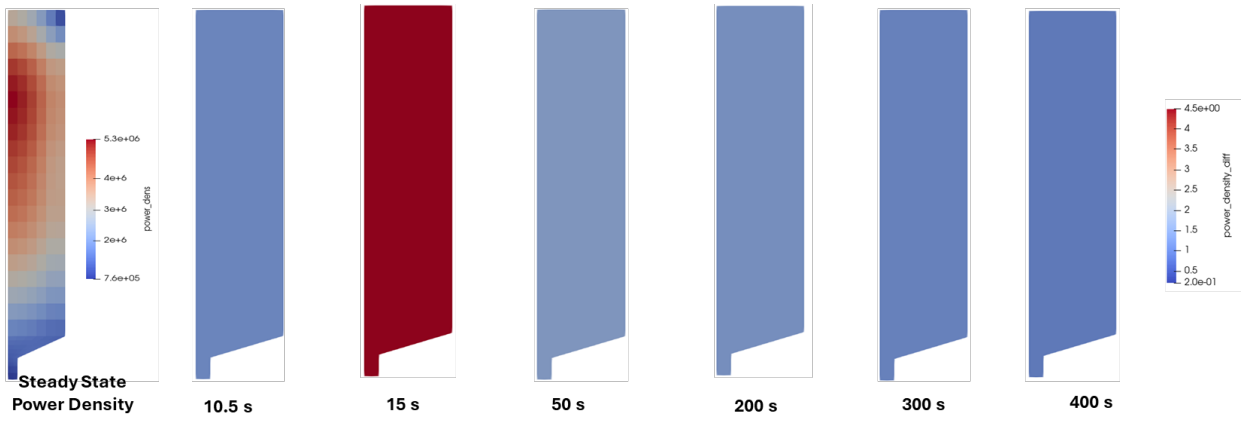

(c) 0D/PKE

Figure 131. Power density distribution and ratio relative to steady-state power density during the prompt supercritical control rod withdrawal.

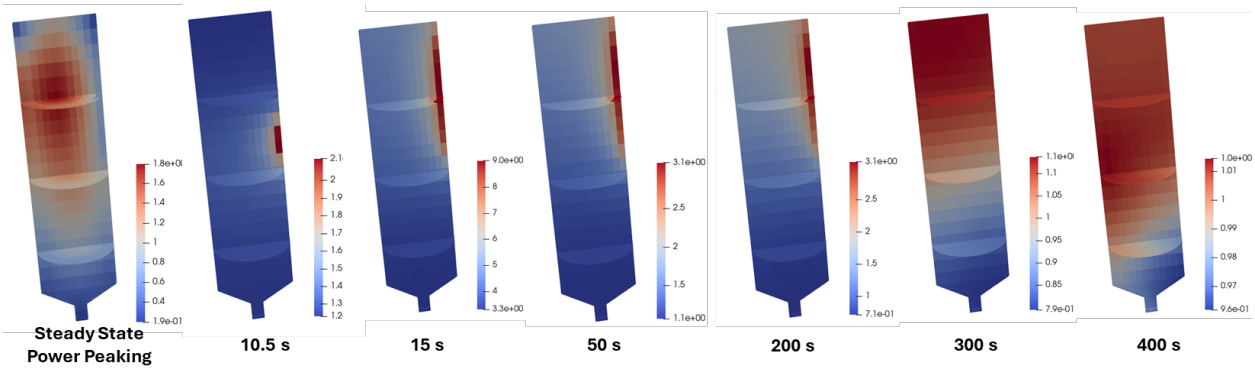

(a) 3D

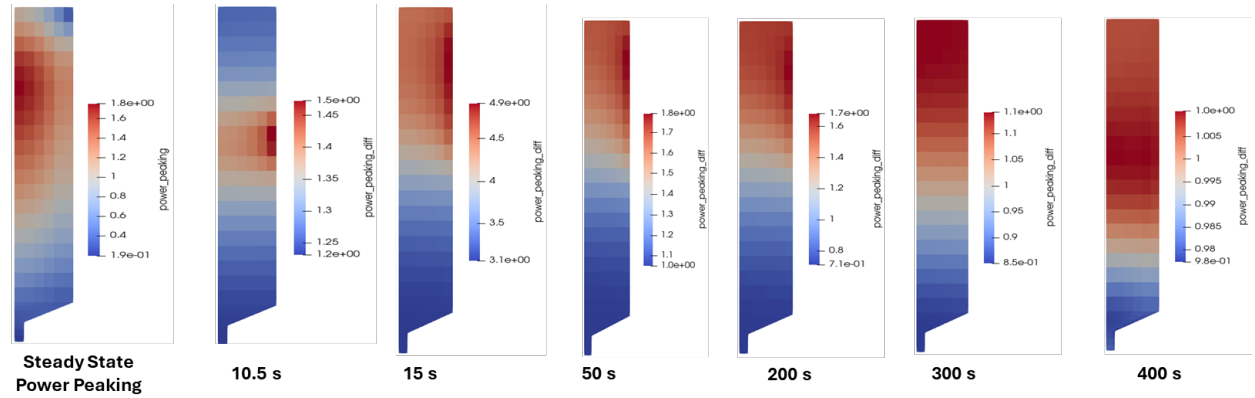

(b) 2D

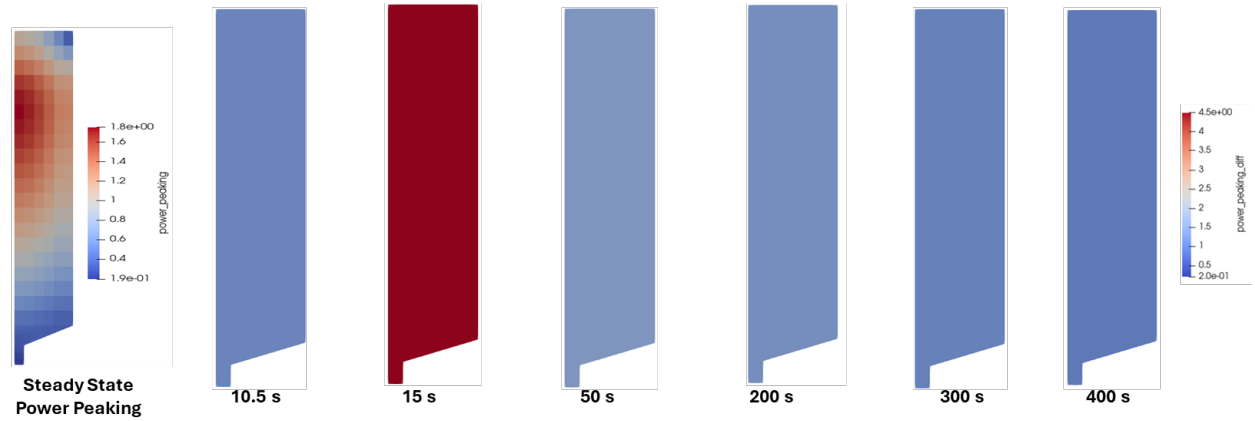

(c) 0D/PKE

Figure 132. Peak power distribution and ratio relative to steady-state peak power during the prompt supercritical control rod withdrawal.

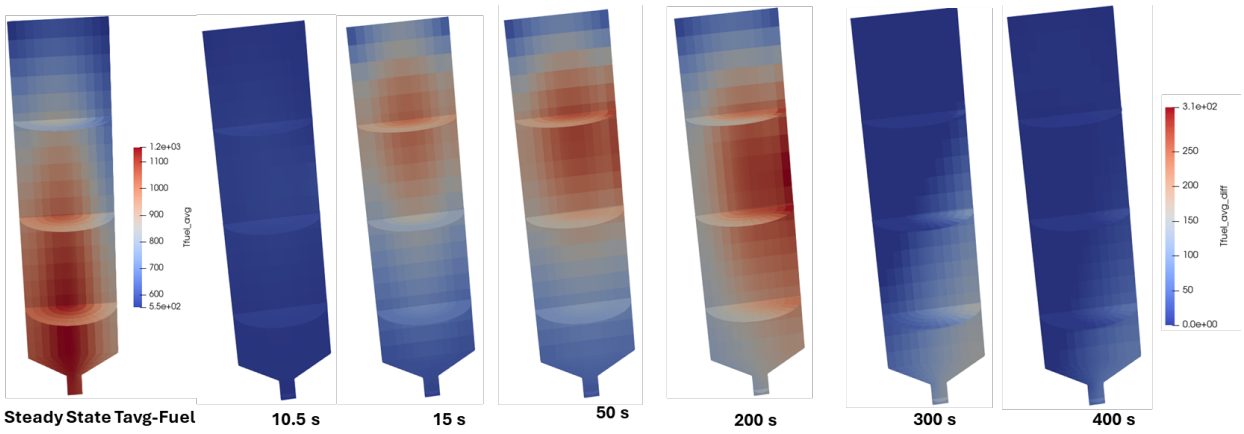

(a) 3D

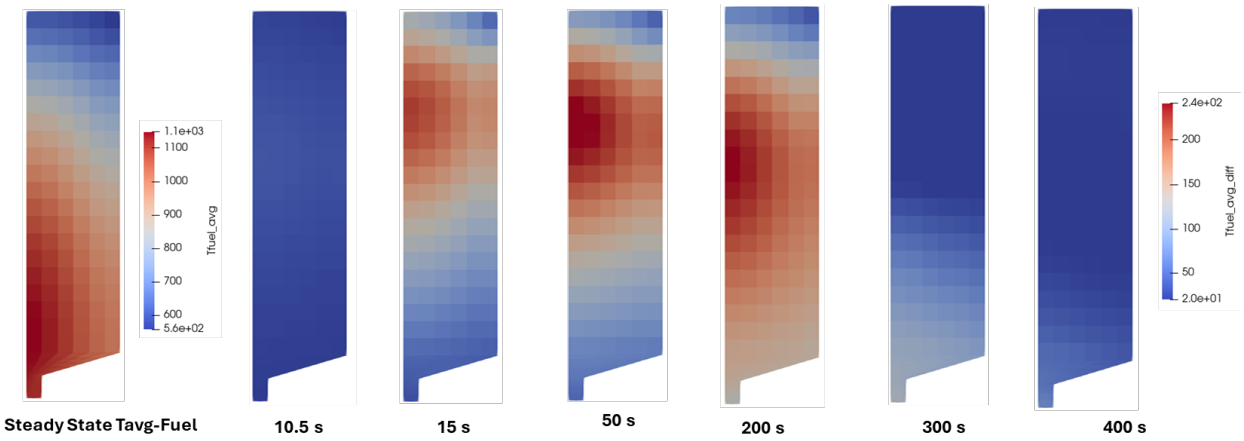

(b) 2D

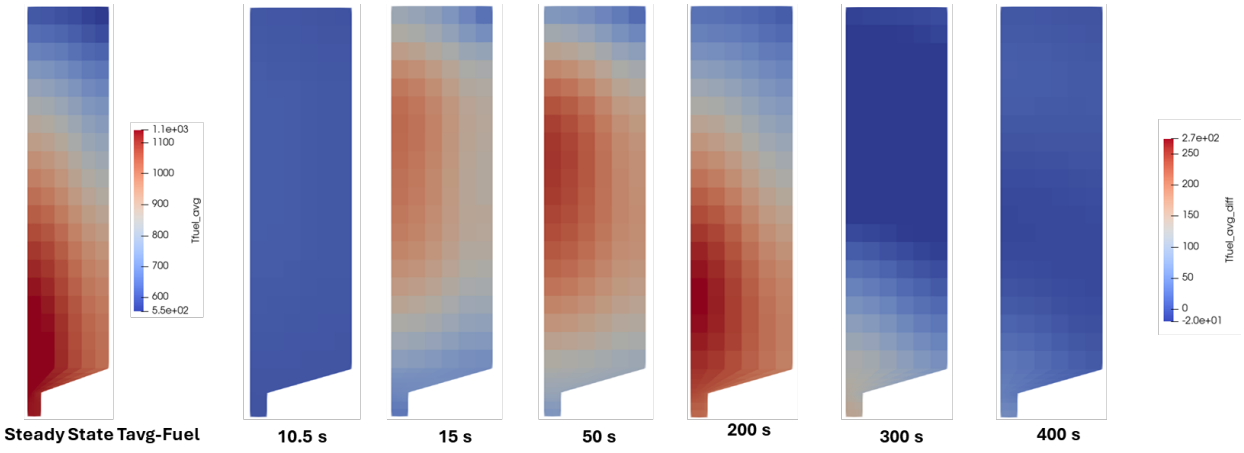

(c) 0D/PKE

Figure 133. Average fuel temperature distribution and its change relative to steady-state average fuel temperature during the prompt supercritical control rod withdrawal.

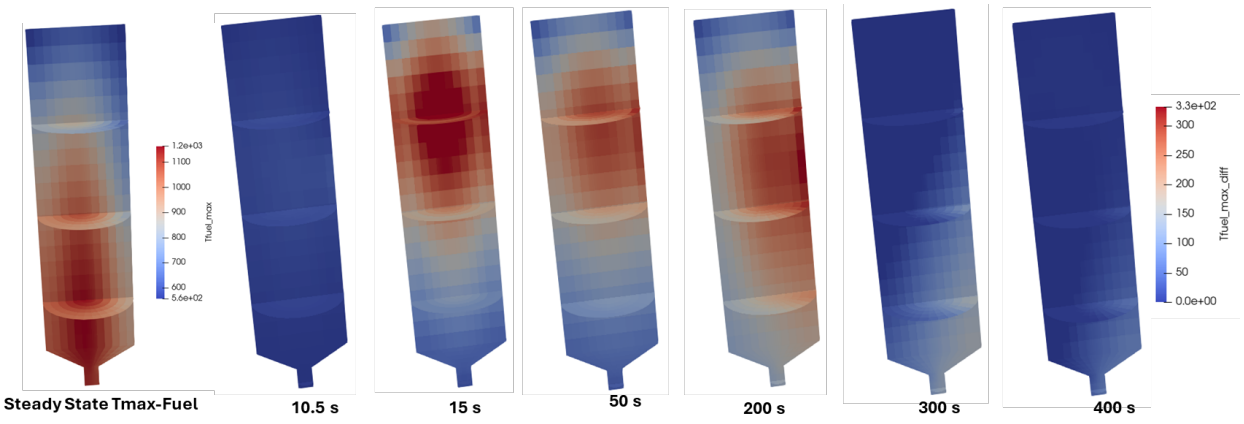

(a) 3D

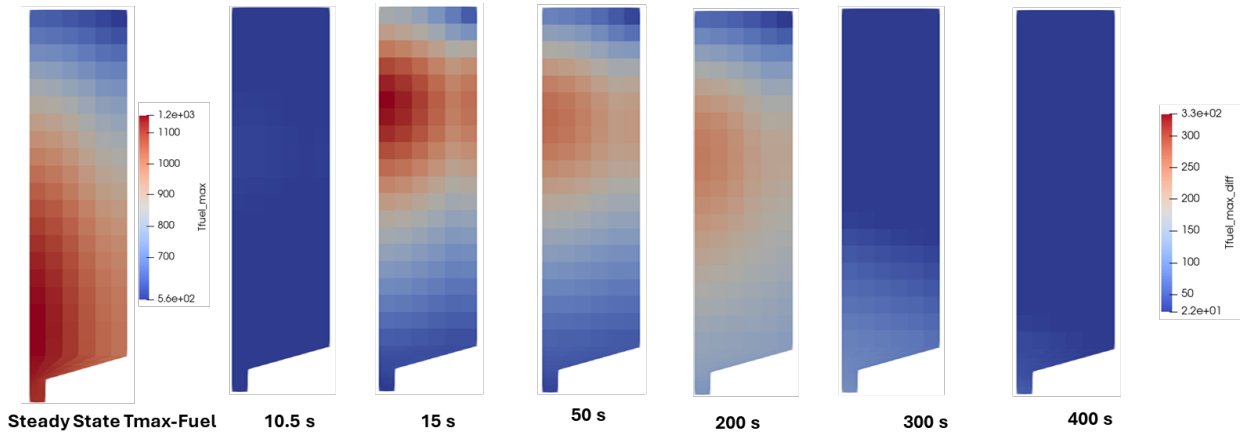

(b) 2D

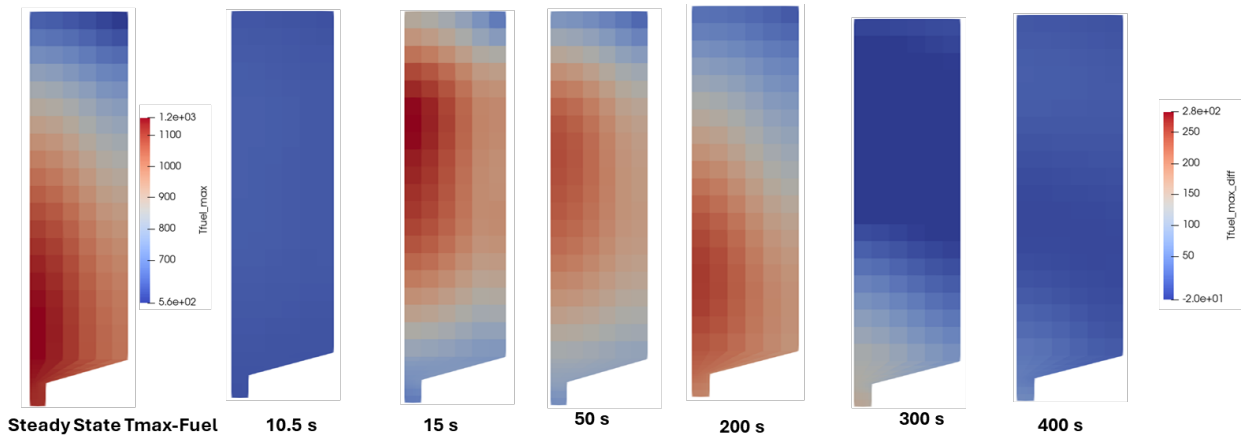

(c) 0D/PKE

Figure 134. Maximum fuel temperature distribution and its change relative to steady-state maximum fuel temperature during the prompt supercritical control rod withdrawal.

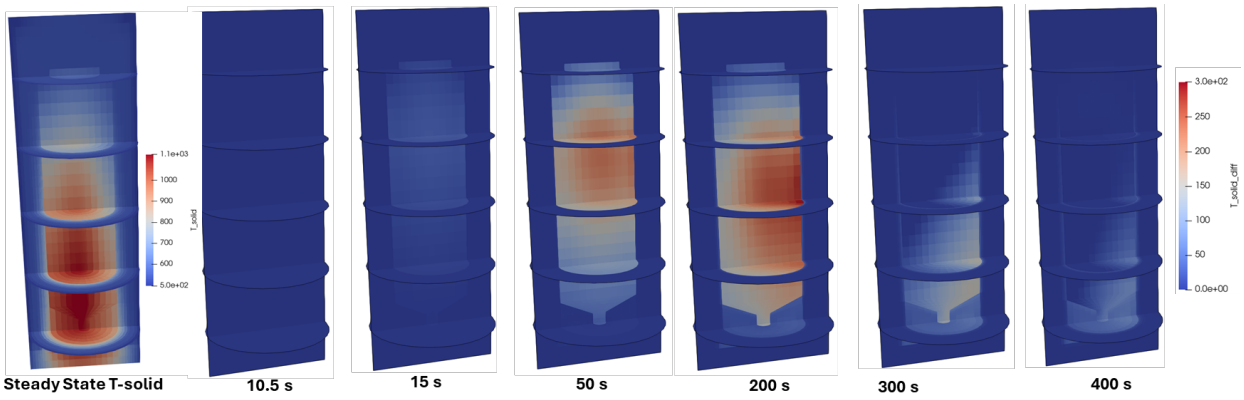

(a) 3D

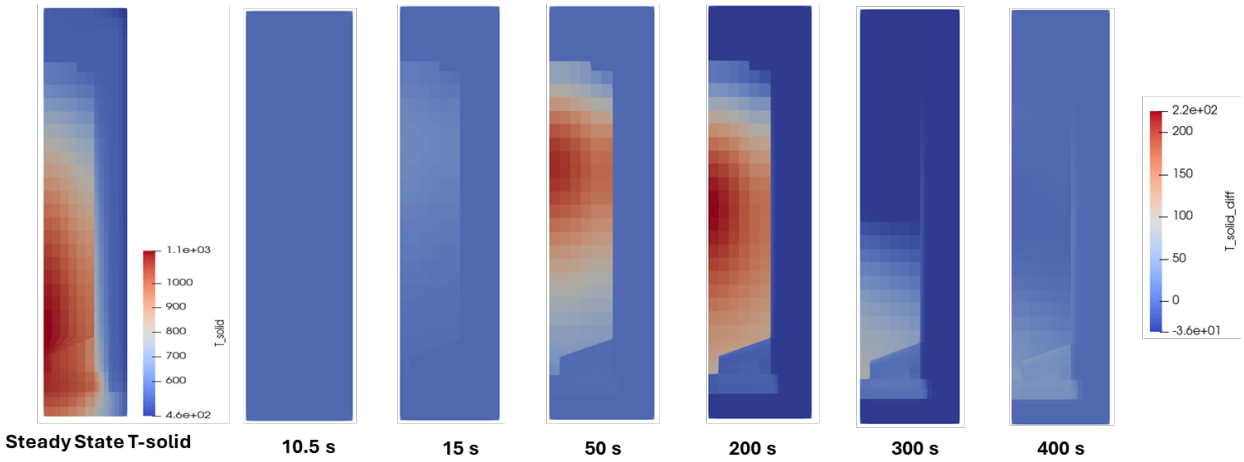

(b) 2D

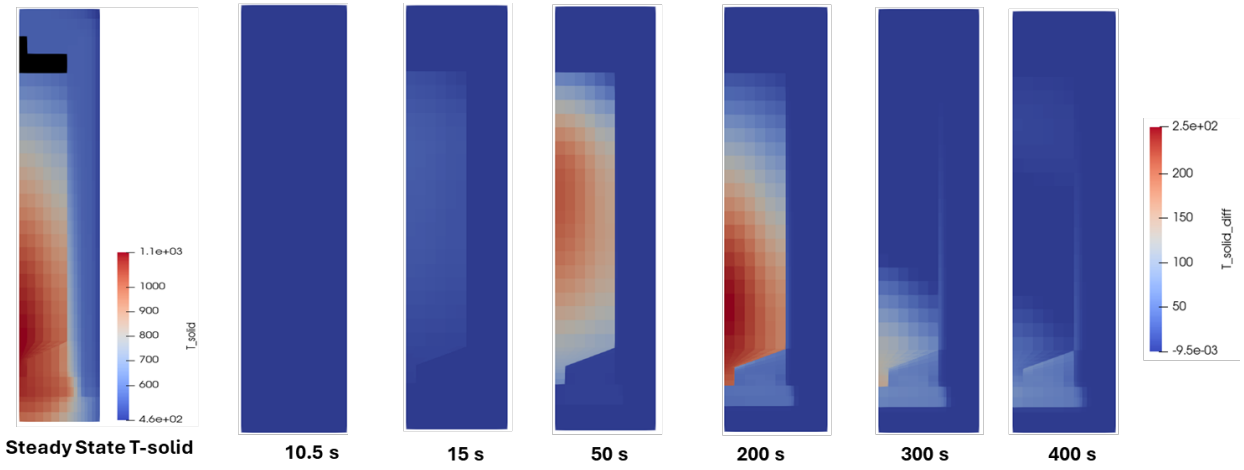

(c) 0D/PKE

Figure 135. Solid temperature distribution and its change relative to steady-state solid temperature during the prompt supercritical control rod withdrawal.

4. DISCUSSION AND CONCLUSION

This work presented the development of reference plant models of a pebble-bed high-temperature gas-cooled reactor (PB-HTGR) for the U.S. Nuclear Regulatory Commission (NRC) with the High-Temperature Gas Cooled Reactor–Pebble-Bed Module (HTR-PM) reactor as the reference. The reference plant models will serve as the foundation for the future development of detailed evaluation models based on license applications. The models were built with the Comprehensive Reactor Analysis Bundle (CRAB, or alternatively BlueCRAB), which is the code suite proposed to analyze the safety of non-light-water reactor (non-LWR) systems. Specifically, this work utilized the Griffin code for reactor physics, the Pronghorn and System Analysis Module (SAM) codes for core thermal fluids, the BISON code for solid conduction and fuel performance, and the SAM code for system-level analysis.

We performed equilibrium core steady-state and transient analyses using various models and coupling schemes with different codes and compared the results. Overall, the system responses were similar; some discrepancies due to differences in the modeling assumptions in different codes or models were observed. These findings are consistent with our understanding of the porous medium models in SAM and Pronghorn, as well as of the differences in 3D, 2D neutron diffusion, or point kinetics equation (PKE) models of reactor kinetics.

The main objective of this work was to assess BlueCRAB's level of readiness for modeling the PB-HTGR. This was achieved via the following tasks:

- Developing numerical models in BlueCRAB that include the majority of the physics relevant to this technology to ensure an adequate level of fidelity for modeling core performance during accident scenarios. This effort included various models of the equilibrium core:
    - 3D, 2D, and 0D/PKE core neutronics models with Griffin
    - 1D pebble streamline depletion models with Griffin
    - 3D and 2D thermal fluids porous media models with Pronghorn
    - 2D thermal fluids porous media models with SAM
    - 1D system-level models for the primary loop and reactor cavity cooling system (RCCS) with SAM
    - 1D pebble heat conduction model with BISON.
- Comparing the thermal fluid porous media models in Pronghorn and SAM with a 2D geometry for steady state with and without coupling to Griffin.
- Comparing the Pronghorn 2D porous media core model with boundary conditions and the coupled SAM 2D porous media core with the SAM 1D loop model for protected depressurized loss of forced cooling (DLOFC), pressurized loss of forced cooling (PLOFC), and unprotected over-cooling (UOC) transients.
- Comparing the SAM/Griffin/SAM, SAM/PKE/SAM, Pronghorn/Griffin/BC, and Pronghorn/PKE/BC models for the UOC transient.
- Performing a sensitivity analysis with SAM/PKE/SAM model for the UOC transient.
- Comparing Pronghorn/Griffin/BC and SAM/Griffin/SAM for the control rod withdrawal scenario.
- Testing the 3D capabilities of the thermal fluid porous media models in Pronghorn.
- Testing the 3D capabilities for a coupled equilibrium model with Griffin reactor physics and Pronghorn thermal fluids.
- Comparing 3D, 2D, and 0D/PKE models for two reactivity insertion accidents (RIAs) with control rod withdrawal scenarios that considered delayed and prompt supercritical reactivity insertions.

This work shows that the BlueCRAB models lead to physically intuitive solutions for the scenarios examined. The changes in the various scalar and vector fields such as neutron flux, power, temperature, density, pressure, and velocity are within the expected ranges, and their distributions can be explained by the system response during the transients. Several comparisons demonstrate that the porous media models in

Pronghorn and SAM can lead to similar solutions as long as the models are consistent and the same or similar closure models are used. The comparison of the SAM/Griffin/SAM and Pronghorn/Griffin models under steady-state equilibrium conditions shows that the solutions predicted by both models agree well with each other. In the core region, the results from the SAM and Pronghorn porous medium models agreed well as long as the same set of closure models was used. Some differences at the hot plenum due to differences in the modeling approaches adopted in the SAM versus the Pronghorn 2D models were observed.

This work also presented comparisons of the solutions obtained by 2D thermal fluid models of SAM and Pronghorn coupled to neutronics models of Griffin or PKE for different transient scenarios.

- Protected DLOFC accident: The comparisons showed good agreement between the 2D SAM and Pronghorn models. The predicted pebble surface temperatures from both models agreed well in terms of the maximum and average values as well as general trend. The same can be said about the overall time evolution of the temperature distribution in the reactor during the transient.
- Protected PLOFC accident: The average pebble surface temperatures from both models agreed well in terms of trend and peak values. The predicted maximum pebble surface temperatures showed good agreement in the early stage of the transient, but differences were observed in the later part of the transient, stemming from the modeling differences for the top plenum region and the RCCS. More importantly, both models predicted the formation of in-core natural circulation, which plays a crucial role in the redistribution and removal of decay heat during the transient.
- UOC transient: The overall trends of the reactor power, fuel, moderator, and pebble temperatures were similar. The peak power predicted by the SAM/Griffin/SAM model was slightly higher than that predicted by the Pronghorn/Griffin model, which in turn led to a higher peak fuel temperature. In both models, the reactor behaved as expected with respect to temperature change due to reactivity feedback, in which a drop in core temperature leads to an increase in power and vice versa.
- UOC transient coupled solution with PKE compared to the coupled solution with Griffin: There were power and temperature evolution differences for the SAM/PKE-standalone and SAM/Griffin. The solution of the Pronghorn/PKE-Griffin showed good agreement with the Pronghorn/Griffin solution for power and peak temperatures, and some differences in average temperatures were observed. The differences might relate to the PKE models developed with Pronghorn/Griffin being more sophisticated, the fuel and moderator temperatures being evaluated with heat conduction models, and/or the spatial variation of the feedback model being accounted for.
- RIA via control rod withdrawal transient: Generally, the solutions of SAM/Griffin and Pronghorn/Griffin agreed well in terms of power and temperature evolutions and peak power. The differences observed in the peak temperature values can be attributed to the differences in the developed models.

The performance of the 3D solution capabilities of the coupled code system of Pronghorn/Griffin was tested for steady-state and transient equilibrium core calculations. The 3D solution was used as a reference solution to assess the performance of the reduced-order models using 2D and 0D/PKE models for delayed and prompt supercritical RIAs via control rod withdrawal. With the same reactivity induced in both systems, the coupled 2D diffusion model produced results similar to those of the reference 3D diffusion model. It was determined that the coupled 2D diffusion model produces similar results compared to the reference 3D diffusion model with the same reactivity induced in both systems. However, the equivalent 2D model with the same control rod movement underpredicted the reactivity insertion and, as a result, the total power. Overall, the 0D/PKE results were reasonably close to the reference 3D diffusion model with the same reactivity induced in both systems, but it did exhibit evident differences in the time evolution of the solution. There were difficulties determining the precise value of the control rod reactivity insertion for the PKE models that would be equivalent to those in the 3D and 2D models. This indicates that either the feedback model requires

further improvement or that the procedure used to determine the value of the reactivity insertion needs further review. It is noteworthy that the reduced-order models were developed based on the 3D diffusion model; therefore, they do not constitute a credible predictive capability outside the evaluated transients.

In conclusion, this study demonstrates that BlueCRAB shows a satisfactory level of readiness for modeling PB-HTGRs. Considering the HTR-PM as a reference model, the simulation results for steady-state equilibrium core and various transient scenarios indicate that there is an ample safety margin based on the specifications, assumptions, and approximations in our models. While the results are promising, it is important to recognize that the validation of the BlueCRAB codes that are used to develop reference plant models and conduct analyses remains an area for future work. We want to emphasize that the objective of this study was not to validate BlueCRAB or perform a detailed safety analysis, but rather to assess its current applicability and readiness for modeling this reactor technology.

5. FUTURE WORK

In addition to demonstrating BlueCRAB's satisfactory level of readiness for modeling a PB-HTGR, this work also identified several potential areas for improving and refining the code, which are recommended for consideration by the Nuclear Energy Advanced Modeling and Simulation (NEAMS) program. Additionally, various aspects of the current models could be enhanced when the reference plant models are updated with detailed design information in support of NRC licensing activities. Below are the modeling methodologies refinement suggestions that we offer for NRC's consideration.

Suggested refinement areas for the neutronics model:

- Perform calculations for control rod withdrawal events using neutron transport instead of diffusion.
- Consider a higher-fidelity control rod model to provide a better approximation of the power peak that occurs during the transient.
- Develop a Monte Carlo reference model to verify the Griffin solution. Currently, we have a Serpent model with fresh fuel. We recommend developing an equilibrium core model.
- Include gamma heating of structures and components.
- Consider the Griffin calculation of fuel burnup in fissions per initial metal atom (FIMA).
- Deploy improved fluence calculation or radiation damage models for structures and components.
- Use fully correlated reactivity PKE models with surrogate reactivity models.
- Deploy macroscopic cross sections for transients with poison (Xe and Sm chains) tracking and a PBR decay heat model.

Suggested refinement areas for the thermal fluids modeling:

- Include the top plenum in the SAM 2D model to improve heat dissipation modeling in the top region of the core during a PLOFC.
- Add the capability to track fuel pebble failure in the core if the fuel temperature exceeds the safety limit.
- Determine the maximum power to fail a particular number of fuel particles.
- Improve and adopt the domain overlapping approach developed in Reference [48] for coupling the Pronghorn core model and SAM primary loop model in various transient simulations.
- Adopt the single-solve approach in coupling the SAM core model and the primary loop model in steady-state and transient simulations, and perform comparisons with the results of the domain-overlapping approach.

Furthermore, future work should include transient scenarios of interest for which the 2D or 3D modeling

can provide important insights, as listed below

- Steam/moisture ingress event: This event is caused by a steam generator tube rupture that allows steam/moisture to enter the primary loop and eventually the core. Possible consequences include positive reactivity insertion due to additional neutron moderation and graphite corrosion caused by the C/H_2O reaction.
- Air-ingress event: This event assumes a rupture in the primary loop or a double guillotine break at the co-axial duct leading to depressurization followed by air entering the system. Possible consequences include the oxidation of graphite due to C/O and C/CO_2 reactions, which can potentially compromise the integrity of the fuel pebbles and the graphite support structures in the core.
- Unprotected DLOFC with recriticality: An unprotected DLOFC could lead to a recriticality event following the decay of xenon and the cooldown of the system, considering a better neutron source to improve the prediction of the recriticality.
- Reactivity insertion events with concurrent pump trip.
- Station blackout.
- Seismic event.
- Loss of ultimate heat sink.

6. REFERENCES

[1] Wu, Z., Lin, D., and Zhong, D. (2002) The design features of the HTR-10. *Nuclear Engineering and Design,* **218**, 25–32.

[2] Tian, D., Shi, L., Sun, L., Zhang, Z., Zhang, Z., and Zhang, Z. (2020) Installation of the graphite internals in HTR-PM. *Nuclear Engineering and Design,* **363**, 110585.

[3] Zheng, Y., Stempniewicz, M. M., Chen, Z., and Shi, L. (2018) Study on the DLOFC and PLOFC accidents of the 200 MWe pebble-bed modular high temperature gas-cooled reactor with TINTE and SPECTRA codes. *Annals of Nuclear Energy,* **120**, 763–777.

[4] Zhang, Z., Dong, Y., Li, F., Zhang, Z., Wang, H., Huang, X., Li, H., Liu, B., Wu, X., Wang, H., Diao, X., Zhang, H., and Wang, J. (03, 2016) The Shandong Shidao Bay 200 MWe High-Temperature Gas-Cooled Reactor Pebble-Bed Module (HTR-PM) Demonstration Power Plant: An Engineering and Technological Innovation. *Engineering,* **2**, 112–118.

[5] Tang, C., Tang, Y., Zhu, J., Zou, Y., Li, J., and Ni, X. (2002) Design and manufacture of the fuel element for the 10 MW high temperature gas-cooled reactor. *Nuclear Engineering and Design,* **218**(1), 91–102.

[6] , Evaluation of the Initial Critical Configuration of the HTR-10 Pebble-bed reactor.. Technical Report HTR10-GCR-RESR-001, International Reactor Physics Experiment Evaluation Project (2006).

[7] Zheng, Y., Shi, L., and Dong, Y. (2009) Thermohydraulic transient studies of the Chinese 200MWe HTR-PM for loss of forced cooling accidents. *Annals of Nuclear Energy,* **36**(6), 742–751.

[8] Gou, F., Chen, F., and Dong, Y. (2018) Preliminary phenomena identification and ranking tables on the subject of the High Temperature Gas-cooled Reactor-Pebble Bed Module thermal fluids and accident analysis. *Nuclear Engineering and Design,* **332**, 11–21.

[9] Reitsma, F., Ivanov, K., Sartori, E., Lee, H. C., Daavittila, A., Leppanen, J., Girardi, E., Grimod, M., Koeberl, O., Massara, S., et al., PBMR Coupled Neutronics/Thermal-hydraulics Transient Benchmark. The PBMR-400 Core Design-Volume 1 The Benchmark Definition. Technical report, Organisation for Economic Co-Operation and Development (2013).

[10] Wang, Y., Prince, Z. M., Park, H., Calvin, O. W., Choi, N., Jung, Y. S., Schunert, S., Kumar, S., Hanophy, J. T., Labouré, V. M., et al. (2025) Griffin: A MOOSE-based reactor physics application for multiphysics simulation of advanced nuclear reactors. *Annals of Nuclear Energy,* **211**, 110917.

[11] Novak, A., Schunert, S., Carlsen, R., Balestra, P., Andrs, D., Kelly, J., Slaybaugh, R., and R., M., Pronghorn Theory Manual. Technical Report INL/EXT-18-44453-Rev001, Idaho National Laboratory (2020).

[12] Hu, R., Zou, L., Hu, G., Nunez, D., Mui, T., and Fei, T., SAM theory manual. Technical report, Argonne National Lab.(ANL), Argonne, IL (United States) (2021).

[13] R.L. Williamson et al. (2012) Multidimensional Multi-physics Simulation of Nuclear Fuel Behavior. *Jou. Nucl. Mat.,* **423**(149–163).

[14] Morris, R., CUBIT 15.0 User Documentation. Technical report, ETI, UT (2014).

[15] Sjaardema, G. D., Schoof, L. A., and Yarberry, V. R. EXODUS: A Finite Element Data Model Sandia National Laboratories (2008).

[16] Marleau, G., Hébert, A., and Roy, R., A USER GUIDE FOR DRAGON VERSION5. Technical Report IGE–335, Ecole Polytechnique de Montreal (10, 2020).

[17] Brown, D., Chadwick, M., Capote, R., Kahler, A., Trkov, A., Herman, M., Sonzogni, A., Danon, Y., Carlson, A., Dunn, M., Smith, D., Hale, G., Arbanas, G., Arcilla, R., Bates, C., Beck, B., Becker, B., Brown, F., Casperson, R., Conlin, J., Cullen, D., Descalle, M.-A., Firestone, R., Gaines, T., Guber, K., Hawari, A., Holmes, J., Johnson, T., Kawano, T., Kiedrowski, B., Koning, A., Kopecky, S., Leal, L., Lestone, J., Lubitz, C., Márquez Damián, J., Mattoon, C., McCutchan, E., Mughabghab, S., Navratil, P., Neudecker, D., Nobre, G., Noguere, G., Paris, M., Pigni, M., Plompen, A., Pritychenko, B., Pronyaev, V., Roubtsov, D., Rochman, D., Romano, P., Schillebeeckx, P., Simakov, S., Sin, M., Sirakov, I., Sleaford, B., Sobes, V., Soukhovitskii, E., Stetcu, I., Talou, P., Thompson, I., van der Marck, S., Welser-Sherrill, L., Wiarda, D., White, M., Wormald, J., Wright, R., Zerkle, M., Žerovnik, G., and Zhu, Y. (2018) ENDF/B-VIII.0: The 8th Major Release of the Nuclear Reaction Data Library with CIELO-project Cross Sections, New Standards and Thermal Scattering Data. *Nuclear Data Sheets,* **148**, 1–142 Special Issue on Nuclear Reaction Data.

[18] Park, H., Jung, Y. S., Lee, C., Wang, Y., and Ortensi, J. (2024) Initial Assessment of Online Cross Section Generation Capability of Griffin for Gas-Cooled Pebble-bed Reactor. In *Int. Conf. on Physics of Reactors*.

[19] Jaradat, M. K., Schunert, S., and Ortensi, J., Gas-Cooled High-Temperature Pebble-Bed Reactor Reference Plant Model. Technical report, Idaho National Laboratory (INL), Idaho Falls, ID (United States) (04, 2023).

[20] Schunert, S., Ortensi, J., Wang, Y., Balestra, P., Jaradat, M., Calvin, O., Hanophy, J., and Harbour, L. (2023) An equilibrium core depletion algorithm for pebble-bed reactors in the Griffin code. *Annals of Nuclear Energy,* **192**, 109980.

[21] She, D., Xia, B., Guo, J., Wei, C.-L., Zhang, J., Li, F., and Zhang, L. S. Z.-Y. (2021) Prediction calculations for the first criticality of the HTR-PM using the PANGU code. *Nuclear Science and Techniques,* **32**.

[22] Slaughter, A. E., Prince, Z. M., German, P., Halvic, I., Jiang, W., Spencer, B. W., Dhulipala, S. L., and Gaston, D. R. (2023) MOOSE Stochastic Tools: A module for performing parallel, memory-efficient in situ stochastic simulations. *SoftwareX,* **22**, 101345.

[23] Jaradat, M. K., Schunert, S., Gleicher, F. N., Labouré, V. M., and DeHart, M. D. (2024) Forward and inverse predictive transient models of TREAT using surrogate reactivity models. *Annals of Nuclear Energy,* **201**, 110449.

[24] Jaradat, M. K., Schunert, S., Gleicher, F. N., and DeHart, M. (2025) Temperature Prediction for the Sirius-2c Nuclear Propulsion Fuel Experiment Conducted at the TREAT Facility. *Nuclear Science and Engineering,* **0**(0), 1–17.

[25] Ortensi, J. and Balestra, P. (2022) Initial study on cross-section generation requirements for a PBR equilibrium core. In *PHYSOR 2022, Making Virtual a Reality - Advancements in Reactor Physics To Leap Forward Reactor Operation and Deployment*.

[26] Lieberoth, J. and and, A. S. (1980) Neutron Streaming in Pebble Beds. *Nuclear Science and Engineering,* **76**(3), 336–344.

[27] Benoist, P. (1968) Streaming Effects and Collision Probabilities in Lattices. *Nucl. Sci. Eng.,* **34**, 285–307.

[28] Kadak, A. C. and Bazant, M. Z. (2004) Pebble Flow Experiments For Pebble Bed Reactors.

[29] Gaston, D. R., Permann, C. J., Peterson, J. W., Slaughter, A. E., Andrs, D., Wang, Y., Short, M. P., Perez, D. M., Tonks, M. R., Ortensi, J., Zou, L., and Martineau, R. C. (2015) Physics-based multiscale coupling for full core nuclear reactor simulation. *Annals of Nuclear Energy,* **84**, 45–54.

[30] Lemmon, E. W., McLinden, M. O., and Friend, D. G. (June 24, 2021) Thermophysical Properties of Fluid Systems, NIST Chemistry WebBook, NIST Standard Reference Database Number 69, Eds. P.J. Linstrom and W.G. Mallard, National Institute of Standards and Technology, .

[31] Ausschuss, K. (1983) Auslegung der Reaktorkerne von gasgekühlten Hochtemperaturreaktoren. *Sicherheitstechnische Regel des KTA,* **3102**.

[32] Van Antwerpen, W., Du Toit, C., and Rousseau, P. G. (2010) A review of correlations to model the packing structure and effective thermal conductivity in packed beds of mono-sized spherical particles. *Nuclear Engineering and design,* **240**(7), 1803–1818.

[33] Lindsay, A., Giudicelli, G., German, P., Peterson, J., Wang, Y., Freile, R., Andrs, D., Balestra, P., Tano, M., Hu, R., Zou, L., Gaston, D., Permann, C., and Schunert, S. (2023) MOOSE Navier–Stokes module. *SoftwareX,* **23**, 101503.

[34] Giudicelli, G., Green, C., Hansel, J., Andrs, D., Novak, A., Schunert, S., Spaude, B., Isaacs, S., Kunick, M., Salko, R., Henderson, S., Charlot, L., and Lindsay, A. (2025) The MOOSE fluid properties module. *Computer Physics Communications,* **307**, 109407.

[35] Schunert, S., Mohammad Jaradat, M. K., Calvin, O. W., Giudicelli, G. L., Lindsay, A. D., Wang, Y., Tano Retamales, M. E., and Walker, S. A., Improvements in High Temperature Gas Cooled Reactor Modeling Capabilities in the Pronghorn Code. Technical report, Idaho National Laboratory (INL), Idaho Falls, ID (United States) (09, 2022).

[36] Zhang, Z., Wu, Z., Wang, D., Xu, Y., Sun, Y., Li, F., and Dong, Y. (2009) Current status and technical description of Chinese 2 x 250MWth HTR-PM demonstration plant. *Nuclear Engineering and Design,* **239**(7), 1212 – 1219.

[37] Roberto, T. D., Lapa, C. M., and Alvim, A. C. (2020) Scaling analysis of reactor cavity cooling system in HTR. *Nuclear Technology,* **206**(4), 527–543.

[38] Huxford, A., Leite, V. C., Merzari, E., Zou, L., Petrov, V., and Manera, A. (2023) A hybrid domain overlapping method for coupling System Thermal Hydraulics and CFD codes. *Annals of Nuclear Energy,* **189**, 109842.

[39] Ortensi, J., Reger, D., Jaradat, M. K., Yang, G., Zou, L., and Hu, R., Fluoride-Cooled High-Temperature Pebble-Bed Reactor Reference Plant Model Updates. Technical report, Idaho National Laboratory (INL), Idaho Falls, ID (United States) (06, 2025).

[40] Ooi, Z. J., Zou, L., Hua, T., Fang, J., and Hu, R., Modeling of a Generic Pebble Bed High-temperature Gas-cooled Reactor (PB-HTGR) with SAM. Technical report, Argonne National Laboratory (ANL), Argonne, IL (United States) (09, 2022).

[41] Jaradat, M. K., Schunert, S., and Ortensi, J. (2023) Modeling The DLOFC Accident Scenario of HTR-PM Equilibrium Core Using NEAMS Tools. In *American Nuclear Society* American Nuclear Society.

[42] Breitbach, G. and Barthels, H. (1979) Radiant heat transfer in the HTR core after failure of the afterheat removal systems. *Trans. Am. Nucl. Soc.;(United States),* **31**(CONF-790519-).

[43] (2001) Heat Transport and Afterheat Removal for Gas Cooled Reactors under Accident Conditions, Number 1163 in TECDOC SeriesInternational Atomic Energy Agency, Vienna.

[44] Zhang, Z., Dong, Y., Li, F., Huang, X., Zheng, Y., Dong, Z., Zhang, H., Chen, Z., and Li, X. (2024) Loss-of-cooling tests to verify inherent safety feature in the world's first HTR-PM nuclear power plant. *Joule,* **8**(7), 2146–2159.

[45] , PBMR coupled neutronics/thermal-hydraulics transient benchmark the PBMR-400 core design. Technical Report Tech. Rep. NEA/NSC/DOC(2013)10, OECD/NEA (2013).

[46] Adams, B., Bohnhoff, W., Dalbey, K., Ebeida, M., Eddy, J., M.S., E., Hooper, R., Hough, P., Hu, K., Jakeman, J., et al., Dakota 6.21.0 Documentation. Technical Report SAND2024-154920, Sandia National Laboratories (November, 2024).

[47] Mui, T., Hu, R., and Zhang, G. (2019) Uncertainty Quantification on SAM Simulations of EBR-II Loss-of-Flow Tests. In *International Topical Meeting on Nuclear Reactor Thermal Hydraulics (NURETH-18)*.

[48] Schunert, S., Tano Retamales, M. E., and Mohammad Jaradat, M. K., Overlapping Domain Coupling of Multidimensional and System Codes in NEAMS - Pronghorn and SAM. Technical report, Idaho National Laboratory (INL), Idaho Falls, ID (United States) (05, 2023).